Solar wind – Predicted magnetospheric influence and near-Sun environment

Dissertation
zur Erlangung des mathematisch-naturwissenschaftlichen Doktorgrades
"Doctor rerum naturalium"
der Georg-August-Universität Göttingen

im Promotionsprogramm PROPHYS
der Georg-August-University School of Science (GAUSS)

vorgelegt von
Malte S. Venzmer
aus Bremerhaven

Göttingen, 2018

Betreuungsausschuss

Name, Arbeitsgruppe, Institut

Name, Arbeitsgruppe, Institut

Name, Arbeitsgruppe, Institut

Mitglieder der Prüfungskommission

Referent:
Name, Arbeitsgruppe, Institut

Koreferent:
Name, Arbeitsgruppe, Institut

ggf. 2. Koreferent:
Name, Arbeitsgruppe, Institut

Weitere Mitglieder der Prüfungskommission:

Name, Arbeitsgruppe, Institut

Name, Arbeitsgruppe, Institut

Name, Arbeitsgruppe, Institut

Name, Arbeitsgruppe, Institut

Tag der mündlichen Prüfung: ________________

Solar wind – Predicted magnetospheric influence and near-Sun environment

Malte S. Venzmer

title?

middle name?

english vs deutsch?

make cover page image...; combine figs 4.9+4.10

University of Göttingen logo?

Institute for Astrophysics logo?

January 2012 – April? 2018

german title and abstract?

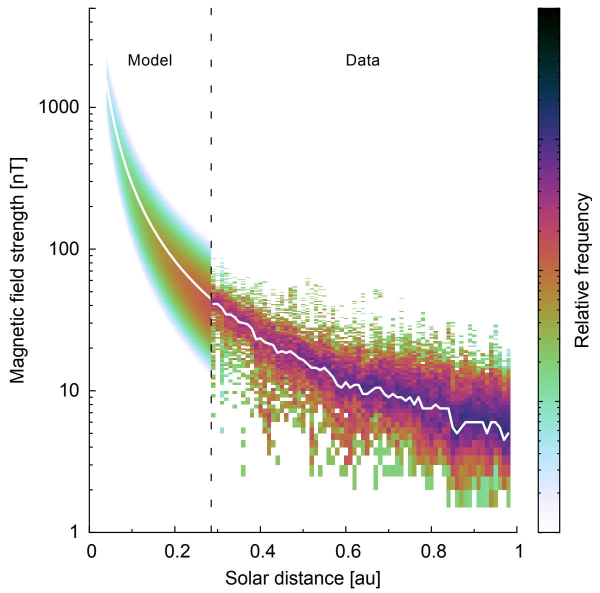

The electronic version of this document is fully hyperlinked. The external links in some figure captions and in the references are not accessible in the printed version. All external links in this document were valid in 2018-XX-XX.

version log:

1 2013-11-06

2 2013-11-07 inserted lem excerpt

3 2014-09-01 outlined introduction structure and appendix key words

4 2014-09-11 bibtex included, lem excerpt citet

5 2014-09-12 included italic titles in bibliography

6 2015-01-12 worked on introduction structure and included magnetic butterfly diagram

7 2015-05-04 first printout, small additions

8 2015-07-03 coupling functions, content structure

9 2015-09-09 Alfvén wave velocity formula

10 2015-09-10 Appendix physics: Alfvén and compressional MHD waves, plasma beta; citation sources Cranmer2005, Kivelson1995

20 2015-10-14 variance fit values; log-normal citation Bronstein

30 2015-12-09 splitting analyses chapter into two; browsing folders for usable things for thesis

40 2016-02-18 analysesI structure

50 2016-03-18 solar surface

65 2016-04-14 analysesI sws structure draft plots

80 2016-06-10 Offline Anmerkungen einarbeiten

100 2016-07-30 line-up structure

120 2016-09-27 minor tweaks in analyses II

140 2017-04-22 set up git repository

160 2017-11-17 Zhao copyright symbol included; solar wind; commata and sentence wording

180 2017-12-21 B-field: four plots upgraded

200 2018-01-28 chapter2 implemented into thesis; figure folders rearranged; figures floatrow implemented

220 2018-02-20 HCS in sw section

230 2018-03-04 CMEs.tex VI, BSS

240 2018-03-16 chapter2 offline corrections implemented

250 2018-03-31 Adams comments for PSP chapter; sectioning space weather + magnetosphere

260 2018-04-11 magnetosphere 3; reconnection figure

270 2018-04-25b R-M effect

275 2018-05-02 geomagnetic storms 3

280 2018-05-08 kp index

285 2018-05-12 coupling functions

286 2018-05-13 coupling functions 3

287 2018-05-14 coupling functions 4

288 2018-05-17 implementing offline comments: coupling functions

289 2018-05-30 coupling functions 5

290 2018-05-31 Kp forecast

291 2018-06-01 implementing offline comments: Kp forecast

292 2018-06-02 implementing offline comments 2: coupling functions
293 2018-06-03 Kp empirical functions
294 2018-06-04 Kp empirical functions 2
295 2018-06-05 Wing Kp model
296 2018-06-07 prediction performance and true skill score
297 2018-06-10 appendix: true skill statistics
298 2018-06-11 appendix: true skill statistics; Kp persistence
299 2018-06-12 chapter2: prediction performance, TSS, statistics table
300 2018-06-13 chapter2: TSS
2018-06-13 18:22 – last save

"Despite the 'Dr.' before his name, he had completed no course of study and received no degree. When people tried to pin him down about this, he would say that the letters were merely an abbreviation of his first name - Drummond - which he did not use. But it was as 'Dr.' Sam Laserowitz that he appeared in a number of science-fiction magazines; he was also known, in the circles of the fans of that genre, as a lecturer, and spoke on 'cosmic' themes at their many conferences and convention. Laserowitz's speciality was earthshaking discoveries, wich he happened upon two or three times a year. [...] We really have no idea what a multitude of con men and crackpots inhabit the domain that lies halfway between contemporary science and the insane asylum."

Excerpt from Stanisław Lem 1968, *His Master's Voice* (Lem & Kandel 1984, p. 38).

Abstract

This thesis analyzes, and derives predictions of how strong solar wind and coronal mass ejections impact the terrestrial magnetosphere and how the solar wind environment scales in the near-Sun region. Near-Earth in-situ solar wind measurements, consisting of 35 years of minutely OMNI data, are analyzed together with the time series of the planetary geomagnetic disturbance indicator *Kp*. Correlations and functional dependencies are compiled with regard to nowcast the magnitude of the geomagnetic disturbances from in-situ solar wind measurements and to forecast them from remotely observed solar wind streams and CMEs. Further, 53 years of hourly OMNI data and sunspot number data are correlated for the purpose of deriving functional dependencies with the state of the solar cycle for the key solar wind parameters magnetic field strength, proton velocity, density, and temperature. Solar wind in-situ data from the Helios 1 and 2 missions, operational in the 1970s and orbiting the Sun within the distance range 0.3–1.0 au, are analyzed and empirical solar wind distance dependencies are derived. Additionally, in view of the planned near-Sun spacecraft mission Parker Solar Probe (PSP) with a planned launch in mid 2018, the solar wind environment is estimated down to PSP's closest perihelion at 9.86 solar radii.

Contents

1 Introduction

Background -> problems -> motivation -> methods -> results

The abundance of modern technological systems that are sensitive to disturbances in the terrestrial mangetic field increases.
These include critical systems, such as ..., whose potential disruptions would not only have severe economical impacts but would affect human lives as well.
The disturbances in the terrestrial magnetic field (geomagnetic storms) are evoked by the field's interaction with streams of particles emitted by the Sun (solar wind).
Variations in some solar wind parameters lead to a direct response in geomagnetic activity.
This work aims to quantify this response for different solar wind forecast situations.
For when magnetic field and velocity information is available and for when only velocity information is available and it is known whether it is ambient solar wind or a CME event.

Open key questions are which mechanisms heat the corona and accelerate the solar wind.
The PSP mission is intended to clarify this.
As it is the first s/c to fly that near to the Sun, the solar wind environment is not known.
This is the motivation for the second part of this work.
This work derives estimates of that solar wind environment.

thesis goal: finding more precise relationships between parameters/quantities for being able to make better forecasts

catch from chapter abstracts...

This thesis presents quantitative analyses of the solar wind impact strengh on the terrestrial magnetosphere and of the estimated near-Sun solar wind environment.

I structured this work as follows: The fundamentals about the Sun, its activity, solar wind, and space weather are laid in Chapter 2. The instrumentation and data sources used in this work are described in Chapter 3. The influences on the *Kp* index from solar activity, solar wind, CMEs, and solar wind streams are analyzed in Chapter 4. In Chapter 5, which is followed by the published paper on the same topic (integrated as Chapter 6), an empirical solar wind model for the inner heliosphere is developed and used to estimate the near-Sun solar wind environment for the planned PSP mission. Chapter 7 summarizes the results and gives an outlook for further studies. Useful equations and information are located in the Appendix A.

2 Background knowledge

This chapter summarizes the basic knowledge necessary for understanding the analyses performed in this work. First, the Sun's origin, inner structure, atmosphere and heliosphere are described. Then, the Sun's dynamics with its differential rotation and magnetic field generation are outlined. Further, the solar activity cycle is described, including the meridional flow circulation, appearance of active regions, the surface magnetic field change, and sunspot cycles. The heliospheric magnetic field is pictured from its photospheric emergence in magnetic bright points and coronal superradial expansion, through the formation of the heliospheric current sheet and the Parker spiral to the heliosheath. The solar wind and its properties, the origins of slow and fast streams, stream interaction regions, and coronal mass ejections are described. Furthermore, space weather, solar influence on Earth, the magnetosphere, solar wind-magnetosphere coupling, and geomagnetic indices are portrayed.

2.1 The Sun

13.8 billion years ago the Big Bang formed our universe. The energy density of our universe consists of 69.1 % dark energy, 25.9 % dark matter and 4.9 % baryonic matter, according to calculations using the inflationary ΛCDM[1] cosmology together with the latest cosmic microwave background temperature measurements (Planck Collaboration et al. 2016). After a few minutes the primordial nucleosynthesis left the universe in a state where the baryonic matter was composed of 75.33 %[2] hydrogen, 24.67 % helium and traces of deuterium, tritium and lithium (Planck Collaboration et al. 2016).

Over millions of years this gas cooled down and gravitationally accreted into molecular clouds and formed stars. The first generations of stars (Population III) fused this gas to heavier elements (metals) and supernovae distributed them into space as a foundation for the formation of new stars of low and high metallicity (Population II and I). Likewise, supernovae of these stars constantly enriched the interstellar medium with metals. Now, the interstellar medium in the Milky Way consists of about 32 % helium and traces of other metals (Danziger 1970).

Our Sun, a metal-rich Population I yellow dwarf star, emerged 4.6 billion years ago (Bahcall et al. 1995) from an accretion disk, formed by a collapsing rotating cloud. The compression within its center resulted in high temperatures, which initiated the fusion of hydrogen to helium (primarily pp chain reaction). The fusion reactions produce huge amounts of energy and heat the solar center to a temperature of 15.7 million kelvins (Christensen-Dalsgaard et al. 1996). The generated energy is transported through the solar body to its surface and eventually into space. The core region extends to about 0.25 solar radii ($R_\odot$), where the declining temperature becomes insufficient for fusion reactions. The energy transport is dominated by thermal radiation until, because of declining ionization and density, at 0.71 $R_\odot$ up to the surface convective motion takes over (Christensen-Dalsgaard et al. 1991).

The temperature at this transition region, called tachocline, is about 2 million kelvins and decreases up to the solar surface to between 4400–6600 K[3]. Here at the photosphere, the energy is radiated away with an effective black body temperature of 5772 K (Mamajek et al. 2015), classifying the Sun as a spectral type G2V star. At this surface layer, granules, the tops of convection cells, and temporary sunspots are visible. Strong magnetic flux inhibits the convection at sunspots, leading to lower temperature and brightness (for more on sunspots see the following Sections 2.2 and 2.3). Figure 2.1 illustrates these photospheric features along with the inner solar structure.

Above the photosphere at the base of the chromosphere, the temperature declines to its solar minimum of 3800 K until it raises to 2–3 million kelvins in the corona (Billings 1959; Liebenberg et al. 1975). Up to now it is not fully understood why the corona is so much hotter than the underlying chromosphere – this question is known as the coronal heating problem (Klimchuk 2006; McComas et al. 2007; Fox et al. 2015). The generally considered energy transfer mechanisms are magnetic reconnections, wave heating and type II spicules or a combination of these (Cranmer et al. 2017).

[1] ΛCDM: Lambda cold dark matter
[2] Percentages by mass.
[3] NASA Sun fact sheet: https://nssdc.gsfc.nasa.gov/planetary/factsheet/sunfact.html

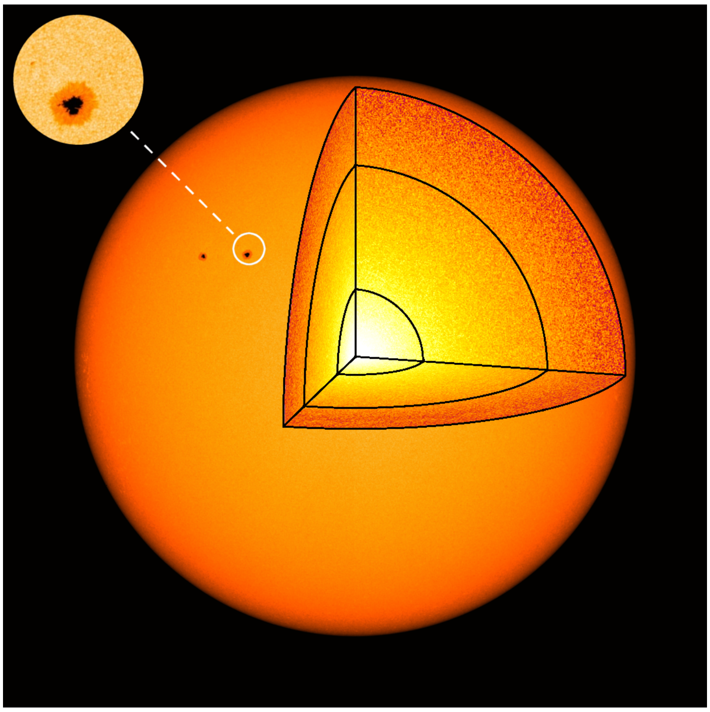

Figure 2.1 Image of the photosphere from 20 March 2016 together with a schema of the solar interior structure. The inset shows the granular surface with a sunspot. I created this figure based on a SDO/HMI continuum image, credit: NASA/SDO and the AIA, EVE and HMI science teams.

The chromosphere is a 2000 km thick region, whose features – numerous spicules, filaments, and prominences – can reach far into the corona. They consist of chromospheric material, channeled by the solar magnetic field, and are enveloped by a thin transition region where the temperature jumps up from about 30 000 K[4] to coronal temperatures. Reconnection of magnetic field lines can result in the eruption of filaments into the corona and beyond, termed coronal mass ejections (CMEs), see also Subsection 2.5.4. Details of chromospheric features are shown in Figure 2.2 – the images were taken on the same day as in Figure 2.1.

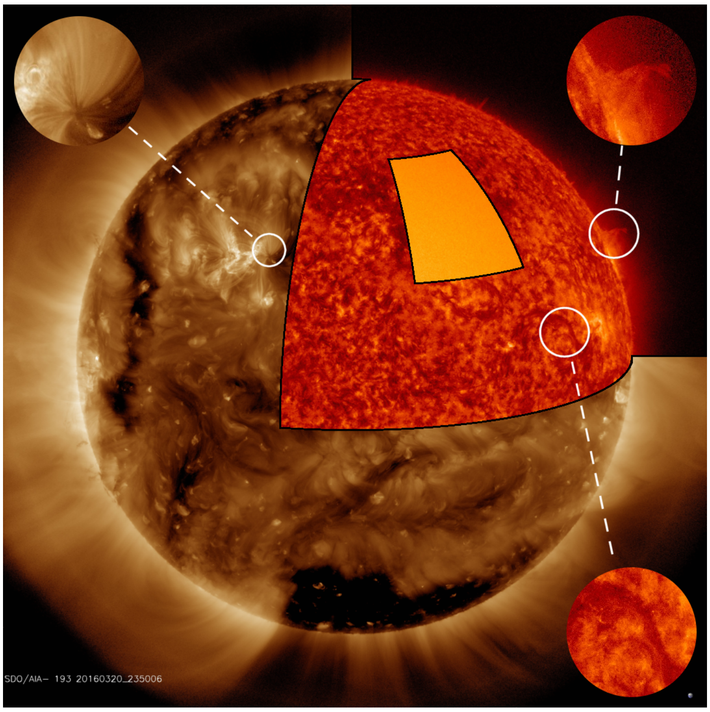

Figure 2.2 Composite image of the solar atmosphere from 20 March 2016 and some details of its features. Corona, chromosphere and photosphere are seen in wavelengths of 193 Å, 304 Å, and continuum. Chromospheric spicules are visible on the northern limb. The enlargements on the right show a prominence and a filament. The dark region at the south pole is a coronal hole. The left inset shows details of the active region belonging to the sunspots shown in Figure 2.1. I created this figure based on SDO/AIA images, credit: NASA/SDO and the AIA, EVE and HMI science teams.

The Sun's atmosphere is dominated by the varying small- and large-scale solar magnetic field configuration. There are regions where the magnetic field lines arc back to the surface and regions with open field lines. In the latter areas the coronal plasma can – guided by the field – escape into space. Thus these coronal areas are less

[4] NASA Sun fact sheet: https://nssdc.gsfc.nasa.gov/planetary/factsheet/sunfact.html

dense, cooler and therefore appear darker in extreme ultraviolet (EUV) and are called coronal holes (CHs). In Figure 2.2 a coronal hole is visible at the solar south pole.

From Earth, the faint corona and chromosphere can only be observed during eclipses, because of the brightness of the solar disk. There are three effects contributing to the visibility of the corona: photons scattering off free electrons, producing a continuous spectrum; photons scattering off dust particles, their spectrum contains Fraunhofer absorption lines; and ion spectral emission lines – these contributions to the corona are termed K-, F- and E-corona[5]. Images from solar eclipses reveal the coronal plasma, shaped by the magnetic field, and red prominences from the chromosphere. The solar eclipse imaged in Figure 2.3 shows the magnetic field's dipole structure and the equatorial streamer belt, characteristic for a quiet Sun during cycle minimum.

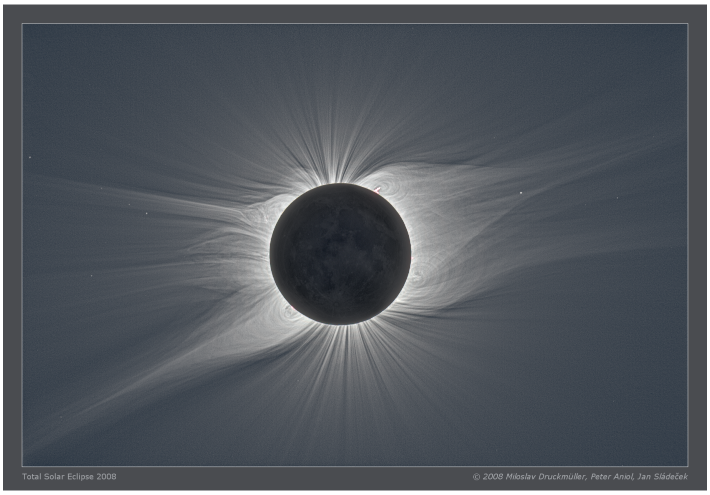

Figure 2.3 Total solar eclipse image of the inner corona up to a distance of five solar radii. The picture was taken in Mongolia, 1 August 2008 and is processed from multiple images. Credit: Miloslav Druckmüller, Peter Aniol, Jan Sládeček, 2008, reproduced with permission.

Due to the high coronal temperatures, plasma escapes the solar gravitational field (Parker 1958) with velocities of 200–800 km s^{-1}. Its acceleration is linked to the coronal heating – however, the exact location and process remain an open question (Hollweg 1985; McComas et al. 2007; Fox et al. 2015; Cranmer et al. 2017). The magnetic field becomes too weak to guide the coronal plasma at a distance of a few solar radii. From this so-called source surface, the solar wind flows radially outward into space until it reaches the termination shock. Eventually it collides with the local interstellar medium, creating the boundary of the heliosphere, the heliopause. The heliopause is expected to be a bubble of either teardrop or croissant shape, caused by the Sun's relative velocity of 23 km s^{-1} with respect to the local interstellar medium (Owens & Forsyth 2013; Opher et al. 2015). Thus, there may exist a leading bow shock. Measurements of the Voyager 1 and 2 spacecraft indicate their passage of the termination shock at about 94 au and 84 au, entering the heliosheath region (Owens & Forsyth 2013). Gurnett et al. (2013) report that in 2012 Voyager 1 actually crossed the heliopause into interstellar space at a solar distance of 121 au. The heliosphere and its surrounding flow structure is illustrated in Figure 2.4.

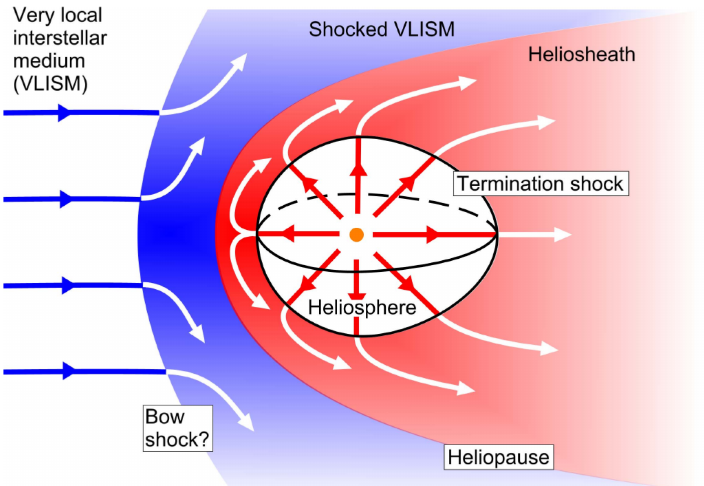

Figure 2.4 Schema of the heliosphere and its surrounding flow structure, formed by the interaction of the solar wind (red) with the local interstellar medium (blue) at the heliopause. Credit: Owens & Forsyth (2013, Fig. 9), licensed under CC BY-NC 3.0 DE.

On its way outwards through the solar system, the solar wind – carrying the solar magnetic field – interacts

[5] K from kontinuierlich (continuous in german), F from Fraunhofer, and E from emission.

with the planets, their magnetic fields and other solar system bodies. This has various effects, for instance disturbances in planetary magnetic fields with appearance of aurorae and enhanced radiation, atmospheric losses and stripping of cometary tails. Some of these effects can have disruptive consequences for humans and their technology, creating a high interest in understanding space weather and forecasting its effects, the topic of space weather is further addressed in Section 2.6. The magnitudes of these effects depend highly on spatial and temporal variations in the solar wind, which are rooted in the dynamics of the solar magnetic field, described in the following sections.

2.2 Solar dynamo

The conservation of the angular momentum in the contracting molecular cloud led to a rotation of the Sun. Although the Sun experiences loss of angular momentum due to solar wind (Weber & Davis 1967), its rotation still has a current average period of about 25 days. The radial convective motion within the solar interior above the tachocline leads to a transport of momentum away from the rotation axis and therefore to a slower polar and faster equatorial rotation in the convection zone (Miesch 2005). This differential rotation is visible on the surface and was first discovered from sunspot observations by Scheiner (1630). With a rotation period of about 34 days, the poles have a lag of almost 9 days (for further information on solar rotation see appendix Section A.1). The differential rotation in the solar interior can be inferred from helioseismological observations. Below the differential rotation of the convection zone, a nearly solid rotation with a period of about 26.6 days (this corresponds to a frequency of 435 nHz) exists in the radiation zone, as shown in Figure 2.5.

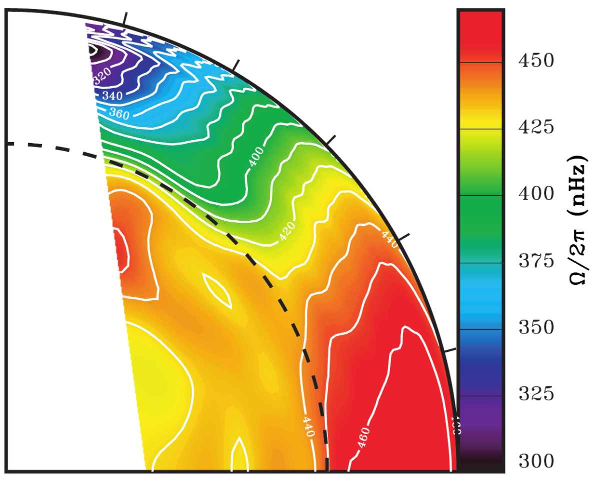

Figure 2.5 Rotation frequency profile of the solar interior. The location of the tachocline is indicated by the dashed line. The rotation frequency is inferred from helioseismology via observations from the Michelson Doppler Imager (MDI) at the Solar and Heliospheric Observatory (SOHO) spacecraft. Credit: Thompson et al. (2003, Fig. 3), © Annual Reviews, reproduced with permission.

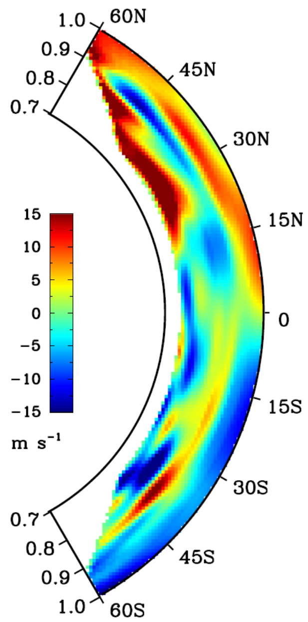

Figure 2.6 Meridional flow velocity profile in part of the convection zone. Positive values are directed towards north. The velocity is inferred from helioseismology via observations from the Helioseismic Magnetic Imager (HMI) at the Solar Dynamics Observatory (SDO) spacecraft. Credit: Zhao et al. (2013, Fig. 4, panel (a), I moved the colorbox), © AAS, reproduced with permission.

Turbulent plasma motions from convective flows in the convection zone generate and carry disorganized magnetic flux. The large rotational shear at the tachocline stretches and amplifies the magnetic fields to strong coherent toroidal flux (ω-effect) with intensities of the order 1–10 T. These toroidal fields, generated near the bottom of the convection zone, can be stored in a deep magnetic layer located in the stably stratified region below the convection zone (Ossendrijver 2003). The stronger flux ropes become buoyant and raise to the surface. The Coriolis force twists them systematically on their way through the convection zone (α-effect). The twist is stronger at higher latitudes (Joy's law). The flux ropes emerge then in the photosphere as bipolar active regions of opposite magnetic polarity – the stronger ones forming pairs of sunspots, as seen in Figure 2.7. Turbulent convective diffusion of this surface flux contributes to the build-up of poloidal fields. Their resulting

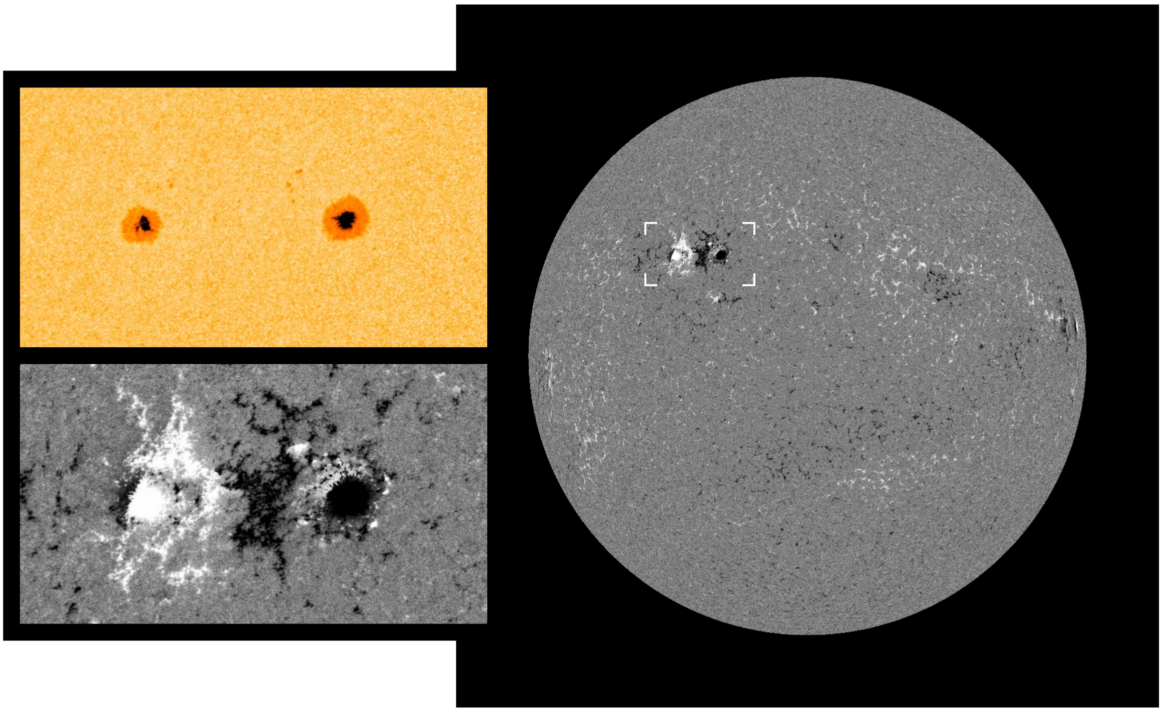

Figure 2.7 Continuum image of the two sunspots pictured in Figure 2.1 (top left), magnetogram from the same region (bottom left), and magnetogram from the whole solar disk (right). The magnetogram shows the polarity of the line-of-sight magnetic field component at the photosphere (black/white: inward/outward polarity). The highly concentrated magnetic flux at the sunspots is visible as well as the extended bipolar magnetic field structure of the whole active region, which is divided by the so-called magnetic neutral line. The solar disk is scaled to the same size as in Figure 2.1. I created the figure based on SDO/HMI continuum and magnetogram images from 20 March 2016, credit: NASA/SDO and the AIA, EVE and HMI science teams.

polarity is opposite to the prevailing global field due to the directional way the rotational shear at the tachocline and the Coriolis force in the convection zone act. Fluctuating motions further amplify the mean fields in these processes. This solar α-ω-dynamo is thought to create the major part of the solar magnetic field. Still, with regard to the magnetic field's high variability, the long-term mean fields are governed by intermittent localized structures, that is, active regions, filaments and coronal loops (Miesch 2005).

2.3 Solar activity cycle

Helioseismic measurements reveal that the large-scale convective flow is aggregated into large convection cells with slow meridional flows of a few $\mathrm{m\,s^{-1}}$, as can be seen in Figure 2.6. A poleward subsurface flow and equatorward backflow beneath with a further poleward flow below are detected within each hemisphere, comprising a stacked double-cell profile (Zhao et al. 2013). The meridional circulation flow speed has a major influence on the average 22-year period of the emerging magnetic flux at the solar surface. This period varies and is influenced by the stochastic emergence rate and tilts of active regions and the diffusion from random convective motions (Hathaway & Upton 2016). The surface magnetic field configuration changes within one period from a dipole structure to a reversed dipole structure with opposite polarity and back, completing a so-called Babcock-Leighton dynamo cycle. Thus, the transition time from one dipole state to the next lasts about 11 years, this period is defined as one solar cycle.

In the transition phase, magnetic flux emerges in belts above and below the solar equator, manifesting as bipolar active regions with sunspots, resulting in a toroidal/multipolar structured magnetic field. Sunspots appear at about $\pm 20°$ latitude at the beginning of a cycle, this shifts towards lower latitudes at the end of a cycle. Thus the plot of sunspots over latitude and time reveals a butterfly pattern (Maunder 1904). This butterfly pattern appears in surface radial magnetic field observations as well, see Figure 2.8. The leading polarity of bipolar regions is opposite in both hemispheres and the leading polarity changes with each solar cycle, this is called Hale's polarity law. The emerging flux is carried by the slow meridional surface flow poleward, canceling the current dominating polar field polarity and eventually resulting in the polar field switch (Hathaway 2015).

Since regions of strong magnetic flux are visible as sunspots on the photosphere, they were known well

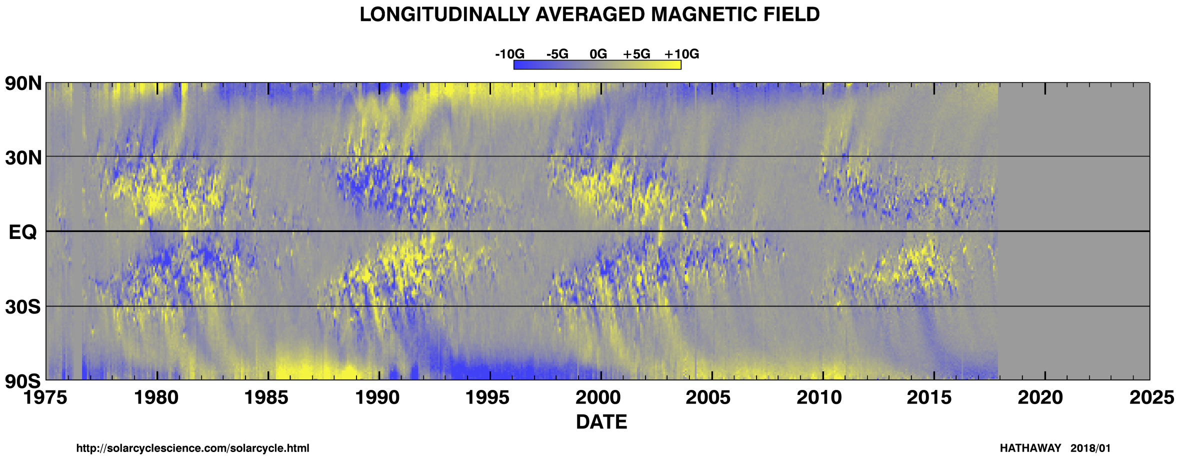

Figure 2.8 Magnetic butterfly diagram of the longitudinally averaged radial magnetic field on the solar surface. Yellow represents an outward directed magnetic field (positive), blue inward (negative). The data is obtained from instruments on Kitt Peak National Observatory and from the MDI at the SOHO spacecraft. Courtesy of David Hathaway, Solar Cycle Science, 2018, updated version of Hathaway (2015, Fig. 17).

before the common era by greek and chinese scholars (Clark & Stephenson 1978; Vaquero 2007). Systematic sunspot observations exist since 1610, shortly after the invention of the telescope. In 1843 Schwabe discovered the 11-year periodicity in the sunspot occurence (Schröder 2004, p. 124). In 1848 Wolf introduced the sunspot number (SSN) and the solar cycle number to record these cycles (Hathaway 2015). The SSN observations, see Figure 2.9, show large variations in cycle length (9–14 years) and cycle amplitude, with peak SSNs in the range 0–300, (Hathaway 2015). There also exist long-term variations, such as secular cycles of different

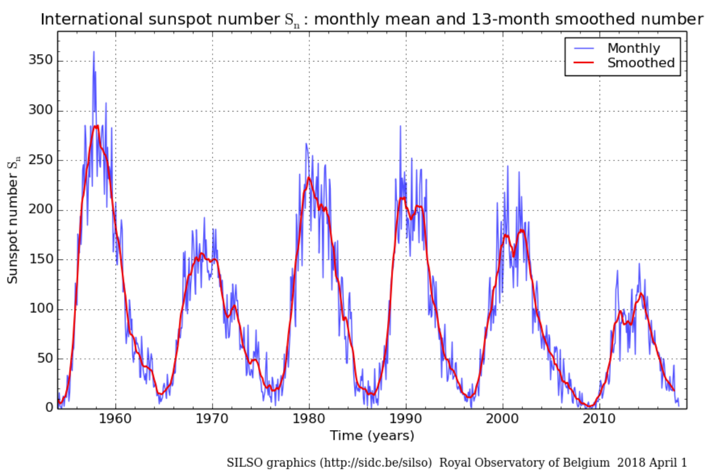

Figure 2.9 Monthly mean sunspot number (blue) and 13-month smoothed monthly sunspot number (red) since 1954. Credit: SILSO data/image, Royal Observatory of Belgium, Brussels, 2018.

periodicity or the 70-year Maunder Minimum, during which from 1645 on almost no sunspots were observed, (Maunder 1890). The source of the variations in the solar cycle periods and amplitudes are variations in the meridional circulation, because their fluctuations are larger than those found in the differential rotation and in the convective motions (Hathaway 2015).

As the SSN is commonly used as an indicator for solar activity, there exists interest in its prediction for the course of the actual and upcoming solar cycles. The continuing prediction of an already commenced activity cycle is reliable, but then the prediction of a cycle before it began is more difficult. Though, there are indications that the polar magnetic field strength during the preceding activity minimum is correlated to the strenght of the next solar cycle (Schatten & Sofia 1987). However, Hathaway & Upton (2016) suggest that the predictability of solar cycles is generally limited – accumulated uncertainty produced by stochastic motions in the convection zone makes predicitons further than the next solar cycle very unreliable.

2.4 Heliospheric magnetic field

In the quiet Sun during solar cycle minimum, open coronal regions – coronal holes – are the photospheric sources of the heliospheric magnetic field (HMF). Bright points between the granules on the photosphere are detected in G-band (430 nm) images. They are identified as magnetic flux tubes with field strenghts of 100–200 mT (Cranmer & van Ballegooijen 2005). Together, these magnetic bright points (MBPs) cover around 1–2 % of the solar surface and carry many times the flux that active regions do (Sánchez Almeida et al. 2010). These thin flux tubes expand laterally in the low chromosphere and merge to homogeneous network fields, which expand and merge again to a large-scale canopy below the transition region (see Figure 2.10).

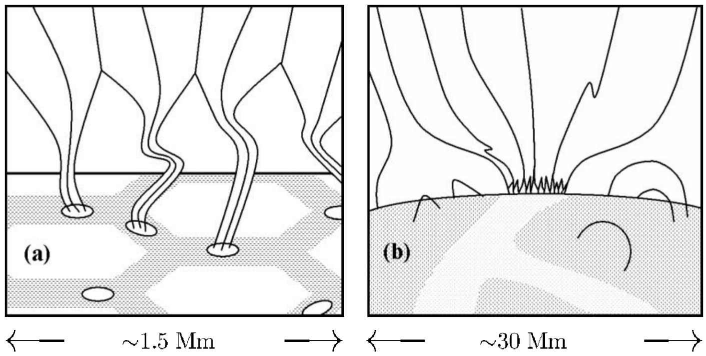

Figure 2.10 Schemata of superradially expanding magnetic flux. (a) MBPs between granules on the photosphere are indicated by ellipses. The protruding lines are thin magnetic flux tubes that merge to a homogeneous network field. (b) Pictured is the network field which expands again to the large-scale canopy field of the lower corona. Credit: Cranmer & van Ballegooijen (2005, Fig. 1, panels (a) and (b)), © AAS, reproduced with permission.

The MBPs' convective appearance and stochastic motions on the photosphere result in wavelike fluctuations that propagate upward through the superradially expanding flux tubes. There exist three types of magnetohydrodynamic (MHD) waves within the plasma: compressional fast- and slow-mode waves, and an incompressible wave mode, which is the result of bending magnetic field lines (Alfvén 1942), called shear Alfvén wave. Alfvén waves propagate with a characteristic speed along magnetic field lines. As they transport energy from the photosphere outwards, it is assumed that they play a major role in the coronal heating process and that the solar wind is accelerated up to the so-called Alfvén critical surface at around 17 $R_{\odot}$, where the local Alfvén speed equals the solar wind speed (Sittler & Guhathakurta 1999; Exarhos & Moussas 2000). Alfvén waves are dominant in coronal regions that have open magnetic field lines and thus they leak into the fast solar wind (Cranmer & van Ballegooijen 2005). Within solar wind at 1 au, their average velocity is about 57 km s^{-1} (Veselovsky et al. 2010) – for more details about the Alfvén velocity see appendix Section A.4.

The coronal plasma in CHs expands superradially, following the magnetic field lines. However, the field strength decreases with increasing solar distance and at a distance of about 2.5 $R_{\odot}$ the thermal pressure becomes larger than the magnetic pressure. Thereby the magnetic field gets frozen within the plasma and is carried by the solar wind radially outwards into the heliosphere. The distance from which the solar wind propagation gets released from the magnetic field lines is called the source surface (Schatten et al. 1969) and the thermal to magnetic pressure ratio is called plasma beta – for more details on plasma beta see appendix Section A.3. The magnetic field changes from superradial expansion below the source surface to a radial configuration above it, this field geometry is also visible in the total eclipse image in Figure 2.3.

Open field lines expand over adjacent closed field regions. Above the cusps of these regions' closed loops, the surrounding plasma flows encounter each other and stream outwards, forming so-called helmet streamers. Above the helmet streamers, magnetic boundaries are created by plasma flows, carrying opposite magnetic polarity. These boundaries constitute an extensive coronal neutral line around the Sun. Within the heliosphere, the two dominating magnetic polarity regions, originating from both solar magnetic poles, are separated by the extension of this neutral line: a large plasma boundary surface, called the heliospheric current sheet (HCS) (Smith 2001).

Under solar cycle minimum conditions, the magnetic dipole axis is near the rotation axis and thus the HCS is roughly located near the equatorial plane, dividing both hemispheres. The analytical solar magnetic field model for solar minimum conditions, constructed by Banaszkiewicz et al. (1998), shows this field geometry as seen in Figure 2.11. The quadrupole part of their dipole plus quadrupole plus current sheet (DQCS) model considers the closed equatorial fields and allows equatorial outflow along the current sheet. Commonly around solar minimum, the HCS's warped surface looks like a wavy ballerina skirt, due to the varying tilt angle between the dipole axis and the rotation axis, see Figure 2.12, and also due to local magnetic field variations (Jokipii & Thomas 1981).

During the field transition at solar maximum, the dipole axis rotates to lower latitudes, crosses the solar equator, and eventually the field ends up in a reversed dipole configuration (Jones et al. 2003). During this process, the HCS rotates almost rigidly together with the dipole axis and remains a single connected structure

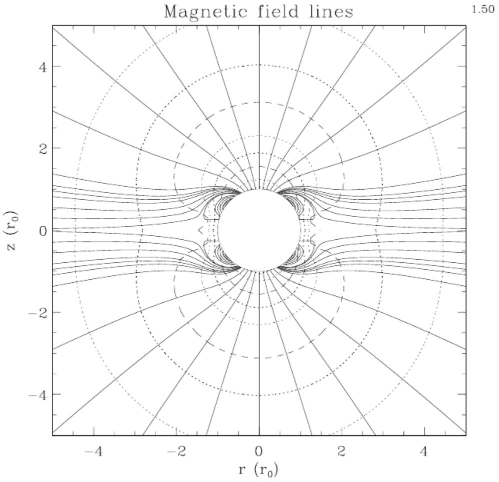

Figure 2.11 Model of the solar magnetic field geometry in the polar plane for solar cycle minimum. Magnetic field lines (solid) and constant field strength surfaces (dashed) from the DQCS model are plotted. The field line spacing does not represent the field strength but provides better detail where needed. Credit: Banaszkiewicz et al. (1998, Fig. 3), © ESO, reproduced with permission.

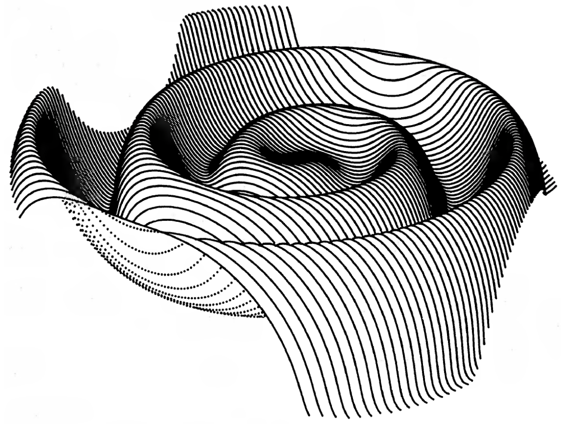

Figure 2.12 A simple HCS model, where its wavy surface shape solely stems from a solar dipole tilt of 15° to the rotation axis. The figure's extend is 25 au across. Credit: (Jokipii & Thomas 1981, Fig. 2), © AAS, reproduced with permission.

in the inner heliosphere (Jones et al. 2003). Hence during cycle maximum, the HCS has a very complex shape, is largely inclined to the solar equator, and reaches near-polar latitudes.

The solar wind source surface rotates with the Sun and thus shears the HMF into an Archimedean spiral pattern, adding an azimuthal component to the radial HMF. This geometry was anticipated by Parker (1958) and is today called Parker spiral. The Parker spiral, viewed in the ecliptic plane, is illustrated in Figure 2.13. The solar rotation axis tilt of up to 7.25° to the ecliptic leads to a slight diving into both hemispheres of opposite polarity. Thus, together with the ballerina topology of the HCS, the Parker spiral has typically a structure of either two or four sectors of alternating magnetic polarity (Ness & Wilcox 1965), which are separated by the HCS.

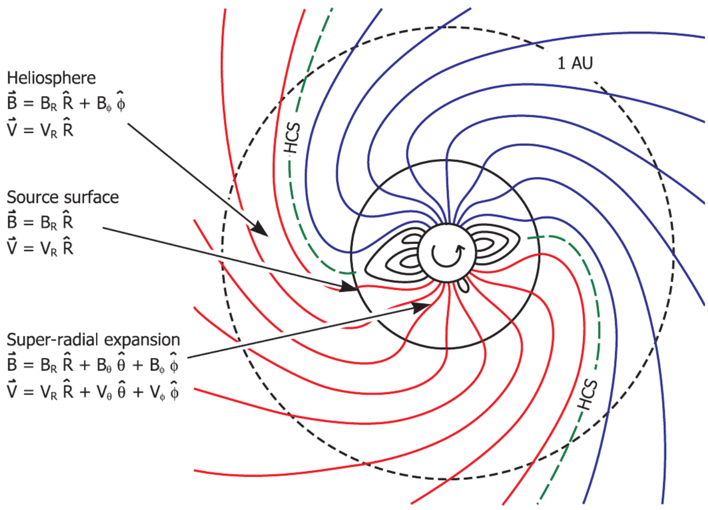

Figure 2.13 Illustration of the Parker spiral formation in the ecliptic plane outside the source surface. The HCS (green) is located between solar wind flows of opposite magnetic field polarity (red/blue). Credit: Owens & Forsyth (2013, Fig. 1), adapted from Schatten et al. (1969, Fig. 1), licensed under CC BY-NC 3.0 DE.

The just described magnetic structures in the solar wind are overlaid by magnetic clouds (MCs) carried within CMEs. The MC's frequency and magnetic configuration vary with the solar activity cycle. Further, speed differences between solar wind streams, and between solar wind and CMEs cause enhanced field amplitudes and can result in shocks in the HMF.

That way, the HMF and its structures are carried out to the termination shock by the solar wind. MHD simulations, based on in-situ measurements of Voyager 1 and 2 within the heliosheath and based on IBEX observations of energetic neutral atoms, provide indications about the outer structure of the heliosheath. Behind the termination shock, the magnetic sector boundaries are compressed and they reconnect, forming magnetic bubbles (Opher et al. 2011). These bubbles – unconnected to the HMF – flow away to the heliosheath tail region. Even beyond the termination shock, the solar wind plasma seems confined and collimated by the twisted solar magnetic field and driven into a northern and a southern jet (Opher et al. 2015). Hence, the Sun's magnetosphere has likely a croissant-like shape with two turbulent tail-lobes, where eventually the solar wind and the HMF are being mixed into the interstellar medium.

2.5 Solar wind

It is observed that cometary tails lag a few degrees from the radial direction with respect to the Sun, sometimes they also show fluctuations and become kinked. As such behavior could not be explained by interaction with sunlight pressure, eventually Biermann (1951) concluded that cometary ion tails are influenced by a continuous flow of particles from the Sun. Parker (1958) considered the consequences of Biermann's conclusions and built a solar wind model, adopting an expanding isothermal solar atmosphere. Parker also incorporated the implications for the solar magnetic field in his model and hence he laid the theoretical foundations for a continuous supersonic radial outflow of magnetized plasma. Thus, the existence of the solar wind was postulated before the first satellites measured it in situ in 1959 (Gringauz et al. 1960; Neugebauer & Snyder 1966). Since that time, spacecraft are able to measure the solar wind almost continuously with magnetometer and plasma instruments in situ (see Chapter 3). Pronounced solar wind structures, such as CMEs and streamers, become visible with the use of space-based coronagraph imagers. From Earth, the outflow of near-Sun solar wind can be observed during solar eclipses, see the eclipse photo in Figure 2.3.

The solar wind is a magnetized plasma consisting of electrons and ions. The ions are mainly composed of hydrogen, a small percentage of helium, and traces of oxygen, carbon, and other metals. The average abundance of helium is about 4.5 % and in slow wind at solar cycle minimum conditions less than 2 % (Feldman et al. 1978; Schwenn 1983; Kasper et al. 2012). The solar wind is commonly approximated by an ideal incompressible MHD plasma (viscosity $\mu = 0$ and electrical conductivity $\sigma = \infty$) and can be viewed as a neutral plasma. Also, its helium share is often viewed as being constant, in this case the proton density determines both the helium and electron densities. This work adopts these assumptions and treats the solar wind throughout as a proton plasma.

The properties of solar wind are highly variable in time and space. The key properties are determined by the values of the solar wind parameters magnetic field strength, proton velocity, density, and temperature. Their average magnitudes scale with solar activity, heliographic latitude, and solar distance. At a solar distance of Earth however, most of the time these parameter's typical values lie in the ranges 3–8 nT, 300–500 $\mathrm{km\,s^{-1}}$, 2–8 $\mathrm{cm^{-3}}$, and 10^4–10^5 K (Kivelson & Russell 1995, p. 92; Venzmer & Bothmer 2018). The low density of solar wind can be illustrated with a short comparison: 1 liter of air at standard pressure, expanded to a typical solar wind density of 6.5 $\mathrm{cm^{-3}}$, would occupy a volume of a cube with edge length of about 155 km. Solar wind quantities, such as particle flux densities, mass flux, pressures, and plasma beta, can be derived from the four listed parameters. Having the parameters in the aforementioned ranges, the solar wind is a plasma with a beta mostly greater than unity, that is, the average solar wind carries the HMF and its motions are not influenced by the field direction (for more on plasma beta see appendix Section A.3).

However, solar wind is structured by its different sources in the solar corona. It consists of fast continuous streams, slow variable flows, and transient CME events. These different flows have highly variable velocities, which result in compressed or rarefied regions at their interfaces. Additionally, the source region's magnetic field configuration organizes the HMF, transported within the solar wind plasma. Regardless, pronounced magnetic structures embedded in the solar wind, such as field polarity changes or magnetic clouds, still influence the properties of the plasma.

This multitude of structures is apparent in the two months – beginning in May 2013 – of in-situ measured solar wind, which I plotted as an example period in Figure 2.14. The IMF and solar wind ion parameters were measured with the MAG and SWEPAM instruments onboard the Advanced Composition Explorer (ACE) spacecraft, located around the first Lagrange point (L1). The data have a time resolution of 64 seconds and are obtained from the ACE Science Center web interface[6].

Some general solar wind tendencies can be seen from this plot: The temperature of the solar wind scales with its stream velocity; compressed plasma regions enhance the magnetic field and the density; HCSs, magnetic sector boundaries, and MCs come with high densities and low temperatures; MCs in CMEs have high magnetic fields and low temperatures. I indicated the periods of occurring solar wind structures, that is, HSSs, CIRs, HCSs, and CMEs, with colored bars – these types are further described in the following sections.

[6]ACE Science Center website: http://www.srl.caltech.edu/ACE/ASC/

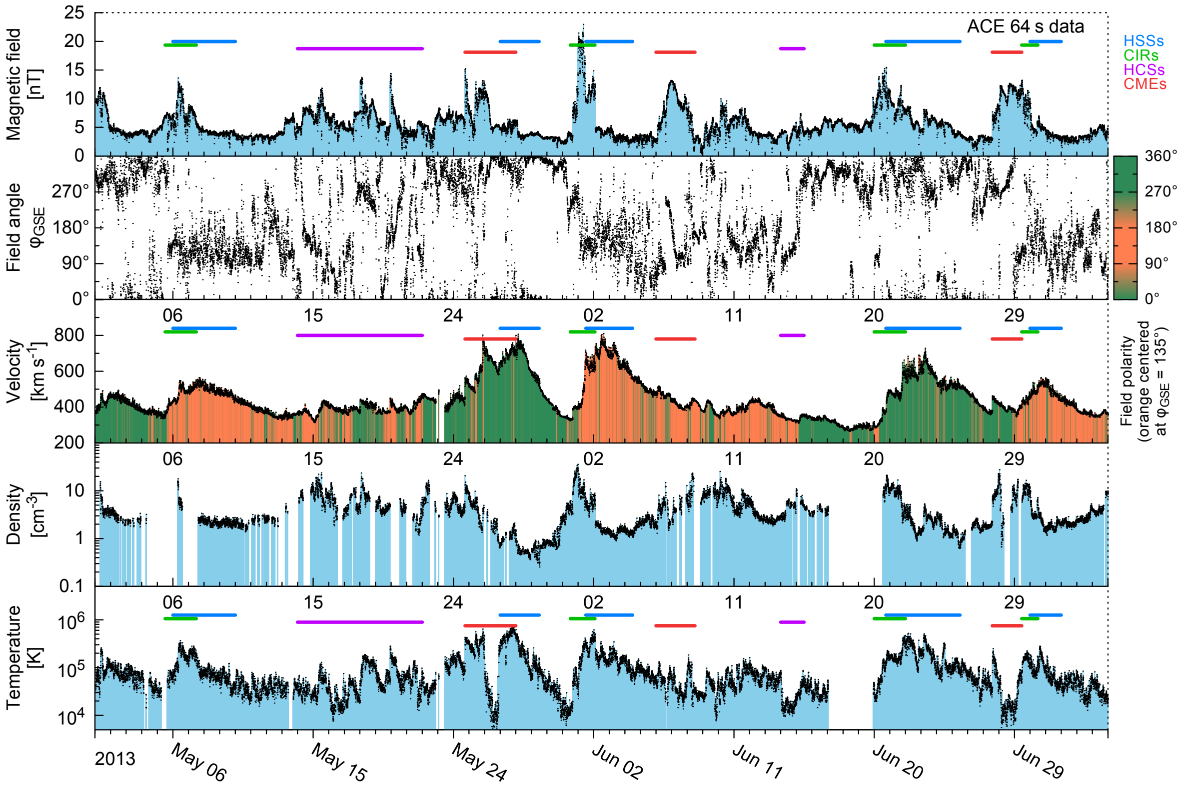

Figure 2.14 Solar wind with several structures, measured at L1 during the time period 1 May to 5 July in 2013. The parameters are the magnetic field strength, its field angle in the ecliptic in GSE coordinates, the proton velocity, density, and temperature. I indicated periods of prominent solar wind structures with color bars: HSSs in blue, CIRs in green, HCSs in purple, and CMEs in red. In the velocity panel also the field polarity is color coded – assuming a Parker spiral angle of 135° at L1. Blank periods indicate bad or missing data. The data are 64 s measurements from the ACE spacecraft.

There exist a lot more aspects related to solar wind, i.e., MHD waves, the electron pitch angle, solar energetic particles, dust particles, and neutral energetic atoms. Yet, they are not covered here, because their relevance to the analyses in this work is considered minor.

2.5.1 Slow and fast streams

It is observed at 1 au that the continuous solar wind comes in streams roughly focused at two major velocity ranges (Neugebauer & Snyder 1966; Schwenn 1983), slow and fast streams with 250–450 km s^{-1} and 450–800 km s^{-1} respectively. Both types possess differences in their typical characteristics and ion compositions. Apart from its higher speeds, fast solar wind has most prominently lower proton densities ($\sim 3\,\mathrm{cm}^{-3}$) and higher temperatures ($\sim 2 \times 10^5$ K) than the slow solar wind, which has higher densities ($\sim 10\,\mathrm{cm}^{-3}$) and lower temperatures ($\sim 4 \times 10^4$ K) (Schwenn 1990). The fast solar wind has a nature of coming in steady high-speed streams (HSSs) with a unique magnetic field polarity, whereas slow solar wind is much more variable in all its properties except its velocity (Bame et al. 1977). HSSs are further overlaid with Alfvén waves, which modulate the stream velocity with typical periods of 15–60 min.

First soft X-ray observations of the corona, made during sounding rocket flights in the early 1970s, showed clearly that the fast solar wind emerges from extended areas of reduced X-ray emission, subsequently called coronal holes (CHs) (Krieger et al. 1973; Hundhausen 1977). The magnetic field polarities found in CHs are associated with the magnetic field directions observed in HSSs, as seen in Figure 2.15. In coronal regions with closed magnetic field lines, the plasma is trapped, though in CHs it can escape, following the open magnetic field lines outwards into space. Wave-particle interactions heat and accelerate the ions in CHs, leading to the emission of a fast solar wind (Hollweg & Isenberg 2002). Superradial expansion of the magnetic field lines in the corona has an influence on the wind speed – actually the expansion factor is anticorrelated with the final wind velocity (Wang & Sheeley 1990). As the field expansion is larger near the border of CHs, faster wind emerges from the mid regions of CHs, forming into HSSs. However, there are indications that the slow and fast solar wind are not only generated at different sources but from distinct mechanisms (McGregor et al. 2011a).

The high variability in the slow solar wind points to the existence of different types of slow wind flows,

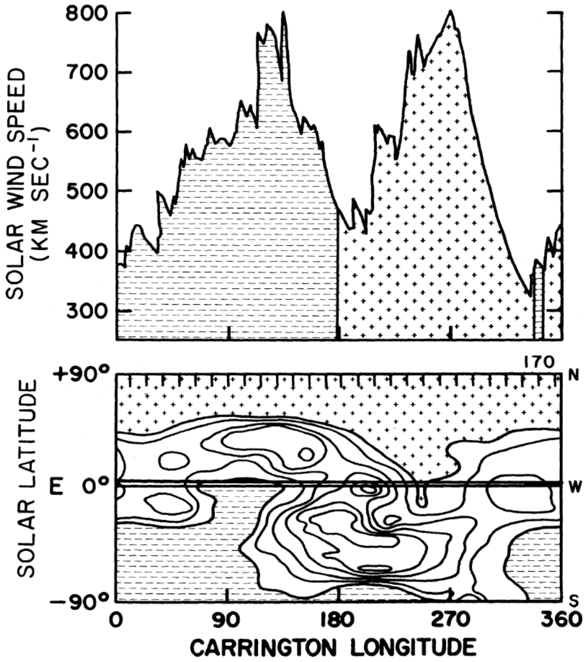

Figure 2.15 Solar wind velocity with respect to its estimated source longitude (top) and coronal brightness contour map at $0.5\,R_\odot$ above the photosphere (bottom) for the Carrington rotation 1616. The velocity is based on IMP spacecraft data, back-extrapolated to $20\,R_\odot$. Brightness values below a fixed threshold are shaded corresponding to the magnetic field polarity (+/−) of the underlying photosphere. The map is based on observations from the K-coronameter at the Manua Loa Observatory. Credit: Hundhausen (1977, Fig. 10), © Colorado Associated University Press, reproduced with permission.

originating from separate coronal locations and mechanisms (Schwenn 1983). It is still under debate if the variability is produced by the formation mechanism of the slow solar wind or if the variability is caused during the acceleration/propagation phase (Sanchez-Diaz et al. 2016). Still, at least a part of its variability can be attributed to the interactions between slow and fast solar wind, which result in a general reduction in velocity differences and thus let solar winds of different speeds (having different properties as well) converge to a common intermediate speed regime in the range 400–500 $\mathrm{km\,s^{-1}}$ (McGregor et al. 2011b; Sanchez-Diaz et al. 2016). Studies using remote white-light tracing of coronal material and in-situ measurements of solar wind suggest that multiple sources of slow solar wind flows exist (Wang et al. 2000; Kilpua et al. 2016). To the best of my knowledge, the generally considered sources are listed in the following:

- CH boundaries and small CHs, because their plasma outflow is slower due to the high superradial expansion of its open field lines (Wang & Sheeley 1990).
- CH boundaries, when trapped plasma is released by reconnection between open and closed field lines (Madjarska et al. 2004).
- Helmet/pseudo-streamers in active regions, where transient plasma blobs are released from the cusps of closed field loops (Wang et al. 1998, 2000). This slow and dense material is associated with the heliospheric plasma sheet belt.
- Edges of active regions, which have hot plasma outflows with a single mangetic polarity (Kojima et al. 1999).
- Jets originating from coronal bright points might contribute to the slow solar wind (Subramanian et al. 2010).
- Slow unidentified CMEs can be a source of slow wind as well.

It is found to be difficult to use in-situ measurements for tracing the slow solar wind flow types to different origins and distinguishing between them, because most properties are also highly variable in time (Kilpua et al. 2016). However, some indicators show tendencies to differentiate between the slow winds from different source regions. Some notable indicators are: elemental ion ratios, heavy ion charge states, and the specific entropy.

The elemental composition of the coronal plasma varies with height/location in the solar atmosphere, therefore the solar wind's elemental ion ratios (e.g., He/H, Fe/O) are used to determine its origin. The charge states of coronal heavy ions depend on the local temperature. However, the density of the outwards expanding plasma decreases fast, preventing further ionization/recombination. The charge states decouple from the local temperature and freeze in still close to the Sun. Thus, heavy ion charge ratios (e.g., C^{+6}/C^{+4}, O^{+7}/O^{+6}) in the solar wind track the coronal source temperature and especially the C^{+6}/C^{+4} ratio is sensitive to the solar wind type (Landi et al. 2012). At solar minimum the specific proton entropy is found to correlate with the O^{+7}/O^{+6} ratio and thus able to trace slow solar wind sources as well (Pagel et al. 2004).

The solar wind stream pattern varies strongly with solar activity. The Sun's ordered dipole structure during solar cycle minima leads to polar regions with open magnetic fields, constituting large coronal holes, and to a large equatorial belt region with closed magnetic fields – this state is clearly visible in Figures 2.3 and 2.11. This state results in fast solar wind coming exclusively from the poles and higher latitudes, whereas active regions form an equatorial streamer belt around the Sun, emitting slow solar wind. This structure was confirmed from solar wind speed measurements done by the Ulysses spacecraft, which flew in an out-of-ecliptic solar orbit and whose mission covered a duration of more than one solar cycle (McComas et al. 2008), see Figure 2.16. The transition of the solar magnetic field during the solar cycle maxima induces the chaotic appearance of

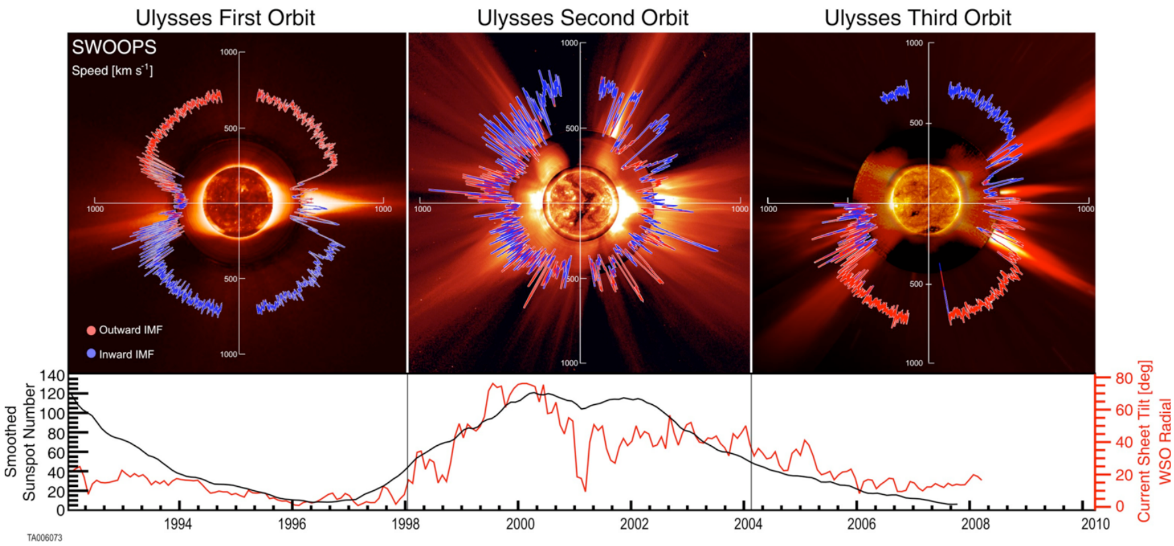

Figure 2.16 Solar wind velocity and magnetic field polarity (red/blue) with respect to heliographic latitude for the three orbits of the Ulysses spacecraft during low and high solar activity (upper panels). The data starts top left and runs couter-clockwise. The corresponding smoothed SSN (black) and HCS tilt angle (red) are plotted beneath. The background consists of solar images for solar cycle 22 minimum (1996-08-17), solar cycle 23 maximum (2000-07-12), and solar cycle 23 minimum (2006-03-28). The solar disk, inner corona, and outer corona images are from SOHO/EIT (Fe XII at 1950 nm), Mauna Loa K coronameter (700–950 nm), and SOHO/C2 white light coronagraph. Credit: McComas et al. (2008, Fig. 1), © American Geophysical Union, reproduced with permission.

closed magnetic fields at higher latitudes and even at the poles. Further, coronal holes begin to invade parts of the equatorial region, this leads to recurring phases of HSSs in the ecliptic. This can be seen from the solar wind period in Figure 2.14, where recurrent HSSs of the same field polarity but changing peak velocity exist – beginning on 6 May, 2 June, and 29 June 2013. The succeeding streams of different velocity result in interaction regions and alternating magnetic polarities result in magnetic sector boundaries.

2.5.2 Stream interaction regions

The sources of the slow and fast solar wind rotate together with the Sun. Their uneven distribution on the solar surface – due to a significant inclination of the dipole axis or variations of the solar magnetic field – lead to the alternation of slow and fast wind streams that flow into the heliosphere (Owens & Forsyth 2013). In case of a fast stream being followed by a slow stream, a rarefaction region expands at their interface. If it is the other way around, the stream of fast solar wind catches up to that of slow wind ahead of it and a compression region forms at their interface, which is encompassed by two compressional waves (Balogh & Jokipii 2009). The latter are stream interaction regions (SIRs) and they take the shape of spiral fronts, as seen in the left panel of Figure 2.17.

When the solar dipole field is in a quasi-stable configuration, SIRs can stay for multiple solar rotations, recurrently sweeping over the heliosphere in 27-day periods (Gosling et al. 1972). Hence, they are referred to as co-rotating interaction regions (CIRs) (Smith & Wolfe 1976; Balogh et al. 1999). In the ecliptic at 1 au, CIRs occur commonly during the declining phase of the solar cycle when polar CHs form equatorial extensions (Balogh & Jokipii 2009).

The spiral shape of the stream interfaces and their inclination to the solar rotation axis lead to a deflection of both streams (Balogh & Jokipii 2009). Due to the fast and slow streams' collision, the fast wind is decelerated and the slow wind is accelerated and their flow directions are systematically deflected away from the interface, as shown in the right panel of Figure 2.17.

The plasma pressure inside SIRs is increasing with heliocentric distance and therefore, the leading and

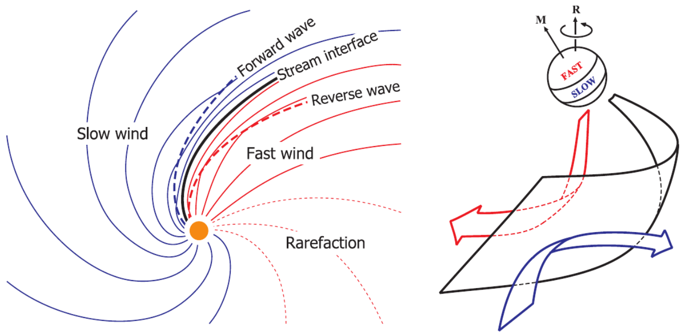

Figure 2.17 Schemata of the formation of a stream interface (left) and the deflection of streams along the interface (right). The stream interface (black) is located between regions of slow (blue) and fast (red) solar wind. Credit: Owens & Forsyth (2013, Fig. 7), right panel adapted from Pizzo (1991, Fig. 2), licensed under CC BY-NC 3.0 DE.

trailing compressional waves form into foreward and reverse shocks – typically at solar distances between 2–10 au (Smith & Wolfe 1976; Balogh & Jokipii 2009). The solar wind speed increases abruptly at both shock fronts. With increasing solar distance, the leading and trailing shock fronts travel away from the stream interface. This widens the interaction regions and eventually they gain on the close-by interaction regions (Burlaga et al. 1984). Beyond 10 au they fuse to merged interaction regions, which are narrower and more compressed (Burlaga et al. 1985).

Due to the compression within SIRs, the magnetic field strength and the plasma density are higher than in the ambient streams. These signatures can be seen in the in-situ solar wind plot in Figure 2.14. The CIRs on 5 May, 1 June, and 29 June 2013 are followed by recurrent HSSs and they contain sector boundaries as well. They are not yet accompanied by strong shocks owing to the measurement location at 1 au.

2.5.3 Heliospheric current sheet

The heliospheric current sheet (HCS), the boundary surface between solar wind streams of opposite magnetic polarity, is formed by open magnetic fluxes, expanding from both sides over closed field regions and coming into contact above. At the boundary between open and closed fields, local coronal plasma gets released and flows slowly between the fast wind streams along the current sheet into the heliosphere, creating a helmet streamer. This is why near the Sun, the HCS is typically located within slow solar wind stemming from the coronal streamer belt (Owens & Forsyth 2013). However, with increasing solar distance, the shock wave of an adjacent SIR can pass the HCS, so that sector boundaries are often found to be embedded within SIRs (Gosling & Pizzo 1999).

When sector boundaries in the solar wind are observed in situ, they come with significant depletions in He^{++}/H^{+} values (Borrini et al. 1981). The other solar wind parameters, such as velocity, density, and temperature, change with distance from the HCS as well (Smith 2001). The HCS region itself is quite narrow with a thickness of around 3000–10 000 km; it is embedded in a region of 20–30 times its thickness, the heliospheric plasma sheet (HPS) (Winterhalter et al. 1994). The HPS contains the magnetic polarity reversal and is of low magnetic field strength and high density, resulting in a significantly enhanced value of plasma beta (Crooker et al. 2004). In the slow solar wind, the HPS can also be identified from its particularly low specific entropy, arising from its low temperature and high density (Kilpua et al. 2016).

2.5.4 Coronal mass ejections

Coronal mass ejections (CMEs) are eruptions of coronal magnetized plasma, which expand within hours to bubbles with sizes of a few solar radii. They continuously expand further while moving farther away from the Sun into the heliosphere with velocities often surpassing even the high speed solar wind. When measured in-situ in interplanetary space, they are often called interplanetary CMEs (ICMEs). They are transient structures found to be embedded in the ambient slow and fast solar wind streams, having durations of a few days. CMEs make up about 5 % of the solar wind's flow share during solar cycle minima, but can represent up to about 50 % during solar cycle maxima (Richardson & Cane 2012). Indeed, their frequency correlates with the sunspot number (Hildner et al. 1976) and follows solar activity in amplitude and phase (Webb 1991).

Long before the origins of geomagnetic disturbances were actually attributed to CMEs, a solar influence was identified as their source by Carrington (1859). Indeed, CMEs are the major drivers for strong geomagnetic storms, because they carry the most extreme conditions found in the solar wind. Thus, they are of major importance to space weather – their impacts on the terrestrial magnetosphere are covered in Section 2.6.

I will cover the CME formation processes only briefly, because this work is focused on in-situ measurements. Generally speaking, CMEs are products of the instability in the coronal magnetic field. The solar differential rotation wraps the coronal magnetic field, which is rooted at the surface. Accumulated tension and emerging magnetic flux eventually initiate sudden field reconfigurations. These field line reconnections result in a lower state of potential energy, releasing a lot of energy in form of solar X-ray flares and CMEs. Indeed, CMEs are often associated with flares and eruptive prominences, coming from their source regions (Webb & Hundhausen 1987). The sources of CMEs are located near active regions and are frequently identified with eruptive prominences (Subramanian & Dere 2001).

CMEs emerge from coronal magnetic flux rope structures that hold plasma filaments embedded along their base (Webb & Hundhausen 1987; Cremades & Bothmer 2004). Reconfiguration of the ambient magnetic field can lead to a release and a subsequent ascend of the flux rope through the corona. During this process, the filament is lifted by the flux rope and forms a prominence eruption. The accompanying sudden magnetic reconnections often cause a multitude of other dynamic coronal phenomena: enhanced X-ray flaring; the formation of post-eruptive arcades where the filament disappeared; local decreases in soft X-ray intensity (coronal dimmings) due to depletion of the plasma density caused by magnetic field expansion; and large-scale coronal disturbances observed in extreme ultraviolet (EUV-waves) that can spread across the whole corona.

The onset of CMEs is often accompanied by solar energetic particles (SEPs) and by solar radio bursts. SEPs consist of protons, electrons, and ions with relativistic energies that can cover the distance to Earth within half an hour and pose a radiative threat to humans in space. The intensity of energetic protons correlates well with the CME speed (Kahler et al. 1978) and it is established that these coronal particles are accelerated by shocks formed in front of the rapidly expanding magnetic structures of CMEs in the corona (Cliver et al. 1982; Gosling 1993). Solar radio bursts are radio emissions from the corona that change over time in frequency space. There are different kind of radio bursts, but especially type II radio bursts are seen as indicators for coronal shocks that accelerate electrons. They are emitted in the low corona and are drifting to lower frequencies over time. There is still a debate whether type II bursts originate from flares or CMEs, favoring the latter (Gosling 1993; Cliver et al. 2005; Cho et al. 2011).

CMEs were detected in the white-light observations of the K-corona made by the first space-based coronagraphs on board the OSO 7 satellite (Tousey 1973) and the Skylab space station (MacQueen et al. 1974). These observations show the steady outflow of solar wind, broken by intermittent ejections of coronal plasma. Subsequently, the kinematic properties of CMEs were identified from the white-light images (MacQueen 1980). Now, coronagraphs observe the corona and hence CMEs continuously from the first Lagrange point (L1) in front of Earth with the SOHO spacecraft and from changing equatorial perspectives with the STEREO Ahead (A) and Behind (B) spacecraft. The image of the corona from 23 September 2012, made by the SECCHI/COR2 coronagraph onboard STEREO A, shows a CME to the top right, see Figure 2.18.

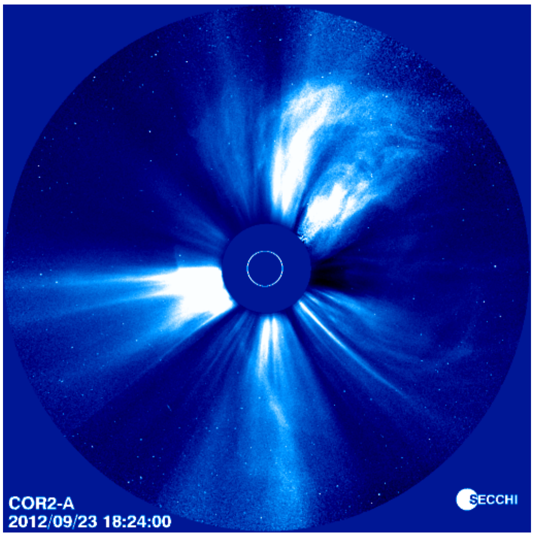

Figure 2.18 Image of the solar corona out to 15 $R_\odot$ from 23 September 2012 taken by the SECCHI/COR2 coronagraph onboard the STEREO A spacecraft. The solar disk is covered by the occulter disk and its position is indicated by the white circle. The bright blob to the top right is the CME; the smooth elongated radial lines are solar wind streamers. Courtesy of STEREO/COR2 consortium (NASA).

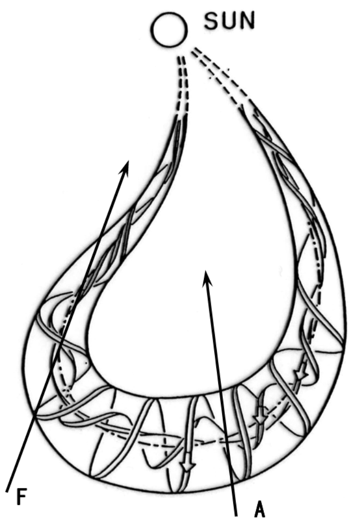

Figure 2.19 Schema of a magnetic flux rope structure in a CME. The arrows depict passings through its flank (F) and its apex (A). Credit: Marubashi & Lepping (2007, Fig. 1, panel (a)), licensed under CC BY 3.0.

It was early determined by Gold (1962) that solar ejecta should drive shock waves ahead. In fact, shocks with trailing low proton temperatures caused by fast CMEs were then found in in-situ measurements (Gosling et al. 1973, 1974). Burlaga et al. (1981) analyzed magnetic field and plasma in-situ data from five spacecraft and identified a shock wave with a trailing turbulent sheath region followed by an organized helical magnetic structure that they called a magnetic cloud (MC). MCs have an enhanced magnetic field, a smooth rotation in the azimuthal magnetic field component and they show low densities and temperatures (Burlaga et al. 1981). Thus, MCs have a low thermal to magnetic pressure ratio (i.e., a small plasma beta) and the magnetic field dominates the plasma. Furthermore, the overall pressure in MCs is higher than in the ambient solar wind, resulting in the expansion of MCs on their way out. Shock-driving CMEs containing a helical MC are actually identified with magnetic flux ropes that expand self-similarly and that remain in connection with the solar surface (Chen et al. 1997). The surface connection is indicated by bi-directional streams of electrons that are found in MCs (Gosling et al. 1986). The shape and magnetic topology of such a magnetic flux rope is pictured in Figure 2.19. It is apparent that in-situ measurements should look significantly different depending on where the CME is pierced.

Solar wind in-situ measurements reveal the magnetic structure of CMEs. In particular, the orientation of magnetic flux ropes can be determined via applying a minimum variance analysis (MVA) to the MCs' magnetic field components (Sonnerup & Cahill 1967; Burlaga & Behannon 1982). An MVA determines the direction of minimum variance in the sequence of field vectors passing by during an MC encounter. This direction is interpreted as the principal axis of the flux rope.

Bothmer & Schwenn (1998) used the MVA on an extensive set of MCs which they found in the data of the Helios 1 and 2 probes. They related the results with the magnetic polarity structures of the MCs' apparent solar source regions. Connecting the derived flux rope directions with the orientation of disappearing filaments and magnetic neutral lines on the solar surface, they recognized a scheme that is able to infer the orientation and helicity of MCs found in CMEs. This Bothmer-Schwenn scheme (BSS) relates these magnetic flux rope properties to whether the solar cycle number is even or odd and depending on which solar hemisphere the CME originates from (northern/southern) – utilizing that the hemispheric polarity is alternating with each solar cycle, see Figure 2.20. As the probability is greater than 80 % that the magnetic topology of an active region

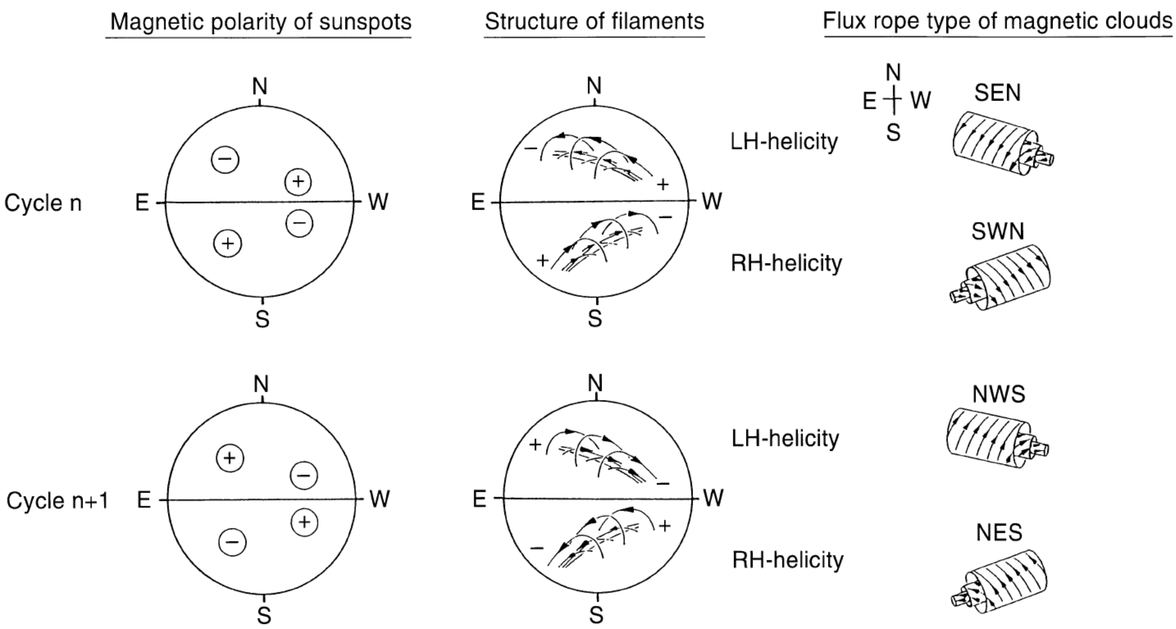

Figure 2.20 Explaining sketch of the BSS. The two rows represent odd (n) and even ($n + 1$) solar cycle numbers. The magnetic polarity of sunspots, the structure of filaments, their helicity, and the corresponding flux rope type of magnetic clouds are shown. Credit: Bothmer & Schwenn (1998, Fig. 18), © EGS – Springer-Verlag, reproduced with permission.

conforms to the hemispheric rule (Wang 2013), an MC configuration predicted with the BSS is expected to have a reliability that is of the same order (Savani et al. 2015).

Three CMEs can be seen in the solar wind in-situ measurements showed previously in Figure 2.14, passing by the ACE spacecraft at L1 on 24 May, 6 June, and 27 June in 2013. The latter CME has a well-structured MC, which is presented in detail in Figure 2.21 – I use this event as an example throughout this section. In addition to showing the solar wind in-situ parameters, I indicated the shock, compression zone and the MC with dotted

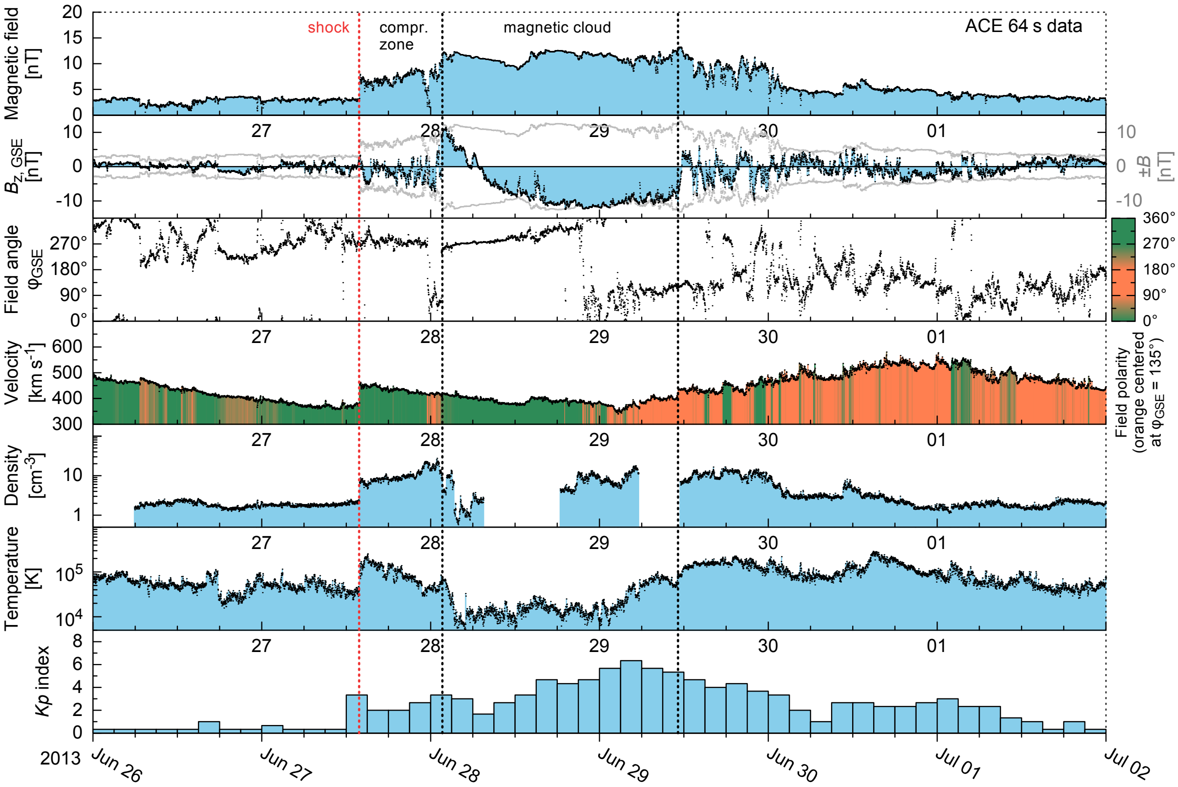

Figure 2.21 Solar wind with a CME, measured at L1 during the time period 26 June to 2 July in 2013. The solar wind parameters are the magnetic field strength, its z-component and ecliptic field angle in GSE coordinates, the proton velocity, density, and temperature; in addition, the geomagnetic *Kp* index is plotted in the bottom panel. In the velocity panel also the field polarity is color coded – assuming a fixed Parker spiral angle of 135°. I indicated the shock, the compression zone, and the duration of the magnetic cloud with dotted lines. Blank periods indicate bad or missing data. The solar wind data was measured with the MAG and SWEPAM instruments onboard the ACE spacecraft and is obtained from the ACE Science Center. The *Kp* data is obtained from the GFZ Potsdam.

lines, and plotted the geomagnetic *Kp* index in order to visualize the CME's impact on the magnetosphere. This MC contains a sector boundary and is trailed by an interaction region caused by a following HSS.

The CME occured in solar cycle 24. The MC's IMF z-component changes from positive (northern) to negative (southern) values – during this process, the field angle in the ecliptic, ϕ, stays pointing roughly towards 270° (west). Thus, it has a NWS configuration, which is expected from the BSS during even numbered solar cycles for CMEs with source regions located in the northern hemisphere.

The combination of white-light images with in-situ data enables relating the observed structures of CMEs. Even disturbances in front of fast CMEs can be identified as shock waves in the white-light images made by the SOHO coronagraph (Sheeley et al. 2000). The diffuse leading feature of a CME is the shock sheath, its brightness is caused by the density jump after the shock, which itself is not visible in coronagraphs. The trailing void is identical to the low density of the magnetic flux rope, which drives the whole structure.

The CME described before is indeed coming from the northern hemisphere, as can be seen from the STEREO A coronagraph image displayed in Figure 2.22 taken three days earlier. Apparently, the CME only grazes the ecliptic and its lower part passes Earth. Also in this image, the event originates from the backside of the solar disk, considering the observing spacecraft's position in relation to Earth at that time, see Figure 2.23.

Relating CME white-light images to observations of magnetic neutral lines on the solar surface, Cremades & Bothmer (2004) interpreted the white-light appearances of CMEs as projections of their 3D geometry and developed a scheme for their orientation depending on the orientation and location of the neutral lines on the solar surface. Neutral lines on the solar surface are the lines of polarity inversion between two areas of opposite magnetic polarity. The scheme is based on the topology of the flux rope model and the observation that its major axis stays roughly aligned to the underlying neutral line during the eruption process. Thus, Cremades & Bothmer (2004) concluded that CMEs look systematically different depending on their source region's position and magnetic configuration, as described in Figure 2.24. For the solar backside, the neutral lines are reversed

[7] STEREO Science Center website: https://stereo-ssc.nascom.nasa.gov/

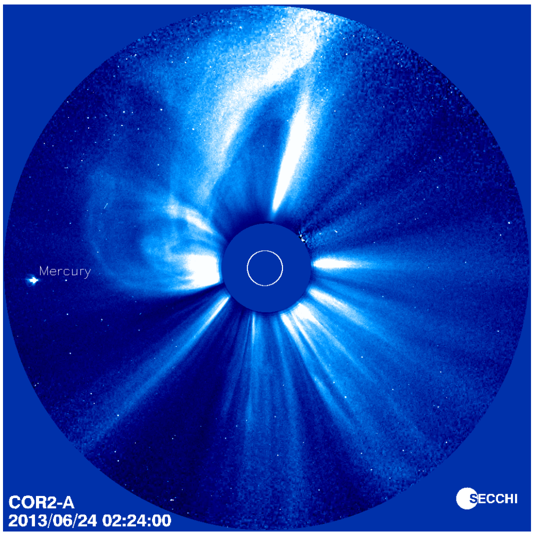

Figure 2.22 Image of the solar corona from 24 June 2013 made with the same coronagraph as the image in Figure 2.18. The CME is the extended structure to the upper left. Courtesy of STEREO/COR2 consortium (NASA).

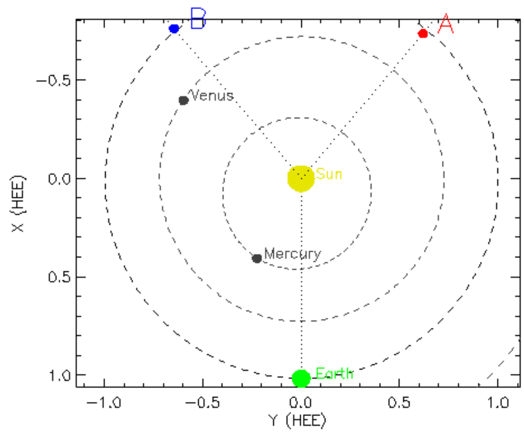

Figure 2.23 Positions of the STEREO A and B spacecraft for 24 June 2013 02:24 UT. This figure is made with the online STEREO Orbit Tool at the STEREO Science Center website[7].

and according to the scheme so are the CME orientations – thus the broad backside CME seen in Figure 2.18 matches this scheme. The scheme can effectively be applied for CMEs with source regions located less than 50° from the solar equator (Webb & Howard 2012).

This white-light CME projection scheme as well as the BSS for MCs are based on the notion that the orientation of flux ropes propagating outwards generally stays aligned with the neutral polarity inversion line on the solar surface where the filament erupted (Marubashi 1997; Bothmer & Schwenn 1998). In fact, it is shown that flux ropes are not likely to rotate significantly after their initiation but maintain the orientation of their main axis parallel to the magnetic neutral line even in interplanetary space (Marubashi et al. 2015). However, during and shortly after their eruption, CMEs are frequently observed to be deflected to other directions by the surrounding coronal magnetic field structure (Sterling et al. 2011).

The revelation that all CMEs may be flux ropes (Vourlidas et al. 2013; Marubashi et al. 2015) led to the expansion of the CME definition based on white-light images made by Hundhausen et al. (1984). Vourlidas et al. (2013); Vourlidas (2014) include magnetic flux ropes in their recent CME redefinition: *"A CME is the eruption of a coherent magnetic, twist-carrying coronal structure with angular width of at least* 40° *and able to reach beyond* $10\,R_\odot$ *which occurs on a time scale of a few minutes to several hours."*

However, CMEs generally do not have a perfect flux rope geometry: Often their more complex structure can be seen in kinks of the corresponding filament before the eruption; and strong distortions can happen during the eruption process. Their cross section is only initially of circular shape, it distorts due to the pressure-driven self-expansion and the radial solar wind expansion (Owens et al. 2006). Though, the inner core of the flux rope is believed to stay of circular shape. For these reasons, the properties of CMEs vary widely and imaging projection effects contribute further to that (Cremades & Bothmer 2004).

There still exist a lot of unresolved questions about CMEs, their formation, and the effects observed along with them: Multiple mechanisms/processes are debated for the release of CMEs and their subsequent acceleration. It is also not known if there exist CMEs without magnetic flux ropes (Vourlidas et al. 2013). The relation between flux ropes observed in the near-Sun corona and measured in situ at interplanetary distances is still not entirely clear (Vourlidas 2014). Nobody knows yet when a CME will erupt on the Sun, at what exact time it will pass a given point in the heliosphere, and how its detailed magnetic configuration would look like in situ (Gopalswamy 2016).

2.6 Space weather

Space weather is the field of research that comprises all dynamic effects generated by the Sun in its domain of influence – the heliosphere. Naturally, it is especially focused on the solar effects observed on Earth and in its local environment – the ionosphere and the magnetosphere. There exist several different effects caused by

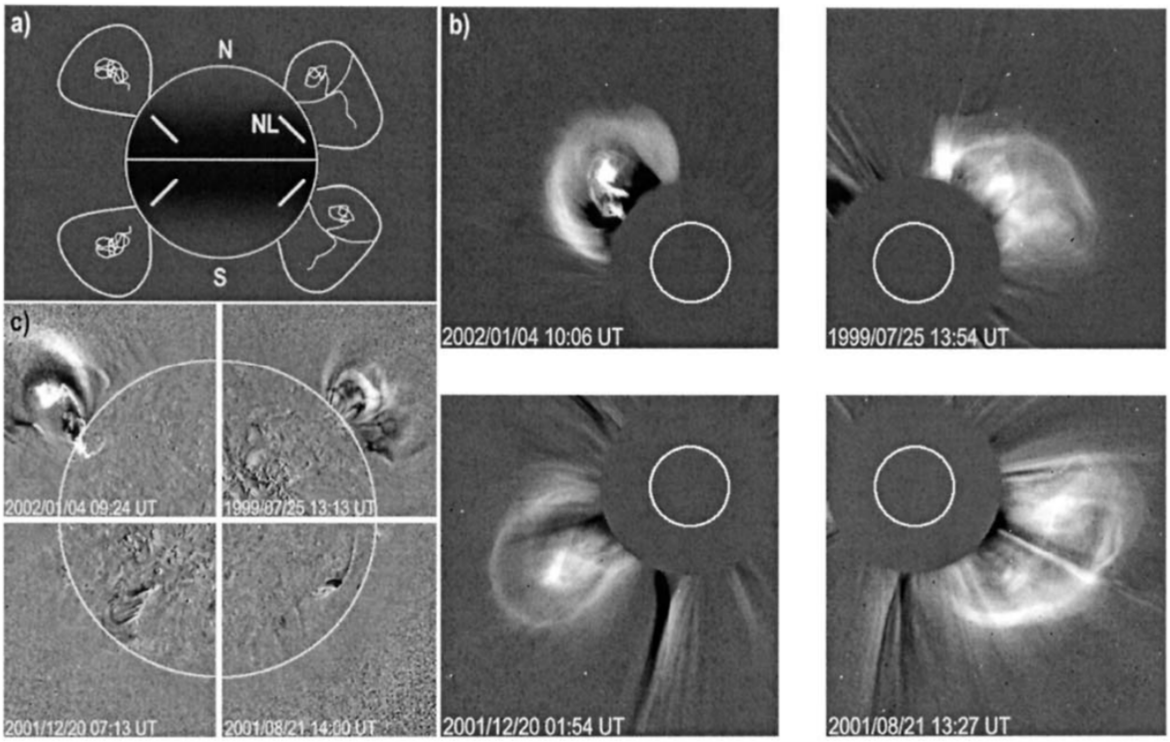

Figure 2.24 White-light CME projection scheme for frontside events, showing the case for each quadrant of the solar disk. (a) Schema showing the expected white-light appearance of CMEs and the orientation of the underlying magnetic neutral lines. (b) White-light images of CME example events, made with the LASCO C2 coronagraph on the SOHO spacecraft. (c) Details (prominences and post-eruptive arcades) of the source regions related to the CMEs shown in panel (b). Note that for events originating from the backside, panel (a) has to be mirrored vertically. Credit: Cremades & Bothmer (2004, Fig. 15), © ESO, reprinted with permission.

independent solar events occurring on different time scales that can affect humans directly or indirectly. Solar events affect sensitive technical systems and strong events are even able to disrupt them and pose a threat to humans (Bothmer & Daglis 2007). Space weather deals with effects on time scales similar to the terrestrial weather, that is, hours, days, and weeks.

The existence of a direct solar-terrestrial relation was known of early on. Carrington (1859) made the first connection between solar flares and disturbances in the terrestrial magnetic field when he observed a brightening on the solar disk on 1 September 1859 and suggested its connection to a strong geomagnetic storm that occurred about 17 hours later. Categories of solar-terrestrial correlations were already listed by Bartels (1962): Events initiated by irregular solar X-ray flares and CMEs, by the 11-year solar activity cycle, and by the periodic 27-day solar rotation. Other time related variations include seasonal effects caused by the Earth's orbital distance oscillation over the year and the inclinations of the Sun's and Earth's rotation axes to the ecliptic normal. The terrestrial magnetic field's dipole axis tilt to the rotation axis further contributes to the daily effects.

The major driving forces behind severe space weather events are CMEs, solar X-ray flares, and solar energetic particle (SEP) events. Most of the terrestrial space weather effects are introduced through the events' influence on the magnetosphere, ionosphere, and upper atmosphere. Space weather effects, commonly classified into geomagnetic storms, solar radiation storms, and radio blackouts[8], are listed in the following.

The solar wind's internal structures, such as CMEs and CIRs, affect the magnetosphere and can cause large disturbances in its magnetic field. These disturbances are called geomagnetic storms and are described in more detail in Section 2.8. Notable consequences of these major disturbances in the terrestrial magnetic field are listed below (Bothmer & Daglis 2007):

- Impact on the magnetic navigation and behavior of animals, such as migratory birds (Moore 1977) and whales (Vanselow et al. 2017).
- Enhanced auroral activity and shift of the auroral oval to lower latitudes[9].

[8]NOAA Space Weather Scales website: https://www.swpc.noaa.gov/noaa-scales-explanation
[9]NOAA/SWPC Tips on Viewing the Aurora: https://www.swpc.noaa.gov/content/tips-viewing-aurora

- The equatorward auroral oval shift leads to direct risks for humans from enhanced radiation doses during high altitude flights through an enlarged polar cap[10].
- Enhanced radiation in the Van Allen belt can lead to faulting electronics and disturb satellite operations.
- Geomagnetic storms can rapidly heat the upper atmosphere, causing it to expand, and generate an increased drag for satellites in low Earth orbits[11].
- Geomagnetically induced currents are created in long conducting infrastructure, such as oil pipelines, rail tracks, and power lines. The currents can lead to increased steel corrosion and power grid outtages.
- The sunward magnetopause distance can shrink under extreme solar wind pressure below the geostationary Earth orbit (GEO) at a distance of $6.6\,R_{\mathrm{E}}$. GEO satellites crossing the magnetopause are then directly exposed to the radiation of SEPs.

Solar extreme ultraviolet (EUV) and X-ray radiation events (solar flares) affect the ionosphere apart from the radiation's regular day/night cycle influence. Solar flares can create sudden ionospheric disturbances (Gosling 1993), that is, abrupt enhancements in the ionospheric total electron content (TEC). These TEC variations threaten the following technical systems (Kraaikamp & Verbeeck 2015):

- Increased TEC leads to larger positioning errors in global navigation satellite systems (GNSS).
- Scintillation and absorption of high frequency signals on their way through the ionosphere can lead to signal disturbances and loss of satellite communications.
- Induced changes in the stratification of the ionosphere (D-, E-, and F-layers) disturb radio communication and lead to outtages in various frequency bands.

Flares and CME shock fronts accelerate coronal particles, producing SEPs. These are guided by the IMF along the Parker spiral through the heliosphere. High fluxes of SEPs induce solar radiation storms with durations ranging from hours to days that have the following effects (Bothmer & Daglis 2007):

- Enhanced radiation damage to electronic circuits in satellites and spacecraft.
- Enhanced radiation damage to biological tissue in humans and organisms brought to space.
- SEPs are guided by the terrestrial magnetic field down to the polar regions. Thus, humans flying in aircraft near polar latitudes are exposed to higher radiation doses during strong radiation storms. Especially humans in orbit outside the protective atmosphere are endangered.
- Free electrons, created by SEPs colliding with the atmosphere, form ionospheric layers that disturb/block high frequency radio communications[12].

Obviously there also exist lots of space weather effects on the rest of the solar system bodies. Notable effects are (Bothmer & Daglis 2007):

- Other planetary magnetospheres are impacted in similar ways as the terrestrial is (e.g., the Jovian and Saturnian magnetospheres).
- Induced magnetospheres on nonmagnetic bodies, as is the case at Venus, are affected by the varying external plasma of the solar wind (Luhmann et al. 2004).
- The solar system regions outside of protective magnetospheres suffer directly from episodes of enhanced solar radiation, that is, from flare and SEP events.
- Solar wind structures can strip off cometary tails and can enhance atmospheric losses in bodies without magnetosphere.
- The average solar wind pressure and HMF scale with solar activity and therefore modulate the shape and size of the heliosphere. As cosmic rays are influenced by the HMF, the local cosmic ray radiation level scales inversely with solar activity. Even the passings of strong shocks and MCs lead to reductions in local cosmic ray radiation, which are called Forbush decreases.

As can be seen, most terrestrial space weather effects are connected with economic interests and some impacts on technical systems can even influence human lives. This creates strong interest in forecasting the space weather conditions of the upcoming hours and days. Space weather forecasting is a relatively new field of study, however, it becomes more and more important, not only because of the increasing use of sensitive technology at Earth, but also because of the anticipated expansion of interplanetary space activities within the near future, such as human space missions to Moon and Mars. There exist lots of dedicated institutions and a multitude of forecasting techniques for the different aspects of space weather and more are being developed. This study contributes to that as one of its main foci is the forecast of the intensity of geomagnetic disturbances.

[10] NOAA/SWPC Galactic Cosmic Rays: `https://www.swpc.noaa.gov/phenomena/galactic-cosmic-rays`
[11] NOAA/SWPC Satellite Drag: `https://www.swpc.noaa.gov/impacts/satellite-drag`
[12] NOAA/SWPC Solar Radiation Storm: `https://www.swpc.noaa.gov/phenomena/solar-radiation-storm`

Predictions of magnetospheric disturbances are based on knowledge of the solar wind properties which the magnetosphere will encounter. Thus in a first step, forecast methods have to predict the solar wind at Earth in advance and derive its expected impact on the magnetosphere in a second step. The first part of this present study contributes to the second step with predicting the amplitude of magnetospheric disturbances caused by solar wind. The basic structure of the magnetosphere, its coupling to the solar wind, its convection cycle, and geomagnetic indices are detailed in the following Section 2.7. Section 2.8 portrays geomagnetic storms and the *Kp* index as a measure for their severity. Section 2.9 describes the common solar wind coupling functions and existing methods to forecast geomagnetic disturbances and their solar wind sources.

2.7 Magnetosphere

In first-order approximation, the terrestrial magnetic field can be seen as a dipole aligned with the rotation axis of the Earth. Its magnetic south pole is located near the geographic North Pole and there is currently only a small tilt of about 9.5° between both axes (Thébault et al. 2015) – this angle varies slightly over the years. The magnetic field strength on the surface at the poles is around 60 μT, whereas at the equator it is about half that magnitude. At the Earth's surface, there are major field irregularities that deviate from the dipole approximation, such as the prominent South Atlantic Anomaly whose field is lower than 24 μT (Thébault et al. 2015).

The geomagnetic field's strength decreases while it extends out into space. Its influence ends where its magnetic pressure balances the ram pressure of the solar wind. Gold (1959) named the region governed by the terrestrial magnetic field the magnetosphere. The outer boundary is the magnetopause – in average it has a sunward distance of about 11.0 R_E (Fairfield 1971). In response to the continuous changes in the solar wind pressure, the magnetopause usually is in a state of fast radial inward-outward motion and its displacement can reach several Earth radii (de Keyser et al. 2005). The solar wind flow shapes the magnetopause into a surface of teardrop form, whose length of its so-called magnetotail varies around 100 R_E and points away from the Sun.

The compression of the solar wind plasma at the front of the magnetopause creates a bow shock, whose average standoff distance to Earth is about 15.1 R_E but varies largely under extreme solar wind conditions (Fairfield 1971). The shocked solar wind plasma flows within the magnetosheath around the magnetosphere as seen in Figure 2.25. The IMF in the magnetosheath is weaker but has a larger variability than the terrestrial

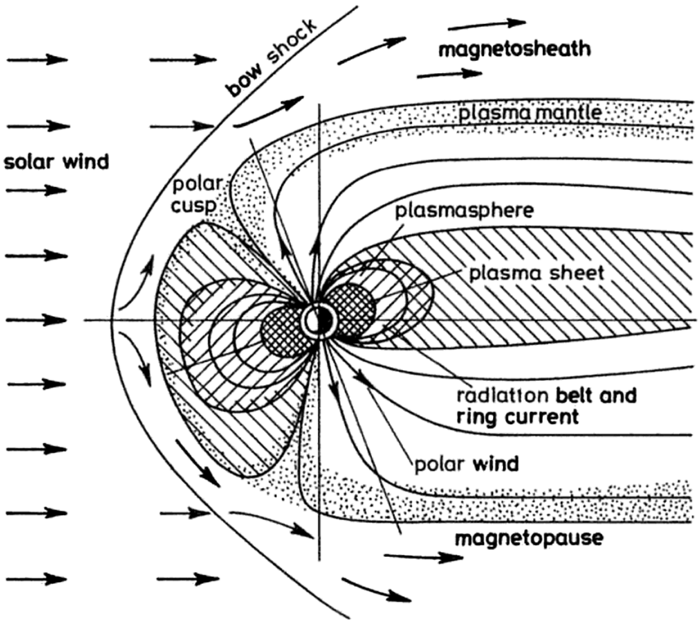

Figure 2.25 Schema of the magnetosphere's geometry in the plane spanned by the solar wind flow direction and the ecliptic normal (vertical line). The arrows show the flow of solar wind around the Earth's magnetic field. The diagonal line indicates the inclination of the rotation axis to the ecliptic. Credit: Davies (1990, Fig. 2.12), © IET, reproduced with permission.

magnetic field on the other side of the magnetopause (de Keyser et al. 2005).

At the front of the magnetopause, the incoming solar wind ions and electrons are being deflected in direction of dawn and dusk by the magnetospheric field, creating a current layer at the surface of the magnetopause. This current induces another magnetic field that cancels the geomagnetic field outside of the magnetopause and enhances it inside to about twice the strength of a pure dipole field at that distance (de Keyser et al. 2005). At the magnetotail side, the magnetopause current flows into the opposite direction – an overview, also of the inner magnetosphere's current systems is illustrated in Figure 2.26.

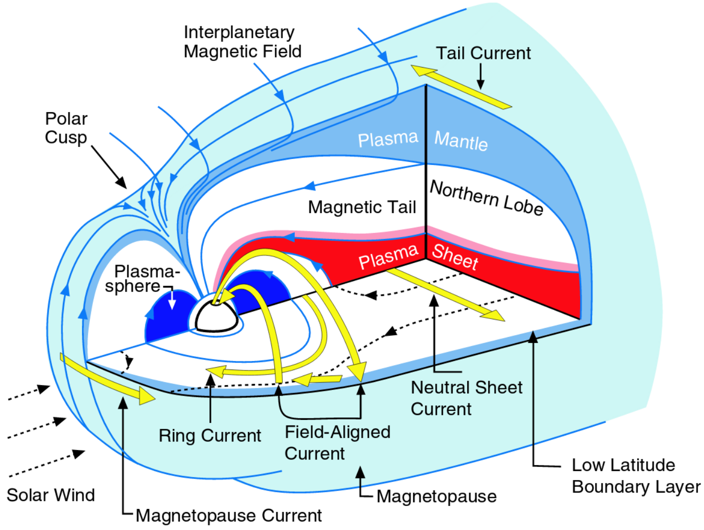

Figure 2.26 Schema of the magnetosphere's inner 3D structure with focus on its current systems and plasma regions. The directions of the magnetic field lines and electric currents are indicated with blue and yellow arrows respectively. Credit: de Keyser et al. (2005, Fig. 2.12), adapted from Kivelson & Russell (1995, Fig. 1.18), © Springer, reproduced with permission.

2.7.1 Solar wind coupling mechanisms

There exist several ways of how solar wind couples to the magnetosphere and deposits energy and plasma within. The contributions of the different mechanisms by which energy is transferred and solar wind plasma is able to penetrate the magnetopause are not yet established (Phan et al. 2005). High solar wind pressure during times when the IMF direction is parallel to the terrestrial magnetic field leads to compression of the sunward magnetosphere and enhances its potential energy. Solar wind energy is also transferred via the induction of currents. However, the major interaction processes are magnetic reconnection and turbulence – their underlying physical mechanisms are described in the following.

Magnetic reconnection occurs where the IMF comes into antiparallel contact with the terrestrial magnetic field. At these regions on the magnetopause, the magnetosphere opens up to the IMF and reconnection of the field lines occurs, resulting in a change of the local magnetic topology (Phan et al. 2005). The magnetic field reconnects along a line that shows an X-geometry. The reconnection process at this so-called X-line harbors a narrow diffusion region, where the plasma ions and electrons decouple to get accelerated in jets of particles by the reconnected field lines (Phan et al. 2005), see the Figure 2.27. Thus, the magnetopause is left with a small

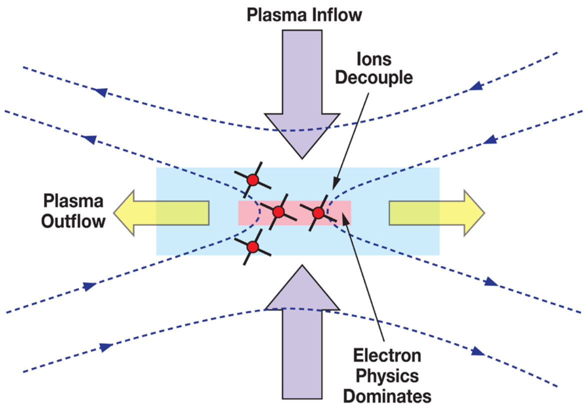

Figure 2.27 Schema of an X-line reconnection region. The dashed arrowed lines represent magnetic field lines and their direction. The large arrows indicate the plasma flow direction and the shaded areas are the ion and electron diffusion regions. The red crosses represent four Magnetospheric Multiscale (MMS) spacecraft that are built to analyze the magnetopause reconnection. Credit: NASA/GSFC MMS mission.

magnetic field normal to it, which has an opposite polarity on each side of the X-line (de Keyser et al. 2005).

The reconnection location on the magnetopause shifts depending on the direction of the incoming IMF as seen in Figure 2.28. During periods of southern IMF, the terrestrial field and IMF are antiparallel at the sunward point of the magnetosphere, owing to the Earth's dipole orientation. The rate of reconnection becomes highest in this case, whereas, when the IMF is directed northward, reconnection tailward of both polar cusps has been observed (Phan et al. 2005). The magnetic flux opened at the front of the magnetosphere is in average balanced by reconnections in the magnetotail, closing the field again. This process is part of the Dungey convection cycle which is described in the next Subsection 2.7.2.

Although the microphysical processes leading to magnetic reconnection are yet little understood (Phan et al. 2005), there is evidence that magnetic reconnection is the dominant plasma transport mechanism into the magnetosphere (de Keyser et al. 2005).

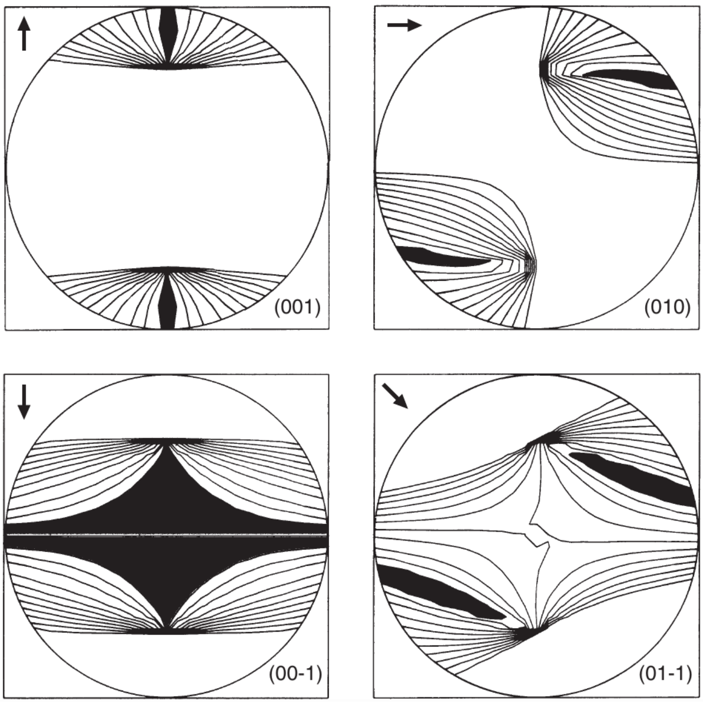

Figure 2.28 Modeled sites of antiparallel magnetic fields (black areas) on the magnetosphere as seen from the Sun. The four different IMF directions are indicated by the arrows and indices. Credit: Russell (2007, Fig. 4.10), © Praxis Publishing, reproduced with permission, after Luhmann et al. (1984, Fig. 2).

Viscous interaction with the solar wind plasma is also able to insert energy into the magnetosphere (Alfvén 1942). Solar wind drag at the flanks of the magnetopause creates Kelvin-Helmholtz (KH) instabilites in form of turbulent eddies. It is observed that even during northern IMF, these turbulent vortices are able to channel solar wind plasma into the magnetosphere – either through forced magnetic reconnection (see Figure 2.29) or non-reconnection processes (Otto & Nykyri 2003; Phan et al. 2005). MHD simulations of the velocity shear at the magnetopause during northern IMF even suggest the presence of a double-vortex sheet structure (Merkin et al. 2013).

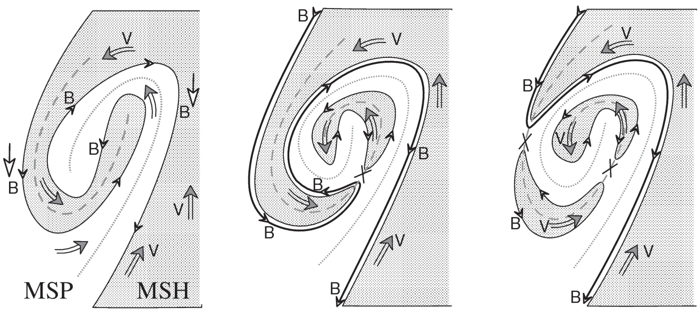

Figure 2.29 Schemata showing reconnection in a turbulent vortex, forming between the magnetosphere (MSP) and the magnetosheath (MSH, shaded area) when both magnetic fields are parallel. The boundary magnetic field line is indicated by the arrowed line, the plasma flow direction by the gray arrows, and the locations of reconnection by crosses. Credit: Merkin et al. (2013, Fig. 5), © American Geophysical Union, reproduced with permission.

2.7.2 Dungey convection cycle

After the reconnection at the sunward magnetopause, the previously closed magnetospheric field lines are open to the IMF. They are still connected to one of Earth's magnetic poles, but their IMF part is transported by the flow of the solar wind. The field lines are stretched behind Earth and form eventually the extended magnetotail, where in its central plane reconnection recloses the field. The closed field lines migrate around the flanks of the magnetosphere to its front again, completing one magnetic convection cycle (Dungey 1961, 1963). The course of this so-called Dungey convection cycle, induced by the solar wind, is illustrated in Figure 2.30. The Dungey cycle imprints a twin-cell convection pattern in the high latitude ionospheric plasma, where the footpoints of the geomagnetic field lines are swept from the day- to the nightside and wander back again along the lower latitudes of dusk and dawn.

Reconnection at the magnetopause and in the magnetotail releases and accelerates the local plasma from the reconnection site along the magnetic field lines. Thus, this plasma reaches the field lines' polar footpoints and interacts with the atoms and molecules of the upper atmosphere, creating the aurorae. The auroral ovals are located at the boundaries between the closed terrestrial field and the field open to the IMF. The open

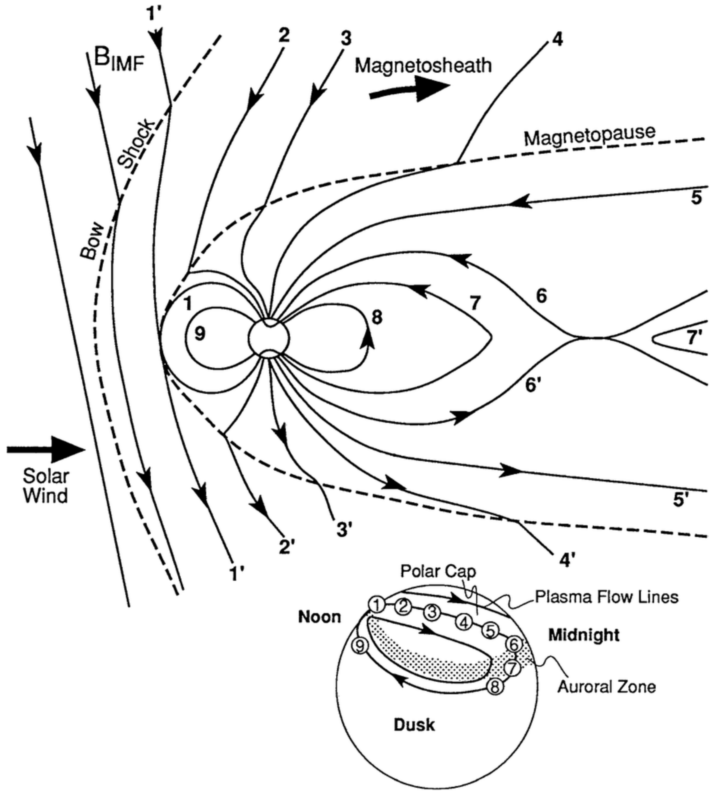

Figure 2.30 Dungey's magnetic convection cycle illustrated in a cut through the magnetosphere (top) and on the ionosphere polar cap (bottom). The numbers on the magnetic field lines (arrowed lines) correspond to the numbered positions in the twin-cell polar cap convection cycle. Credit: Hughes (1995, Fig. 9.11), © Cambridge University Press, reproduced with permission.

field regions, enclosed by the auroral ovals, are the polar caps. The increased reconnection during southward IMF erodes the magnetopause (Aubry et al. 1970), shifting the auroral ovals to lower latitudes. Likewise, the azimuthal IMF component shifts the auroral oval towards dawn or dusk.

The Dungey cycle is not a steady-state process, that is, the rates of opened and reclosed terrestrial magnetic flux are equal only in the long term. The dayside opening flux rate Φ_D is modulated by the dynamic behavior of the solar wind and the orientation of the IMF, whereas the nightside closing flux rate Φ_N depends on the situation in the magnetotail (Milan et al. 2007), see Figure 2.31. The propagation time of the solar wind from

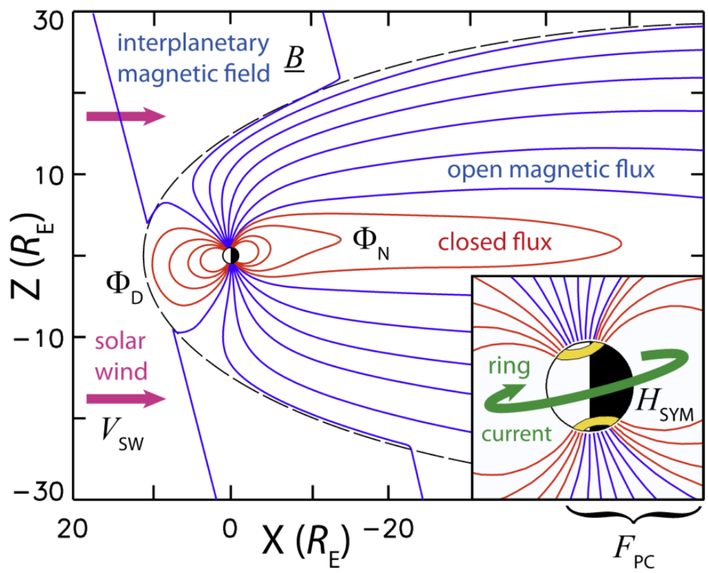

Figure 2.31 Schema of the magnetosphere for the case of southern IMF direction with emphasis on open (blue lines) and closed (red lines) magnetic flux. The magnetopause is indicated by the dashed line. The opening flux rate at the dayside is denoted with Φ_D and the closing flux rate at the nightside with Φ_N. The inset shows day- and nightside of Earth and the relation between auroral ovals (yellow areas) and the open flux at the polar caps (F_{PC}). The ring current intensity H_{SYM} and direction (green arrow) are plotted as well. Credit: Milan (2009, Fig. 1), © American Geophysical Union, reproduced with permission.

the sunward magnetopause to the magnetotail amounts to a lag of about half an hour. Thus, because the rate of reconnection scales with the changing dynamic pressure of the solar wind, the total amount of open flux F_{PC} varies with time so that the ionospheric polar caps expand/contract with time as well (Siscoe & Huang 1985):

$$\frac{\mathrm{d}F_{PC}(t)}{\mathrm{d}t} = \Phi_D(t) - \Phi_N(t)\,. \tag{2.1}$$

Continuous reconnection on the sunward magnetopause builds up the polar cap flux and thus increases stress in the magnetotail, which leads there to regular reconnection bursts, releasing the flux again.

During sunward reconnection, the magnetic field component normal to the magnetopause undergoes regular bipolar oscillations that are interpreted as temporary reconnection events, transferring magnetic flux to the magnetotail. These flux transfer events occur with a period of about eight minutes (Russell et al. 1996). When solar wind conditions are steady, the reconnection process at the sunward magnetopause is found to be steady as well (Phan et al. 2005). During changing IMF direction, the reconnection site moves and intermittent reconnection has been locally observed, but the overall reconnection keeps being continuous and never ceases (Phan et al. 2005).

The reconnection in the magnetotail occurs in regular intermittent reconnection bursts. These bursts can produce magnetic plasmoids that release from the tail and are swept away with the solar wind. This pulsed reconnection has a period of a few hours and is the major nightside flux closure process (Milan et al. 2007). The subsequent effects on the magnetospheric field are called substorms. Their duration varies greatly around an average value of 70 minutes and they vary in intensity as well. Substorms create sudden brightenings and increased activity in the aurora, which also show characteristic patterns matching the substorm cycle. Substorms are found to occur spontaneously during southward IMF periods, however, in 60 % of the cases they are triggered by changing upstream solar wind conditions – either by switches in the IMF orientation or by shocks in the solar wind ram pressure (Milan et al. 2007).

The arrival of extreme solar wind conditions, such as found in CMEs and CIRs, generates geomagnetic disturbances larger than substorms, these geomagnetic storms are described in Section 2.8.

2.7.3 Russell-McPherron effect

Geomagnetic activity varies semiannually with the maxima around the equinoxes and the minima around solstices (Cortie 1912). Russell & McPherron (1973) suggested a model, now called the Russell-McPherron (R-M) effect, that is able to predict the correct phase and the observed variation in strength seen yearly in geomagnetic activity. They define a solar wind-magnetosphere interaction in GSM coordinates that is set to zero during northward IMF and is otherwise proportional to the southward IMF component – analog to a half-wave rectifier. As solar wind and IMF are naturally ordered in the geocentric solar equatorial (GSEQ) coordinate system, their flow angle against the magnetosphere undergoes seasonal changes. The mechanism then is provided by the changing probability over the year of getting a north- or southward IMF, viewed in the GSM-frame of the magnetosphere. This variation is found to be sufficient to generate the observed effect (Russell & McPherron 1973).

In addition to the R-M effect, the interaction depends on the dipole tilt angle to the solar wind, which is shown to regulate the extent of the sunward reconnection region and therefore the reconnection rate and geomagnetic activity (Russell et al. 2003). There exist other hypotheses describing the semiannual variation: the axial and the equinoctial hypotheses. However, the R-M effect is the most prevailing and is even able to explain the variation of geomagnetic activity under extreme solar wind conditions, such as interplanetary shocks (Zhao & Zong 2012).

2.7.4 Geomagnetic indices

In order to monitor the state of the magnetospheric system and disturbances therein, geomagnetic observatories are widely distributed over the globe, measuring the local magnetic field at their position. Magnetic measurements from several sets of stations define several geomagnetic indices. The measurements cover specific regions in order to monitor the state of different parts of the magnetospheric system. The major global geomagnetic indices are supported by the International Association of Geomagnetism and Aeronomy (IAGA) and serviced by the International Service of Geomagnetic Indices (ISGI)[13]. These indices and their purpose are listed in the following: The aa index is designed to represent the amplitude of the global geomagnetic activity, normalized to a geomagnetic latitude of ±50°. The am index characterizes the global geomagnetic activity. The Kp index is designed to measure geomagnetic disturbances from solar particle radiation. The Dst index monitors the intensity of the magnetospheric ring current. The PC index monitors the polar cap magnetic activity – it approximates the amount of energy which entered the magnetosphere through solar wind coupling. The AE index and its relatives AU, AL and AO measure the magnetic effects of the northern auroral electrojet. The first three listed indices (aa, am and Kp) are calculated from different sets of local 3-hourly K indices, which measure the local magnetic disturbances at the observatories. The Kp and Dst indices are described in more detail in the following section.

[13] ISGI website: http://isgi.unistra.fr/

2.8 Geomagnetic storms

Geomagnetic storms are major disturbances in the geomagnetic field, generated under extreme solar wind conditions. In contrast to substorms which originate in the magnetotail, geomagnetic storms are directly caused by the incoming solar wind flow at the sunward magnetopause. Indeed, the main phase of geomagnetic storms is always accompanied in parallel by substorms (Gonzalez et al. 1994). During geomagnetic storms, substorms even occur in higher frequencies and can overlap each other.

Carrington (1859) was the first to associate a geomagnetic storm with an event of solar origin, that is, he noticed a major solar flare appearing a few hours before the storm. The corresponding solar event is known as the Carrington event, as the resulting geomagnetic storm is the largest ever observed. Forbush (1937) found a rapid reduction in cosmic-ray intensity occurring parallel to a geomagnetic storm, now known as Forbush decreases, and attributed both to a common external cause. Eventually, Wilson (1987) demonstrated the connection between geomagnetic storms and MCs by finding simultaneous decreases in the Dst index during episodes of southward IMF within MCs. The order in which north- and southward IMF appears in an MC does not matter for the final observed Dst magnitude, but the Dst activity is always in phase with the southward field (Zhang & Burlaga 1988). Finally, Gosling (1993) established that CMEs rather than flares are the main cause of major geomagnetic storms and large SEP events. Indeed, single and multiple CME events are found to be the most geoeffective solar wind structures in that they are accountable for about 87 % of the major geomagnetic storms, whereas the remainder is produced by CIR events (Zhang et al. 2007).

Solar wind injects plasma and energy into the magnetosphere, varying the number of particles in the magnetospheric equatorial current system, the so-called ring current, illustrated in Figures 2.26 and 2.31. The ring current is located between 2–7 R_E (Gonzalez et al. 1994). When the ring current is increased due to incoming CMEs or CIRs, it generates an enhanced magnetic field of opposite polarity to the magnetospheric field. This leads to a decrease in the local terrestrial magnetic field.

The decrease is measured by four magnetic observatories located near the dipole equator. Their magnetic field measurements are the base for the disturbance storm time index Dst (Sugiura & Kamei 1991). Therefore, Dst represents the intensity of the ring current and is a quantitative measure for geomagnetic disturbances. The Dst index is derived and published through the IAGA at the World Data Center for Geomagnetism in Kyoto[14].

Historically, the size of a geomagnetic storm was defined as the peak negative disturbance in the Dst index. Though, the onset of a geomagnetic storm is typically an aprupt increase in Dst, referred to as a storm sudden commencement (SSC). The initial period of positive Dst lasts some hours and is caused by the compression of the magnetosphere due to the increased pressure of arriving shocked solar wind plasma. The intensity of a geomagnetic storm can be gauged by the minimum Dst that is reached in its main phase – during moderate storms Dst falls below -50 nT and during intense storms below -100 nT (Gonzalez et al. 1994). The main phase lasts a few hours, but the recovery to average Dst levels is gradual and can take up to several days.

However, for the assessment of the planetary geomagnetic activity, another index has been used more widely than Dst, the Kp index (Gonzalez et al. 1994). Kp is the most prevalent index used by space weather forecasters to indicate the severity of geomagnetic storms (Wing et al. 2005), for instance, Kp is the basis for NOAA's G-Scale[15].

Field-aligned currents, called Birkeland currents, connect ionospheric currents located in the nightside auroral oval, called the auroral electrojets, to the magnetopause and the partial ring current (Coxon et al. 2014), see Figure 2.26. In addition to the ring current, this current system generates large magnetic disturbances as well. Collectively, all currents contribute to the planetary geomagnetic disturbances, which are quantified on the ground with the planetary geomagnetic disturbance index Kp.

2.8.1 *Kp* index

Julius Bartels introduced a K index in 1938 and designed it to measure the intensity of geomagnetic disturbances (Bartels et al. 1939). Its name originates from 'Kennziffer' – the german word for characteristic digit. The K index is a measure for the maximal variation of the surface magnetic field, observed in a magnetogram within 3-hour intervals. Its scale in the range 0–9 is a quasi-logarithmic representation of the actual magnetic field strength's variations.

The Planetary K index (Kp) is a planetary geomagnetic disturbance index, introduced by Bartels in 1949 at the Institute for Geophysics, University of Göttingen (Bartels & Veldkamp 1949). Kp is the weighted average of 13 Ks indices, which are the standardized versions of the local K indices measured at 13 observatories.

[14] WDC for Geomagnetism, Kyoto; Dst index service: http://wdc.kugi.kyoto-u.ac.jp/dstdir/index.html
[15] NOAA Space Weather Scales website: https://www.swpc.noaa.gov/noaa-scales-explanation

These contributing observatories are located around ±50° geomagnetic latitude and their distribution is biased towards Europe, as can be seen in the map in Figure 2.32.

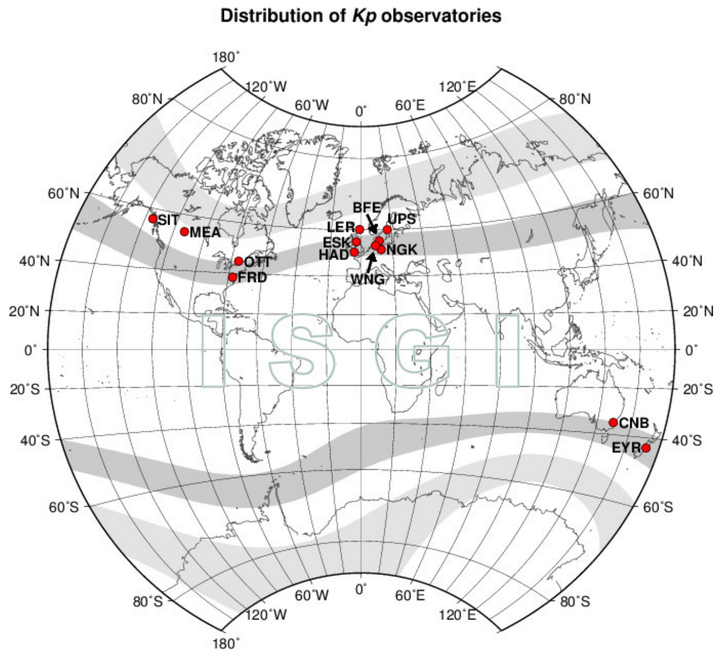

Figure 2.32 Distribution of the 13 *Kp* observatories. The shaded belts indicate regions of equal geomagnetic latitude. Courtesy of International Service of Geomagnetic Indices (ISGI), 2013.

To benefit from its higher precision, its scale, in the range 0–9 as well, is further divided into thirds, represented by the suffixes '+', 'o' and '−' (e.g., 3o, 3+, 4−, 4o). The *Kp* indices are often visualized in musical diagrams, where they are stacked into periods of 27 days to enable the detection of recurrent geomagnetic activity, as seen in Figure 2.33.

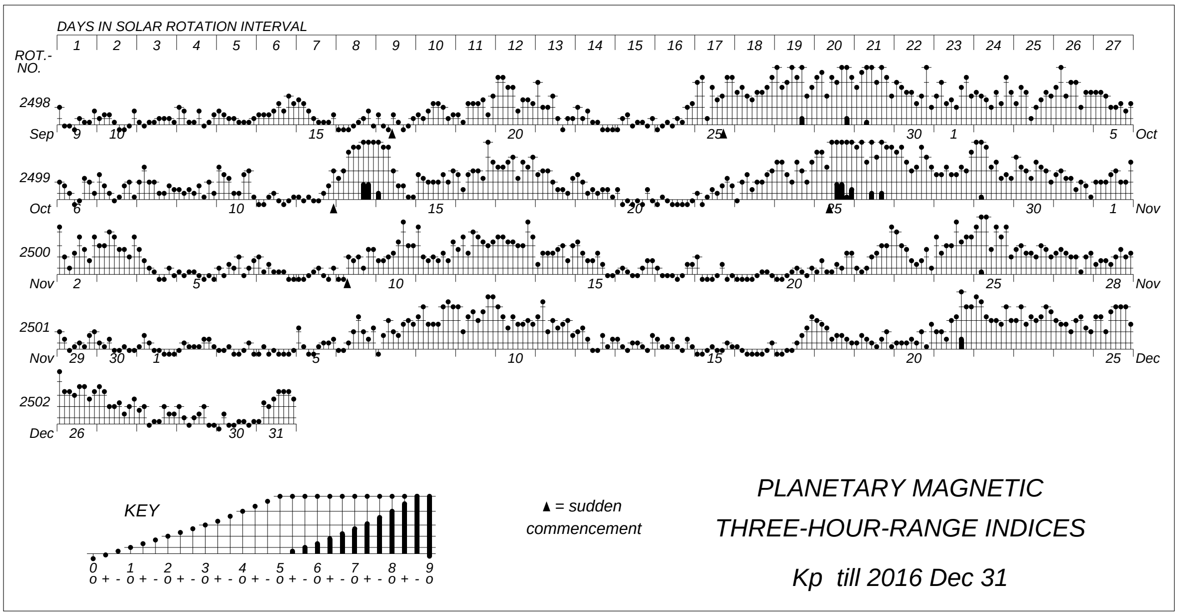

Figure 2.33 Bartels musical *Kp* diagram for the time period from September until end of December 2016. Two sudden commencements with following geomagnetic storms, having a maximal *Kp* of 6+, can be seen in October. Credit: GFZ Potsdam, 2017, licensed under CC BY 4.0.

The *Kp* index can be converted to the 3-hour equivalent *ap* index, which represents the magnetic field strength at a surface position of about ±50° dipole latitude. The conversion is done via a table specified by Bartels, in which the value of the *ap* index is scaled in units of 2 nT, as seen in Table 2.1. There are further geomagnetic indices which are derived from the *Kp* index. They include Ap, the daily *ap* average, Cp, the daily *ap* sum mapped via a fixed table to the range 0–2.5, and *C*9, a mapping of Cp via a fixed table to the range 0–9. The definitions of Q-days (quiet days) and D-days (disturbed days) are also obtained from the *Kp* index.

Table 2.1 Table for the fixed conversion from the *Kp* index to the equivalent *ap* index, which represents the magnetic field strength in units of 2 nT.

Kp	0o	0+	1−	1o	1+	2−	2o	2+	3−	3o	3+	4−	4o	4+
ap	0	2	3	4	5	6	7	9	12	15	18	22	27	32
Kp	5−	5o	5+	6−	6o	6+	7−	7o	7+	8−	8o	8+	9−	9o
ap	39	48	56	67	80	94	111	132	154	179	207	236	300	400

The IAGA adopted the *Kp* index in 1954. The *Kp* index was maintained in Göttingen until January 1997 – now the German Research Centre for Geosciences (GFZ) in Potsdam supplies the *Kp* index and thereof derived indices. See also the *Kp* data description in Section 3.3.

2.9 Geomagnetic activity forecast

The timing and intensity of geomagnetic storms is sought to be forecasted from knowledge about the upcoming solar wind conditions. This means that there are two questions to this task: First, how does the incoming magnetized solar wind plasma result in magnetospheric disturbances? In order to resolve this, coupling functions relating geomagnetic indices to solar wind parameters are essential. Second, what state will the arriving solar wind be in at the magnetopause? Hence, a forecast using remote observations is required which is able to predict the arrival time and conditions of solar wind streams and CMEs. Both questions are addressed in the following sections.

2.9.1 Coupling functions

In order to quantify geomagnetic activity, solar wind coupling functions that correlate sufficiently well with geomagnetic indices are necessary. These relations can then be used to connect solar wind parameters with geomagnetic indices via empirically fitted functions, as is described for the *Kp* index at the end of this section.

The major interaction mechanisms between solar wind and magnetosphere are magnetic reconnection and viscous turbulence, as mentioned previously in Subsection 2.7.1. Newell et al. (2008) found that a single coupling function, consisting of a merging and a viscous part, is able to describe the solar wind-magnetosphere interaction best, in that it correlates with the behavior of a broad range of geomagnetic indices.

The rate magnetic flux is opened at the magnetopause generally depends on the following independent factors (Newell et al. 2007):

- The rate magnetic flux is transported towards the magnetopause, represented by the solar wind velocity.
- The amount of opened flux, which scales with the IMF strength.
- The merging probability, which depends on the IMF clock angle.
- The extent of the reconnection region, represented by the length of the X-line on the magnetopause.

Many coupling functions were proposed in order to characterize the solar wind's interaction processes with the magnetosphere. They consist of functional terms of differing complexity, mostly including and approximating some of the factors listed above. There exist a lot of coupling functions based on combinations of the same physical quantities, often including the IMF direction (Newell et al. 2007; Lockwood 2013). Here I list and discuss a few of the most used coupling factors and functions:

- v, the solar wind velocity. Snyder et al. (1963) found a strong correlation of the daily average velocity with geomagnetic activity from Mariner 2 solar wind measurements.
- B, the IMF strength. The long-term average IMF strength is observed to be proportional to the level of geomagnetic activity (Stamper et al. 1999; Lockwood 2013).
- B_z, the IMF z-component. Fairfield & Cahill (1966) deduced from early satellite IMF measurements that the southern IMF component is linked with geomagnetic disturbances, whereas a northward IMF is connected with quiet geomagnetic conditions.
- B_s, the half-wave rectifier as defined by Russell & McPherron (1973), see also the R-M effect in Subsection 2.7.3. It describes a simple interaction in GSM coordinates that is proportional to the southward IMF component and zero during northward IMF:

$$B_s = \begin{cases} 0 & \text{for } B_z > 0\,, \\ -B_z & \text{for } B_z \leq 0\,. \end{cases} \tag{2.2}$$

- $|\boldsymbol{B}|\sin^n(\theta_c/2)$, a term depending on the IMF clock angle θ_c and in shape similar to the half-wave rectifier. However, it is continuous around zero and therefore often preferred over B_s (Lockwood 2013). The IMF clock angle is defined as $\theta_c = \tan^{-1}\left(B_y/B_z\right)$ and the exponent is often chosen as $n = 2$ or $n = 4$, see also Figure 2.34. The term stands for the fraction of IMF field lines which merge with the magnetopause, that is, the merging probability of those IMF field lines which impact the magnetopause.

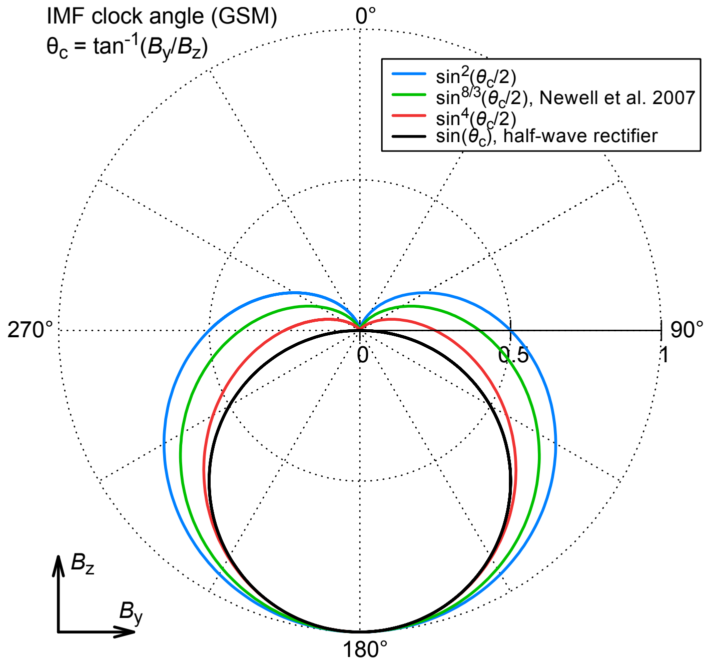

Figure 2.34 IMF clock angle (θ_c) dependency of the coupling functions' relative amplitudes. The different coupling functions include the IMF clock angle factor by Newell et al. (2007) and the half-wave rectifier (black). I plotted the GSM coordinate directions in the upper left for orientation.

- $\boldsymbol{E}$, the solar wind electric field which is, with the help of some assumptions, often reduced to its y-component E_y:

$$\boldsymbol{E} = -\boldsymbol{v} \times \boldsymbol{B}\,, \tag{2.3}$$

$$\approx -v_x B_z = E_y\,. \tag{2.4}$$

It is one of the most prominent coupling functions and represents the rate at which southward magnetic flux is transported to the magnetosphere (Russell 2007, p. 103). How this relation is derived and which assumptions are made for the reduction to E_y is described in the appendix Section A.2.

- ε, the epsilon parameter which is based on the solar wind's energy density (Perreault & Akasofu 1978). It represents the Poynting flux entering the magnetosphere:

$$\varepsilon \propto {l_0}^2 v B^2 \sin^4\left(\frac{\theta_c}{2}\right), \tag{2.5}$$

where l_0 is a scaling factor for the cross-sectional area of the magnetosphere.

- P_α, the solar wind power coupled into the magnetosphere (Stamper et al. 1999; Lockwood 2013). It consists of the product of the solar wind power density, the cross sectional area of the magnetosphere, and the fraction of the incident power that crosses the magnetopause:

$$P_\alpha \propto n^{2/3-\alpha} v^{7/3-2\alpha} B^{2\alpha} \sin^4\left(\frac{\theta_c}{2}\right). \tag{2.6}$$

The coupling exponent α depends on the coupling to the solar wind Alfvén Mach number and has a value around 0.4.

- $\mathrm{d}\Phi/\mathrm{d}t$, a relation derived by Newell et al. (2007). It represents the rate magnetic flux is opened at the magnetopause:

$$\frac{\mathrm{d}\Phi}{\mathrm{d}t} = v^{4/3}|\boldsymbol{B}|^{2/3} \sin^{8/3}\left(\frac{\theta_c}{2}\right). \tag{2.7}$$

The X-line length is approximated with $(v/|\boldsymbol{B}|)^{1/3}$ and is included within the first two factors. The value of the sinus exponent, $n = 8/3$, is determined empirically. This relation shows the highest correlation with 9 out of 10 geomagnetic indices out of various tested coupling functions, aiming to be an universal solar wind-magnetosphere coupling function (Newell et al. 2007). The coupling function's correlation coefficient with the Kp index reaches a value of $r = 0.760$.

Newell et al. (2008) found recently that coupling functions show the highest correlation when they consist of a merging term combined with a viscous term. As the viscous term describes another kind of interaction process, that is, reconnections due to Kelvin-Helmholtz instabilies at the flanks of the magnetosphere, it is independent from the dayside reconnection term. The viscous term accounts for the smaller fraction of variance and usually depends on the solar wind plasma quantities velocity and density. Newell et al. (2008) deduced that one of the best combinations for the Kp index is the merging term $\mathrm{d}\Phi/\mathrm{d}t$ together with the viscous term $\sqrt{n} \cdot v^2$, resulting in a correlation coefficient as high as $r = 0.866$.

The correlation of a coupling function only shows which quantities are involved in the interaction and how much they contribute to the observed variance. In order to quantify the interaction and relate the coupling functions to geomagnetic indices, empirical relations can be obtained by fitting both time series.

As the Kp index is the measure for the size of geomagnetic disturbances, many simple and more complex analytical functions connecting Kp with different solar wind coupling functions were determined.

- Snyder et al. (1963) deduced the following relation for the daily sum of the eight Kp values from Mariner 2 data: $\sum Kp(v) = (v - 330)/8.44$.
- Newell et al. (2008) developed a relation comprising the previously mentioned coupling function set of a merging and a viscous term. Their equation for the least variance linear prediction of Kp is

$$Kp = 0.05 + 2.244 \times 10^{-4} \frac{\mathrm{d}\Phi}{\mathrm{d}t} + 2.844 \times 10^{-6} \sqrt{n} \cdot v^2 \,. \tag{2.8}$$

- Mays et al. (2015) fitted $\mathrm{d}\Phi/\mathrm{d}t$ with the Kp index and obtained the empirical relation

$$Kp = 9.5 - \exp\left(2.18 - 5.20 \times 10^5 \left(\frac{\mathrm{d}\Phi}{\mathrm{d}t}\right)\right) , \tag{2.9}$$

  with the velocity measured in $\mathrm{km\,s^{-1}}$ and the magnetic field in nT.

The present study adds more empirical Kp relations – for the cases when only the solar wind velocity v or its electric field vB_z are known.

2.9.2 *Kp* forecast methods

The different empirical functions are utilized in various methods for Kp prediction. That includes the now- and forecast of Kp from different data sets and real-time measurements...

Kp nowcast with L1 data; f/c see next sec.
Kp prediction methods

List of Kp prediction models (now- and forecast):

- The Wing Kp models have 1- and 4-hour predictions. They are based on neural network models that take as input the solar wind real-time measurements made at L1 and the current Kp nowcast (Wing et al. 2005). The model is provided by the U.S. Air Force Weather Agency and hosted at NOAA/SWPC: `https://www.swpc.noaa.gov/products/wing-kp`.
- Kp quicklook, GFZ Potsdam
- Aleksei's f/c model; Ukraine
- Newell's coupling relation is being implemented into forecast procedures (Savani et al. 2017).
- Elliott2013? Kp-v
- Bala & Reiff (2012); their Kp forecast website: `http://mms.rice.edu/realtime/forecast.html`. Improvements in short-term forecasting of geomagnetic activity; Ramkumar Bala and Patricia Reiff 2012 We have improved our space weather forecasting algorithms to now predict Dst and AE in addition to Kp for up to 6 h of forecast times. These predictions can be accessed in real time at `http://mms.rice.`

edu/realtime/forecast.html. In addition, in the event of an ongoing or imminent activity, e-mail alerts based on key discriminator levels have been going out to our subscribers since October 2003. The neural network–based algorithms utilize ACE data to generate full 1, 3, and 6 h ahead predictions of these indices from the Boyle index (Boyle1997), an empirical approximation that estimates the Earth's polar cap potential using solar wind parameters. Our models yield correlation coefficients of over 0.88, 0.86, and 0.83 for 1 h predictions of Kp, Dst, and AE, respectively, and 0.86, 0.84, and 0.80 when predicting the same but 3 h ahead.

- NOAA/SWPC; see Savani2017
- NASA/SWRC; see Savani2017

2.9.3 CME and stream forecast to Earth

Space weather effects can be directly attributed to CME sub-structures. While the outermost structure (shock) accelerates particles and causes sudden commencement, the interior structures (sheath and flux rope) cause geomagnetic storms if they possess a strong southward component of the magnetic field (Gopalswamy 2016).

Southward interplanetary field can also occur in the shock sheaths (Gonzalez and Tsurutani 1987; Gosling and McComas 1987), which have been shown to be equally important in causing geomagnetic storms (Tsurutani et al. 1988).
The results of this study indicate the equal importance of both sheath fields or draped fields and driver gas fields for the generation of major geomagnetic storms. Because of the importance of the sheath fields the intensity and duration of geomagnetic storms cannot be predicted by solar observations of active regions alone (Tsurutani et al. 1988).

Savani2015:
The compressed solar wind plasma in between supersonic magnetic flux rope obstacles and their driven shock fronts has not been addressed in this article, even though they have been shown to be significant drivers of magnetospheric storms [Huttunen and Koskinen, 2004].

CME forecast:
- WSA-ENLIL CMEs without B-field forecast
- MC forecast; Savani2015: Predicting the magnetic vectors within coronal mass ejections arriving at Earth: 2. Geomagnetic response
- UGOE CME forecast chain (DDC)

Stream forecast:
- CH sw forecast (Uni Graz)
- WSA-ENLIL sw forecast (CMEs without B-field)

It makes sense to use the geocentric solar magnetospheric (GSM) coordinate system, which is aligned with the Earth's magnetic dipole axis.

2.9.4 CME forecast to Earth

It is important to know in advance if and when CMEs arrive at Earth, because of their possible strong impact on the terrestrial magnetosphere. Knowing the geometry of a CME, it is possible to infer its direction and speed from white-light images. Through kinematic forward-modeling techniques that take advantage of the self-similar expansion observed in CMEs, it is possible to derive an estimated arrival time at Earth. As MCs are the drivers for most severe geomagnetic disturbances (Bothmer & Schwenn 1995; Cane & Richardson 2003), it is also important to forecast their magnetic field strength and configuration.

An early 3D model for a general CME geometry is the ice-cream cone model, which assumes a simple bubble-like CME structure (Fisher & Munro 1984). Though, building on the the study by Cremades & Bothmer (2004), Thernisien et al. (2006) created the more complex graduated cylindrical shell (GCS) model for flux rope-like CMEs. This model assumes an empirically derived electron distribution in order to create synthetic coronagraph images. The GCS model is successfully applied to images of CMEs with well-developed white-light structure (Bosman et al. 2012) and is implemented as a part of current CME forecast procedures.

Depending on whether CMEs are faster or slower than the surrounding solar wind, they decelerate/accelerate on their way through the heliosphere due to solar wind drag forces. Fast CMEs already decelerate substantially during their first few solar radii (Sachdeva et al. 2017). In case a CME interacts with a preceding CME, they both travel on with an intermediate speed (Manoharan et al. 2004; Temmer et al. 2012).

Extreme CME velocities above 2000 km s^{-1} near the Sun are rare, nevertheless, in some cases speeds around 3000 km s^{-1} were measured. From the free energy available in active regions, Gopalswamy et al. (2005) concluded that CME speeds cannot be far greater than 3000 km s^{-1}. This would implicate that CMEs need at least half a day to travel from their source region on the Sun to reach Earth. Gopalswamy et al. (2010) even estimated a maximal limit of free energy active regions can store, which means that CMEs with 4000 km s^{-1} are not possible. Faster CMEs usually come with higher magnetic field strengths, for example the CME observed by STEREO A on 23 July 2012 had a shock speed of about 2000 km s^{-1} at 1 au and its magnetic field magnitude reached values of up to 100 nT (Russell et al. 2013).

Predicting the magnetic field variations in ICMEs from solar observations is a central subject for space weather forecasting because a long-lasting southward-directed field is a primary driver of major geomagnetic storms (Zhang et al. 2007).

Identification of a flux rope near the Sun makes it easier to predict the expected magnetic configuration at Earth, modified by the interaction with the solar wind on its way to Earth. (cite?)

Bz prediction:
Savani2015: Predicting the magnetic vectors within coronal mass ejections arriving at Earth: 1. Initial architecture

Savani2015:
Thus, models used for routine CME forecasts by various space weather services do not include magnetic structures within the simulated CMEs [e.g., Zheng et al., 2013; Shiota et al., 2014]. For example, ENLIL models the propagation of CMEs from 20 solar radii (Rs) to beyond Earth at 215 Rs and includes the background solar wind magnetic field. However, the CME is simplified to a high-pressure plasma pulse with a size and propagation direction estimated from solar imagery [Zheng et al., 2013]. CME arrival time predictions from these models provide lead times of 2–3 days, and their accuracy has been well investigated [Taktakishvili et al., 2010; Vršnak et al., 2014; Colaninno et al., 2013]. In contrast, the important magnetic vector information is only revealed when in situ measurements are made by spacecraft upstream of Earth at the first Lagrangian position (L1) 1 h prior to the CME arriving at Earth, thereby severely limiting the lead time available for reliable, magnetic field-based, storm warnings.
Savani2015:
In this paper, we highlight three key components of a proof of concept developed to improve the prediction of a storm's severity: (1) the use of the hemispheric helicity rule to provide a robust initial magnetic configuration at the Sun; (2) define a "volume of influence" of the CME, within the heliosphere, for which the Earth's trajectory can be estimated; and (3) incorporating magnetic vectors from a simplified magnetic flux rope model to create a time series upstream of Earth.

constant-alpha force-free (CAFF) flux ropes (Burlaga1988)

adjusted BSS scheme (Savani2015)

Savani2017:
inferring the magnetic field direction along the trajectory of Earth through the CME would be a major advance in geomagnetic activity prediction.

Savani2017:
This event highlights the need to forecast the field vectors not only in the flux rope but also in the sheath [e.g., Huttunen and Koskinen, 2004].

Cranmer2017:

Complicating our understanding even more is the fact that processes such as turbulence, stream-stream interactions, and Coulomb collisions can make it difficult to unambiguously map a parcel measured at 1 AU back down to its coronal source.

2.10 notes...

These events (GS) are able to disturb sensitive technical systems. Understanding the properties of the solar wind helps with the prediction and protection of humanity's assets.

put fig. somewhere earlier (p. 10?): see Figure 2.35

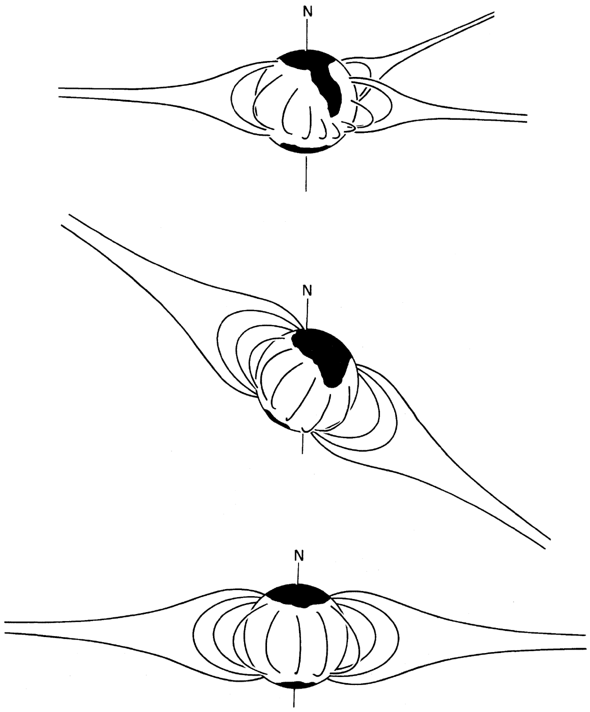

Figure 2.35 Schemata of different coronal configurations during the solar cycle. Visualized are the locations of closed coronal magnetic fields (lines) and coronal holes (black areas) for a post maximum distorted dipole (top panel), for a pre minimum stable tilted dipole (middle panel), and a post minimum axial dipole (bottom panel). Credit: (Hundhausen 1977, Fig. 20, panels (b–d)), © Colorado Associated University Press, reproduced with permission.

The weaker solar activity cycle 24 seems to have important consequences for CMEs in the heliosphere: CMEs expand anomalously due to reduced heliospheric pressure leading to the increased observed rate of small CMEs, halos originating far from the disk center, and mild space weather ((Gopalswamy et al. 2014), 2015a; Petrie 2015).
The total pressure in the heliosphere (magnetic + plasma) is reduced by ca. 40%, which leads to the anomalous expansion of CMEs explaining the increased slope. The excess CME expansion contributes to the diminished effectiveness of CMEs in producing magnetic storms during cycle 24, both because the magnetic content of the CMEs is diluted and also because of the weaker ambient fields (Gopalswamy et al. 2014).

the dayside reconnection is asymmetric

causes (see citetRangarajan1997 p. 1282 and mention Bartels1963 too)
read Bothmer1998 Ch 3...

Sonnerup & Cahill (1967): The rotational discontinuity seems to occur predominantly during magnetic storms and two of these cases, involving substantial normal-field components, provide compelling evidence that field reconnection takes place during the storm main phase.

sources of southward Bz:
- MCs
- compressed material in front of CMEs (highest driving velocities)
- SIRs/CIRs front of HSSs
- sw streams

3-part structure figure ... find event with shock and flux rope?
abbreviate magnetic flux rope to MFR?

why HCS? what currents are there...
why is the CS not the divide between both polarities?

"The principal users affected by geomagnetic storms are the electric power grid, spacecraft operations, users of radio signals that reflect off of or pass through the ionosphere, and observers of the aurora."NOAA cite

strong radio bursts...

at Earth the solar wind total energy flux (1.45 mW/m^2) is only about one millionth of the solar radiation flux (see Schwenn (1990, p. 153))

radiation belts

Phan2005, Magnetopause Processes:
Cluster findings include:
A strong ‘guide field’ detected at a reconnection X-line, i.e., a finite magnetic field along the X-line, has provided direct evidence for component merging.
Tailward-of-the-cusp reconnection has been found to occur only when the IMF has a northward component. The occurrence rate of cusp reconnection is nearly 100% when the IMF has a northward component, implying that cusp reconnection in the northern and southern hemispheres must be common. The high occurrence rate (in contrast to a rate of 50% at the subsolar magnetopause) is thought to be due to the presence of a plasma depletion layer. In this layer, the plasma beta is reduced, rendering the magnetosheath flow sub-Alfvenic and allowing the establishment of a stable X-line at the high-latitude magnetopause.

look into printed paper collection...

(Russell 2007, p. 103)
This half-wave rectification has an important implication on how the reconnection rate must be controlled by the IMF direction and where reconnection occurs.

Lockwood et al. (2014) even used geomagnetic indices (including *aa*) to reconstruct the near-Earth IMF strength and solar wind flow speed back to 1845.

The MC plotted in Figure 2.21 created a *Kp* of 6+.

for overview see chapter 4 in Bothmer2007book

observed coronal transient: 3d structure, directed at Earth, associated with shock wave; (Howard et al. 1982)
-> halo CME

3 Instrumentation and data description

For analyzing the solar wind and related areas on the Sun, there exist remote instruments, such as solar imagers and coronagraphs, and in-situ instruments, such as magnetometers and plasma detectors. In this chapter the basic principles of the latter are described, because the analyses performed in this thesis are based entirely on in-situ measurements – except for the sunspot time series.

Different kind of data, collected from observatories at various locations, are used for the investigations performed in this thesis. In the following sections, I describe the data sets of the magnetospheric disturbance index *Kp* and of the solar activity indicator sunspot number (SSN). Further, the solar wind in-situ data sets are described: the near-Earth OMNI data collections consisting of minutely and hourly data, that is, low resolution OMNI (LRO) and high resolution OMNI (HRO), and the data obtained from the Helios 1 and Helios 2 spacecraft in the 1970s. I plotted a time coverage overview of these data sets in relation to the solar activity cycles in Figure 3.1.

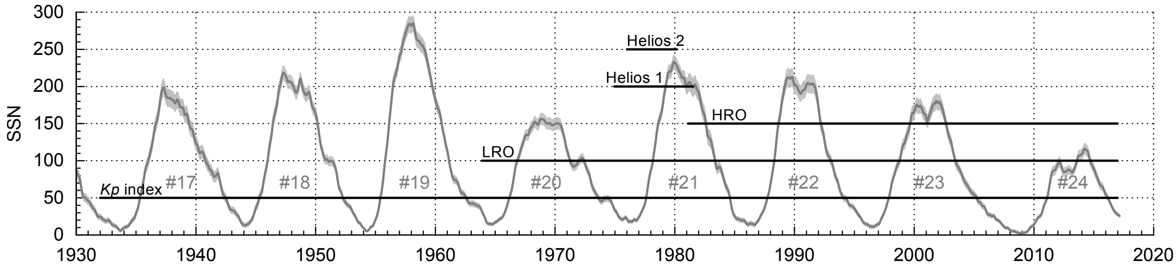

Figure 3.1 Time coverage of the data sets used in this work with the solar activity from 1930 until end of 2016. The individual data sets are the *Kp* index, the low and high resolution OMNI (LRO and HRO) collections, and the Helios 1 and Helios 2 data sets. I plotted the SIDC 13-month smoothed monthly SSN and the cycle number in the background for orientation.

3.1 Magnetometer

Spacecraft nowadays carry two different magnetometer types, one for measuring the magnetic field direction and its strength and the other for observing the magnetic flux and detecting waves.

A flux-gate magnetometer consists of two coils around a core – one coil with alternating current, wich is compared with the induced current signal from the other. Without external magnetic field both patterns match. The core is easier magnetized in direction of an existing external magnetic field, in which case the patterns differ. It measures...
In a search coil magnetometer one coil is placed around a core; measures plasma waves – where?

Because these magnetometer types are directional, they often are placed in two sets of triaxial configurations, attached on booms to minimize the influence of the spacecraft's own magnetic field.
L-> which is generated by surface charges?/electrons?/ionization?/the instruments?

figures and references...!

Ground based magnetometers measure the local magnetic field of the Earth. They already exist since...

examples:
ACE/MAG – flux-gate magnetometer

3.2 Plasma detector

several spectrometers with different energy ranges

isotope spectrometer - isotopic abundances of SEPs
ionic charge analyzer - charge state of SEPs
solar wind ion mass spectrometer -
solar wind ion composition spectrometer -
radio burst tracker

A plasma detector measures the ion energy frequency distribution, which consists basically only of protons and alphas in solar wind. I prepared a synthetic ion energy spectrum for illustration in Figure 3.2.
...read `http://www.goembel.biz/sun.html`

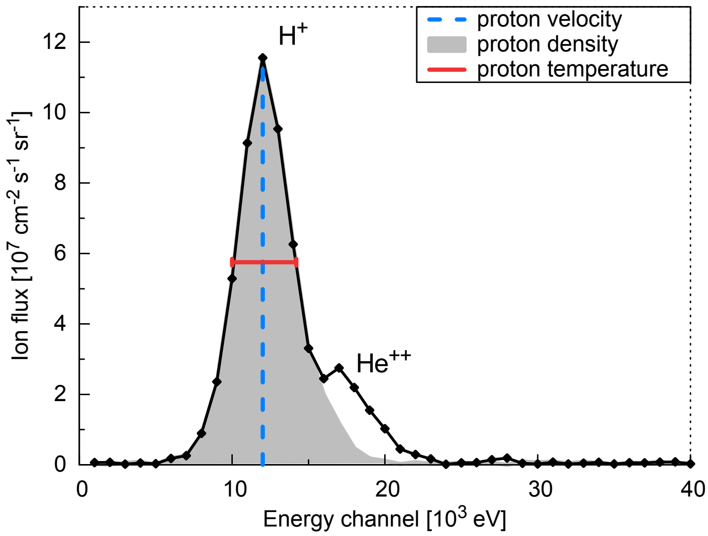

Figure 3.2 Example of an ion energy spectrum for which I prepared some synthetic data points, including a small helium peak. capitalize Proton...

The velocity, density, and temperature can be derived from the energy spectrum.
more details...!

The bulk velocity is derived from the distribution's average energy (or position of Maxwell-Boltzmann distribution?).
The number density is the area of the distribution.
The temperature scales with the distribution's width.

ACE/SWEPAM

3.3 *Kp* data

see also 2.8.1

The GFZ provides historical and quicklook data of the indices via their website[1].

The data series was extended backwards using existing measurements and is now available from 1932 onwards.

There exist several indicators/quantities that scale or are based on the *Kp* index:

- NOAA's Space Weather Prediction Center (SWPC) developed its NOAA G-Scale[2] for geomagnetic storms which relates the *Kp* index to five levels from G 1 to G 5.

[1]GFZ website for geomagnetic indices: `http://www.gfz-potsdam.de/en/kp-index/`
[2]NOAA Space Weather Scales website: `http://www.swpc.noaa.gov/noaa-scales-explanation`

- The equatorward auroral boundary position correlates with the *Kp* index (cite?).
- The variation of the total electron content (TEC) of the ionosphere correlates with the *Kp* index (cite?). The TEC has influence on global navigation satellite systems (GNSS). A part of their positional error scales directly with TEC (in extreme cases up to about 30 m).

'The *Kp* index is designed to measure solar particle radiation by its magnetic effects.'

Because of the geomagnetic disturbance impacts on sensitive technical systems, various methods for now- and forecasting the *Kp* index are developed:

- GFZ Potsdam Nowcast *Kp* index[3].
- USAF Wing *Kp* model (Wing et al. 2005); 1–4 hours foercast from real-time solar wind measurements[4]
- ?Alexej *Kp* correlation forecast model; developed within AFFECTS (link)
- In Chapter 4 of this work, I derive relations to enable *Kp* nowcast from in-situ solar wind measurements and to enable *Kp* forecast from remote CME/solar wind stream observations.

Savani2017:
The Kp difference of 1.5 is tested as there is evidence that a limitation in accuracy is present in the underlying empirical Kp formulation [Mays et al., 2015a]. [...] which is approximately consistent with recent results by Mays et al. [2015a], the Kp empirical formulation is accurate to about Kp = 1.5.

3.4 Sunspot number

The number of sunspots occuring on the solar surface is commonly used as a long-term solar activity indicator, for more information on solar activity and sunspots see Section 2.3. The international sunspot number (SSN) is maintained by the World Data Center – Sunspot Index and Long-term Solar Observations (WDC-SILSO) at the Solar Influences Data Center (SIDC), Royal Observatory of Belgium (ROB). The SIDC provides an online catalogue[5], where I obtained the SSN data. The SSN version 2.0, the current recalibrated version introduced in July 2015, is used in this work. Chapter 4 uses the SSN data from the time period 1932–2016, see Figure 3.1.

Short-term predictions of the SSN are provided by several institutions. The SIDC itself provides 12-month SSN forecasts derived via different methods. The Space Weather Prediction Center (SWPC) at the National Oceanic and Atmospheric Administration (NOAA) supports the SSN prediction of the Solar Cycle 24 Prediction Panel[6].

3.5 OMNI data collection

Solar wind was measured in situ for the first time by spacecraft in 1959 and since 1963 near-Earth measurements were done almost continuously. The OMNI 2 data collection (King & Papitashvili 2005) merges data from solar wind magnetic field and plasma, energetic proton fluxes, geomagnetic indices, and solar indices. The included solar wind data starts in 1963-11-27, the temperature data not before 1965-07-26, and is continuously maintained until today. As the data covers decades from multiple spacecraft at varying locations, the solar wind data is composed of intercalibrated data, which has been time-shifted to the nose of the magnetosphere's bow shock upstream of Earth. I created an overview of the various spacecraft contributing to the IMF and solar wind plasma data and their time coverages to the data set in Figure 3.3.

The OMNI data set is being maintained at NASA's Space Physics Data Facility (SPDF), Goddard Space Flight Center (GSFC). Their OMNIWeb interface[8] and their Coordinated Data Analysis Web[9] (CDAWeb) provide the data – the latter is where I obtained it.

Zhang2015 do with their data: "The data have been lagged by 5 min to allow for propagation from the nose of bow shock to the magnetopause."

[3]GFZ Potsdam Nowcast *Kp* index website: http://www-app3.gfz-potsdam.de/kp_index/ql_bar.gif
[4]USAF Wing *Kp* model website: https://www.swpc.noaa.gov/products/wing-kp
[5]WDC-SILSO website: http://www.sidc.be/silso/
[6]Solar Cycle 24 Prediction Panel website: http://www.swpc.noaa.gov/products/solar-cycle-progression
[7]OMNIWeb Data Documentation: https://omniweb.gsfc.nasa.gov/html/ow_data.html
[8]GSFC OMNIWeb interface: http://omniweb.gsfc.nasa.gov/
[9]GSFC CDAWeb interface: http://cdaweb.gsfc.nasa.gov/

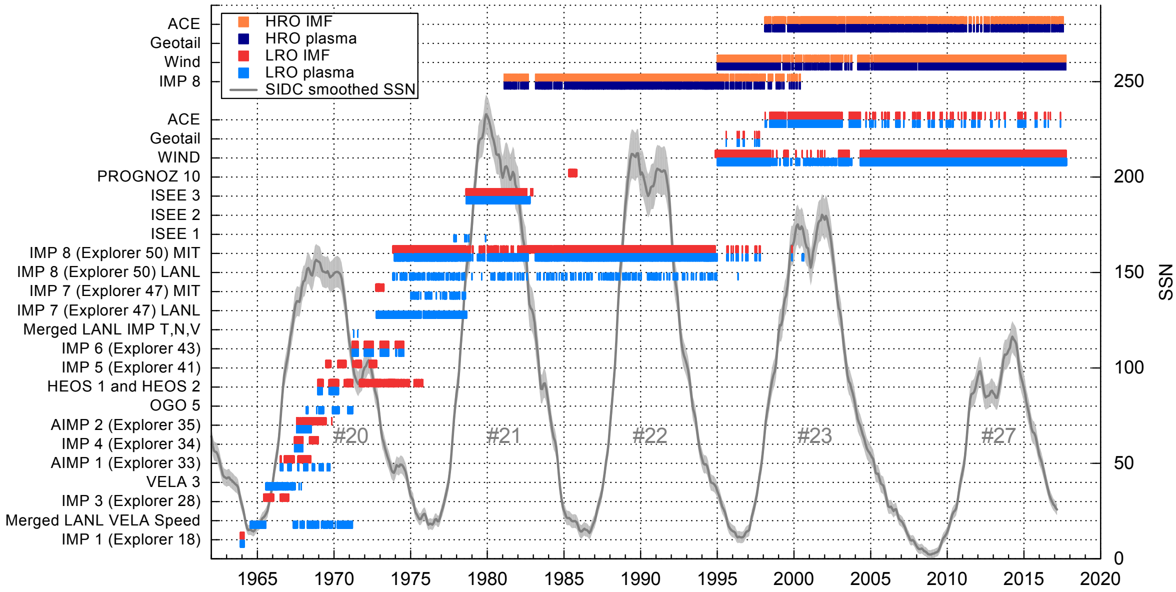

Figure 3.3 IMF and solar wind plasma data sources (spacecraft) for the high and the low resolution OMNI (HRO and LRO) data sets until the end of 2016. I plotted this figure using the spacecraft identifiers noted in the OMNIWeb Data Documentation[7]. The SIDC 13-month smoothed monthly SSN and the cycle number are plotted in the background.

3.6 Helios probes

In order to observe solar wind in situ within the inner heliosphere, the nearly identical solar probes Helios 1 and Helios 2, one is pictured in Figure 3.4, were launched in December 1974 and January 1976 respectively.
Until today, these both probes were the only spacecraft that measured solar wind in situ over large solar

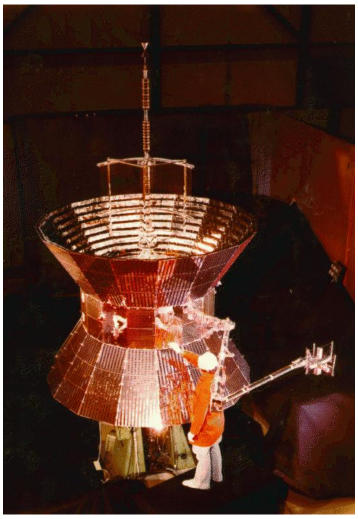

Figure 3.4 One of the nearly identical twin Helios spacecraft[10]. Credit: NASA/Max Planck Institute for Solar System Research.

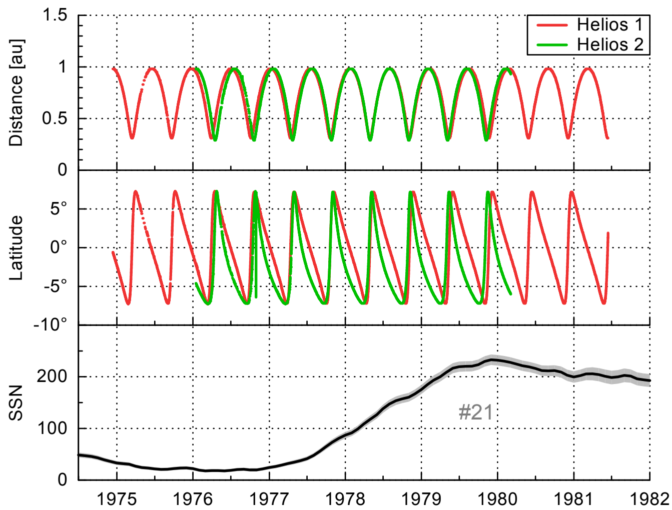

Figure 3.5 Solar distance (top) and heliographic latitude (middle) of Helios 1 (red) and Helios 2 (green) with respect to their mission time. The trajectory data are from GSFC/SPDF and is plotted in HGI coordinates. I plotted the SIDC 13-month smoothed monthly SSN and its cycle number in the bottom panel for orientation.

distance ranges with perihelia as close as 0.31 au and 0.29 au respectively. Their highly elliptical orbits in the ecliptic covered a solar distance range up to 0.98 au. Launched during solar cycle minimum, the data of both probes cover the rise to the maximum of solar cycle 21, that amounts to about 6.5 years of data at varying solar distances. I plotted the probes' solar distance and heliographic latitude with respect to their mission time and sunspot number for illustration in Figure 3.5. The daily trajectory data are available from NASA's Space

[10]I was not able to find out which Helios spacecraft this is.

Physics Data Facility (SPDF) at the Goddard Space Flight Center (GSFC)[11] and are drawn in Heliographic Inertial (HGI) coordinates, see appendix Section A.6. I also plotted the orbits of Helios 1 and Helios 2 in a solar equatorial plane view and in a solar polar plane view, see Figure 3.6.

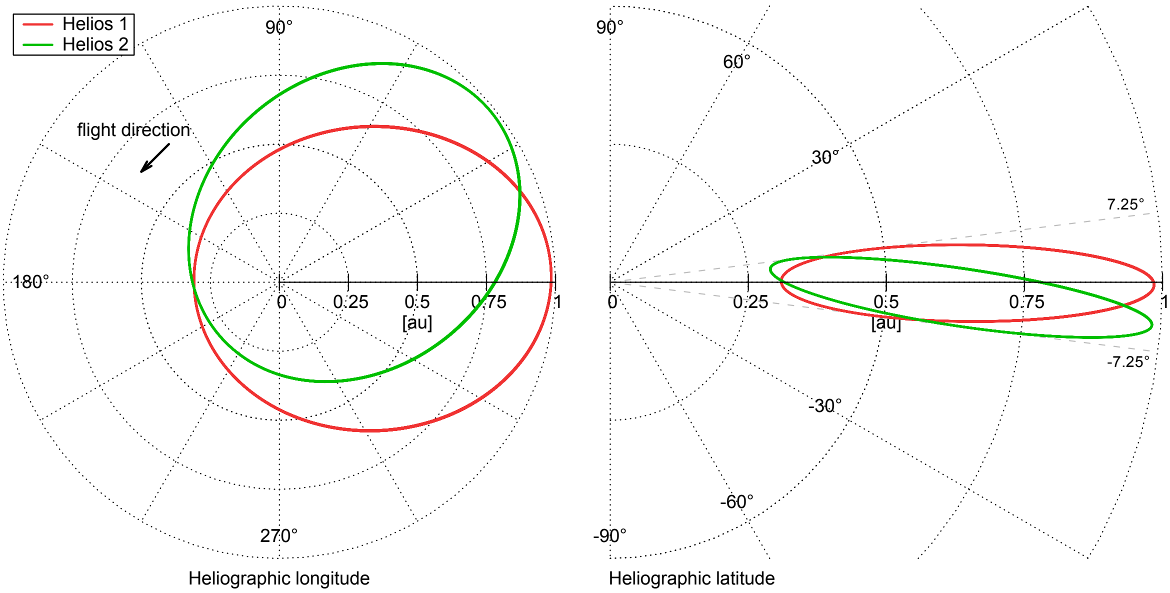

Figure 3.6 Orbits of the Helios 1 (red) and Helios 2 (green) spacecraft in the solar equatorial plane (left) and in the solar polar plane (right). I obtained the trajectory data from GSFC/SPDF and plotted the orbits in HGI coordinates.

The scientific instruments carried by the spacecraft for measuring the magnetic field and solar wind plasma are two different Flux-gate Magnetometers and the Plasma Experiment Investigation. The data from the magnetometer and plasma instruments are merged into a data set with hourly resolution (Rosenbauer et al. 1977). In case of Helios 1 this data set includes about 12.5 orbits in the time range 1974-12-10 to 1981-06-14 and in case of Helios 2 about 8 orbits in the time range 1976-01-01 to 1980-03-04. The Helios data is available via the GSFC/SPDF CDAWeb interface[12].

The Helios 1 (Helios 2) magnetometer data coverage is about 43 % (54 %) and amounts to 2.8 years (2.3 years) in total. The plasma data coverage is 76 % (92 %) and amounts to 5.0 years (3.9 years) in total.

The Helios magnetic field and plasma data frequency over heliocentric distance and over heliographic latitude are plotted in Figure 3.7.

[11] SPDF Helios 1 trajectory data: http://spdf.sci.gsfc.nasa.gov/pub/data/helios/helios1/traj/
[12] GSFC CDAWeb interface: http://cdaweb.gsfc.nasa.gov/

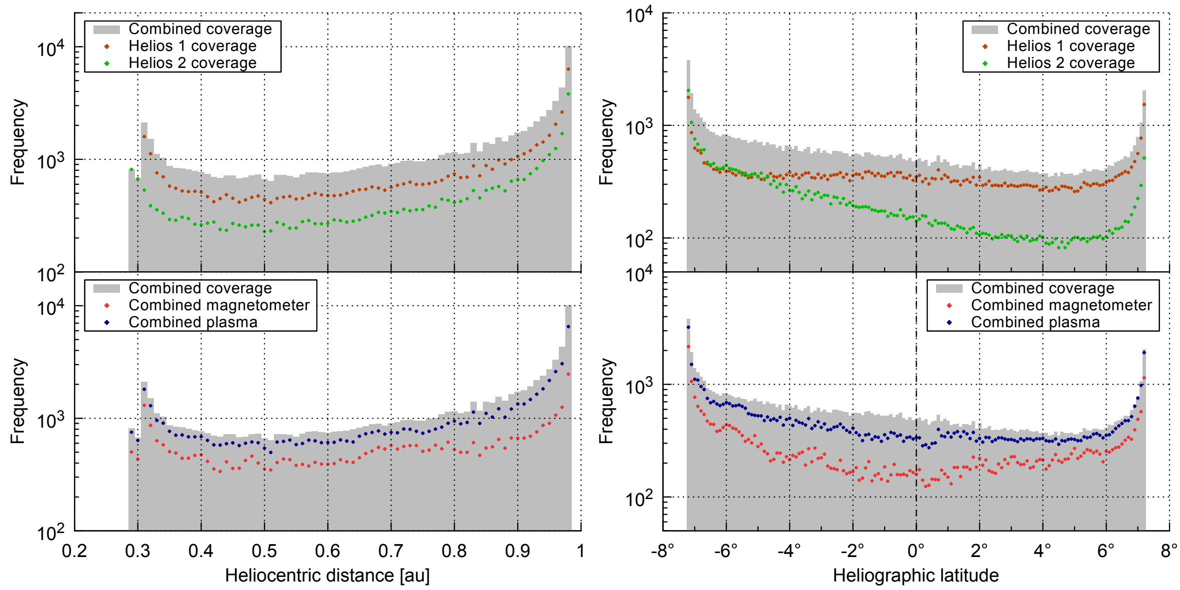

Figure 3.7 Helios data frequency over heliocentric distance with bins of 0.01 au (left panels) and over heliographic latitude with bins of 0.1° (right panels). The frequency data is based on the hourly merged magnetometer and plasma data sets for Helios 1 and Helios 2. The top panels show the frequencies for Helios 1 and Helios 2 individually and the bottom panels those for the magnetometer and plasma data.

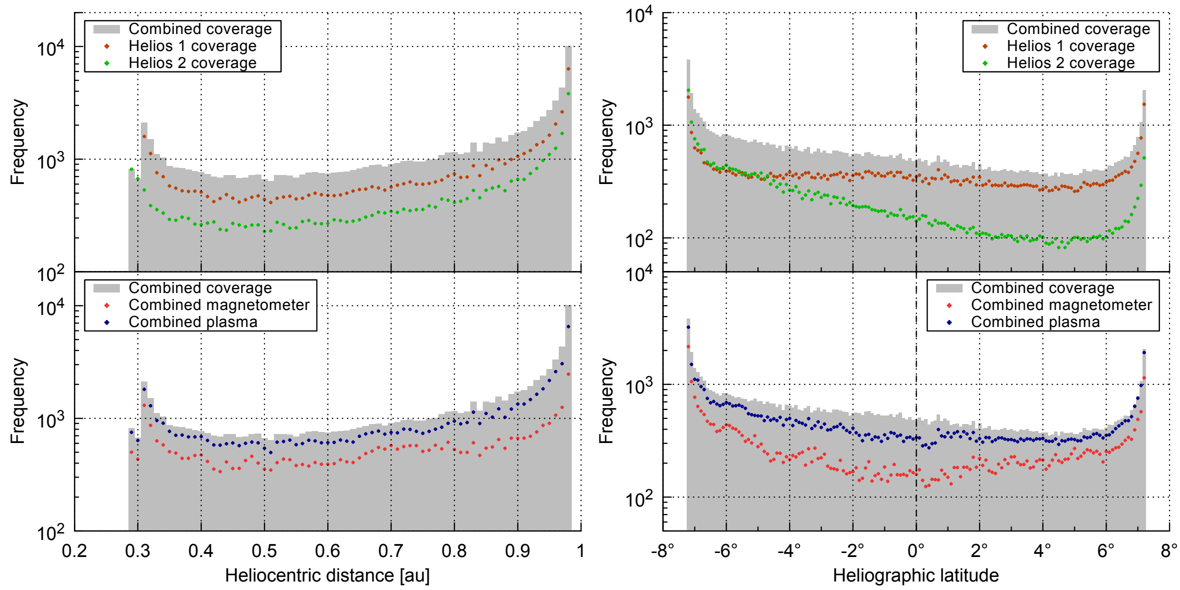

Figure 3.8

4 Solar wind and CME influence on the magnetosphere

Impact estimations derived from empirical correlations between in-situ solar wind measurements and the geomagnetic *Kp* index

Variations in the Earth's magnetosphere are largely evoked by influence through the solar wind. These magnetospheric disturbances have diverse effects on the terrestrial environment. Especially the effects of severe geomagnetic storms created by coronal mass ejections (CMEs) pose various threats to sensitive technical systems and exposed humans. Thus, the development of quantitative forecasts for magnetospheric impacts caused by solar wind and CMEs is of major importance. The analyses in this chapter are based on my work done for the project Advanced Forecast For Ensuring Communications Through Space (AFFECTS).

This study's goals are to estimate the magnetospheric impact from solar activity in general, from solar wind and also to predict it for CMEs in particular. Empirical dependencies between specific solar wind parameters and the magnetospheric disturbance index *Kp* are presented. These dependencies allow to nowcast the *Kp* index from upstream (L1) solar wind in-situ measurements. Hence, also the magnetospheric impact of CMEs is estimated solely based on their arrival velocities, predicted from coronagraph observations. The prediction of solar wind stream velocities, e.g., from coronal hole observations, enables to estimate their impact as well.

First, I estimate the long-term variations of the yearly average *Kp* values, which are contributed by solar activity. This is achieved via logarithmic fitting of a yearly sunspot number (SSN) dependency. In order to nowcast the *Kp* index from general solar wind conditions, I apply a correlation with the product of the parameters velocity and magnetic field z-component in GSM coordinates (vB_z). In order to forecast the *Kp* index from estimated CME and stream velocities, I furthermore filter the solar wind data, using flagged CME times from the solar wind structures (SWS) list provided by Richardson & Cane (2012). The solar wind data considered in these analyses consists of 35 years (1981–2016) of high-resolution minutely OMNI data, which is composed of multi-spacecraft intercalibrated in-situ measurements from 1 au. I analyze the *Kp* frequency distributions with respect to the depending parameters vB_z and velocity, derive their mean *Kp* per interval and further compile functional dependencies via logarithmic fitting.

The obtained functional relations enable empirical estimations of the mean *Kp* impact from measured solar activity, in-situ solar wind, and remotely determined CME and stream velocities.

4.1 Introduction

It is known since the early 19th century that variations in the solar wind evoke disturbances in the magnetosphere (Bartels 1962). Especially strong disturbances, called geomagnetic storms, can be provoked by coronal mass ejections (CMEs), which are embedded within the solar wind. The causes of the strongest geomagnetic storms are the compression of the solar wind magnetic field lines within the CME shock front and the enhanced field strenghts of magnetic clouds, which are enclosed in CMEs (Bothmer 1993; Bothmer & Schwenn 1995). The consequences of strong geomagnetic disturbances are a threat to sensitive technical systems and exposed humans. Therefore it is important to know when magnetospheric disturbances will occur and how large they will become.

Kp is designed for... (cite?). I use this magnetospheric disturbance index to correlate it with near-Earth solar wind measurements. More detailed information on the *Kp* index can be found in Subsection 2.8.1.

current comparable *Kp* forecast models take into account... (NOAA/SWPC, CCMC/SWRC, Wing forecasts) Elliott et al. (2013): The *Kp* index and solar wind speed relationship: Insights for improving space weather forecasts
differences to existing studies:
compare with Newell relation...

With the results presented in this chapter, I elaborate the step from the predicted CME and stream velocities to the forecast of the possible impact strength on the terrestrial magnetosphere. I derive an empirical correlation between the solar wind speed and the geomagnetic *Kp* index, in order to obtain the capability to forecast *Kp* values solely based on the predicted CME and stream velocities. The derived functional dependencies can be used to nowcast/forecast the *Kp* index.

In-situ measurements of solar wind are made almost continuously, e.g., at the first Lagrange point (L1), in front of the magnetosphere. Since 1963 several spacecraft collected more than 50 years of solar wind data. The latest spacecraft, e.g., Wind, ACE and DSCOVR (launched in early 2015), provide real-time solar wind data online[1 2 3]. These solar wind real-time data are used to nowcast various effects on the Earth's magnetosphere, such as the position of the magnetospheric bow shock in front of the Earth, the magnitude of geomagnetic disturbances (e.g., *Kp* index), the positions of the polar auroral ovals, the variation of the total electron content (TEC) of the ionosphere, and the positional error of global navigation satellite systems (GNSS).

The velocity and the direction of CMEs can be determined in their early near-Sun stages via remote tracking with coronagraph white-light observations. Using these parameters as input for CME propagation models, their possible arrival time and arrival velocity at Earth can be derived.

There are efforts to predict the direction and strength of the magnetic field from the flux rope geometry and orientation (Savani et al. 2015). However, the compressed solar wind magnetic field in the sheath region is of at least similar importance for magnetospheric disturbances (Huttunen & Koskinen 2004). As the solar wind Bz is quite random with low autocorrelation time, its prediction is not yet implemented in the current forecast.

Savani et al. (2015): Predicting the magnetic vectors within coronal mass ejections arriving at Earth: 1. Initial architecture
Savani et al. (2017): Predicting the magnetic vectors within coronal mass ejections arriving at Earth: 2. Geomagnetic response

Coronal holes are the origin of the fast solar wind; their area on the solar disk, seen in EUV wavelengths, correlates with the measured velocity of solar wind streams (Vršnak et al. 2007). This relation is used to predict the Earth-arrival velocity of solar wind streams about 4 days in advance (Rotter et al. 2012), as is done in real-time within the empirical solar wind forecast (ESWF) at the University of Graz[4].
+27 day forecast...

mention ENLIL forecast simulation

The objectives of the analyses performed and found in this chapter are to estimate the magnetospheric impact of solar wind and to predict it for CMEs in particular. In Section 4.2 I determine the magnitudes of the long-term *Kp* changes due to solar activity and measure the extent of seasonal variations stemming from the Earth's orbit. In order to nowcast the *Kp* index, I quantify the solar wind influence on *Kp* by deriving a functional relation with the product of solar wind velocity and magnetic field z-component (Section 4.3). Finally, for the purpose of enabling *Kp* forecasts from remote observations, I estimate the *Kp* impact coming from CMEs and solar wind streamers separately by deriving functional dependencies with their velocities (Section 4.4).

4.2 Long-term variations of the *Kp* index

4.2.1 Solar activity influence

The *Kp* data is obtained from the GFZ Potsdam[5], where the index is currently maintained. The data used in this analysis covers the time period 1932–2016, see also 3.3. Its frequency distribution shows that the highest frequencies occur around low *Kp* values of 1+. Going to higher *Kp* values, the frequencies decline asymtotically towards zero (see Figure 4.1) – a *Kp* value of 9o occurred only 29 times in this time interval.

Obviously the general *Kp* distribution (seen in Figure 4.1) averages over solar activity. Solar activity is generally tracked with the international sunspot number (SSN). In the present analyses SSN data from the time

[1]Wind real-time data website: `https://pwg.gsfc.nasa.gov/windnrt/`
[2]ACE real-time data website: `http://www.swpc.noaa.gov/products/ace-real-time-solarwind`
[3]DSCOVR real-time data website: `http://www.swpc.noaa.gov/products/real-time-solarwind`
[4]ESWF website: `http://swe.uni-graz.at/index.php/services/solarwind-forecast`
[5]GFZ Potsdam website: `http://www.gfz-potsdam.de/de/kp-index/`

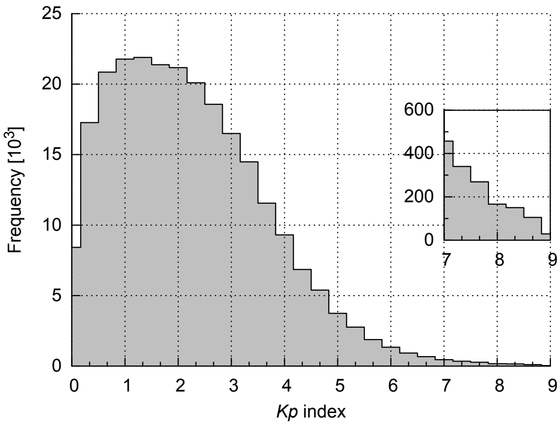

Figure 4.1 *Kp* frequency distribution for the time period 1932–2016. The inset shows a zoomed-in view of the high-value tail. The *Kp* data is obtained from the GFZ Potsdam.

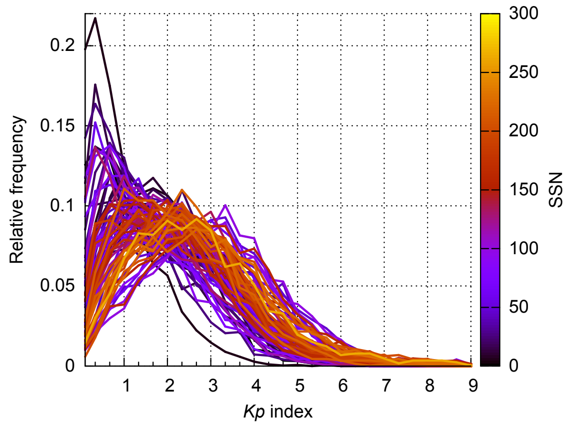

Figure 4.2 Yearly *Kp* frequency distributions during the period 1932–2016, sorted and colored by yearly SSN. All distributions are normed to be of equal area. The *Kp* data is obtained from the GFZ Potsdam and the yearly SSN data from the SILSO World Data Center.

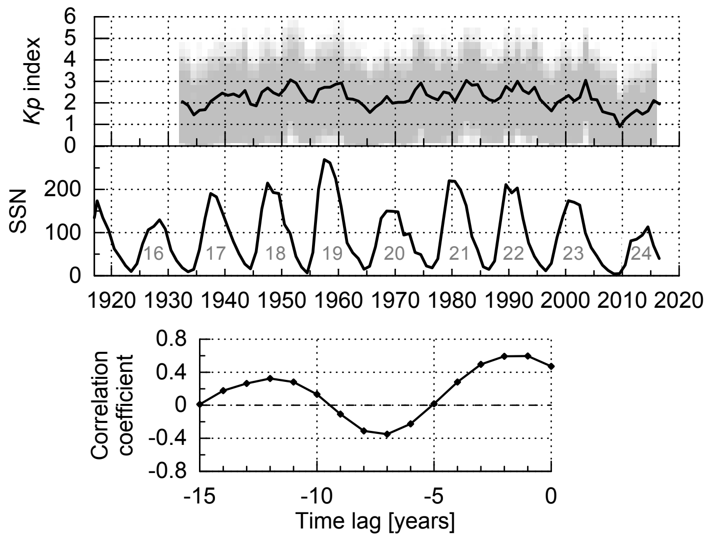

Figure 4.3 Yearly *Kp* index distributions (shaded area) with their mean values for the time period 1932–2016 and yearly SSN with cycle number for the time period 1917–2016 (top panels). The Pearson correlation coefficients with the yearly SSN are calculated for time lags back to -15 years (bottom panel). The *Kp* data is obtained from the GFZ Potsdam and the yearly SSN data from the SILSO World Data Center.

period 1917–2016 is used. The data is obtained from the online catalog[6] provided by the World Data Center – Sunspot Index and Long-term Solar Observations (WDC-SILSO), Solar Influences Data Analysis Center (SIDC), Royal Observatory of Belgium (ROB).

The *Kp* frequency distributions' shape varies with different states of solar activity (cite?). This is visible in the yearly distributions, sorted and colored by yearly SSN in Figure 4.2.

The distribution's peak position scales with SSN, that is, a high yearly SSN results in a higher abundance of large *Kp* values as well (cite?).

The time series of yearly average *Kp* values of the years 1932–2016 shows an imprint of the solar cycles (see the top graphs in Figure 4.3). The *Kp* pattern follows the solar cycle minima and maxima as well as the changes in magnitude between solar cycles (cite?). The yearly mean *Kp* shifts about 1 unit for both variations separately. As expected, the *Kp* index correlation with solar activity shows an 11-year period (cite?) (see bottom graph in Figure 4.3). The highest correlation coefficient of 0.60 is found with a time lag of -1 year, that is, the yearly average *Kp* follows the SSN of the previous year.

The yearly mean *Kp* index with respect to the 1-year lagged SSN shows a raise with increasing SSN, this is seen in Figure 4.4. I perform a fit in order to obtain an analytical relation for this dependency. *Kp* itself is a quasi-logarithmic index, so it is apparent to use a logarithmic fit function:

$$f(x) = a \cdot \ln(x) + b\,. \tag{4.1}$$

[6]WDC-SIDC website: http://www.sidc.be/silso/

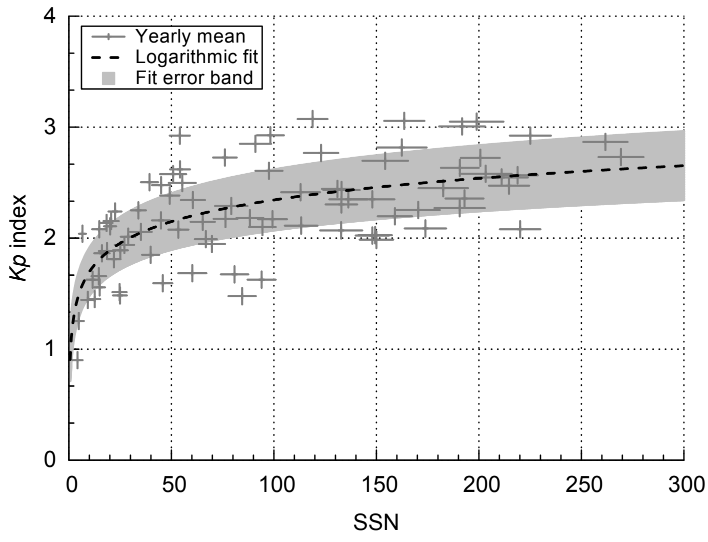

Figure 4.4 Yearly mean *Kp* index with respect to 1-year lagged SSN (+) with the weighted logarithmic fit (dashed line). The error bars denote the SSN standard deviation and the relative weight from the yearly data coverage. The shaded area represents the fit error band derived from the estimated standard deviations of the fit parameters. The logarithmic function (Equation 4.1) is used for the weighted fit. The yearly *Kp* mean values are calculated from GFZ Potsdam data and the yearly SSN is obtained from the SILSO World Data Center.

The fit parameters are $a = 0.281(43)$ and $b = 1.05(19)$ and lead to the relation

$$Kp(ssn) = 0.28 \cdot \ln(ssn) + 1.1\,, \tag{4.2}$$

which is plotted in Figure 4.4. This means that for a SSN of 1 the mean *Kp* is 1.05(20) and for a SSN of 300 it is 2.65(31). The numbers in parentheses are the errors on the corresponding last digits of the quoted value. They are calculated via error propagation from the estimated standard deviations of the fit parameters.

4.2.2 Seasonal variations

On top of the yearly variations, seasonal variations exist in the magnetospheric disturbances as well. In the months May–August the *Kp* peak frequency is higher than in the remaining months of the year, whereas in March/April and September/October the *Kp* values > 3 are more abundant (cite?). This is apparent from looking at the monthly *Kp* frequency distributions, plotted in Figure 4.5. These *Kp* changes arise from seasonal variations of the solar wind parameters at Earth, which stem from Earth's yearly changes in orbital distance and heliographic latitude. Another seasonal effect stems from the Earth's rotation axis tilt, which changes the direction of the Earth's magnetic dipole axis to the Sun over the year (see top panel of Figure 4.6).

Earth's distance to the Sun varies over the course of a year by ±1.67 % (see appendix Section A.5). The solar wind parameters scale via power-law dependencies with solar distance, as it is described in the following Chapter 5 and accordingly in Venzmer & Bothmer (2018). For example, the solar wind proton density scales with about r^{-2}, this leads to yearly variations in density of up to 3.4 %. These yearly solar wind changes have a direct influence on the *Kp* index.

The Sun's rotation axis tilt angle to the ecliptic is ±7.25° and that for Earth is ±23.44°, see also appendix Section A.5. The solar wind magnetic field strength varies with heliographic latitude (cite?). The solar wind influence on the *Kp* index depends on its coupling efficiency with the magnetosphere. Furthermore, the rate of magnetic reconnection between solar wind and the Earth's magnetosphere depends on both fields' orientation to each other (parallel/antiparallel). Additionally, the tilt of the magnetic dipole axis to the rotation axis – a few degrees for the Sun during cycle minima (extreme during solar maxima...) and about 10° for the Earth – complicates this system even more.

So the *Kp* variation effects originate from the seasonal change in the solar tilt, the Earth's tilt, and the Earth's distance. Thorough analyses of the seasonal variations were already performed by (Cortie 1912) (more cites!?). Thus, I just quantify the bulk magnitude of these effects in order to consider them as relative uncertainties when using the solar activity relation (4.2). Looking at the *Kp* frequency distributions by month – seen in the bottom panel of Figure 4.6 – it is apparent that for high *Kp* values (> 4), there exist yearly frequency maxima at the equinoxes and frequency minima at the solstices, as described by (Cortie 1912). It can be seen from the plotted quantiles that this semiannual variation amounts to 1/3 *Kp* unit at small *Kp* values and up to 4/3 units at higher *Kp* values.

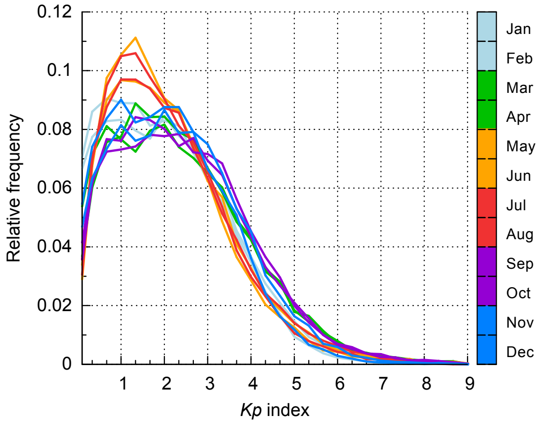

Figure 4.5 Average monthly *Kp* frequency distributions of the time period 1932–2016, colored by month of the year. The *Kp* data is obtained from the GFZ Potsdam.

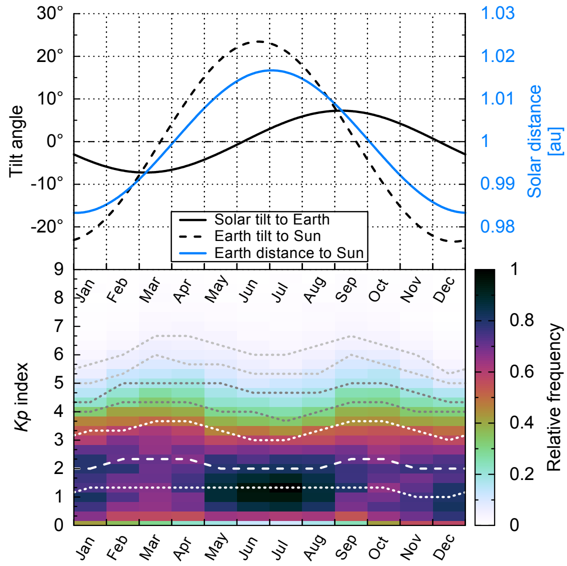

Figure 4.6 Seasonal changes in the solar tilt angle to Earth, Earth tilt angle to Sun, and Earth distance to Sun – the curves are approximated with trigonometric fuctions (top panel). *Kp* frequency distributions by month for the time period 1932–2016 (bottom panel) with median (white dashed) and quartile values (white dotted). The other dotted lines mark the upper eighth, 16th, 32nd, and 64th parts. The bin size is 1 month and 1/3 *Kp* unit respectively.

4.3 *Kp* nowcast from in-situ solar wind measurements

4.3.1 Coupling function

The coupling between the solar wind and the magnetosphere is governed by reconnection and compression of the magnetic field lines, as described in Subsection 2.7.1.

In this work I settle and work with the electric field as the coupling function, Equation 2.4, because...
For which reason do I choose this coupling function over others?

The solar wind electric field $\boldsymbol{E}$ is the product of the proton velocity v and the magnetic field z-component B_z:

$$|\boldsymbol{E}| = -v_x \cdot B_z \,. \tag{4.3}$$

If not specified otherwise, B_z is always meant to be in GSM coordinates hereafter.

The solar wind velocity sticks mostly to its radial flow direction, that is, it rarely deviates up to 0.0° (correct and cite...). Thus, the absolute flow speed can be used instead of the vector component.

argue for vB_z:
- 3hmin(vB_z) performs in rank correlation slightly better than the sophisticated Newell formula. really?
- simple to calculate
- ...

Using vB_z implies that both quantities are sufficiently independent. B and v are dependent, as can be seen from fig XX, however, as v and θ_c are, so are v and B_z, see fig XX.

It is also known that the solar wind velocity itself already correlates strongly with the *Kp* index.

I use this velocity relationship for obtaining *Kp* proxies from CME and solar wind stream data.

4.3.2 Data correlation

The *Kp* time series started in 1932 when there existed no spacecraft to measure solar wind in situ. Thus, the maximal surveyed time range is defined by the available in-situ solar wind data.

Savani2017:
"Although Kp is defined for 3 h periods, predicted variations in the IMF are made on shorter time scales and can influence the level of geomagnetic activity (e.g., geomagnetically induced currents). Hence, averaging the IMF over intervals that match those of Kp may suppress features that are important drivers of geomagnetic activity. Nevertheless, for the purpose of this paper, we choose to average the Kp estimate from the field vectors predicted by the BSS model over the same 3 h intervals as the Kp values, as this currently represents the service provided by NOAA/SWPC."

The *Kp* index represents maximal variations within 3-hour time intervals (see Subsection 2.8.1). Any solar wind parameter that will be correlated with *Kp* also has to have the same time resolution. In addition to adapting the time resolution, it has to be considered by which means this should be done. Simple 3-hour average values are expected to have a weaker correlation than the solar wind parameter's 3-hourly maximal variation. The 3-hour maximal variations should obviously be stronger when using high resolution data. Thus, to be able to correlate *Kp* with solar wind data, high resolution data (that is, much shorter than 3 hours) are needed to determine the maximal solar wind variations within each 3-hour interval.

The OMNI data set collects the longest continuous solar wind measurements at 1 au. The longest time coverage has the hourly OMNI data set (since 1963), however, I choose to use the minutely OMNI data with the time range 1981–2016, to benefit from the stronger correlation (see Figs?).

The *Kp*-vB_z Pearson correlation coefficients for 3-hour mean and minimum data are plotted in Figure 4.7. The largest correlation is found for the 3-hour minimum data without time shift. It is a negative correlation

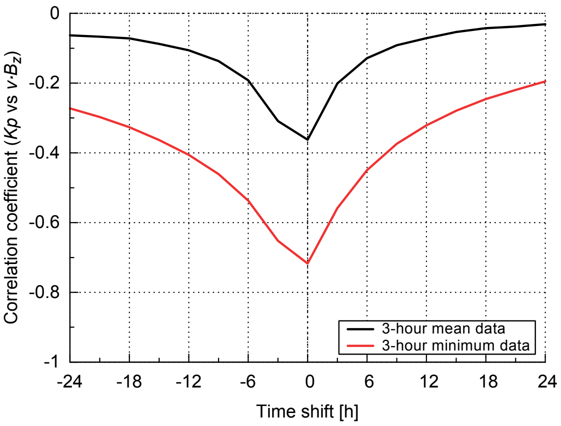

Figure 4.7 *Kp*-vB_z correlation coefficients for different time shifts up to ±24 hours. The minutely OMNI data from 1981–2016 is processed with mean (black) and minimum (red) 3-hour averaging.

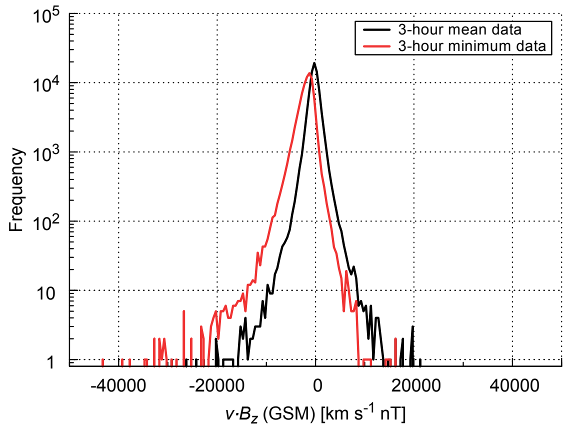

Figure 4.8 Frequency distributions of vB_z for 3-hour mean (black) and minimum (red) minutely OMNI data from 1981–2016.

whose coefficient is −0.72. The *Kp*-vB_z frequency distribution is asymmetrically shifted to negative values when using 3-hour minimum values, this is visible in Figure 4.8.

4.3.3 Functional dependency for solar wind

The frequency distribution in *Kp*-vB_z space is shaped like a candle flame, inclined to negative values by a light breeze, see top panel in Figure 4.9. In order to determine a functional dependency, I focus on the relative frequencies per vB_z-interval and their mean *Kp* values, which are plotted in the bottom panel of Figure 4.9. The mean absolute deviation (MAD) of the mean has a mean size of 0.7 *Kp* units. This probability distribution is asymmetrically V-shaped around zero, having a larger and steeper negative arm than positive arm. The asymmetry also exists for 3-hour mean data, thus this effect is not a result of the data reducing method (3-hour

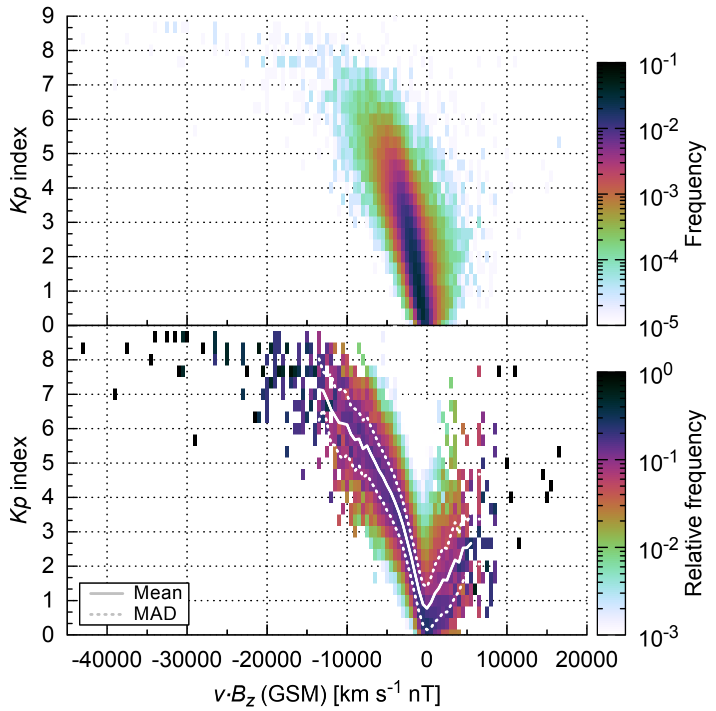

Figure 4.9 *Kp* versus vB_z frequency distribution (top) and its relative distribution (bottom) with the mean *Kp* values (solid line) and their mean absolute deviation (dotted lines). It is 3-hour minimum data from the minutely OMNI data set (1981–2016). The bin size is 500 km s^{-1} nT and 1/3 *Kp* unit respectively.

minimum) (fig...?). Rather the steeper negative arm is a consequence of the half-wave rectifier coupling of the solar wind magnetic field direction to the magnetosphere, as described in Subsection 2.7.1.

stress that it is an empirical fit...
using an appropriate type of a fit function...

Since the *Kp* index has a quasi-logarithmic scaling (see Subsection 2.8.1), a logarithmic function is the obvious choice as a fit function. Furthermore, the depending argument consists of a product of two solar wind parameters which individually scale logarithmically with *Kp*. These reasons are why I use the logarithm of a parabola for the fitting approach:

$$f(x) = \ln\left(x^2\right) . \tag{4.4}$$

I also introduce a horizontal shifting parameter x' because the distribution's center is slightly offset. To be able to replicate the asymmetry in both arms, I further split the fit function into a negative and a positive part:

$$f(x) = \begin{cases} f_-(x) & \text{for } x < 0\,, \\ f_+(x) & \text{for } x \geq 0\,. \end{cases} \tag{4.5}$$

This way, both arms can be scaled individually with scaling factors for the negative and positive parts a_- and a_+. The resulting logarithmic fit function parts are

$$f_-(x) = a_- \cdot \ln\left((x + x')^2 + b\right) + y' , \tag{4.6}$$

$$f_+(x) = a_+ \cdot (f_-(x) - f_-(-x')) + f_-(-x') , \tag{4.7}$$

with the vertical shifting parameter y' and the depth parameter b. The resulting fit curve is plotted in Figure 4.10 with the fit coefficients $a_- = 1.258(19)$, $x' = 163(20)$, $b = 1.416(68) \times 10^6$, $y' = -17.04(33)$, and $a_+ = 0.467(20)$ for units of [km s^{-1} nT]. The mean MAD is about 0.7 *Kp* units. Thus, the solar wind dependency relation condenses to:

$$Kp_-(vB_z) = 1.258 \cdot \ln\left((vB_z + 163)^2 + 1.416 \times 10^6\right) - 17.04 , \tag{4.8}$$

$$Kp_+(vB_z) = 0.467 \cdot (Kp_-(vB_z) - Kp_-(-163)) + Kp_-(-163) . \tag{4.9}$$

This relation can be used together with real-time in-situ measurements from spacecraft located at L1 (see Section XX rt sources) to nowcast the actual *Kp* index.

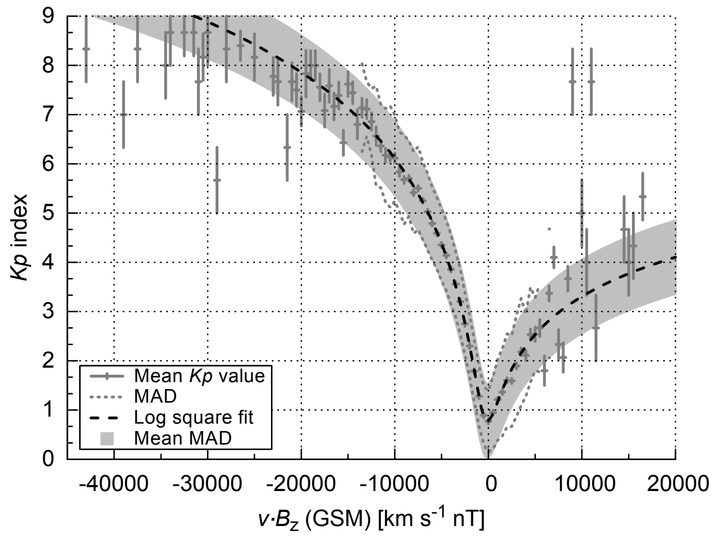

Figure 4.10 Mean Kp values (+) and MAD values (dotted lines) per vB_z interval. The error bars represent the relative data count. The logarithmic fit (dashed line) is plotted with a mean MAD band (shaded area). The splitted function (4.5) is used for the weighted fit.

In order to demonstrate this relation with actual in-situ data, I calculate the Kp estimate for the example CME from Figure 2.21 and include the 3-hour minimum value of vB_z in the plot, see Figure 4.11. It can be seen that in this period the Kp estimate traces the actual Kp index pretty well within the mean MAD band. However, deviations are found at the times of the initial shock, and the start and middle of the MC.

4.4 *Kp* forecast from remote CME and stream observations

It makes sense to separately look at CMEs and solar wind streams -> see event comparison fig.
same velocity -> different Kp effect

CMEs are already sighted raising from their source regions on the solar surface. Some CME properties can be estimated from remote coronagraph observations and modeled to Earth, such as its propagation direction, its arrival time, and arrival velocity (cites?). Thus, early observations enable a heads-up time depending on the CME's propagation speed to Earth. This travel duration can be more than 4 days for slow events with average solar wind speeds, about 40 hours for fast events with speeds of 1000 km s^{-1}, and down to 20 hours and even below for the rare extreme cases, e.g., about 21 hours for the event on 23 July 2012 (Russell et al. 2013; Temmer & Nitta 2015) and about 19 hours for the event observed by Carrington (1859) on 1 September 1859. The theoretical minimal heads-up time for CMEs is estimated to be half a day (Gopalswamy et al. 2005).

To make use of the heads-up time for CMEs, I neglect its magnetic field part, which is difficult to determine from remote observations and simplify the coupling relation (2.4) from before. Therefore, the only coupling parameter remaining is the solar wind velocity.

Savani2017:
"*Prior evidence has suggested the reason be due to southerly IMF strength being the most dominant solar wind parameter for driving geomagnetic activity at Earth. The strong correlation of solar wind speed to geomagnetic activity is evident during CME conditions but is only considered the most dominant parameter during high-speed streams* [Holappa et al., 2014]."

4.4.1 Velocity forecast methods

CME velocity estimation
methods and modeling...?
GCS, CAD modeling -> propagation direction and apex height-time profile -> acceleration and velocity kinematics...
-> example event CME?
see Basics...

Solar wind stream velocity estimation
CH analysis (Graz)

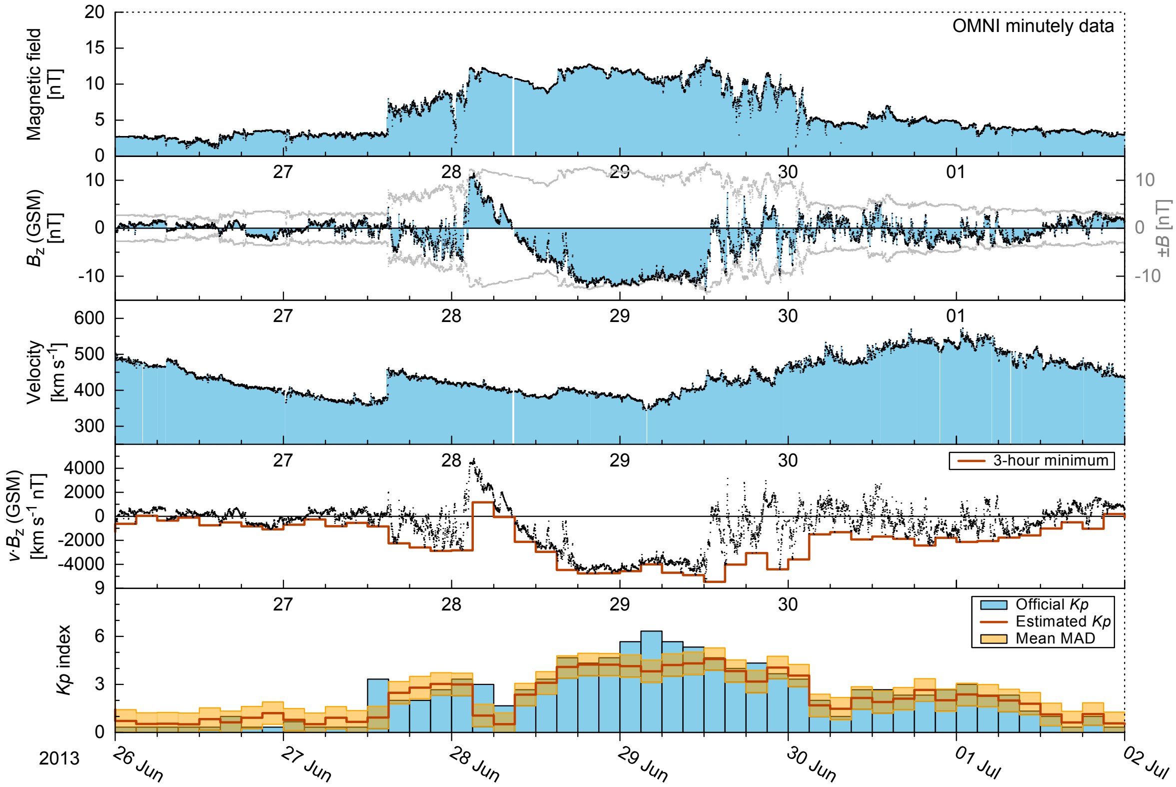

Figure 4.11 Solar wind measurements, official *Kp* index, and estimated *Kp* for the time period 26 June to 2 July 2013. The solar wind parameters are the magnetic field strength, its z-component in GSM coordinates, and the velocity. I also plotted the product vB_z with its 3-hour minimum for illustration. The solar wind data are from the minutely OMNI data set. The official *Kp* index is obtained from the GFZ Potsdam. The *Kp* estimate is derived via Equations 4.8 and 4.8. The orange band indicates the mean MAD.

L4 shift (Graz)
WSA-ENLIL MHD simulation
see Basics...

4.4.2 Solar Wind Structures list

For the following analysis, I use the list of solar wind structures (SWS) created and updated by Richardson et al. (2000) and Richardson & Cane (2012), who characterized the near-Earth solar wind structures since 1963. All periods related to ICMEs in the OMNI solar wind data set were identified and flagged.

list identifying criteria... look into their paper!

The SWS list for 1963–2016 was kindly provided by Ian Richardson (private communication). into acknowledgments...

SWS list for 1963–2015 by (Richardson et al. 2000; Richardson & Cane 2012) is available via registration at CEDARweb[7].

The CME fraction in the OMNI data is 15.8 % during the time period 1981–2016 (this accumulates to 5.53 years). This percentage is an average value. It varies heavily with the solar activity cycle and with the appearance of individual active regions on the solar surface. In the following, I refer to the remaining part without CMEs as "solar wind streams", because it is composed entirely from a mixture of slow wind flows, fast wind streams, and their interaction regions.

[7]CEDARweb website for Solar Wind Structures: http://cedarweb.vsp.ucar.edu/wiki/index.php/Tools_and_Models:Solar_Wind_Structures

Table 4.1 Time lags with the highest correlation coefficients for the *Kp*-velocity relation for the whole OMNI data, for stream data, and for CME data. The values are based on the 3-hour maximum of the minutely high resolution OMNI data from the time period 1981–2016.

Data	Time lag [hours]	Correlation coefficient
All data	6	0.622
Streams	9	0.661
CMEs	0	0.511

from OMNI data only?
permission received.

4.4.3 Data correlation

Again, I calculate 3-hour extreme values using the minutely OMNI data to profit from higher correlation coefficients, as done before for the data processing of the vB_z analysis in Subsection 4.3.2. The velocity only has positive values, thus its extreme values are 3-hour maximum values. The comparison between the 3-hour maximum and the 3-hour mean frequency distributions shows that their mean position shifts from a velocity of 405 to 425 km s^{-1}, see Figure 4.12. The CME part and solar wind stream part of the data can be examined

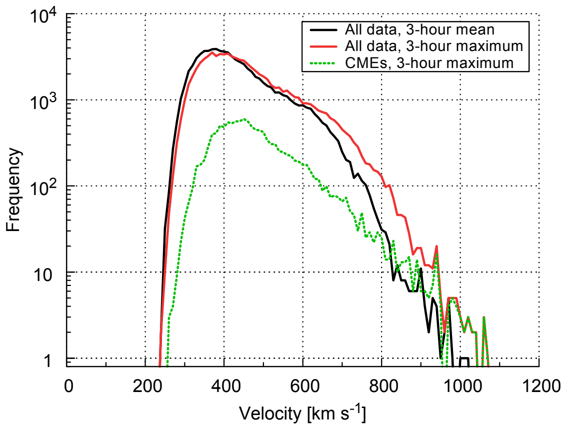

Figure 4.12 Solar wind velocity frequency distributions for 3-hour mean (black), maximum (red), and maximum of the CME part (green). The minutely OMNI data from the period 1981–2016 is used.

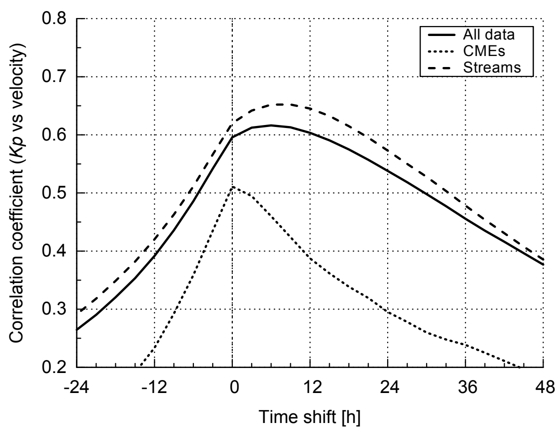

Figure 4.13 *Kp*-velocity correlation coefficients for time shifts in the range −24–48 hours. The correlations are plotted for the whole solar wind data (solid), for solar wind streams without CMEs (dashed), and for CMEs only (dotted). The data used is the 3-hour maximum of the minutely high resolution OMNI data from the period 1981–2016.

separately, filtering the CME related periods using the SWS list. Their frequency distributions show that the CME share is rising in faster solar wind until eventually in the region above about 900 km s^{-1} there only exist CMEs, see Figure 4.12.

The CME part of the data is correlated with the *Kp* index independently from the remaining solar wind streams, see Figure 4.13. The correlation for CME related data is lower than that for the regular solar wind (all data). Its maximal correlation coefficient with a value of 0.51 is without time shift, see Table 4.1. The solar wind streams show a higher correlation with *Kp* and the maximal coefficient of 0.66 has a positive time shift of 9 hours, that is, the *Kp* index forecasts the velocity of solar wind streams 9 hours in advance.

The positive time shift can be explained with the occurence of interaction regions followed by high speed streams (HSS). When a slow solar wind stream is followed by a fast one, the compression at their interface leads to enhanced solar wind densities and magnetic field strengths. The peak velocity of a HSS naturally appears after the interaction region. Therefore the *Kp*-impact from the enhanced magnetic field is correlated with the higher velocity of the HSS, yielding the observed positive time shift.

In fact, Machol et al. (2013) even proposed a linear function of the *Kp* index as a best proxy for corrupted real-time velocity measurements made by the Advanced Composition Explorer (ACE) spacecraft.

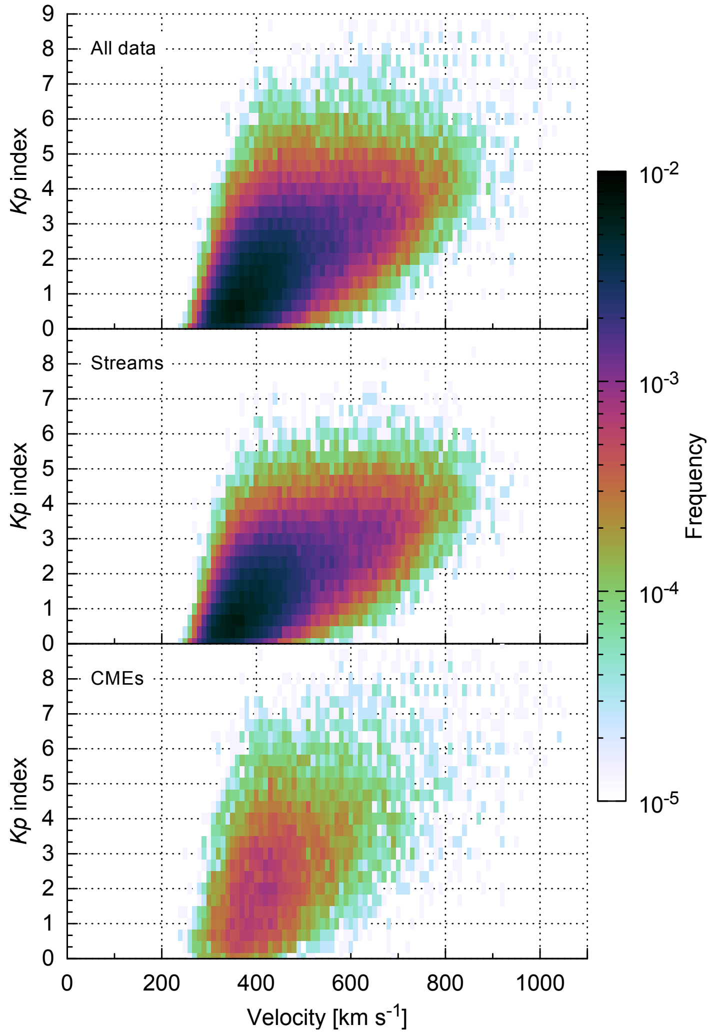

Figure 4.14 *Kp*-velocity distributions for all solar wind data, for solar wind streams and for CMEs. The data used is the 3-hour maximum of the minutely high resolution OMNI data from the time period 1981–2016. The SWS list from Richardson & Cane (2012) is used for the separation between CME and stream data. The bin size is 10 km s^{-1} and 1/3 *Kp* unit respectively.

4.4.4 Functional dependency for CME velocity

The general *Kp*-velocity dependency in the solar wind is apparent from the tilt of its distribution, see top panel of Figure 4.14. The distribution is inclined to positive values but very broad. The comparison with the filtered data shows that *Kp* values > 6 and velocities $> 850\,\mathrm{km\,s^{-1}}$ are almost always associated with CME related periods, see middle and bottom panel of Figure 4.14.

In order to find a functional relation for the mean *Kp* value, I look at the relative frequencies per velocity interval, which are plotted in the bottom panel of Figure 4.15. The mean *Kp* value seems to scale almost linear with the solar wind velocity. The MAD of the mean has a mean size of about 1.1 *Kp* units.

Again, as the *Kp* index has a quasi-logarithmic scaling, a logarithmic function is the obvious choice for the fitting process. Thus, the logarithmic function

$$f(x) = a \cdot \ln(x + x') + y' \tag{4.10}$$

is used for the fit, with the scaling factor a, the location parameter x', and the vertical shifting parameter y'. The resulting fit is plotted in Figure 4.16 and its parameters are $a = 10.6(34)$, $x' = 8.1(43) \times 10^2$, and $y' = -73(28)$, with the velocity in units of [km s^{-1}]. The MAD is about 1.1 *Kp* units. This leads to the CME dependency function

$$Kp_{\mathrm{CME}}(v) = 10.6 \cdot \ln(v + 810) - 73\,, \tag{4.11}$$

which can be used to forecast the *Kp* index from the estimated CME arrival velocity.

solar wind stream example in Figure 4.17

It becomes obvious how important the influence of the magnetic field z-component is, when looking at the same example CME from Figure 4.11. I plotted its in-situ magnetic field strength and velocity in Figure 4.18

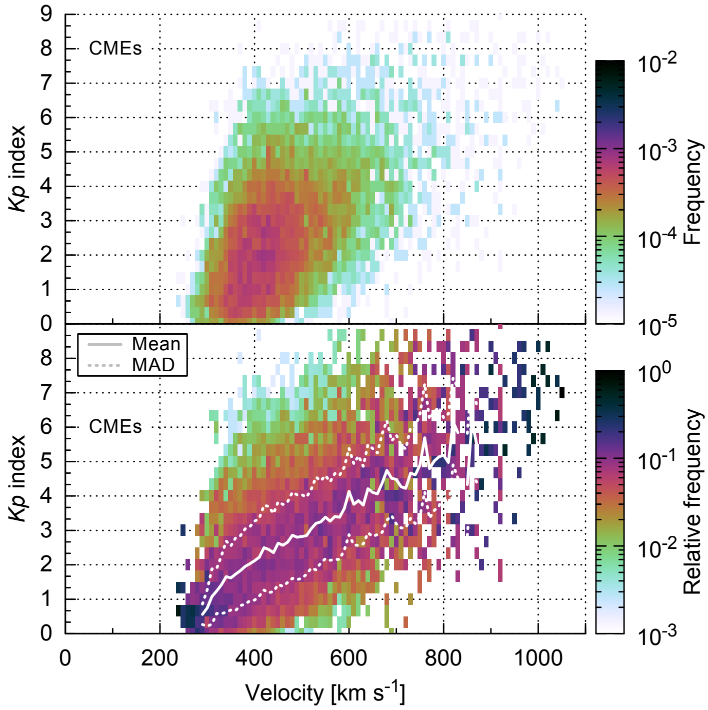

Figure 4.15 CME part of the *Kp*-velocity distribution (same as third panel of Figure 4.14) and its relative distribution per velocity interval with the mean *Kp* values (solid line) and their mean absolute deviation (dotted lines). The bin size is $10\,\mathrm{km\,s^{-1}}$ and $1/3$ *Kp* unit respectively.

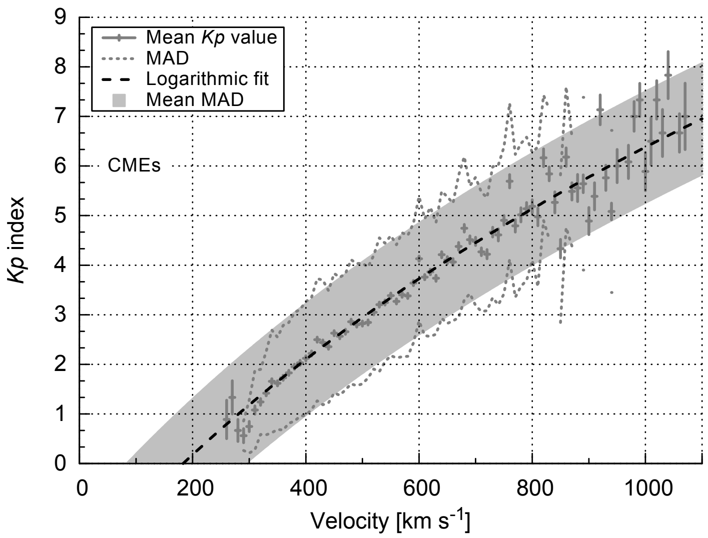

Figure 4.16 Mean *Kp* values (+) and MAD values (dotted lines) per velocity interval for the CME part of the data. The error bars represent the relative data count. The logarithmic fit (dashed line) is plotted with a mean MAD band (shaded area). The function (4.10) is used for the weighted fit.

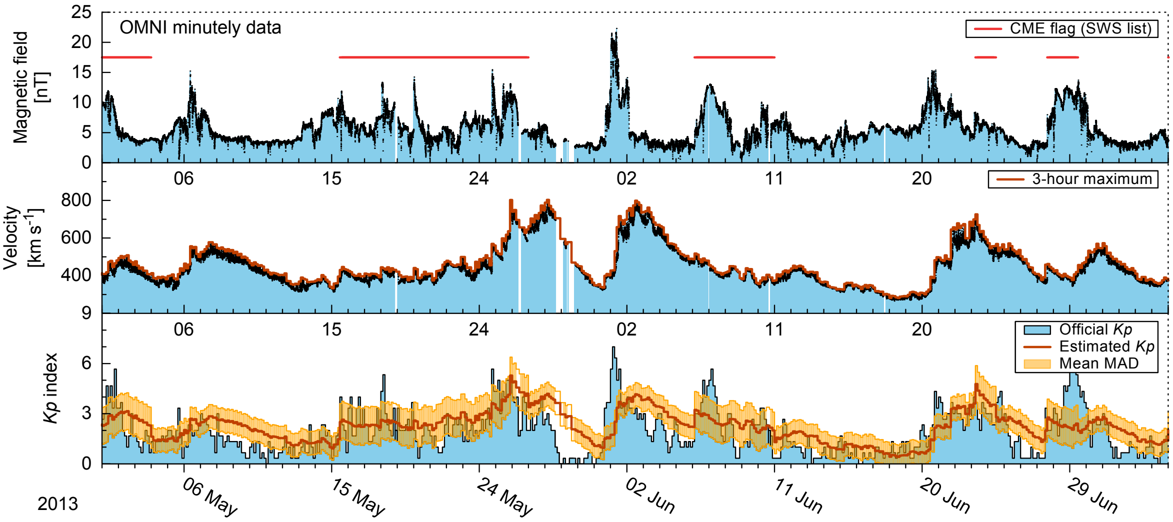

Figure 4.17 Solar wind measurements, official *Kp* index, and estimated *Kp* for the time period 1 May to 5 July 2013. The solar wind parameters are the magnetic field strength and the velocity. I also plotted the velocity's 3-hour maximum for illustration. The solar wind data are from the minutely OMNI data set. The official *Kp* index is obtained from the GFZ Potsdam. I plotted the *Kp* estimate depending on whether the period is flagged as a CME in the SWS list (red line in top panel) or not, that is, via Equation 4.11 or Equation 4.12. The orange band indicates the mean MAD.

together with the official *Kp* index and the derived *Kp* estimate. The latter do not coincide well during this

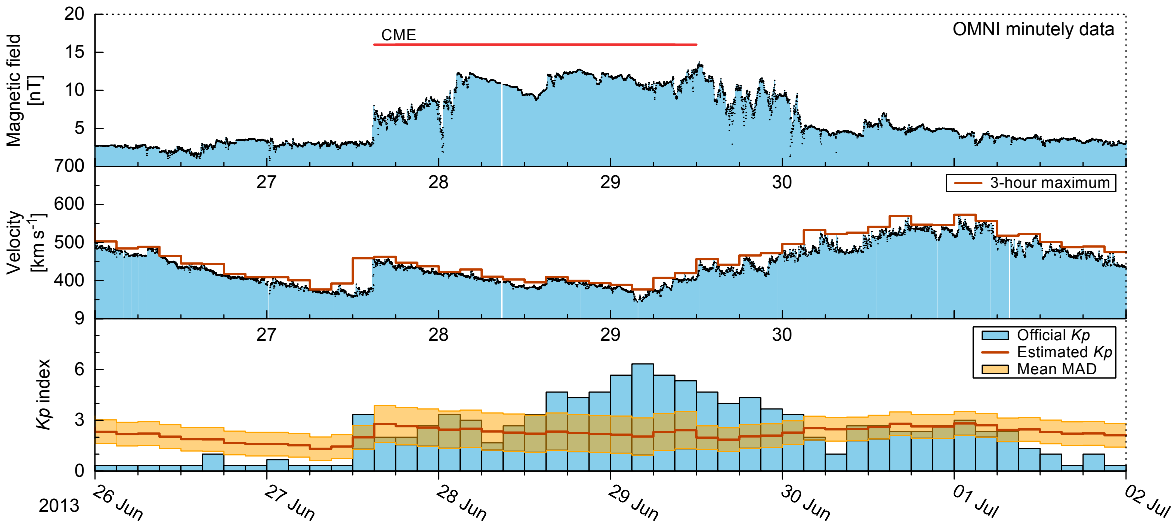

Figure 4.18 Solar wind measurements, official *Kp* index, and estimated *Kp* for the time period 26 June to 2 July 2013. The solar wind parameters are the magnetic field strength and the velocity. I also plotted the velocity's 3-hour maximum for illustration. The solar wind data are from the minutely OMNI data set. The official *Kp* index is obtained from the GFZ Potsdam. I plotted the *Kp* estimate depending on whether the period is flagged as a CME in the SWS list (red line in top panel) or not, that is, via Equation 4.11 or Equation 4.12. The orange band indicates the mean MAD.

period. The *Kp* estimate performs okay during the initial sheath region and around the peak of the trailing HSS. The rarefaction regions of declining velocity at the start and end of the considered interval are overestimated, whereas the MC and the trailing compression region are underestimated.

4.4.5 Functional dependency for stream velocity

The procedure in this section is similar to that in the previous section. The correlation coefficient is higher for solar wind stream velocities when the data is shifted by 9 hours, see Figure 4.13. I use the shifted data and look at the relative frequencies per velocity interval in order to find a functional dependency for the mean *Kp* value, see bottom panel of Figure 4.19. Again, the mean *Kp* value scales almost linear with the velocity. The MAD

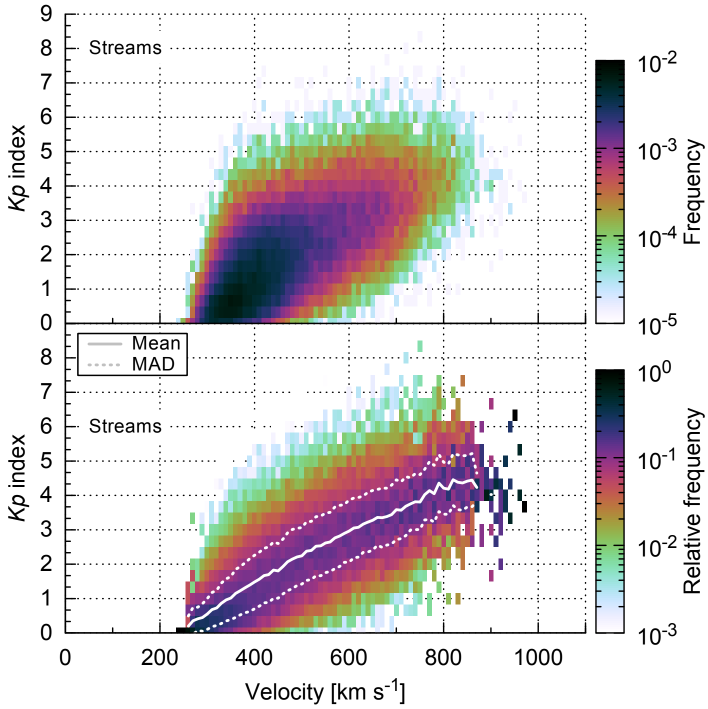

Figure 4.19 Stream part of the *Kp*-velocity distribution (similar to second panel of Figure 4.14, but with the data shifted by 9 hours) and its relative distribution per velocity interval with the mean *Kp* values (solid line) and their mean absolute deviation (dotted lines). The bin size is 10 km s^{-1} and 1/3 *Kp* unit respectively.

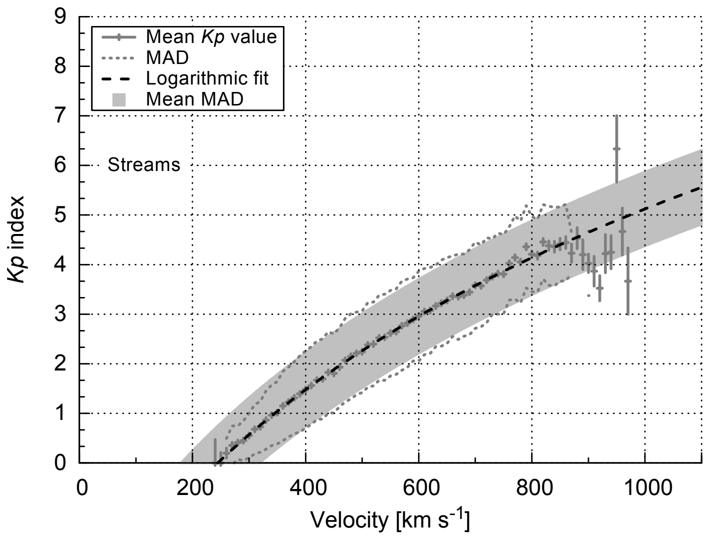

Figure 4.20 Mean *Kp* values (+) and MAD values (dotted lines) per velocity interval for the stream part of the data, shifted by 9 hours. The error bars represent the relative data count. The logarithmic fit (dashed line) is plotted with a mean MAD band (shaded area). The function (4.10) is used for the weighted fit.

of the mean has a mean size of about 0.7 *Kp* units.

Again, I use the logarithmic function (4.10) for the fitting process. The resulting fit is plotted in Figure 4.20 and the fit parameters are $a = 5.88(38)$, $x' = 2.99(49) \times 10^2$, and $y' = -3.70(29) \times 10^1$, with the velocity in units of [km s^{-1}]. The MAD is about 0.7 *Kp* units. This leads to the solar wind stream dependency function

$$Kp_{\text{Stream}}(v) = 5.88 \cdot \ln(v + 299) - 37.0\,, \tag{4.12}$$

which can be used to forecast the *Kp* index from the estimated stream velocity, e.g., obtained from remote coronal hole analyses.

4.5 Discussion and summary

The following results/relations are obtained from the analyses:

- solar activity: *Kp*-SSN relation with an error of about 1/3 *Kp* unit
- seasonal variations of up to 4/3 *Kp* units
- solar wind nowcast: *Kp*-vB_z relation (average and worst case)

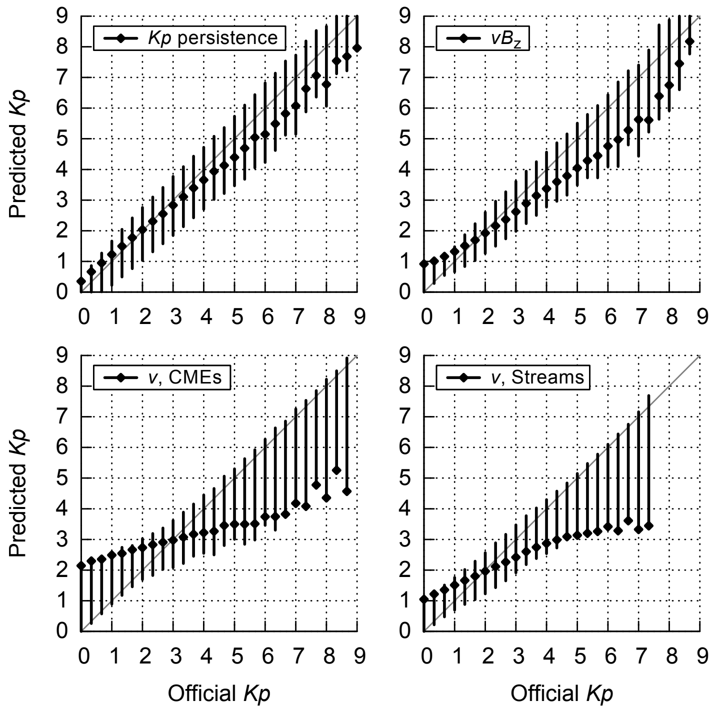

Figure 4.21 Prediction performance of *Kp* persistence and the three derived empirical *Kp* relations. The forecast errors are the difference between the predicted and the actual value and are calculated from the same data and time range as the relations themselves. The errorbars denote one positive and negative standard deviation. Perfect predictions are indicated by the gray diagonal lines.

- CME forecast: *Kp*-velocity relation (average and worst case)
- stream forecast: *Kp*-velocity relation (average and worst case)

The derived empirical relations are chosen for their high correlation coefficients. However, the correlation coefficient itself does not represent the performance of a model as the coefficient depends highly on the scatter of the underlying distribution. Therefore Wing et al. (2005) advise to additionally provide scatterplots and skill scores for the evaluation of predictive models. In the following, I present the forecast errors and determine the true skill statistics as measures for the prediction performance of the empirical models.

The quality of predictions can be assessed by how they compare to a simple persistence model (Detman & Joselyn 1999). In the case at hand the persistence consists of the official *Kp* value from the previous 3-hour interval. In order to evaluate the models' prediction performances, their forecast errors are calculated. Forecast errors are the difference between the predicted and the actual value. The resulting performances of the persistence and the three models and the corresponding standard deviations are displayed in Figure 4.21. The persistence performance is obtained from the complete *Kp* time span 1981–2016. It does fairly well, as its forecast error is less than 0.7 *Kp* units up to a *Kp* of 5.7. At and above a *Kp* of 6 the error is underestimated with a maximum deviation of 1.3 *Kp* units.

The derived empirical functions do not cover the whole *Kp* range from 0 to 9 within the distributions of observed values. Only the *Kp* ranges with more than one observed data point are considered for deriving the relations' prediction performances. This excludes the *Kp* 9 values and in case of the velocity relation for streams also the values *Kp* 7.7 and above.

The derived vB_z function (4.8 + 4.9) does only coincide with significant data in the *Kp* range 1 to 8.7. Especially because the minimum of the vB_z function is larger than 0.7 *Kp*, as can be seen from Figure 4.10. The model performs reasonably well at and below a *Kp* of 5 with forecast errors smaller than 1 *Kp* unit. Larger *Kp* values are underestimated and deviate up to 1.7 *Kp* units from the predicted values.

In the case of the velocity relation for CMEs, the derived function (4.11) does only coincide with significant data in the *Kp* range 1.3 to 6.3, as can be seen from Figure 4.16. The magnitude is overestimated below a *Kp* of 3 and underestimated above. In the range between a *Kp* of 1 and 5 the forecast errors are smaller than 1.3 *Kp* units. Above, the error rises up to 4 *Kp* units at a *Kp* of 8.7.

For the velocity relation for streams, the derived function (4.12) does only coincide with significant data in the *Kp* range 0.3 to 4.3, as can be seen from Figure 4.20. The magnitude is overestimated below a *Kp* of 2 and underestimated above. Throughout the valid range the forecast errors are smaller than 1.3 *Kp* units. Above, the error rises up to 4 *Kp* units at a *Kp* of 7.3.

The model based on the vB_z relation is more accurate than those based purely on the velocity. This is expected, however, the vB_z relation is still eclipsed by the persistence model.

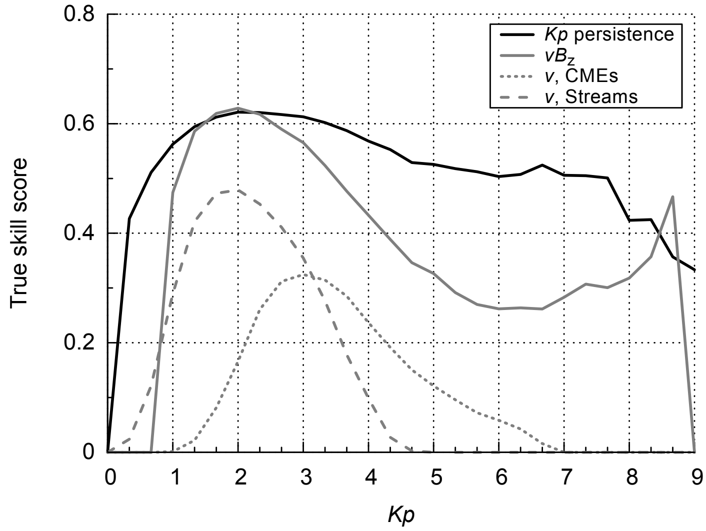

Figure 4.22 True skill scores for the *Kp* persistence and the three prediction relations as a function of *Kp* threshold.

In order to further test the derived models for their predictive value, I derive their true skill statistic (TSS) – a common tool for forecast verification. The TSS is a skill score based on the contingency table that categorizes forecasted and observed events. The score is the difference between the forecast hit rate and the false alarm rate. Its range is between -1 and 1, where 1 indicates an ideal prediction and 0 a random prediction. I give a more detailed description on the TSS in the appendix Section A.7. This method is the prevalent form of forecast verification in *Kp* models (Detman & Joselyn 1999; Wing et al. 2005; Savani et al. 2017). It is defined that each single 3-hour *Kp* interval represents an event and a hit occurs when both the forecasted and observed *Kp* exceed a specified threshold. I adopt these criteria to make the results comparable. Therefore the TSS is derived as a function of *Kp* threshold – the results for persistence and the three models are plotted in Figure 4.22.

The E-field relation reaches its peak at a *Kp* of 2 with a TSS of 0.63, it then decreases to a minimum at *Kp* 6 with a TSS of 0.26. To higher *Kp* values, the TSS increases again and reaches 0.47 at a *Kp* of 8.7. This increase is due to the dominant number of correct null forecasts that make the TSS approach the hit rate (Doswell et al. 1990). It is a bias inherent to the TSS in case of rare event forecasting. Both velocity relations have throughout their *Kp*] ranges a significantly lower TSS. The CME relation shows a peak TSS of 0.32 at a *Kp* of 3 and the stream relation a peak TSS of 0.48 at a *Kp* of 2. Thus, the TSS gain from the additional B_z component is about 1.5–2 *Kp* units.

The persistence forecast clearly outperforms the other prediction models, especially in the high *Kp* range. However, as Detman & Joselyn (1999) stated, it has no warning value because it can only predict a high *Kp* value after a high *Kp* value was already observed. Thus, the persistence always misses the onset of a geomagnetic storm, whereas solar wind based models can provide at least a nowcast if not actually a short lead time from the distance of the in-situ measurement location at L1.

In order to compare their *Kp* forecast skill metrics with other models, Savani et al. (2017) use a threshold of $Kp \geq 5$. They choose this value because of the NOAA/SWPC geomagnetic storm scale (G-scale) definition: The G-scale starts with G1, which translates to a *Kp* of 5. I stick to this definition and provide a statistics summary of the *Kp* persistence and the three derived models in Table 4.2. Obviously the defined *Kp* threshold is of little use for the stream velocity relation as by this definition geomagnetic storms cannot be predicted.

The E-field model has a TSS of 0.33 at a *Kp* of 5 and can be compared with the Wing APL model 3 (Wing et al. 2005, Fig. 13). The Wing APL model 3 predicts *Kp* 1 hour in advance and uses the solar wind parameters $n, v_x, |\boldsymbol{B}|$, and B_z as input sources for a neural network. The additionally considered parameters density and magnetic field strength boost the corresponding TSS to about 0.7.

Costello model (neural network, input: sw): about 0.45
Wing APL model 1 (1 h, neural network, input: Kp nowcast + sw): about 0.8
Wing APL model 2 (4 h, neural network, input: Kp nowcast + sw): about 0.7
Wing APL model 3 (1 h, neural network, input: sw): about 0.7
BSS model for eight CME events has $TSS = 0.34$ (Savani et al. 2017, Tab. 3)

Table 4.2 Statistics of the different prediction models. The metrics are calculated for a threshold hit criteria of $Kp \geq 5$.

Parameter	*Kp* persistence $Kp(t-1)$	E-field $Kp(vB_z)$	CME velocity $Kp(v_{\mathrm{CME}})$	Stream velocity $Kp(v_{\mathrm{Streams}})$
Time shift [hours]	3	0	0	9
Event count	105 192	79 276	12 116	65 774
Correlation coefficient	0.81	−0.72	0.51	0.66
Proportion correct	0.96	0.97	0.88	0.98
Hit rate	0.55	0.33	0.13	0
False alarm rate	0.02	0	0.01	0
True skill score	0.53	0.33	0.12	0
Valid *Kp* range	0.3–8.7	1.0–8.7	1.3–6.3	0.3–4.3

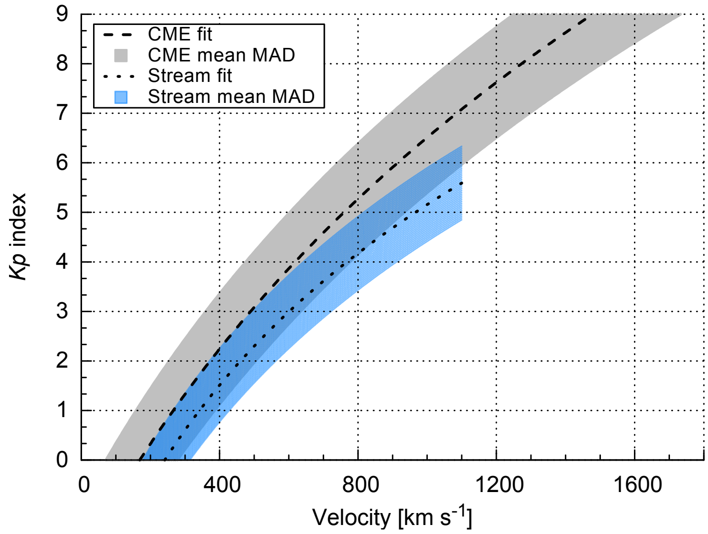

Figure 4.23 Logarithmic fit curves for CMEs (dashed line) and streams (dotted line) with their corresponding mean MAD bands (shaded areas).

CMEs can be faster than the maximal velocities included in the OMNI data. Instrumental effects (specify...) lead to data gaps during these periods. Yet, CME speeds of up to XX km/s at 1 au were observed (cite?). According to Equation 4.11, a CME speed of 2000 km s^{-1} at L1 would lead on average to a theoretical *Kp* of 12.2, however, the *Kp* scale is capped at 9o. A *Kp* of 9o is reached already at a velocity of 1489 km s^{-1}, see Figure 4.23.

The maximal velocity of regular solar wind is limited by the coronal temperatures (Parker 1958) and is observed to be around 900 km s^{-1}. That is why streams on average provoke *Kp* values below 5o.

comparison:
Kp-velocity correlation
similar to Elliott et al. (2013); different data time period, resolution and averaging method (3-hour maximum of 1 min data)
see Akasofu1981 p. 126, table

It is obvious that the derived relations are not suited to be used inversely, i.e., to deduce solar wind properties from existing *Kp* data.

4.6 Applications and outlook

'scientists develop an advanced prototype space weather warning system to ensure the operation of telecommunication and navigation systems on Earth to the threat of solar storms' from AFFECTS

Prototype/precursor relations are integrated into applications developed within the Advanced Forecast For Ensuring Communications Through Space (AFFECTS) project which ran from 2011 to 2013. The following services, accessible via the AFFECTS website[8], contain results from this *Kp* study:

- Real-time plot: Solar Wind and *Kp* forecast plot – DSCOVR real-time solar wind and *Kp* forecast plot. The *Kp* is estimated from the solar wind relation.
- RSS feed: L1 Kp Alert – threshold based RSS feed that gets triggered when a specified *Kp* is reached.
- RSS feed: L1 GNSS Alert – threshold based RSS feed that gets triggered when a specified GNSS error is reached... The value is derived from the *Kp* estimate.
- RSS feed: L1 Aurora Alert – threshold based RSS feed that gets triggered when a specified auroral location is reached... The value is derived from the *Kp* estimate.

note: repair RSS feeds before submitting!

Further applications of resulting *Kp*-relations:

- CME *Kp* impact (part of UGOE DDC)
- iPhone app L1 Alerts (Solar wind latest 2-hour extreme values and derived forecast values): http://www.affects-fp7.eu/app-services/L1-Alerts/dataL1Alerts.txt, https://itunes.apple.com/au/app/affects/id893579846
- Android app L1 Alerts... https://play.google.com/store/apps/details?id=com.afects.forecasts
- has SW-Display Kp forecast??

outlook:
Separate structures such as CIRs and HCSs for their *Kp*-impact separately...

All provided web links in this work were existent in [date].

CME Kp impact as part of DDC
- *Kp* nowcast with L1 solar wind measurements (L1 alerts, disseminated as RSS feeds; integrated in smartphone app and space weather display)
- Forecast of the possible CME impact on the Earth's magnetosphere (*Kp* index) from the predicted CME arrival velocity (integrated in UGOE CME forecast chain (aka DDC))

In the present study, the solar activity is neglected for deriving the empirical solar wind-*Kp* relations. It would be worth, examining their dependency on the solar cycle, especially as Wing et al. (2005) note that the predictability of *Kp* slightly scales with solar activity.

4.7 notes...

What kind of solar wind structures create the individual regions in this distribution? (B-V-Kp circle plot)
What is their individual contribution to the Kp ranges (e.g. high Kp: CMEs 70% and CIRs 30%)?

ACE solar wind time series and event list (ACE OPTIMAP "Zeitreihe"-events)

How can the impact field strength of CMEs be forecasted (V->B correlation for CMEs)?
Internal solar wind correlations: B-V correlation
ACE MAGSWE 64 s data -> yearly overlay plot

rt data errors/gaps... vs science data (see paper Kp as V replacement)
DSCOVR as replacement was launched on 11 Februar 2015. It is NOAA's SWPC real-time solar wind prime source since 27 July 2016.[9]

[8]AFFECTS website: http://www.affects-fp7.eu/services/
[9]http://www.swpc.noaa.gov/products/real-time-solarwind

5 Empirical solar wind model for the inner heliosphere

5.1 Introduction

The analyses in the previous chapter are focused on the solar wind's influence on the magnetosphere – this chapter changes the main focus to the solar wind upstream of the magnetosphere, in a first step down to a solar distance of 0.3 au and then even further down to the region around $10\,R_{\odot}$, close to the solar wind's origin near the Sun. The solar wind's evolution on its way to 1 au from the near-Sun region is modeled with the goal of predicting the solar wind environment for the upcoming PSP mission.

context of motivation in thesis and paper introduction and context of results in thesis

This chapter is constructed as follows, the PSP mission, its scientific goals, and the spacecraft are described, I introduce the analyses done in the publication Venzmer & Bothmer (2018), which is a major part of this chapter. An alternative to the magnetic field solar distance dependency is derived, which changes the power law from our article to support a Parker magnetic field geometry. An outlook is given, describing different effects that further could be analysed, quantified, and implemented into the solar wind model, such as flux conservation, seasonal and latitudinal effects, and the distance behavior of solar wind structures.

The major part of this chapter is published under the title "Solar-wind predictions for the Parker Solar Probe orbit" in Venzmer & Bothmer (2018), which is referred to as 'the paper' in this work. The article, published online on 20 March 2018 in Astronomy and Astrophysics (A&A), is included following this chapter, denoted as Chapter 6, copyright to ESO and reproduced with permission.

The analyses described in the paper were entirely done by me, as well as the tables, figures and equations. My coauthor Volker Bothmer contributed to the text and the anonymous referee helped clarifying a few aspects. The text was further improved by the A&A language editor Joshua Neve.

5.2 Parker Solar Probe mission

motivation written in McComas et al. (2007)
mission goals (see paper + Fox et al. (2015))
A photo of PSP during testing is shown in Figure 5.1 and an illustration of PSP flying near the Sun is shown in Figure 5.2.

orbit figure? ref. to distance figure?
WISPR instrument
CGAUSS project – context of this work in project objectives
Sun angular diameter comparison, see presi S^3

5.3 Paper content

We obtain lognormal representations of the frequency distributions' shapes of the four key solar wind parameters magnetic field strength, proton velocity, density and temperature. We derive analytical relations for the parameters' solar activity dependencies and for their solar distance scaling. An empirical solar wind model is build from the combination of the obtained frequency distributions, SSN dependence relations and solar distance dependence functions, representing the solar wind's solar activity and distance behavior. This empirical model is fed with SSN predictions and is extrapolated to the orbit of PSP. We estimate solar wind median values during PSP's first perihelion and model the values for PSP's closest perihelia.

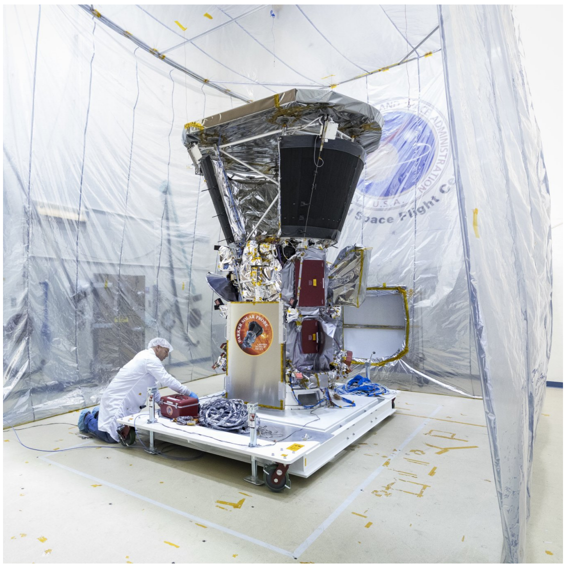

Figure 5.1 PSP in the Acoustic Test Chamber at NASA's Goddard Space Flight Center in November 2017. Credit: NASA/Johns Hopkins APL/Ed Whitman, 2017.

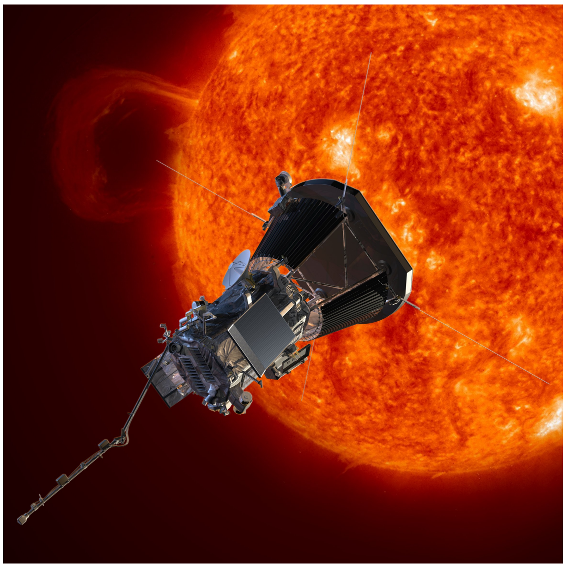

Figure 5.2 Artist's concept of PSP near the Sun. Credit: NASA/Johns Hopkins APL, 2015.

In order to derive the solar wind environment for the PSP orbit, finally the general solar wind model derived in the previous sections will be extrapolated to the PSP orbit, taking into account predictions of the SSN.

5.4 Alternative magnetic field solar distance dependency

note: comparison plot between models in range 0–20 au...

In our article, we scaled the magnetic field strength via a power-law function and obtained a solar-distance dependency proportional to $r^{-1.662}$. We also noted there that the model's near-Sun field magnitude, extrapolated to PSP's closest perihelion, will be lower than the actual values to be found. However, it is a simplified approach – in the following I present a procedure, leading to an improved distance dependency, which is intended to account for a Parker IMF geometry, respecting the different power-law scalings of the contributions of the individual field vector components. This new distance dependency, extrapolated to the PSP orbit and combined with the solar activity dependency described in the paper, yields 8 % higher values at the first perihelion and 32 % higher values at the 22nd perihelion.

A possibly more accurate distance dependency for the model is derived in the following.

The coronal magnetic field near the Sun rotates rigidly, holding on to the coronal plasma. At the solar wind source surface (at around $2.5\,R_\odot$), where the thermal plasma pressure overcomes the magnetic pressure, the magnetic field gets radially transported outwards, maintaining only its radial vector component $\boldsymbol{B}_r$. From there on, the solar rotation begins to shear the magnetic field, building up a longitudinal component $\boldsymbol{B}_\phi$ as well. The solar wind magnetic field model formulated by Parker (1958) has the following components in spherical coordinates (θ is the colatitude):

$$\boldsymbol{B}_r(r) = B_0 \left(\frac{r_0}{r}\right)^2 \cdot \boldsymbol{e}_r\,, \tag{5.1}$$

$$\boldsymbol{B}_\phi(r) = -B_0 \left(\frac{r_0}{r}\right)^2 \cdot \frac{\omega\, r\, \sin\theta}{v_{\mathrm{sw}}} \cdot \boldsymbol{e}_\phi\,, \tag{5.2}$$

$$\boldsymbol{B}_\theta(r) = 0 \cdot \boldsymbol{e}_\theta\,. \tag{5.3}$$

B_0 represents the radial field component at the solar distance r_0. The solar surface equatorial angular rotation rate ω and the solar wind velocity v_{sw} are involved as well. From these equations it can be seen that $\boldsymbol{B}_r$ scales with increasing solar distance with r^{-2}, as it is expected for a spherical outflow, and $\boldsymbol{B}_\phi$ scales with r^{-1} as expected for a two-dimensional point source. In-situ observations support the component's scaling according to these theoretical exponents, although in slow solar wind the scaling for $\boldsymbol{B}_\phi$ deviates somewhat from theory (Mariani et al. 1978).

From the magnetic field's absolute value

$$B(r) = \sqrt{\boldsymbol{B}_r^2 + \boldsymbol{B}_\phi^2 + \boldsymbol{B}_\theta^2}\,, \tag{5.4}$$

$$B(r) = \sqrt{\left(B_0 \left(\frac{r_0}{r}\right)^2\right)^2 + \left(-B_0 \left(\frac{r_0}{r}\right)^2 \cdot \frac{\omega\, r\, \sin\theta}{v_{\mathrm{sw}}}\right)^2}\,, \tag{5.5}$$

it is apparent that the magnetic field strength does not scale with a simple power law. If the solar dipole axis tilt to the solar rotation axis is neglected and the radial field component B_0 is set to be in the equatorial plane at $r_0 = 1$ au, then $\theta = 90°$ and therefore

$$B(r) = B_0 \cdot \sqrt{r^{-4} + \left(\frac{\omega\, r}{v_{\mathrm{sw}}}\right)^2 r^{-4}}\,, \tag{5.6}$$

with the distance r in units of [au].

The magnetic field angle in the solar equatorial plane is distance dependent and is calculated via

$$\phi_B(r) = \arctan\left(-\frac{\omega \cdot r}{v_{\mathrm{sw}}}\right). \tag{5.7}$$

The angle becomes $\phi_B(1\,\mathrm{au}) = -46.23°$ when using the Sun's equatorial angular velocity $\omega_{\mathrm{eq}} = 14.37\,°\,\mathrm{d}^{-1}$ (for more details on solar rotation see appendix Section A.1) and the median solar wind velocity $v_{\mathrm{sw}} = 416\,\mathrm{km\,s^{-1}}$ from our paper.

During solar cycle minimum, the solar wind in the equatorial plane outside the source surface originates from polar regions at about ±60° heliolatitude. This leads to a slightly underwound Parker spiral, because of the slower rotation rate at higher latitudes (Banaszkiewicz et al. 1998). Using the differential rotation rate $\omega(\pm 60°) = 13.69\,°\,\mathrm{d}^{-1}$ (see appendix Equation A.1), the field angle becomes $\phi_B(1\,\mathrm{au}) = -44.84°$.

As the solar rotation axis tilt to the ecliptic normal only has a maximum angle of 7.2°, I consider its influence on ϕ_B minor, and choose to neglect it in this calculation. Thus from theory, in the ecliptic at a solar distance of 1 au, the Parker spiral's observed magnetic field angle ϕ_B is centered most of the time at −45° or for the opposite field polarity at 135°. Indeed, this is confirmed by the angle's frequency distribution, apparent in measurements made at 1 au, such as the OMNI data of the time period 1963–2016 plotted in Figure 5.3.

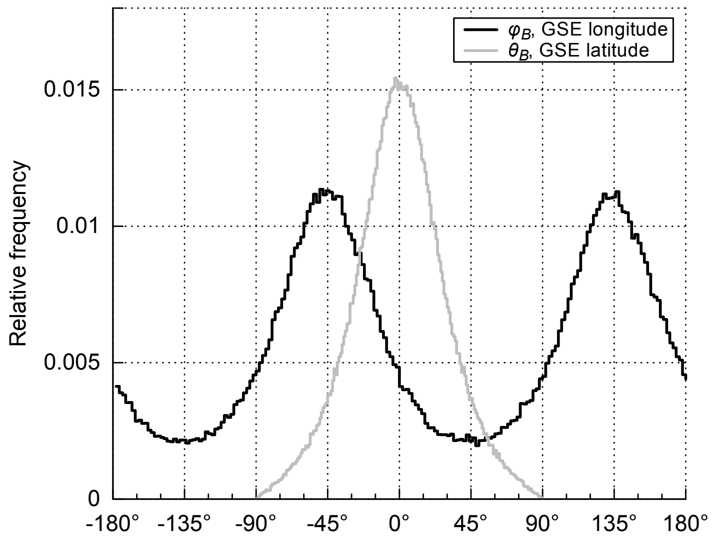

Figure 5.3 Frequency distributions of the magnetic field angles ϕ_B and θ_B in GSE coordinates. The frequencies are based on the hourly OMNI data during the period 1963–2016.

For ϕ_B being in average centered around these two directions, both vector components $\boldsymbol{B}_r$ and $\boldsymbol{B}_\phi$ have to be of equal amplitude. It can be seen from Equations 5.4 and 5.6 that this leads to

$$B(1\,\mathrm{au}) = B_0 \cdot \sqrt{2} \qquad \text{with} \qquad \left(\frac{\omega \cdot 1\,\mathrm{au}}{v_{\mathrm{sw}}}\right) = 1\,. \tag{5.8}$$

Table 5.1 Fit coefficients for the curve fits (Equation 5.9) and for the distribution fit (using the lognormal function of Equation (4) from the paper), derived from the combined Helios 1 and 2 data. The numbers in parentheses are the errors on the corresponding last digits of the quoted value. The crossing distance indicates where the median and mean fits intersect each other. This distance is calculated numerically and its corresponding error only represents an estimated value.

Fit		Factor	Exponents		Crossing distance
		a	e_1	e_2	[au]
Curve	Median	4.04(13)	-1.852(25)	-0.97(23)	0.336(10)
	Mean	4.47(12)	-1.740(18)	-0.99(23)	
Distribution	Median	3.833(27)	-1.858(42)	-1.32(12)	–
	Mean	4.081(29)			

However this way, ω and v_{sw} are treated as time independent constants.

Considering the longitudinal field component, the magnetic field strength's distance dependency is derived in a similar way to that in the paper, see paper Section 6.4. Also, the same Helios data set is used for the fit as is in the paper.

In order to get an analytical representation of the radial dependence of the magnetic field, I derive a suitable fit function, assuming a nonexistent $\boldsymbol{B}_\theta$,

$$x(r) = a \cdot \sqrt{(r^{e_1})^2 + (r^{e_2})^2} \tag{5.9}$$

with the scaling parameter a, and the exponents e_1 and e_2, is used in a least squares regression fit. From the theoretical considerations sketched above, the expected fit parameter values are: $a \approx \frac{B(1\,\mathrm{au})}{\sqrt{2}}$, $e_1 \approx -2$, and $e_2 \approx -1$.

The resulting fit curves for the mean and median field strength are plotted with respect to solar distance in Figure 5.4. In the Helios distance region 0.3–1.0 au, the fit curves are very similar to those in the paper – as they are expected to be. This is why this graph is visually almost indistinguishable to the corresponding one in the paper (paper Section 6.4, Figure 7). The resulting fit parameters are presented in Table 5.1[1].

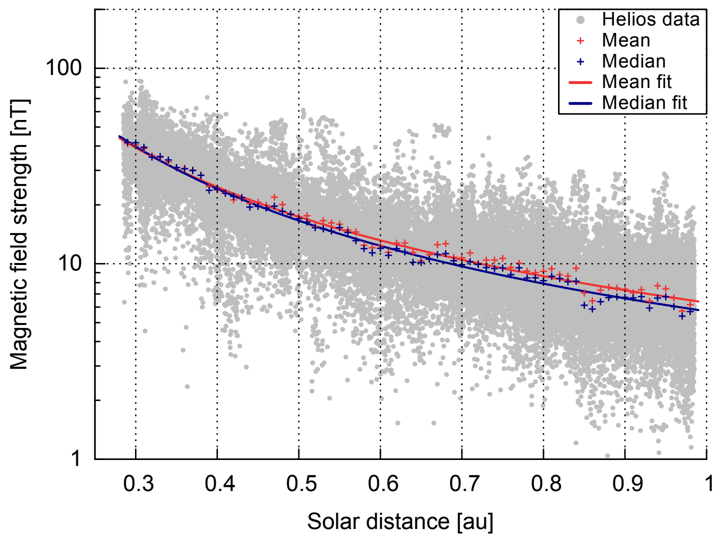

Figure 5.4 Magnetic field strength with respect to solar distance. The mean and median per 0.01 au data bin and their fit curves are plotted as well. The hourly Helios data has a native distance resolution of 0.01 au, thus, to make the distribution visible in this plot, I added a random distance value of up to ±0.005 au.

The weighted sum of the squared residuals (WSSR) of this fit slighly improved in comparison to that of the simple power-law function $x(r) = d \cdot r^e$ used in Venzmer & Bothmer (2018) – 6 % for the median and 9 % for the mean. However, the mean and median fit curves are fairly similar and still cross each other at a similar value as in the paper.

The here obtained fit parameter values are closer to the theoretical values than those derived in the paper. The exponents $e_{1,med} = -1.852$ and $e_{1,avg} = -1.740$ are up to 13 % larger than the theoretical exponent 2 and

[1] Concerning the error notation, I adhere to the parentheses notation documented in the "Guide to the expression of uncertainty in measurement" (GUM) published by Joint Committee for Guides in Metrology (2008), where the numbers in parentheses are the errors on the corresponding last digits of the quoted value.

lead to a less steep slope near the Sun. However, they are about 12 % smaller than the power-law exponents derived in the paper, which have values of −1.655 and −1.546.

It can be seen from Figure 5.5 that although the new fit curve is slightly curved, both fits are congruent in the Helios data range.

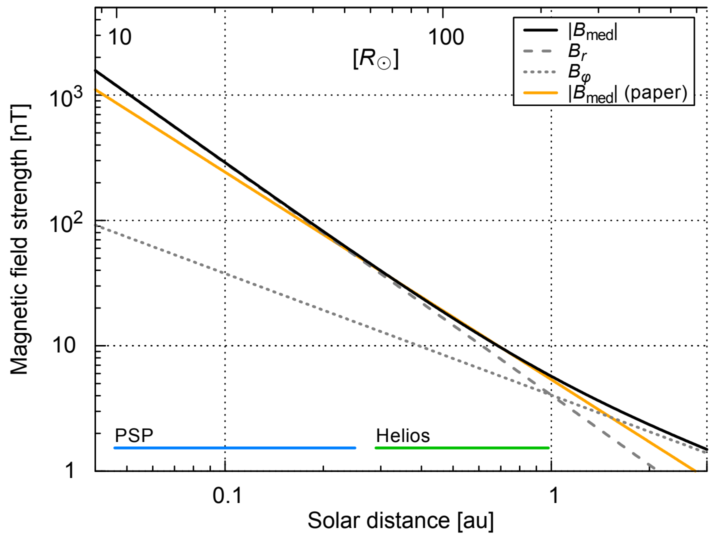

Figure 5.5 Magnetic field strength fit curves with respect to solar distance. Plotted are the derived absolute median field strength and its radial and azimuthal components. I added the absolute median field strength from Equation (10) of the paper as well. The orbital distance ranges from PSP and the Helios probes are indicated by the blue and green lines.

In the following paragraph I use the same method and reasoning as explained in the paper Section 6.4, thus I do not go into detail here.

...and it can be fitted via a lognormal function

see fit distribution in Figure 5.6 and resulting fit parameters in Table 5.1.

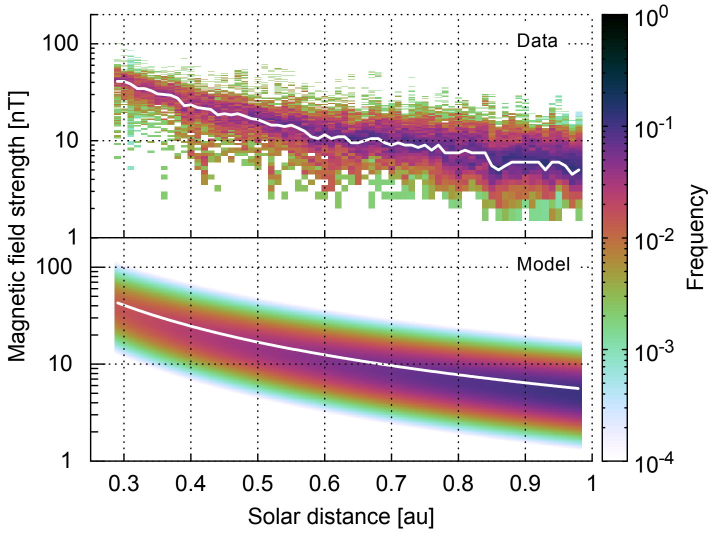

Figure 5.6 Frequency distribution of the solar wind magnetic field strength with respect to solar distance. I plotted the binned Helios data (top panel) and the square-root power-law lognormal fit model (bottom panel) with their median values (white lines).

The result of this analysis can be used to scale the SSN-relation derived in the paper:

$$B(ssn, r) = \frac{B(ssn)}{\sqrt{2}} \cdot \sqrt{(r^{e_1})^2 + (r^{e_2})^2}\,. \tag{5.10}$$

The resulting equation, combined with the values obtained from the solar activity analysis in the paper Section 6.3, yields

$$B_{\text{med}}(ssn, r) = (0.0131\,\text{nT} \cdot ssn + 4.29\,\text{nT}) \cdot \sqrt{(r^{-1.86})^2 + (r^{-1.3})^2}\,, \tag{5.11}$$

$$B_{\text{avg}}(ssn, r) = 1.0879 \cdot B_{\text{med}}(ssn, r)\,. \tag{5.12}$$

This magnetic field strength model is extrapolated to PSP's orbital range in Figure 5.7.

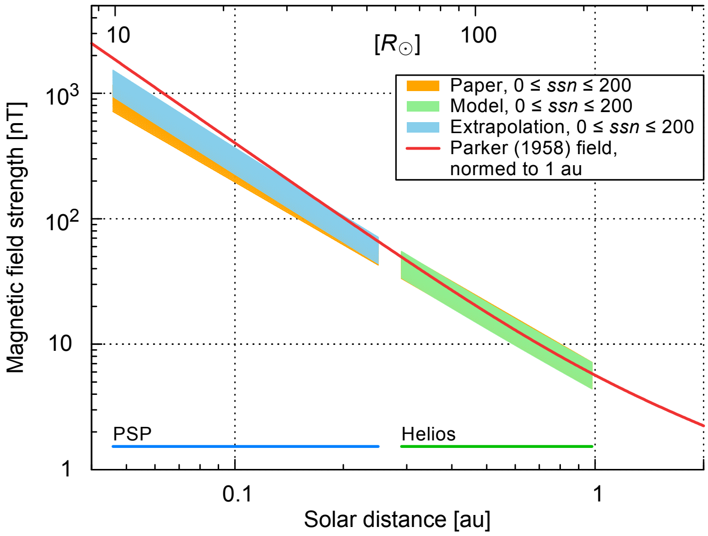

Figure 5.7 Radial extrapolation of the solar wind magnetic field strength to the PSP orbit region. The median value from the model, obtained from Helios and OMNI measurements, is extrapolated to the PSP region for SSN values between solar minimum and maximum, that is, $0 \le ssn \le 200$. The lower edges of the shaded areas correspond to solar minimum, the upper edges to solar maximum. I also added the radial dependency of the field model by Parker (1958), normed to 1 au (red). The orbital distance ranges from PSP and the Helios probes are indicated by the blue and green lines.

Using the SSN prediction as described in the paper, the solar wind environment is forecasted to PSP's orbit and mission time, see Figure 5.8.

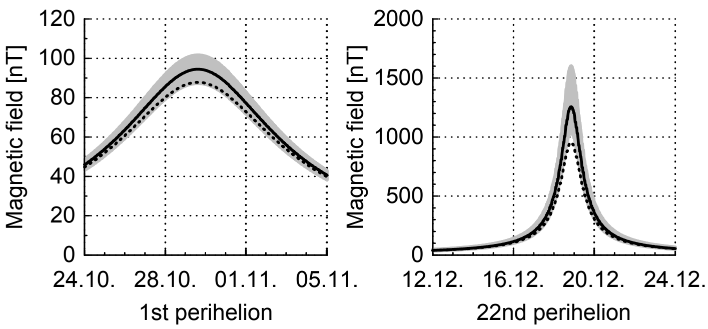

Figure 5.8 Estimated solar wind parameter medians (solid lines) and their error bands (gray area) during 12 days in 2018 and 2024 with PSP's first perihelion at about 0.16 au and PSP's 22nd (the first closest) perihelion at 0.046 au. I indicated the prediction from Venzmer & Bothmer (2018) as well (dotted lines).

The estimated magnetic field strength median value of 94 nT for PSP's first perihelion is 8 % higher than that derived in the paper. However, the median value for the first closest perihelion is even 32 % higher with 1241 nT.

The estimated frequency distributions of the solar wind magnetic field strength at PSP's 1st and 22nd (first closest) perihelion are plotted in Figure 5.9. During the first closest perihelion, high field strengths have multiple times the frequency of those derived in the paper.

5.5 Discussion

The newly derived dependency relation can be used to replace that found in the paper.

comparison with Burlaga1984: Large-scale IMF...; found for 1-5 au: B(r) = 4.75 sqrt(1 + R**2)/R**2

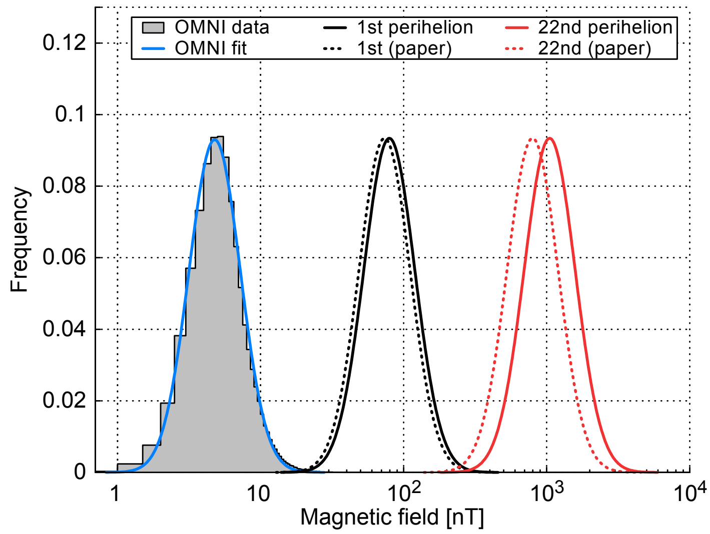

Figure 5.9 Frequency distributions of the solar wind magnetic field strength (OMNI data) and those estimated with the solar wind model for PSP's 1st and 22nd (first closest) perihelion. In this plot the frequencies of both extrapolated curves are scaled for visibility to the same height as the 1 au distribution. I indicated the prediction from Venzmer & Bothmer (2018) is as well (dotted lines).

5.6 Outlook

Currently, the solar wind model described in this chapter and the paper is purely empirical and its four solar wind quantities are characterized independently from each other. In further steps, theoretical relations connecting the parameters could be introduced to make the model self-consistent. For example, flux conservation could be implemented into the radial distance dependencies, relating the two parameters density and velocity (see section XX). Or also, the velocity within the magnetic field's $\boldsymbol{B}_\phi$-component (Equation 5.2) could be respected as a variable (not as a constant as it is done in the previous section).

inclusion of seasonal effects into the model, see Figure 5.10 and Figure 5.11; or error estimation...

latitudinal effects...

further investigations should be done into solar wind structure extrapolations
solar wind structure investigation. solar wind structures differ from the average distance scaling laws, e.g., MCs show a different extrapolation behavior (cite?).

Data captured from spacecraft that studied Mercury (perihelion distance of 0.3 au), such as Mariner 10 and MESSENGER, could be included to refine the distance dependency of the solar wind model. However, PSP's near-Sun in-situ measurements, starting in fall 2018, will eventually reveal how accurate the predictions of the derived models are.

5.6.1 flux conservation

conserved quantities:
- momentum conservation... VBbookp112
- flux conservation...

With consideration of continuity, the mass flux per solid angle has to be constant: $\dot{m}$ = const
conserved quantities:
- mass flux: $\dot{m} = \rho v A$ (with mass density ρ, velocity v and solid angle A)
- particle fluxes (proton flux, electron flux, etc.)
- proton flux: $j_\mathrm{p} = n_\mathrm{p} v_\mathrm{p} A$ (with proton density n_p and proton velocity v_p)

(with proton mass density $\rho = n_\mathrm{p} m_\mathrm{p}$ (with proton number density n_p and proton mass m_p).)

the individual radial dependencies for a spherical radial outflow are:
$A(r) \propto r^2$ –> A/r^2 = const
and assuming exponential dependencies,

$n_{\mathrm{p}}(r) = n_0 r^{c_n}$,
$v(r) = v_0 r^{c_v}$

$$
\begin{aligned}
j_{\mathrm{p}} &= \text{const} && (5.13)\\
n_{\mathrm{p}} v_{\mathrm{p}} A &= \text{const} && (5.14)\\
n_0 r^{c_n} v_0 r^{c_v} r^2 &= \text{const} && (5.15)\\
r^{c_n} r^{c_v} r^2 &= \text{const} && (5.16)\\
\Rightarrow c_n + c_v + 2 &= 0 && (5.17)\\
c_n + c_v &= -2 && (5.18)
\end{aligned}
$$

Thus, an increasing velocity results in a steeper density fall-off.

validity of mass flux continuity: within the heliosphere mass to energy conversion and vice versa is negligible, but there can be flux from and to higher latitudes as the Helios data is localized to a small latitude range in the ecliptic plane.
larger errors should be located near CMEs and CIRs (nonradial flows from deflections)
there is a proton flux difference between slow and fast solar wind streams (see book Schwenn1990 p. 146)
estimate the possible size of error:
(constant mass flux only for mean)
$c_n = -2.114$
$c_v = 0.0990$
$c_n + c_v = -2.024$
difference to -2 is 0.024

simple view: For a spherical constant velocity mass outflow, a per distance squared law is expected for the density, because of the mass flux conservation per solid angle for different distances. Measurements up to the outer heliosphere confirm the r^{-2} dependency (1–38 au by Voyager 2, (Belcher et al. 1993) newer paper?)

5.6.2 Seasonal solar wind variations

seasonal variation by month
quantify variation amplitudes

see Figure 5.10 and Figure 5.11
make 4-panel figure...

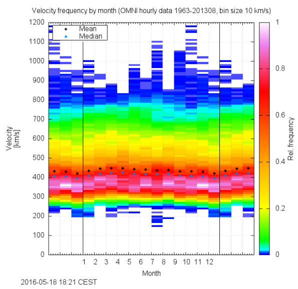

Figure 5.10 Diagram of the velocity frequency by month for the period 1963/01–2013/08. Mean and median values are shown as well.

derived exponent values from simple trigonometric fit on monthly values:
$c_n = -2.234$
maybe figure?

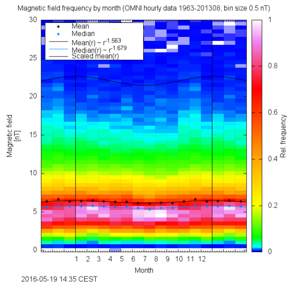

Figure 5.11 Diagram of magnetic field frequency by month for the period 1963/01–2013/08. Mean and median values are shown as well as the expected course from the solar distance variation (obtained from Helios data).

expected influence from Earth's perihelion/aphelion (see Appendix...) distance vs observations
we expect for the mean proton density (scaling law $n(r) \propto r^{-2.114}$):
$n(0.983\ au) = 7.098\ cm^{-3}$
$n(1\ au) = 6.845\ cm^{-3}$
$n(1.017\ au) = 6.605\ cm^{-3}$
we expect for the magnetic field strength (paper scaling law $n(r) \propto r^{-1.662}$):
$B(0.983\ au) = 5.870\ nT$
$B(1\ au) = 5.705\ nT$
$B(1.017\ au) = 5.547\ nT$

5.6.3 Latitude dependency

refer to Ulysses Figure 2.16
Ulysses swoops polar plots...

see Schwenn1990's Fig. 3.14
see also Schwenn (1990) p. 127
see also Richardson et al. (1995)
Balogh et al. (1999) p. 162 ff (origin and formation of CIRs in inner heliosphere with Helios data; latitude V dependence)

Helios latitude; see Figure 5.12

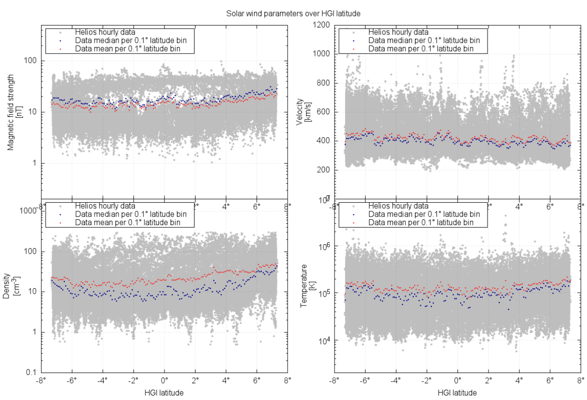

Figure 5.12 The four solar wind parameter's HGI latitude dependency. Their mean and median values per 0.1° bin are plotted as well. I added a random distance value of up to ±0.005 au in order to make the distribution visible in this plot.

with the exponential dependencies to 1 au projected solar wind parameters; there are only small changes with latitude in the range −7.25–7.25°
have a look on distribution widths...

dependence from latitude in interval −7.25–7.25° in Helios data negligible?, see Figure 5.13.
estimate error ranges from latitude influence...

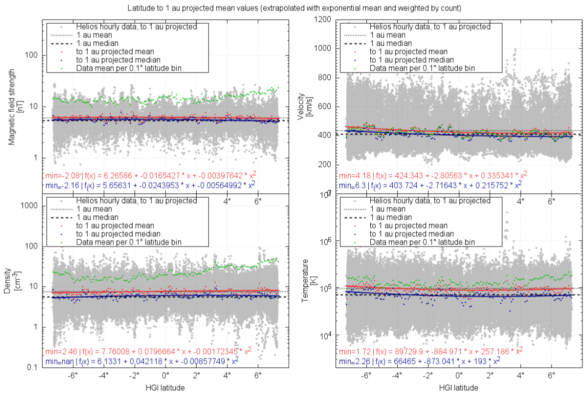

Figure 5.13 Solar wind parameters projected to 1 au with respect to latitude. And their mean values, including weighted fit. I added a random distance value of up to ±0.005 au in order to make the distribution visible in this plot. add projected median...

...plot Ulysses data into plot?

influence from latitude variation in data negligible? (see Ulysses Figure 2.16 in introduction). Helios probes within ecliptic => variation span equal to solar tilt: −7.25–7.25°; solar tilt/obliquity to ecliptic: $i_\odot = 7.25°$ (Sun fact sheet: `http://nssdc.gsfc.nasa.gov/planetary/factsheet/sunfact.html)`
big part of Helios data is from latitudes > ±5°, see Figure XX (data count over latitude) and see Figure 3.6 (Helios orbit polar plane in data section)

5.6.4 Radial evolution of solar wind structures

see CGAUSS `report2015_2`
Helios event lists HSSs, SLOWs, CIRs, CMEs...; event lists for all Helios data
see Liu2004 for Helios ICME list and radial dependencies of B, n, T and v...

200 km s^{-1} slow solar wind at 10 $R_\odot$ is in agreement with blob measurements from Wang2000

very slow sw (VSSW) gets accelerated; see Sanchez-Diaz2016:

radial diameter of MCs increase between 0.3 au and 4.3 au proportional to the distance as $r^{0.8}$ (Bothmer & Schwenn 1998)
MC central axial magnetic field strength radial density dependence $B = 18.1\, r^{-1.64}$ Leitner et al. (2007)
MC average diameter $D = 0.23\, r^{1.14}$ Leitner et al. (2007)
sw structure marked plots

5.7 notes...

Schwenn1983 intro -> sw-averaging comment (beer and wine) (cite him...)
see Hellinger2013 p.1353
see astro70/CGAUSS/dropbox_presis/... (presi 1.07 Inside Helios-Origins and Evolution-Salem.ppt -> Helios reloaded; radial functions for all parameters)
see Balogh1999 from p. 162 (Helios CIR results)
see Marsch1999... (model constraints)
On solar wind acceleration and SPP proposition: McComas2007

Parker1963 book, p. 75 -> isothermal expansion figure

at larger distances (specify...) heating outbalances the adiabatic temperature part (adiabatic cooling vs. pickup proton and stream–interaction heating; 1–68 au by Voyager 2; Richardson & Smith (2003)
solar wind ram pressure $p_{\text{ram}} = \rho V^2$

replace paper with actual print published A&A version...
update paper reference...
remove sidc bib reference...

A&A 611, A36 (2018)
DOI: 10.1051/0004-6361/201731831

Astronomy & Astrophysics

Solar-wind predictions for the Parker Solar Probe orbit

Near-Sun extrapolations derived from an empirical solar-wind model based on Helios and OMNI observations

M. S. Venzmer and V. Bothmer

University of Goettingen, Institute for Astrophysics, Friedrich-Hund-Platz 1, 37077 Göttingen, Germany

Received 25 August 2017 / Accepted 10 November 2017

ABSTRACT

Context. The Parker Solar Probe (PSP; formerly Solar Probe Plus) mission will be humanity's first in situ exploration of the solar corona with closest perihelia at 9.86 solar radii ($R_{\odot}$) distance to the Sun. It will help answer hitherto unresolved questions on the heating of the solar corona and the source and acceleration of the solar wind and solar energetic particles. The scope of this study is to model the solar-wind environment for PSP's unprecedented distances in its prime mission phase during the years 2018–2025. The study is performed within the Coronagraphic German And US SolarProbePlus Survey (CGAUSS) which is the German contribution to the PSP mission as part of the Wide-field Imager for Solar PRobe.

Aims. We present an empirical solar-wind model for the inner heliosphere which is derived from OMNI and Helios data. The German-US space probes Helios 1 and Helios 2 flew in the 1970s and observed solar wind in the ecliptic within heliocentric distances of 0.29–0.98 au. The OMNI database consists of multi-spacecraft intercalibrated in situ data obtained near 1 au over more than five solar cycles. The international sunspot number (SSN) and its predictions are used to derive dependencies of the major solar-wind parameters on solar activity and to forecast their properties for the PSP mission.

Methods. The frequency distributions for the solar-wind key parameters, magnetic field strength, proton velocity, density, and temperature, are represented by lognormal functions. In addition, we consider the velocity distribution's bi-componental shape, consisting of a slower and a faster part. Functional relations to solar activity are compiled with use of the OMNI data by correlating and fitting the frequency distributions with the SSN. Further, based on the combined data set from both Helios probes, the parameters' frequency distributions are fitted with respect to solar distance to obtain power law dependencies. Thus an empirical solar-wind model for the inner heliosphere confined to the ecliptic region is derived, accounting for solar activity and for solar distance through adequate shifts of the lognormal distributions. Finally, the inclusion of SSN predictions and the extrapolation down to PSP's perihelion region enables us to estimate the solar-wind environment for PSP's planned trajectory during its mission duration.

Results. The CGAUSS empirical solar-wind model for PSP yields dependencies on solar activity and solar distance for the solar-wind parameters' frequency distributions. The estimated solar-wind median values for PSP's first perihelion in 2018 at a solar distance of 0.16 au are 87 nT, 340 km s^{-1}, 214 cm^{-3}, and 503 000 K. The estimates for PSP's first closest perihelion, occurring in 2024 at 0.046 au (9.86 $R_{\odot}$), are 943 nT, 290 km s^{-1}, 2951 cm^{-3}, and 1 930 000 K. Since the modeled velocity and temperature values below approximately 20 $R_{\odot}$ appear overestimated in comparison with existing observations, this suggests that PSP will directly measure solar-wind acceleration and heating processes below 20 $R_{\odot}$ as planned.

Key words. solar wind – Sun: corona – Sun: heliosphere

1. Introduction

From observations of cometary tail fluctuations, Biermann (1951) inferred the presence of a continuous flow of particles from the Sun. With his theoretical solar-wind model, Parker (1958) formulated the existence of the solar wind even before the first satellites measured it in situ in 1959 (Gringauz et al. 1960; Neugebauer & Snyder 1966). The idea of a space mission flying through the solar corona dates back to the founding year of NASA in 1958 (McComas et al. 2008). Since then several space missions have measured the solar wind in situ at a wide range of heliocentric distances. In the case of Voyager 1, this was as far away as 140 au[1] in October 2017, having crossed the heliospause into interstellar space at a distance of 121 au (Gurnett et al. 2013). Various spacecraft have provided a wealth of solar-wind measurements near Earth's orbit, with WIND (Lepping et al. 1995; Ogilvie et al. 1995), SOHO (Domingo et al. 1995), ACE (Stone et al. 1998), and DSCOVR (Burt & Smith 2012) currently providing observations while orbiting around the L1 point 1.5 million km ahead of Earth in the sunward direction. Additional measurements at other solar distances were provided by planetary missions to Venus and Mercury, such as PVO (Colin 1980) or MESSENGER (Belcher et al. 1991). Ulysses was the first probe that orbited the Sun out of the ecliptic plane and thus could measure solar wind even at polar latitudes (McComas et al. 1998). The in situ solar-wind measurements closest to the Sun to date were made by the Helios missions. Helios 1, launched in 1974, reached distances of 0.31 au. Helios 2, launched two years later, approached the Sun as close as 0.29 au (Rosenbauer et al. 1977). The NASA Parker Solar Probe[2] (PSP), formerly Solar Probe Plus, six years after its planned launch date in mid 2018, will reach its closest perihelia at a distance of 9.86 solar radii ($R_{\odot}$), that is, 0.0459 au

[1] https://voyager.jpl.nasa.gov/

[2] http://parkersolarprobe.jhuapl.edu/

(Fox et al. 2016). This distance will be achieved through seven Venus gravity assists with orbital periods of 88–168 days. In its prime mission time 2018–2025 PSP provides 24 orbits with perihelia inside 0.25 au (Fox et al. 2016). Even its first perihelion, 93 days after launch in 2018, will take PSP to an unprecedented distance of 0.16 au (35.7 $R_\odot$). In comparison, the ESA Solar Orbiter mission with a planned launch in February 2019 will have its closest perihelia at 0.28 au (Müller et al. 2013).

The key PSP science objectives are to "trace the flow of energy that heats and accelerates the solar corona and solar wind, determine the structure and dynamics of the plasma and magnetic fields at the sources of the solar wind, and explore mechanisms that accelerate and transport energetic particles" as stated in Fox et al. (2016). To achieve these goals, PSP has four scientific instruments on board: FIELDS for the measurement of magnetic fields and AC/DC electric fields (Bale et al. 2016), SWEAP for the measurement of flux of electrons, protons, and alphas (Kasper et al. 2016), IS⊙IS for the measurement of solar energetic particles (SEPs; McComas et al. 2016) and WISPR for the measurement of coronal and inner heliospheric structures (Vourlidas et al. 2016).

The study presented in this paper is undertaken in the Coronagraphic German And US SolarProbePlus Survey (CGAUSS) project, which is the German contribution to the PSP mission as part of the Wide-field Imager for Solar PRobe (WISPR). WISPR will contribute to the PSP science goals by deriving the three-dimensional structure of the solar corona through which the in situ measurements are made to determine the sources of the solar wind. It will provide density power spectra over a wide range of structures (e.g., streamers, pseudostreamers and equatorial coronal holes) for determining the roles of turbulence, waves, and pressure-balanced structures in the solar wind. It will also measure the physical properties, such as speed and density jumps of SEP-producing shocks and their coronal mass ejection (CME) drivers as they evolve in the corona and inner heliosphere (Vourlidas et al. 2016). In order to help optimize the WISPR and PSP preplanning of the science operations, knowledge of the expected solar-wind environment is needed. For this purpose the solar-wind environment is extrapolated down to the closest perihelion of 9.86 $R_\odot$ distance to the Sun using in situ solar-wind data from the Helios probes and near 1 au data from various satellites compiled in the OMNI solar-wind database.

Generally, two types of solar wind are observed in the heliosphere – slow and fast streams (Neugebauer & Snyder 1966; Schwenn 1983). Slow solar wind has typical speeds of <400 km s^{-1} and fast solar wind has speeds >600 km s^{-1} (Schwenn 1990, p. 144). Their different compositions and characteristics indicate different sources and generation processes (McGregor et al. 2011b). Fast streams are found to originate from coronal holes as confirmed by Ulysses' out-of-ecliptic measurements (McComas et al. 1998). The source of slow wind, and its eventually different types (Schwenn 1983), is still a subject of controversial discussions because several scenarios are possible to explain its origin from closed magnetic structures in the solar corona, such as intermittent reconnection at the top of helmet streamers and from coronal hole boundaries (Kilpua et al. 2016). The occurrence frequency of these slow and fast streams varies strongly with solar activity and their interactions lead to phenomena such as stream interaction regions which may persist for many solar rotations ("co-rotating" interaction regions) if the coronal source regions are quasi-stationary (Balogh et al. 1999). Embedded in the slow and fast solar-wind streams are transient flows of CMEs – the faster ones driving shock waves ahead (Gosling et al. 1974). Their rate follows the solar activity cycle and varies in near 1 au measurements between only one CME every couple of days during solar cycle minima up to multiple CMEs observed over several days at times of solar maxima, that is, the CME-associated flow share of the solar wind raises from about 5% up to about 50% (Richardson & Cane 2012).

It is not known which specific solar-wind type or structure PSP will encounter at a given time during its mission, therefore we extrapolate the probability distributions of the major solar-wind parameters from existing solar-wind measurements and take solar cycle dependencies into account. As a baseline we describe the solar-wind environment through the key quantities of a magnetized plasma: magnetic field strength, density and temperature. Furthermore, the bulk flow velocity is the defining parameter of the two types of solar wind. Solar-wind quantities, like flux densities, mass flux, and plasma beta, can be directly derived from these four parameters. In the analyses, we treat the solar wind as a proton plasma – the average helium abundance is about 4.5% and in slow wind at solar cycle minimum is even less than 2% (Feldman et al. 1978; Schwenn 1983; Kasper et al. 2012).

Our approach is to obtain analytical representations of the shapes of the solar-wind parameter's frequency distributions in Sect. 2, of their solar activity dependence in Sect. 3 and of their solar distance scaling in Sect. 4. The solar-wind parameters' frequency distributions and solar activity dependence is derived from near-Earth solar wind and sunspot number (SSN) time series with a duration of almost five solar cycles. Their distance dependency is derived from Helios solar-wind measurements covering more than two thirds of the distance to the Sun and more than half a solar cycle. From a combination of the obtained frequency distributions, SSN dependence functions, and solar distance dependence functions, a general solar-wind model is built in Sect. 5, representing the solar activity and distance behavior. Finally, this empirical model is fed with SSN predictions and extrapolated to PSP's planned orbital positions in Sect. 6.

2. Frequency distributions of the solar-wind parameters

The solar-wind parameters are highly variable due to short-term variations from structures such as slow and fast wind streams, interaction regions, and CMEs, whose rate and properties depend on the phase of the solar activity cycle. Hence, for deriving characteristic frequency distributions for the solar-wind parameters, measurements over long-term time spans are needed. The abundance of the near-Earth hourly OMNI data set is ideally suited for this purpose, because to date it spans almost five solar cycles.

The OMNI 2 data set (King & Papitashvili 2005) combines solar-wind magnetic field and plasma data collected by various satellites since 1963, currently by WIND and by ACE. This intercalibrated multi-spacecraft data is time-shifted to the nose of the Earth's bow shock. The data is obtained from the OMNIWeb interface[3] at NASA's Space Physics Data Facility (SPDF), Goddard Space Flight Center (GSFC). In this study the whole hourly data until 31 December 2016 is used, starting from 27 November 1963 (for the temperature from 26 July 1965). The data coverage of the different parameters is in the range 67–74%, corresponding to a total duration of 36–40 yr. We note that a test-comparison of hourly averaged data with higher-time-resolution data for the available shorter time span 1981–2016 did not show significant differences in our results. According to the OMNI

[3] http://omniweb.gsfc.nasa.gov/

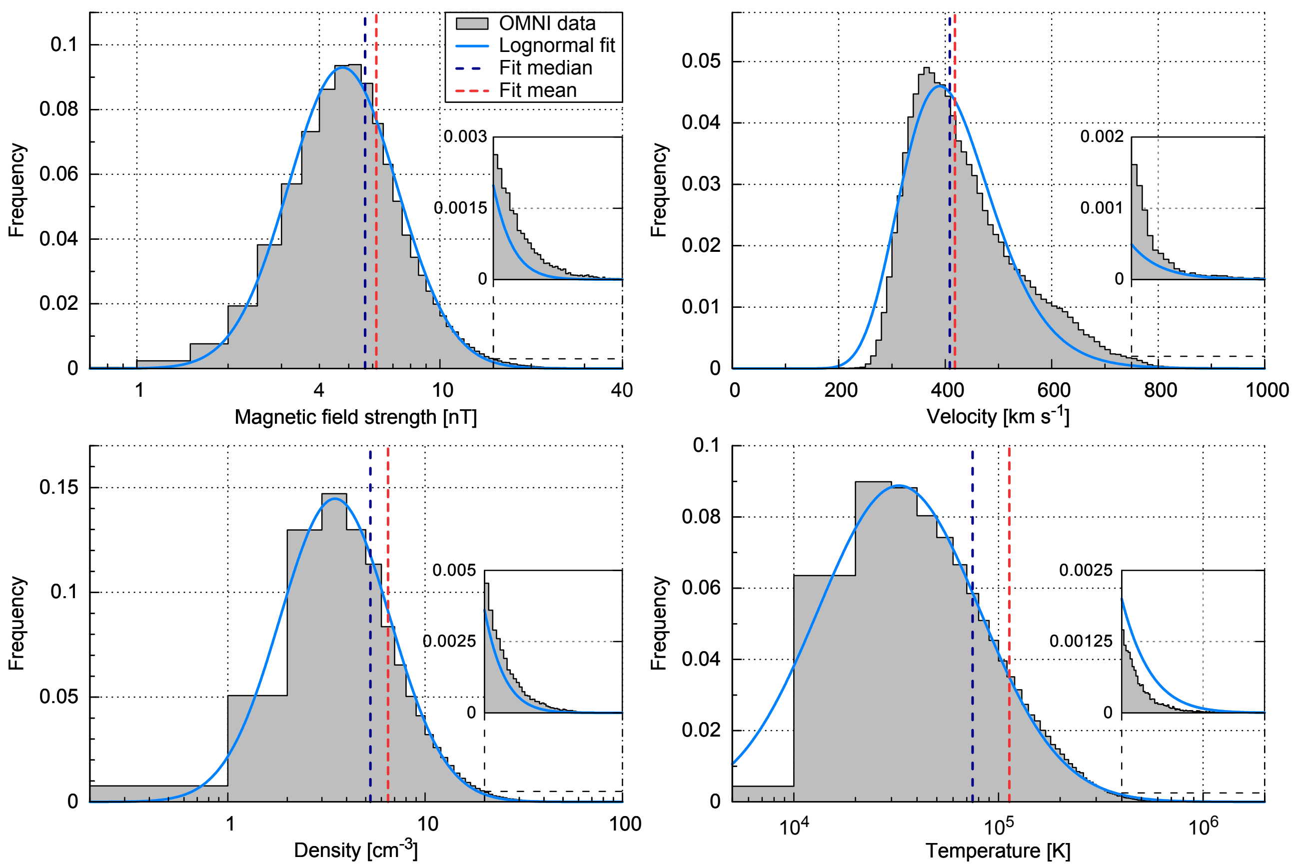

Fig. 1. Frequency distributions of the four solar-wind parameters and their lognormal fits derived from the hourly OMNI data set. The histograms have bins of 0.5 nT, $10\,\mathrm{km\,s^{-1}}$, $1\,\mathrm{cm^{-3}}$, and 10 000 K. The fits' median and mean values are indicated as well. The *insets* show zoomed-in views of the high-value tails of the distributions.

data precision and maximal parameter ranges we specify bin sizes of 0.5 nT for the magnetic field strength, $10\,\mathrm{km\,s^{-1}}$ for the velocity, $1\,\mathrm{cm^{-3}}$ for the density, and 10 000 K for the temperature. The frequency distributions of the solar-wind magnetic field strength, proton velocity, density and temperature are shown in Fig. 1. The solar-wind magnetic field strength is in the range 0.4–62 nT, the velocity in the range 156–1189 $\mathrm{km\,s^{-1}}$, the density in the range 0–117 $\mathrm{cm^{-3}}$, the temperature in the range 3450–6.63×10^6 K, and the mean data values are at 6.28 nT, 436 $\mathrm{km\,s^{-1}}$, 6.8 $\mathrm{cm^{-3}}$, and 1.05×10^5 K. These ranges and mean values are as statistically expected from previous analyses of near 1 au solar-wind data (e.g., Table 3.3 in Bothmer & Daglis 2007, p. 39). Much higher or lower peak values at 1 au have been observed in extraordinary events, such as the 23 July 2012 CME with a speed of over 2000 $\mathrm{km\,s^{-1}}$ and a peak field strength of about 100 nT that was observed by STEREO A (Russell et al. 2013), or the solar-wind disappearance event observed in May 1999 with density values even down to 0.2 $\mathrm{cm^{-3}}$ (Lazarus 2000).

The frequency distributions of the solar-wind parameters, magnetic field strength, proton density, and temperature, can be well approximated by lognormal distributions, whereas the proton velocity's frequency has a differing shape, as shown in Veselovsky et al. (2010). We investigate how well all four solar-wind parameters' frequency distributions can be represented by lognormal functions, which we use in the process of a least squares regression fitting. The lognormal function,

$$W(x) = \frac{1}{\sigma\sqrt{2\pi}x}\exp\left(-\frac{(\ln x-\mu)^2}{2\sigma^2}\right), \qquad (1)$$

depends on the location μ and the shape parameter σ. Changes in μ affect both the horizontal and vertical scaling of the function whereas σ influences its shape. The distribution's median x_{med} and mean x_{avg} (average) positions are easily interpreted and are directly calculated from μ and σ:

$$x_{\mathrm{med}} = \exp(\mu) \quad\Longleftrightarrow\quad \mu = \ln(x_{\mathrm{med}}), \qquad (2)$$

$$x_{\mathrm{avg}} = \exp\left(\mu+\frac{\sigma^2}{2}\right) \quad\Longleftrightarrow\quad \sigma = \sqrt{2\ln\left(\frac{x_{\mathrm{avg}}}{x_{\mathrm{med}}}\right)}. \qquad (3)$$

It is apparent that the mean is always larger than the median. Replacing the variables μ and σ with these relations, the lognormal function (1) becomes

$$W(x) = \frac{1}{2\sqrt{\pi\ln\left(\frac{x_{\mathrm{avg}}}{x_{\mathrm{med}}}\right)}\,x}\exp\left(-\frac{\ln^2\left(\frac{x}{x_{\mathrm{med}}}\right)}{4\ln\left(\frac{x_{\mathrm{avg}}}{x_{\mathrm{med}}}\right)}\right). \qquad (4)$$

The values of x_{med} and x_{avg} obtained from fitting the individual solar-wind frequency distributions are listed in Table 1.

From visual inspection, the resulting fit curves describe the shape of the magnetic field strength, the density and the temperature distributions well, as can be seen in Fig. 1. However, for the velocity, the fit function appears not to be as good in describing the measured distribution's more complex shape around its peak and in the higher velocity range. This also can be inferred from the sum of absolute residuals (SAR) between data and fit, listed in Table 1 as a percentage of the distribution area, being almost three times larger than those from the other parameters. In order to find a better fit result for the velocity distribution, we

Table 1. Resulting fit coefficients from the fitting of the lognormal function (4) to the shape of the solar-wind parameters' frequency distributions from near 1 au OMNI hourly data.

Parameter		Median x_{med}	Mean x_{avg}	Balance c	SAR [%]
Magnetic field [nT]		5.661(16)	6.164(18)	–	6.83
Velocity [10^2 km s^{-1}]		4.085(19)	4.183(20)	–	18.69
Density [cm^{-3}]		5.276(24)	6.484(34)	–	6.48
Temperature [10^4 K]		7.470(17)	11.301(32)	–	5.78
Velocity [10^2 km s^{-1}]	W_1	4.89(14)	5.00(14)	0.504(62)	–
	W_2	3.68(20)	3.72(20)		–
	W_{II}	4.16(14)^a	4.42(14)^a	–	4.20

Notes. For the velocity, the fit parameters of the double lognormal function (5) are also listed, as well as the median and mean values of the resulting velocity fit. The numbers in parentheses are the errors on the corresponding last digits of the quoted value. They are calculated from the estimated standard deviations of the fit parameters. For each parameter, the sum of absolute residuals between data and fit (in percentage of the distribution area) is also listed. [(a)] Error estimates derived from the individual fit part errors.

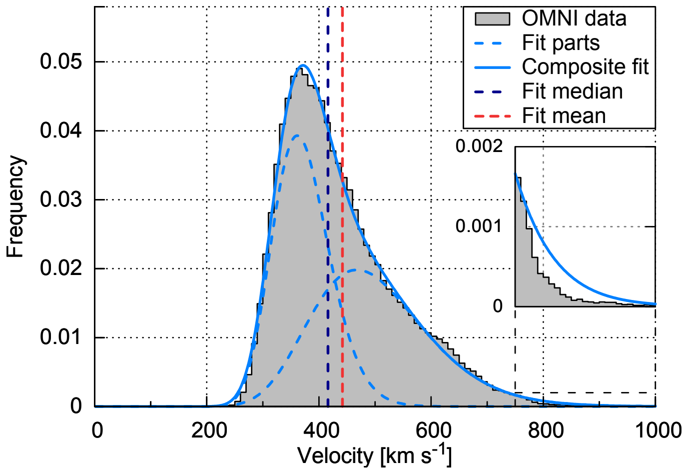

Fig. 2. Velocity frequency distribution (same as in Fig. 1) and its compositional lognormal fit. The fit's median and mean values and its two fit parts are indicated as well. The *inset* is a zoomed-in view of the high value tail of the distribution.

assume that the velocity distribution can be made up of at least two overlapping branches (McGregor et al. 2011a). Therefore a compositional approach is chosen by combining two lognormal functions (4), involving more fit variables:

$$W_{II}(x) = c \cdot W_1(x) + (1 - c) \cdot W_2(x). \quad (5)$$

The balancing parameter c ensures that the resulting function remains normalized as it represents a probability distribution. The fitting of $W_{II}(x)$ to the velocity's frequency distribution yields the values of the now five fit parameters (c, $x_{med,1}$, $x_{avg,1}$, $x_{med,2}$ and $x_{avg,2}$) as listed in Table 1 together with the median and mean values of the composed distribution, which can be derived by solving

$$\int W_{II}(x)\,dx = 0 \qquad \text{and} \qquad \int x\,W_{II}(x)\,dx = 0. \quad (6)$$

This more complex fit function is more accurate in describing the velocity's frequency distribution as shown in Fig. 2. Thus in the following Sections we keep the double lognormal ansatz for all velocity frequency fits.

For the bulk of the solar wind these static lognormal functions describe the parameters' distributions well. The abnormally high parameter values in the distribution functions can be attributed to shock/CME events in agreement with the results of the OMNI solar-wind investigations by Richardson & Cane (2012). The simple lognormal fit functions underestimate the frequencies in their high-value tails, except for the temperature's tail which is overestimated, as seen in the insets of Fig. 1. This appears to be because CMEs do not come with abnormally high temperatures, but rather with temperatures lower than those of the average solar wind (Forsyth et al. 2006). The velocity's compositional lognormal fit only slightly overestimates its tail as seen in the inset of Fig. 2. The slow and fast part contribute almost equally ($c \approx 0.5$) to the long-term velocity distribution function.

3. Solar activity dependence of the solar-wind frequency distributions

In the next step we investigate how the long-term solar-wind distribution functions presented in the previous section depend on general solar activity. Therefore we examine their correlation with the SSN, being a commonly used long-term solar activity index, and determine the time lags with the highest correlation coefficients.

For the correlations we fit lognormal functions to the frequency distributions as in Sect. 2, but implement linear relations to the yearly SSN, allowing shifting of the distribution functions with SSN. For the velocity the approach is different insofar as its two components are kept fixed and instead their balance is modified with the changing SSN. Thus we obtain solar-activity-dependent models for the frequency distributions of all four solar-wind parameters.

The international sunspot number (1963–2016) is provided by the online catalog[4] at the World Data Center – Sunspot Index and Long-term Solar Observations (WDC-SILSO), Solar Influences Data Analysis Center (SIDC), Royal Observatory of Belgium (ROB).

Yearly medians of the solar-wind parameters and the yearly SSN together with the solar cycle number are shown in the upper part of Fig. 3. The reason for correlating the SSN to the solar-wind median values is because the position of a lognormal function is defined by its median. The data are averaged to yearly values to avoid seasonal effects during the Earth's orbit around the Sun caused by its variations in solar latitude and distance. The solar-wind velocity, density, and temperature depend

[4] http://www.sidc.be/silso/

Table 2. Resulting fit coefficients from the OMNI data, based on the linear SSN dependencies (7) and (8).

Parameter		Median		Mean	Balance		SSN lag
		SSN factor a_{med}	baseline b_{med}	scaling factor a_{avg}	SSN factor c_a	baseline c_b	[years]
Magnetic field [nT]		$1.309(19) \times 10^{-2}$	4.285(17)	$8.786(78) \times 10^{-2}$	–	–	0
Density [cm^{-3}]		$3.81(25) \times 10^{-3}$	4.495(26)	$3.050(27) \times 10^{-1}$	–	–	6
Temperature [10^4 K]		$1.974(26) \times 10^{-2}$	5.729(19)	$6.541(28) \times 10^{-1}$	–	–	3
Velocity	W'_1	–	3.633(12)	$1.008(37) \times 10^{-2}$	-1.799(95)e-3	0.638(32)	3
[$10^2\ \text{km s}^{-1}$]	W'_2	–	4.831(81)	$2.31(20) \times 10^{-2}$			

Notes. For the velocity the fit parameters from the double lognormal fit (5) and their balancing function (9) are given. The numbers in parentheses are the errors on the corresponding last digits of the quoted value. They are calculated from the estimated standard deviations of the fit parameters. The listed SSN time lags are used for the fits.

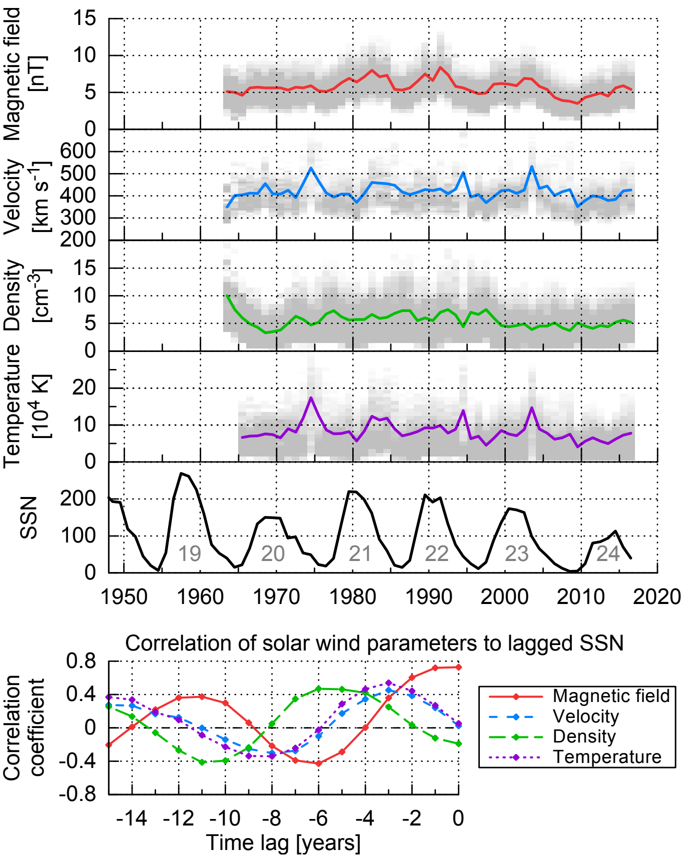

Fig. 3. Solar-wind parameter yearly frequencies (gray shading) with yearly medians (lines) derived from OMNI data and the yearly SSN from the SILSO World Data Center (1963–2016) with solar cycle number (*top*). Their correlation coefficients with the yearly SSN are calculated for time lags back to −15 yr (*bottom*).

on the state of the solar cycle (Schwenn 1983). For instance the fast solar wind occurs at times when polar coronal holes extend to lower latitudes, a typical feature of the declining phase of the solar cycle as pointed out by Bothmer & Daglis (2007, p. 75, Fig. 3.52). Therefore the solar-wind velocity, density, and temperature maxima exhibit time lags relative to the SSN maxima.

The correlation coefficients of the solar wind parameters with the yearly SSN shown in the bottom part of Fig. 3 are calculated for time lags back to −15 yr to cover a time span longer than a solar cycle. As expected, the amplitudes of the variations in the correlations of all parameters decline with increasing time lag and show a period of about 11 yr. The highest correlation coefficient of 0.728 to the SSN is found for the magnetic field strength; it has no time lag. This finding is anticipated because the SSN is found to be directly proportional to the evolution of the photospheric magnetic flux (Smith & Balogh 2003). Velocity and temperature show time lags of 3 yr with peak correlation coefficients of 0.453 and 0.540. The density with a correlation coefficient of 0.468 has a time lag of 6 yr, which is in agreement with the density anticorrelation to the SSN reported by Bougeret et al. (1984).

Next we create solar-activity-dependent analytical representations of the solar wind frequency distributions. This is achieved by shifting the median positions of the lognormal distributions as a linear function of the SSN. To enable these shifts, we add a linear SSN dependency to the median,

$$x_{\text{med}}(ssn) = a_{\text{med}} \cdot ssn + b_{\text{med}}, \tag{7}$$

using a factor to the SSN a_{med} with a baseline b_{med}. We relate the mean with a scaling factor to the median to transfer its SSN dependency:

$$x_{\text{avg}}(ssn) = \left(1 + a_{\text{avg}}\right) \cdot x_{\text{med}}(ssn). \tag{8}$$

These relations, substituted into the lognormal function (4), lead to a new SSN-dependent function $W'(x, ssn)$. This function is then fitted to the yearly data, using the yearly SSN as input parameter. The SSN is offset with the individual time lags determined before for each parameter, to benefit from the higher correlation. The values of the three resulting fit coefficients (a_{med}, b_{med}, and a_{avg}) are presented in Table 2.

Naturally, the fit models match with the general data trends, as can be seen from Fig. 4, though single year variations are not replicated by the model (e.g., the high velocity and temperature values in 1974, 1994, and 2003). The comparison of this model with the yearly data median values with respect to the lagged SSN shows that the medians obtained from the modeling have a similar slope, as shown in Fig. 5.

Again, the solar-wind velocity needs a special treatment because of the application of the double lognormal distribution (5). Since it is well known that slow and fast solar-wind stream occurrence rates follow the solar cycle, we keep the two velocity components' positions SSN-independent ($x_{\text{med}} = b_{\text{med}}$) and vary instead their balance with the SSN:

$$c(ssn) = c_a \cdot ssn + c_b. \tag{9}$$

The fit result (see Table 2) yields a model in which three years after solar cycle minimum (SSN of zero) the contribution of slow solar wind to the overall solar wind distribution reaches a maximum value (about 64%) and decreases with increasing SSN as shown in Fig. 6.

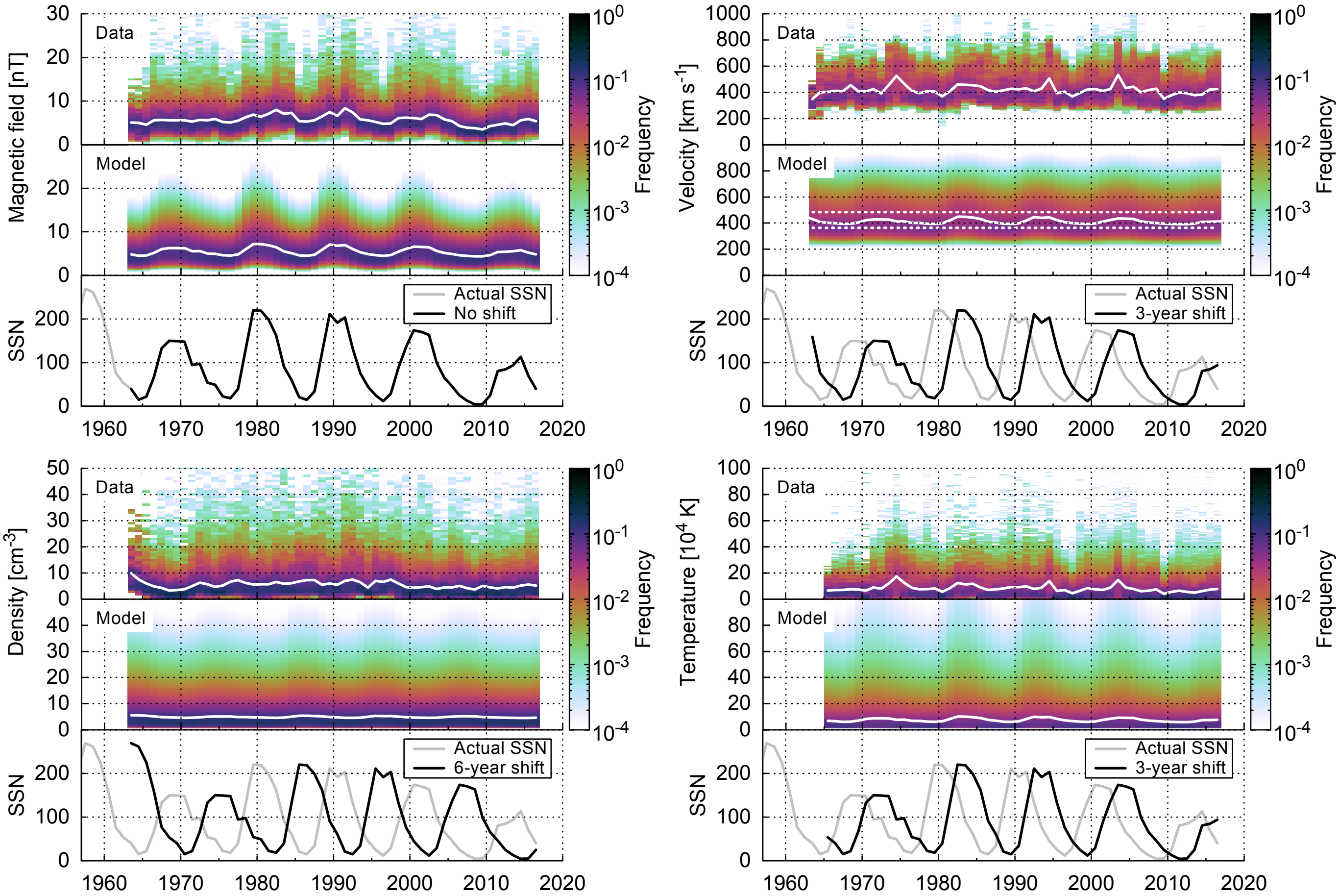

Fig. 4. Solar wind parameter yearly data frequencies and lognormal fit models, both with their median values (white lines) over the OMNI time period 1963–2016. The corresponding yearly SSN and the shifted SSN for the models are indicated by gray and black lines. The velocity median is derived from the SSN-weighted constant lognormal parts (dotted lines).

To investigate the amount of slow and fast wind contributions depending on solar activity, we apply the commonly used constant velocity threshold of $v_{\mathrm{th}} = 400\,\mathrm{km\,s^{-1}}$ (Schwenn 1990, p. 144). The linear fit to the yearly data ratio and the derived model ratio show a good agreement (see Fig. 6). The to-some-degree steeper balance parameter of the double fit function used in this model cannot be compared directly with specific velocity thresholds between slow and fast solar wind. However, it appears to be a more realistic approach than just taking a specific velocity threshold for the slow and fast wind, in agreement with the overlapping nature of the velocity flows reported by McGregor et al. (2011a).

4. Solar distance dependency

In order to derive heliocentric distance relationships of the bulk solar wind distribution functions, we apply and fit power law dependencies to the Helios data. We then examine how the fits may be extrapolated towards the Sun and in particular in to the PSP orbit. We use the fitting methods of Sect. 2 for the distance-binned combined data from both Helios probes. Helios' highly elliptical orbits in the ecliptic covered a solar distance range of 0.31–0.98 au in case of Helios 1 and 0.29–0.98 au in case of Helios 2. Launched during solar cycle minimum, the data of both probes cover the rise to the maximum of cycle 21, covering ~6.5 yr at varying distances to the Sun.

We investigate hourly averages of the Helios data in the same way as with the OMNI data. The Helios 1 merged hourly data from the magnetometer and plasma instruments (Rosenbauer et al. 1977) include ~12.5 orbits for the time range 10 December 1974 to 14 June 1981, and those for Helios 2 include ~8 orbits for the time span 1 January 1976 to 4 March 1980. The data are retrieved from the Coordinated Data Analysis Web (CDAWeb) interface at NASA's GSFC/SPDF[5].

The Helios 1 magnetometer data coverage for this data set is about 43% (i.e., 2.8 yr), and that of Helios 2 amounts to 54% (i.e., 2.3 yr). The plasma data coverage is 76% (i.e., 5.0 yr) in case of Helios 1 and 92% (i.e., 3.9 yr) in case of Helios 2. Thus, using this data, we point out that its time coverage is unequally distributed over the solar cycle. Considering the data gap distributions, the amount of data during solar cycle minimum up to mid 1977, that is, the transition from minimum to maximum, covers about 68% of this period whereas during maximum of cycle 21 data are available only 38% of the time. This Helios data bias towards solar minimum is one reason why in this study the Helios solar wind data are not used to derive long-term frequency distributions and solar-cycle dependencies for the key solar wind parameters.

The radial dependencies of the key solar-wind parameters over the distance range 0.29–0.98 au measured by both Helios probes are plotted in Fig. 7, together with their median and mean values for different solar distances, calculated for the minimal distance resolution 0.01 au of the data set. Assuming a radial solar-wind outflow, it is expected that the distance

[5] http://spdf.gsfc.nasa.gov/

Table 3. Fit coefficients for the median and mean solar distance dependencies (10) of the four solar wind parameters derived from the combined Helios 1 and 2 data.

Parameter	Median		Mean		Crossing distance [au]	Yearly variation Δe
	d_{med}	e_{med}	d_{avg}	e_{avg}		
Magnetic field [nT]	5.377(92)	−1.655(17)	6.05(10)	−1.546(18)	0.339(11)	0.11
Velocity [10^2 km s^{-1}]	4.107(28)	0.058(13)	4.356(24)	0.049(10)	$0.7(83) \times 10^3$	0.012
Density [cm^{-3}]	5.61(27)	−2.093(46)	7.57(30)	−2.010(38)	0.027(73)	0.072
Temperature [10^4 K]	7.14(23)	−0.913(39)	9.67(21)	−0.792(28)	0.082(85)	0.050

Notes. The numbers in parentheses are the errors on the corresponding last digits of the quoted value. They are calculated from the estimated standard deviations of the fit parameters. The crossing distances indicate where the median and mean fits intersect each other. The yearly variation is the weighted standard deviation derived from the yearly fit exponents seen in Fig. 9.

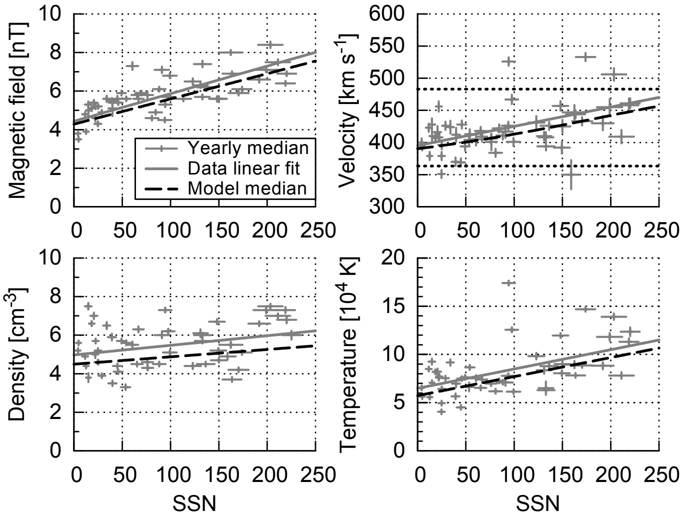

Fig. 5. Solar-wind parameter medians with respect to the lagged SSN. The yearly data medians (+) with their weighted linear fit (solid lines) are obtained from OMNI data. The error bars denote the SSN standard deviation and the relative weight from the yearly data coverage. The SSN-dependent median (dashed lines) is derived from the lognormal model fit. For the velocity the median is derived from the SSN-weighting (9) of the slow and fast model parts (dotted lines), whose magnitudes are SSN independent.

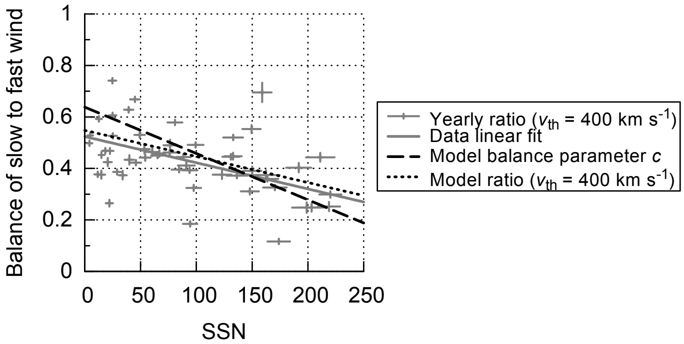

Fig. 6. Ratio of slow to fast solar wind for a SSN lagged by 3 yr. The yearly ratios (+) and their weighted linear fit (solid line) are obtained from OMNI data with a threshold velocity of $v_{\mathrm{th}} = 400$ km s^{-1}. The error bars denote the SSN standard deviation and the relative weight from the yearly data coverage. The model's balance parameter (9) and derived ratio (same threshold) are plotted as dashed and dotted lines.

dependence of the solar-wind parameters over the Helios data range 0.29–0.98 au can be described through power law scaling. Therefore we use the power law function,

$$x(r) = d \cdot r^{e}, \tag{10}$$

for the regression fit of the median and mean, with r being the solar distance in astronomical units, d the magnitude at 1 au, and e the exponent. The fits are weighted through the different data counts per bin. The obtained coefficients for the median and mean power law fits (d_{med}, e_{med}, d_{avg}, and e_{avg}) are listed in Table 3 and their corresponding curves are shown in Fig. 7.

Our derived exponents agree with those found in existing studies from the Helios observations: Mariani et al. (1978) derived the exponents for the magnetic field strength separately for the fast and slow solar wind as $B_{\mathrm{fast}} \propto r^{-1.54}$ and $B_{\mathrm{slow}} \propto r^{-1.61}$, ours is $B_{\mathrm{avg}} \propto r^{-1.55}$. The velocity exponent $v_{\mathrm{avg}} \propto r^{0.049}$ matches with the values found by Schwenn (1983, 1990), who derived the distance dependencies for both Helios spacecraft separately as $v_{\mathrm{H1}} \propto r^{0.083}$ and $v_{\mathrm{H2}} \propto r^{0.036}$. The calculated density exponent $n_{\mathrm{avg}} \propto r^{-2.01}$ agrees well with the Helios plasma density model derived by Bougeret et al. (1984) yielding $n \propto r^{-2.10}$. The temperature exponent $T_{\mathrm{avg}} \propto r^{-0.79}$ is similar to those in the studies by Hellinger et al. (2011, 2013), who also derived the exponents separately for the fast and the slow solar wind: $T_{\mathrm{fast}} \propto r^{-0.74}$ and $T_{\mathrm{slow}} \propto r^{-0.58}$.

The mean and median velocity fit exponents acquired from the Helios data are very similar, which indicates that they can be kept identical so that the basic shape of the frequency distribution does not change with distance. Conversely, the mean and median fits for the magnetic field strength cross each other at 0.339 au (see Table 3) and the mean becomes slightly lower than the median at smaller distances. Thus, below that distance the frequency distribution can no longer be well described by a lognormal function, because the mean of a lognormal function has to be larger than its median (as pointed out in Sect. 2), that is, the location of the crossing indicates that the parameter's distribution is no longer of a lognormal shape thereafter. The fits for the proton temperature show a similar behavior, having an extrapolated intersection at 0.082 au. Therefore the extrapolation of the magnetic field and temperature distribution frequencies to the PSP orbit by applying lognormal functions is limited. The crossing points limit the regions where the distribution's shapes can still be considered lognormal.

In order to still fit and extrapolate lognormal functions with the data, we assume that the shapes can be considered lognormal at all distances. For the frequency distribution fit function to be discussed in the following paragraph, we reduce the fit exponents e_{med} and e_{avg} to only one. We note that this simplification leads to slightly larger modeling errors, especially in case of the magnetic field strength.

Next we retrieve the frequency distributions of the four solar wind parameters in solar distance bins of 0.01 au, choosing the

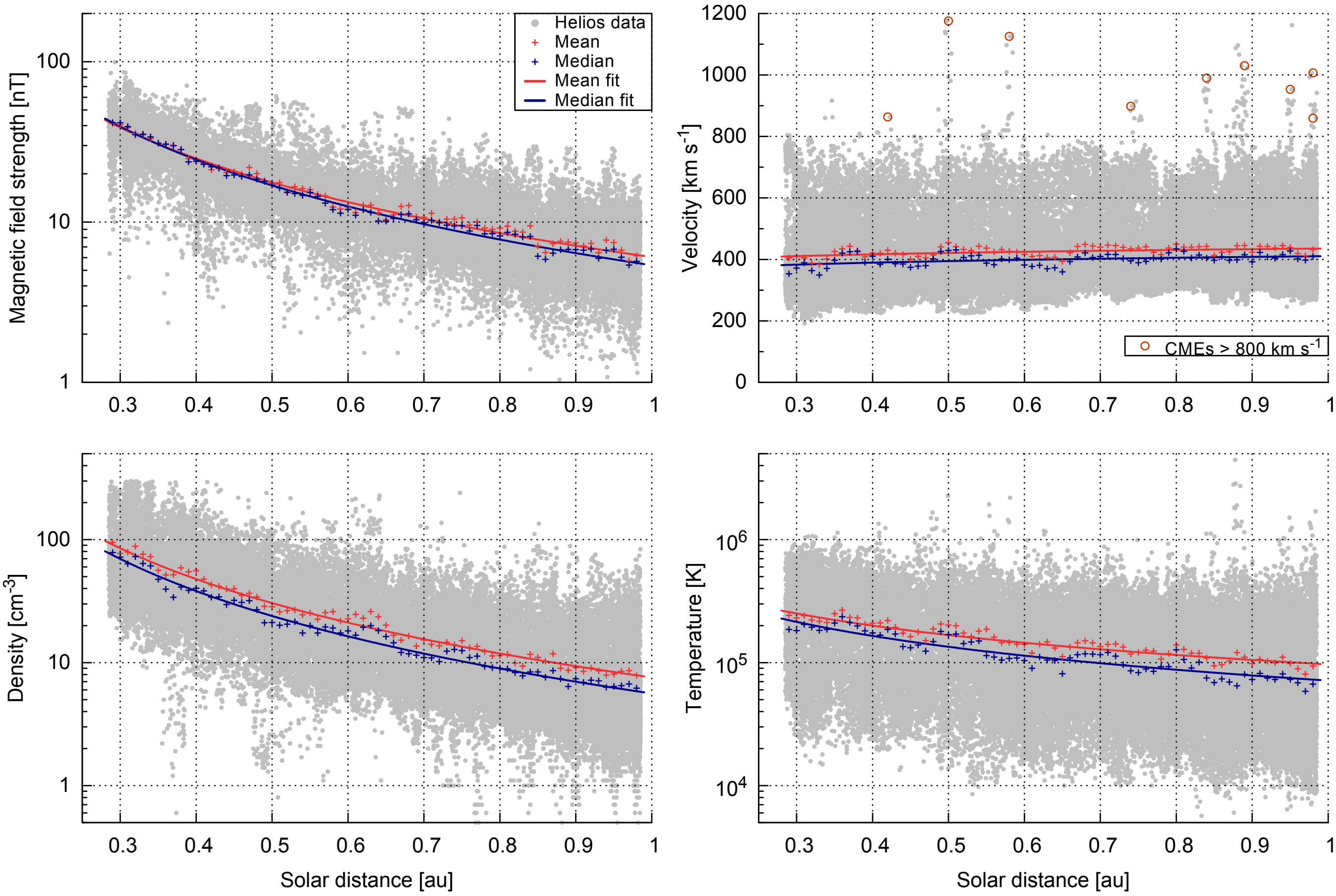

Fig. 7. Helios hourly data plots of the four solar wind parameters over solar distance. The mean and median per 0.01 au data bin and their fit curves are plotted as well. The Helios data has a native distance resolution of 0.01 au, thus, to make the distribution visible in these plots, we added a random distance value of up to ±0.005 au. The high velocity data points above 800 km s^{-1} (circled red) are identified as CME events (e.g., Sheeley et al. 1985; Bothmer & Schwenn 1996, 1998).

Table 4. Fit coefficients for the distance-dependent single lognormal function, based on Eq. (4) combined with (10) from the combined Helios data.

Parameter		Median d'_{med}	Mean d'_{avg}	Exponent e'	Balance c'	Seasonal variation Δd [%]
Magnetic field [nT]		5.358(25)	5.705(28)	−1.662(11)	–	2.8
Density [cm^{-3}]		5.424(33)	6.845(47)	−2.114(20)	–	3.6
Temperature [10^4 K]		6.357(64)	10.72(14)	−1.100(20)	–	1.9
Velocity [10^2 km s^{-1}]	W''_1	3.707(13)	3.748(16)	0.0990(51)	0.557(45)	0.17
	W''_2	5.26(13)	5.42(11)			
	W''_{II}	4.13(13)^{a}	4.47(11)^{a}	–	–	–

Notes. Regarding the velocity, the double lognormal function (5) is used instead. The numbers in parentheses are the errors on the corresponding last digits of the quoted value. They are calculated from the estimated standard deviations of the fit parameters. The seasonal variations are calculated from Earth's orbital solar distance variation and the derived exponents. [(a)] Velocity median and mean 1 au values for the resulting function. Error estimates derived from the individual fit part errors.

same resolution as for the OMNI data analyzed in Sect. 2 – the distributions and their median values are plotted in Fig. 8. For simplification, as mentioned before, we treat the exponents of the median and mean fit functions as being identical, using one fit parameter for both. Implementing the power law distance dependency (10) into the lognormal function (4), we get the fit parameters d'_{med}, d'_{avg} and the common exponent e'. Again, we use the double lognormal function (5) for the velocity distribution fit – resulting in $W''_{\text{II}}(x,r)$. The additional fit parameters are the balancing parameter c' and for the second lognormal part $d'_{\text{med},2}$ and $d'_{\text{avg},2}$. The resulting fit coefficients for the four solar wind parameters are presented in Table 4.

The velocity balancing parameter $c' = 0.557$ is in good agreement with the results for the SSN dependency (9), because with a mean SSN of 59 during the Helios time period, $c(59) = 0.53$, as can be seen from Fig. 6.

The power law lognormal models and the power law double lognormal model for the velocity, which result from the fitting, are plotted in Fig. 8 together with their median values. The model's magnetic field strength is broader around values

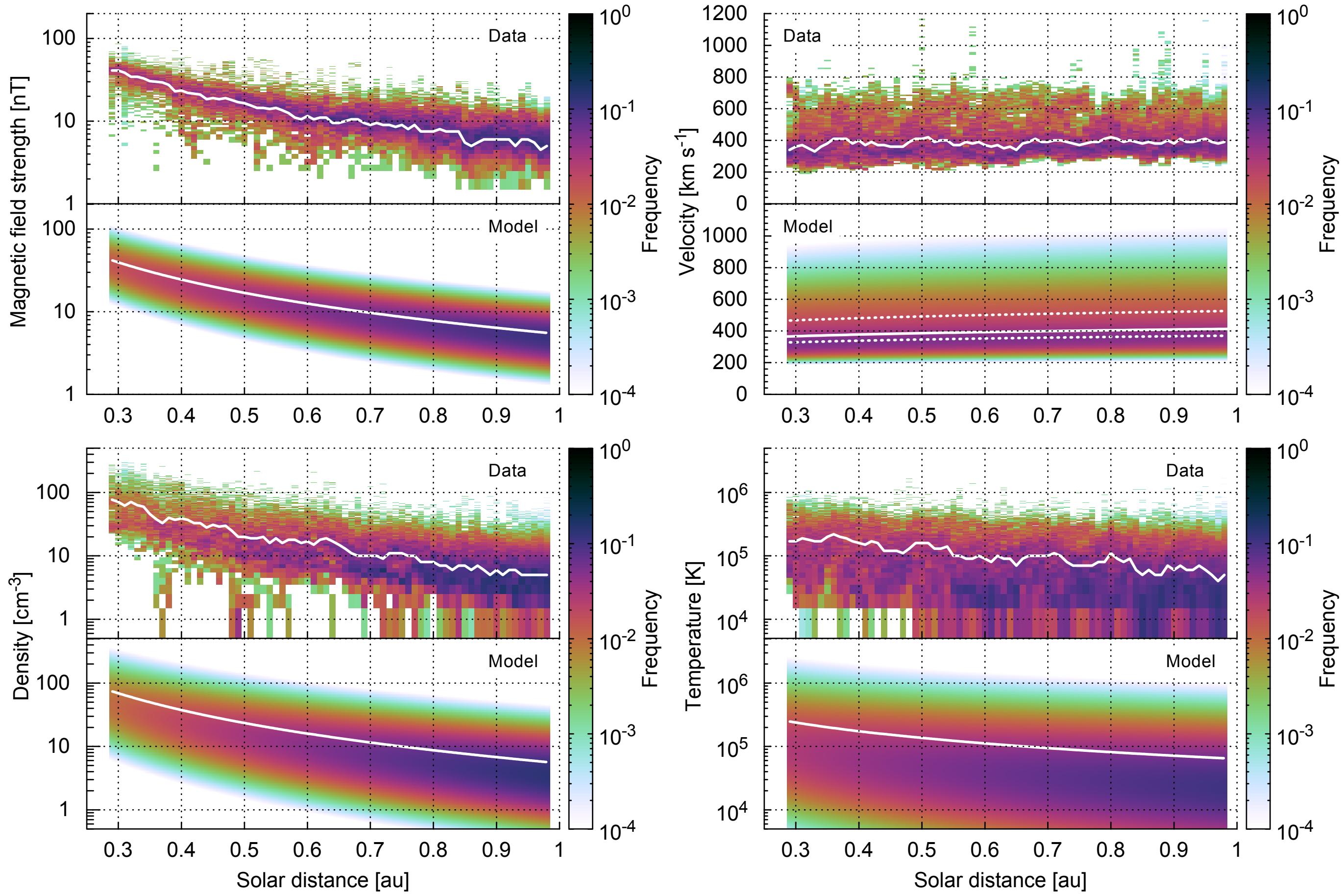

Fig. 8. Frequency distributions of the four solar-wind parameters with respect to solar distance. Plotted are the binned Helios data and the power law lognormal fit models with their median values (white lines). The double lognormal model is used for the velocity, its slow and fast parts are indicated by dotted lines.

of 40 nT at the lower distance boundary than the data's frequency distribution implies. This behavior is expected because of the applied distance-independent shape approximation. The velocity and temperature models' upper values generally show a higher abundance than the actual data; see also zoom boxes in Figs. 1 and 2. The high-velocity tail that increases with distance arises from using the same exponent for both slow and fast components. This effect is not seen in the data; more specifically, not only the slowest wind but also the fastest wind is expected to converge to more average speeds (Sanchez-Diaz et al. 2016).

5. Empirical solar-wind model

In order to estimate the solar-wind environment for the PSP orbit, we combine the results from the solar-wind frequency distributions' solar-activity relationships and their distance dependencies derived from the OMNI and Helios data. The result is an empirical solar-wind model for the inner heliosphere which is then extrapolated to the PSP orbit in Sect. 6.

This solar-wind model for the radial distance dependence is representative for the time of the Helios observations around the rise of solar cycle 21. The variations of the yearly power law fit exponents from fitting the solar-distance dependency (10) are shown in Fig. 9 together with the yearly SSN for the time period 1974–1982. It can be seen that during the Helios time period there might be some systematic variation of the exponents with solar activity – at least for the velocity and temperature

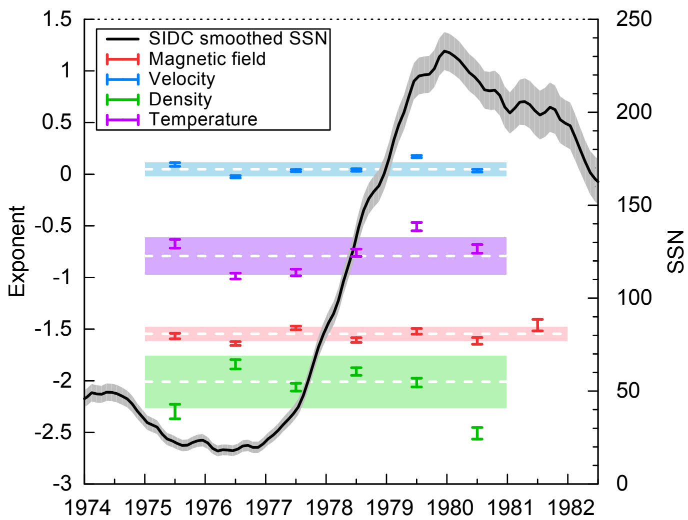

Fig. 9. Helios yearly variation of the solar-wind parameter power exponents for the dependence on radial distance together with the SIDC 13-month smoothed monthly SSN. The weighted standard deviations and average values for all years are indicated by the shaded areas. In this plot, the 21 days since Helios launch in the year 1974 are omitted because a distance range of merely 0.95–0.98 au was covered that year.

exponents. However, for simplicity we assume that the distance scaling laws can be treated as time independent and include the calculated exponents' yearly variations Δe, summarized in Table 3, as relative uncertainties.

Since we neglect possible variations of the distance scaling laws, we combine the frequency distribution's median solar activity dependency (7) derived for 1 au from the OMNI data with the power law exponents (10) derived from the Helios data:

$$x_{\mathrm{med}}(ssn, r) = (a_{\mathrm{med}} \cdot ssn + b_{\mathrm{med}}) \cdot r^{e'}. \tag{11}$$

Thus, implementing the median and mean relations into the lognormal function (4), we obtain the combined model function $W'''(x, ssn, r)$ and for the velocity $W_{\mathrm{II}}'''(x, ssn, r)$ with the double lognormal function (5). The corresponding median and mean relations for each solar-wind parameter, based on the values resulting from our analyses, are listed below. Their numerical values are the fit parameters from Table 2 and the exponents from Table 4.

– The magnetic field strength relations, depending on solar activity and solar distance, are:

$$B_{\mathrm{med}}(ssn, r) = (0.0131\,\mathrm{nT} \cdot ssn + 4.29\,\mathrm{nT}) \cdot r^{-1.66}, \tag{12}$$

$$B_{\mathrm{avg}}(ssn, r) = 1.0879 \cdot B_{\mathrm{med}}(ssn, r). \tag{13}$$

– The proton velocity relations for the slow and fast components, depending on solar distance, are:

$$v_{\mathrm{med}}^{\mathrm{slow}}(r) = 363\,\mathrm{km\,s^{-1}} \cdot r^{0.099}, \quad v_{\mathrm{med}}^{\mathrm{fast}}(r) = 483\,\mathrm{km\,s^{-1}} \cdot r^{0.099}, \tag{14}$$

$$v_{\mathrm{avg}}^{\mathrm{slow}}(r) = 1.0101 \cdot v_{\mathrm{med}}^{\mathrm{slow}}(r), \quad v_{\mathrm{avg}}^{\mathrm{fast}}(r) = 1.023 \cdot v_{\mathrm{med}}^{\mathrm{fast}}(r). \tag{15}$$

The share of both components balanced with solar activity is found to be:

$$c(ssn) = -0.00180 \cdot ssn + 0.64. \tag{16}$$

– The derived relations of the proton density are:

$$n_{\mathrm{med}}(ssn, r) = \left(0.0038\,\mathrm{cm^{-3}} \cdot ssn + 4.50\,\mathrm{cm^{-3}}\right) \cdot r^{-2.11}, \tag{17}$$

$$n_{\mathrm{avg}}(ssn, r) = 1.305 \cdot n_{\mathrm{med}}(ssn, r). \tag{18}$$

– The derived proton temperature relations are:

$$T_{\mathrm{med}}(ssn, r) = (197\,\mathrm{K} \cdot ssn + 57\,300\,\mathrm{K}) \cdot r^{-1.10}, \tag{19}$$

$$T_{\mathrm{avg}}(ssn, r) = 1.654 \cdot T_{\mathrm{med}}(ssn, r). \tag{20}$$

These relations average over seasonal variations because they are based on yearly data. The OMNI data are time-shifted to the nose of the Earth's bow shock; this leads to yearly solar distance variations of ±1.67% as it orbits the Sun. The resulting maximal solar-wind parameter variation amplitudes over the year can thus be derived from the derived power law exponents. They are estimated to be smaller than 4% as seen in Table 4. Bruno et al. (1986) and Balogh et al. (1999) have pointed out that the solar-wind parameters vary with latitudinal separation from the heliospheric current sheet. Its position in heliographic latitude is highly variable around the solar equator (Schwenn 1990) and, furthermore, the Earth's orbit varies over the course of the year by ±7.2° in latitude. Since this latitudinal separation is highly variable and requires significant effort to calculate for an extended time series, we have ignored this aspect in this analysis.

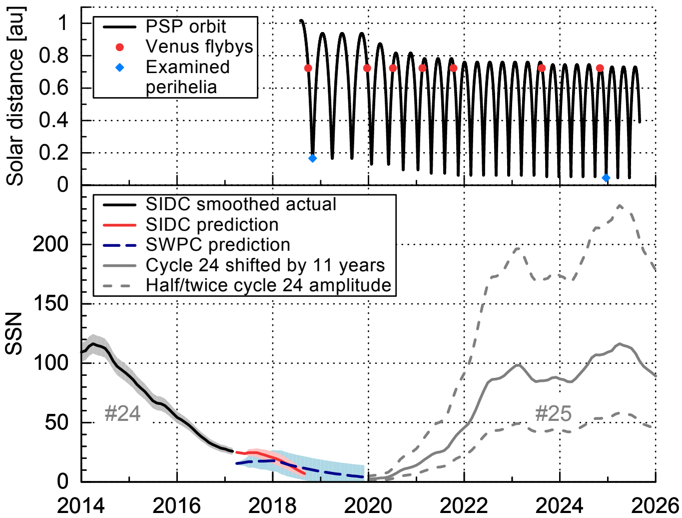

Fig. 10. PSP's solar distance during its mission time (*top*). Consecutive Venus flybys bring its perihelia nearer to the Sun. Actual and predicted SSN (*bottom*), that is, SIDC 13-month smoothed monthly actual SSN, SIDC Standard Curves Kalman filter prediction and SWPC prediction with their corresponding expected ranges (shaded areas). The SSN from previous cycle 24, shifted by 11 yr, is plotted together with two alternative trends of half and twice its amplitude.

6. Model extrapolation to PSP orbit

To estimate PSP's solar-wind environment during its mission time for its orbital positions, predictions of the SSN during the mission are incorporated into the empirical solar-wind model, derived in the previous sections, and extrapolations down to the PSP perihelion region are performed.

PSP is planned to launch in mid 2018. With its first Venus flyby it will swing into Venus' orbital plane, reaching a first perihelion with a distance of 0.16 au just 93 days after launch, in November 2018. Seven additional Venus flybys allow the perihelion distance to be reduced to a minimum of 9.86 $R_{\odot}$. This distance will be reached with the 22nd perihelion in December 2024 (Fox et al. 2016), as plotted in the top panel of Fig. 10.

We extrapolate the derived empirical solar-wind models to PSP's orbital distance range and compare the results with those from the existing models shown in Fig. 11. The model and its extrapolation are visualized for the SSN range between solar minimum and maximum ($0 \leq ssn \leq 200$), indicated by the shaded regions in the figure. The magnetic field strength is found to increase from median values of about 43 nT at 0.25 au to 715 nT at 0.046 au for a SSN of zero. Taking a SSN of 200 increases the values to 69 nT and 1152 nT. Our extrapolation results are slightly flatter than those derived from the analytical magnetic field model by Banaszkiewicz et al. (1998), who constructed an analytic dipole plus quadrupole plus current sheet (DQCS) model for solar minimum. We note that one cannot easily compare the absolute values of our study with the values obtained by Banaszkiewicz et al. (1998) because the DQCS model assumes solar wind originating from coronal holes at higher heliographic latitudes only, neglecting the slow solar-wind belt. We suggest that the difference in slope is due to the previously mentioned (Sect. 4) changing shape of the frequency distribution with heliocentric distance, which for smaller distances deviates more from the model's lognormal distribution. The average velocity is found to decrease from 340 $\mathrm{km\,s^{-1}}$ at 0.25 au to about 290 $\mathrm{km\,s^{-1}}$ at 0.046 au 3 yr after a SSN of zero occurred, whereas using a SSN of 200 it decreases from 390 $\mathrm{km\,s^{-1}}$

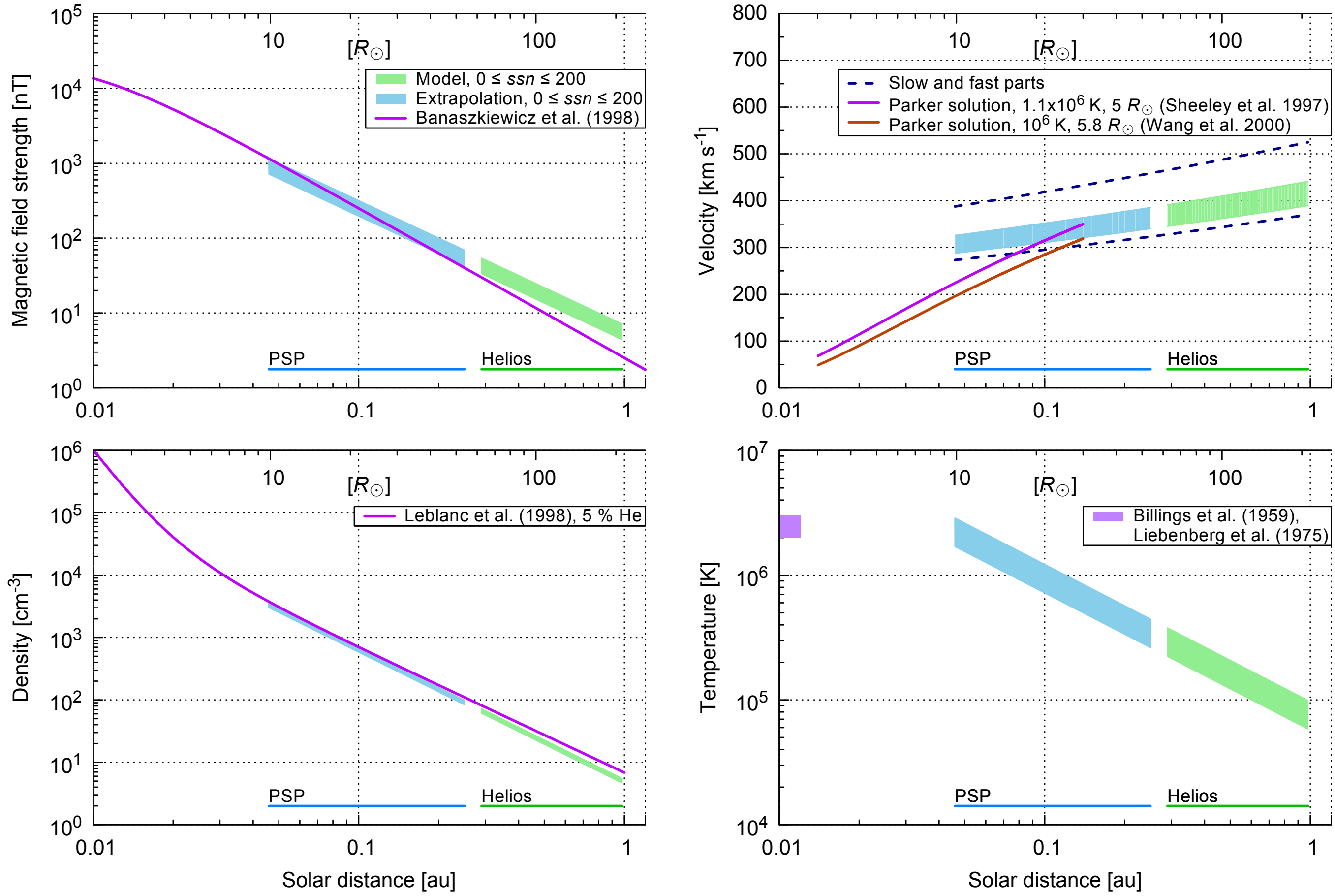

Fig. 11. Radial extrapolation of the solar-wind parameters to the PSP orbit region. The median values from the models, obtained from Helios and OMNI measurements, are extrapolated to the PSP region for SSN values between solar minimum and maximum, that is, $0 \leq ssn \leq 200$. The lower edges of the shaded areas correspond to solar minimum, the upper edges to solar maximum. Also plotted are the radial dependencies of the analytic DQCS magnetic field model for solar minimum from Banaszkiewicz et al. (1998), the slow wind velocity models from Sheeley et al. (1997) and Wang et al. (2000), the density model from Leblanc et al. (1998) and the range of temperature measurements from Billings (1959) and Liebenberg et al. (1975).

to 330 km s^{-1}. Comparing the results with the measurements by Sheeley et al. (1997) and Wang et al. (2000) shows an overestimation in our extrapolated slow solar-wind velocity values for distances below approximately 20 $R_\odot$. They used LASCO coronagraph observations to track moving coronal features (blobs) in the distance range 2–30 $R_\odot$ to determine speed profiles and sources of the slow solar wind and they derived temperature and sonic point values for slow solar wind with the isothermal expansion model from Parker (1958). Therefore, it generally can be expected that PSP will encounter a slower solar-wind environment close to the Sun than our model estimates. Thus PSP will measure solar-wind acceleration processes (McComas et al. 2008), maybe even still at 30 $R_\odot$ as the study by Sheeley et al. (1997) suggests. The proton density increases from about 84 cm^{-3} at 0.25 au to about 3018 cm^{-3} at 0.046 au 6 yr after a SSN of zero occurred. Being almost independent of the SSN, the values for a SSN of 200 are only 17% larger. The results are in good agreement with those of Leblanc et al. (1998), who derived an electron density model from type III radio burst observations. Their model shows that the density distance dependency scales with r^{-2} and steepens just below 10 $R_\odot$ with r^{-6}. We assumed a solar-wind helium abundance of 5% to convert these electron densities to proton densities. The extrapolated proton temperature increases from about 260 000 K at 0.25 au to about 1 690 000 K at 0.046 au 3 yr after a SSN of zero occurred and from 440 000 K to 2 860 000 K for a SSN of 200. Knowing that near-Sun coronal temperatures are in the range of 2–3 MK (Billings 1959; Liebenberg et al. 1975), the model overestimates the extrapolated temperatures at the PSP perihelion distance.

Aside from the solar distance, the derived solar-wind parameter models depend on the SSN. Short-term predictions of the SSN can be used for the solar-wind predictions of PSP's early perihelia and also for refining the solar-wind predictions during PSP's mission. Several sources are available for SSN short-term predictions. The SIDC provides 12-month SSN forecasts[6] obtained from different methods (e.g., Kalman filter Standard Curve method). The SSN prediction of NOAA's Space Weather Prediction Center (SWPC) for the time period until the end of 2019 follows a consensus of the Solar Cycle 24 Prediction Panel[7]. The SSN for PSP's first perihelion will be small – certainly below 20 – whereas the SSN during the closest perihelia, which will commence at the end of 2024 at the likely maximum phase of cycle 25, cannot be predicted at this time. However, Hathaway & Upton (2016) found indications that the next solar cycle will be similar in size to the current cycle 24. Therefore we simply assume a pattern similar to the last cycle for the prediction of the next solar cycle and thus shift the last cycle by 11 yr. Additionally, we consider as possible alternatives

6 http://sidc.be/silso/forecasts
7 http://www.swpc.noaa.gov/products/solar-cycle-progression

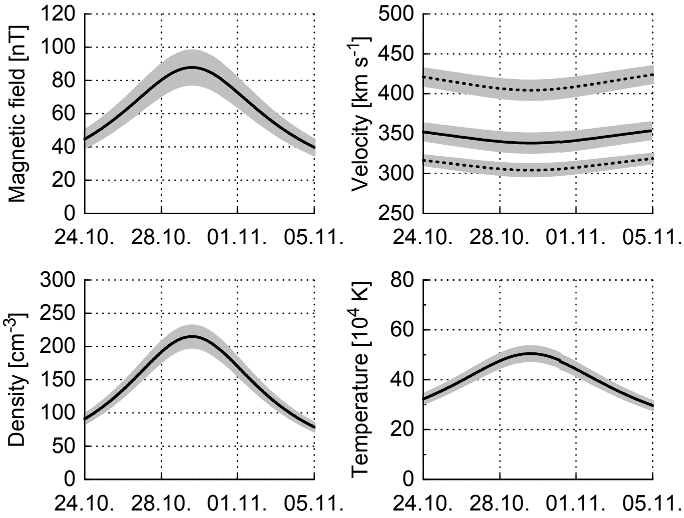

Fig. 12. Estimated solar-wind parameter medians (black lines) and their error bands (gray) during 12 days in 2018 with PSP's first perihelion at about 0.16 au. For the velocity the combined median is calculated and also the SSN-independent slow and fast parts are plotted (dotted lines).

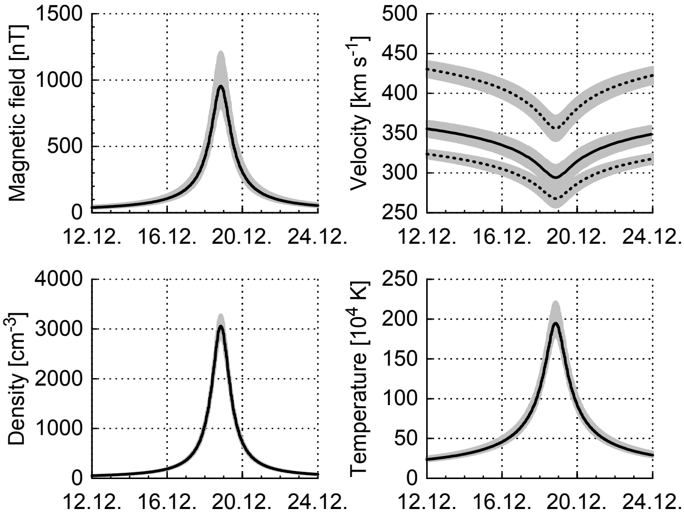

Fig. 13. Estimated solar-wind parameter medians (black lines) and their error bands (gray) during 12 days in 2024 with PSP's 22nd (the first closest) perihelion at 0.0459 au. For the velocity the combined median is calculated and also the SSN-independent slow and fast parts are plotted (dotted lines).

SSN patterns of half and twice its amplitude as shown in the bottom panel of Fig. 10.

Implementing the SSN predictions for the PSP mission time and the orbital trajectory data, we can infer which solar-wind parameter magnitudes can be expected. Figures 12 and 13 show the median values (7) of the considered different solar-wind parameters for 12-day periods, comprising the first perihelion in Novemver 2018 and the first closest perihelion in December 2024. In the beginning of the mission median values of about 87 nT, 340 km s^{-1}, 214 cm^{-3}, and 503 000 K are estimated to be measured at 0.16 au, increasing to about 943 nT, 290 km s^{-1}, 2951 cm^{-3}, and 1 930 000 K during the first closest approach at 0.046 au. Monthly SSNs – shifted by the time lags specific to the solar-wind parameters – are used in the calculation of the solar-wind predictions. These SSNs are either actual smoothed values from the SIDC with their reported standard deviations, short-term predictions from the SWPC with

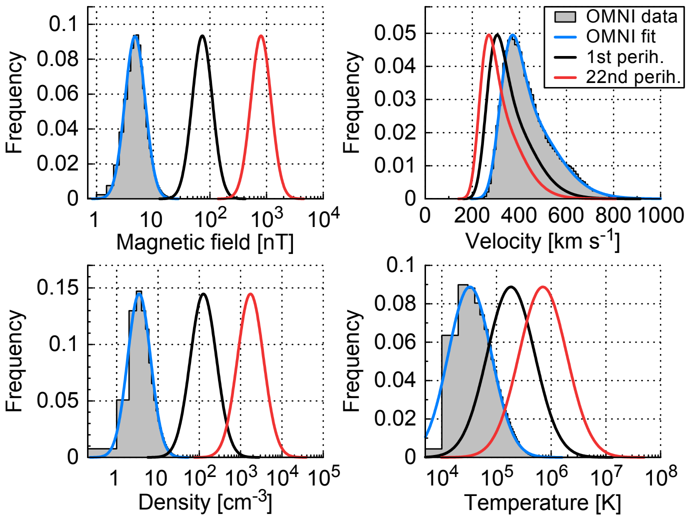

Fig. 14. Frequency distributions of the four solar-wind parameters (same as in Figs. 1 and 2) and those estimated with the solar-wind model for PSP's 1st and 22nd (first closest) perihelion. In these figures the frequencies of both extrapolated curves are scaled for visibility to the same height as the 1 au distribution.

their expected ranges, or actual smoothed values from the SIDC shifted by 11 yr with half/twice their values as uncertainties. The error bands given in both figures, calculated from error propagation, include these SSN ranges and the derived fit parameter errors.

Finally the estimated solar-wind environment can be derived from the function $W'''(x, ssn, r)$. The estimated frequency distributions of the four solar-wind parameters at PSP's 1st and 22nd (first closest) perihelion are plotted in Fig. 14. Again, we point out that the velocity and temperature distributions for the 22nd perihelion are only upper limits and the actual values to be encountered by PSP are expected to be smaller.

7. Discussion and summary

The scientific objective of this study, being part of the CGAUSS project – the German contribution to the WISPR instrument – is to model the solar-wind environment for the PSP mission to be launched mid 2018. For this purpose we started the development of the empirical solar-wind environment model for the near-ecliptic PSP orbit. We derived lognormal representations of the in situ near-Earth solar-wind data collected in the OMNI database, using the frequency distributions of the key solar-wind parameters, magnetic field strength, proton velocity, density, and temperature. Throughout the different analyses in our study, the velocity's frequency distribution is treated as a composition of a slow and a fast wind distribution. Each velocity part is fitted with a lognormal function, which allows for the overlap of both velocity ranges. The OMNI multi-spacecraft solar-wind data is intercalibrated and covers almost five solar cycles. It thus represents solar wind gathered at different phases of solar activity in the ecliptic plane. In the next step we investigated the yearly variation of the solar-wind distribution functions along with the SSN over 53 yr and derived linear dependencies of the solar-wind parameters with the SSN. The radial dependencies of the solar-wind distribution functions were then analyzed, using Helios 1 and 2 data for the distance range 0.29–0.98 au in bins of 0.01 au, deriving power law fit functions that were used to scale the previously calculated SSN-dependent 1 au distribution fit functions to the PSP orbit, taking into account SSN predictions for the years 2018–2025, encompassing the prime mission up to the closest approach of 9.86 $R_\odot$. The reason for performing the analysis this way is based on the fact that the OMNI solar-wind database is much larger than the Helios database.

For determining solar-activity- and solar-distance-dependent relations for the median and mean solar-wind values, we could have used the simpler approach of combining the radial dependence of averaged Helios data with averaged 1 au OMNI data scaled with the SSN. It is expected that the results of a simpler analysis would have similar distance scaling results, as can be inferred from the exponents in Tables 3 and 4. However, in our study we are not only interested in averages but rather in bulk distributions, that is, the whole range of values that might occur. For the determination of the frequency distributions the use of the more complex fit model is important, because the distance between median and mean values determines the width of the lognormal distributions.

It is clear that the calculated distribution functions only represent first-order estimates of the real solar wind to be encountered by PSP. The solar-wind environment to be encountered will depend at times of PSP on the structure of the solar corona and underlying photospheric magnetic field and on the evolution and interaction of individual solar-wind streams and superimposed CMEs and shocks. However, the derived results are in good agreement with existing studies about near-Sun solar-wind magnetic field strengths and densities as shown in Sect. 6. The extrapolation results of the velocity and the temperature differ from the direct measurements seen in existing studies. This suggests that below about 20 $R_\odot$ PSP may dive into the region where the acceleration and heating of the solar wind is expected to occur (see Fig. 11). The near-Sun solar-wind velocity at PSP perihelion is also expected to be slower than our model estimates, because the solar wind is assumed to be accelerated up to the height of the Alfvénic critical surface, which is predicted to lie on average around 17 $R_\odot$ (e.g., Sittler & Guhathakurta 1999; Exarhos & Moussas 2000), scaling with solar activity within a range of between 15 $R_\odot$ at solar minimum and 30 $R_\odot$ at solar maximum (Katsikas et al. 2010; Goelzer et al. 2014).

We have not specifically investigated the occurrences of extreme solar-wind parameters caused by CMEs or enhanced values due to stream interaction or co-rotating interaction regions. The Helios solar-wind measurements plotted over radial distance in Fig. 7 show several extreme values far above the usual solar-wind velocities, which are associated with individual CMEs. The results by Sachdeva et al. (2017) indicate that due to solar-wind drag, the speeds of fast CMEs will commonly slow down substantially from early distances of a few solar radii. Therefore, it is expected that PSP will encounter CMEs with much higher speeds than those observed during the Helios mission. Also, the magnetic field, density and temperature values are expected to be much larger than in the average solar wind in individual fast-shock-associated CME events. PSP will thus also substantially improve our understanding of the near-Sun evolution of CMEs and their expansion with radial distance.

With the resulting CGAUSS empirical solar-wind model for PSP, the following main results for the bulk solar-wind parameters and estimations for their median values at PSP's first perihelion in 2018 at a solar distance of 0.16 au and at PSP's closest perihelia beginning in 2024 at 0.046 au (9.86 $R_\odot$) are obtained:

– The dependency of the magnetic field strength on solar activity and radial distance appears to be valid above 20 $R_\odot$, however near PSP's closest perihelia, the actual values might be found to be slightly higher.
– The estimated magnetic field strength median values obtained from relation (12) for PSP's 1st and 22nd perihelion are 87 nT and 943 nT.
– The radial dependencies of the proton velocity median values for slow and fast solar wind (14) appear to be valid above about 20 $R_\odot$ solar distance; below they overestimate the actual solar-wind velocities obtained from remote measurements. The share of their frequency distributions to the overall solar-wind velocity distribution (5) depends on solar activity with their balance relation (16). Thus, at solar minimum, with a SSN of around zero, the slow-wind component contributes about 64% and drops to 28% during solar maximum conditions with a SSN around 200.
– The calculated median velocity values for PSP's 1st and 22nd perihelion are 340 km s^{-1} and 290 km s^{-1}.
– The proton density relation appears to be valid throughout the full PSP orbital distance range, even down to about 8 $R_\odot$.
– The estimated density median values obtained from relation (17) for PSP's 1st and 22nd perihelion are 214 cm^{-3} and 2951 cm^{-3}.
– The derived correlation function for the proton temperature appears to provide overly high temperature values around PSP's closest perihelion in comparison to coronal measurements.
– The estimated temperature median values obtained from relation (19) for PSP's 1st and 22nd perihelion are 503 000 K and 1 930 000 K.

The results of the modeled solar-wind environment will be useful to help optimize the WISPR and in situ instrument science plannings and PSP mission operations. This also applies for the Heliospheric Imager (SoloHI; Howard et al. 2013) and the in situ instruments on board the Solar Orbiter spacecraft.

Acknowledgements. The authors acknowledge support of the Coronagraphic German and US SolarProbePlus Survey (CGAUSS) project for WISPR by the German Aerospace Center (DLR) under grant 50 OL 1601 as national contribution to the Parker Solar Probe mission. The authors thank the Helios and OMNI PIs/teams for creating and making available the solar-wind in situ data. The Helios and the OMNI data are supplied by the NASA Space Science Data Coordinated Archive and the Space Physics Data Facility at NASA's Goddard Space Flight Center. Additional thanks for maintaining and providing the international sunspot number series goes to the World Data Center – Sunspot Index and Long-term Solar Observations at the Solar Influences Data Analysis Center, Royal Observatory of Belgium. The PSP SPICE kernel was kindly provided by Angelos Vourlidas. The authors thank the referee for the careful review of this manuscript and helpful comments and suggestions.

References

Bale, S. D., Goetz, K., Harvey, P. R., et al. 2016, Space Sci. Rev., 204, 49
Balogh, A., Bothmer, V., Crooker, N. U., et al. 1999, Space Sci. Rev., 89, 141
Banaszkiewicz, M., Axford, W. I., & McKenzie, J. F. 1998, A&A, 337, 940
Belcher, J. W., Slavin, J. A., Armstrong, T. P., et al. 1991, Mercury Orbiter: Report of the Science Working Team (Washington, United States)
Biermann, L. 1951, ZAp, 29, 274
Billings, D. E. 1959, ApJ, 130, 961
Bothmer, V., & Daglis, I. A. 2007, Space Weather – Physics and Effects (Praxis Publishing)
Bothmer, V., & Schwenn, R. 1996, Adv. Space Res., 17, 319
Bothmer, V., & Schwenn, R. 1998, Annales Geophysicae, 16, 1
Bougeret, J.-L., King, J. H., & Schwenn, R. 1984, Sol. Phys., 90, 401
Bruno, R., Villante, U., Bavassano, B., Schwenn, R., & Mariani, F. 1986, Sol. Phys., 104, 431
Burt, J., & Smith, B. 2012, in IEEE Aerospace Conference, 1
Colin, L. 1980, J. Geophys. Res., 85, 7575
Domingo, V., Fleck, B., & Poland, A. I. 1995, Sol. Phys., 162, 1
Exarhos, G., & Moussas, X. 2000, A&A, 356, 315

Feldman, W. C., Asbridge, J. R., Bame, S. J., & Gosling, J. T. 1978, J. Geophys. Res., 83, 2177
Forsyth, R. J., Bothmer, V., Cid, C., et al. 2006, Space Sci. Rev., 123, 383
Fox, N. J., Velli, M. C., Bale, S. D., et al. 2016, Space Sci. Rev., 204, 7
Goelzer, M. L., Schwadron, N. A., & Smith, C. W. 2014, J. Geophys. Res. (Space Phys.), 119, 115
Gosling, J. T., Hildner, E., MacQueen, R. M., et al. 1974, J. Geophys. Res., 79, 4581
Gringauz, K. I., Bezrokikh, V. V., Ozerov, V. D., & Rybchinskii, R. E. 1960, Soviet Physics Doklady, 5, 361
Gurnett, D. A., Kurth, W. S., Burlaga, L. F., & Ness, N. F. 2013, Science, 341, 1489
Hathaway, D. H., & Upton, L. A. 2016, J. Geophys. Res. (Space Phys.), 121, 10
Hellinger, P., Matteini, L., Štverák, Š., Trávníček, P. M., & Marsch, E. 2011, J. Geophys. Res. (Space Phys.), 116, A09105
Hellinger, P., Trávníček, P. M., Štverák, Š., Matteini, L., & Velli, M. 2013, J. Geophys. Res. (Space Phys.), 118, 1351
Howard, R. A., Vourlidas, A., Korendyke, C. M., et al. 2013, in Solar Physics and Space Weather Instrumentation V, Proc. SPIE, 8862, 88620
Kasper, J. C., Stevens, M. L., Korreck, K. E., et al. 2012, ApJ, 745, 162
Kasper, J. C., Abiad, R., Austin, G., et al. 2016, Space Sci. Rev., 204, 131
Katsikas, V., Exarhos, G., & Moussas, X. 2010, Adv. Space Res., 46, 382
Kilpua, E. K. J., Madjarska, M. S., Karna, N., et al. 2016, Sol. Phys., 291, 2441
King, J. H., & Papitashvili, N. E. 2005, J. Geophys. Res. (Space Phys.), 110, A02104
Lazarus, A. J. 2000, Science, 287, 2172
Leblanc, Y., Dulk, G. A., & Bougeret, J.-L. 1998, Sol. Phys., 183, 165
Lepping, R. P., Acũna, M. H., Burlaga, L. F., et al. 1995, Space Sci. Rev., 71, 207
Liebenberg, D. H., Bessey, R. J., & Watson, B. 1975, Sol. Phys., 44, 345
Mariani, F., Ness, N. F., Burlaga, L. F., Bavassano, B., & Villante, U. 1978, J. Geophys. Res., 83, 5161
McComas, D. J., Bame, S. J., Barraclough, B. L., et al. 1998, Geophys. Res. Lett., 25, 1
McComas, D. J., Acton, L. W., Balat-Pichelin, M., et al. 2008, Solar Probe Plus: Report of the Science and Technology Definition Team, Tech. Rep. NASA/TM-2008-214161, National Aeronautics and Space Administration, Goddard Space Flight Center, Greenbelt, MD
McComas, D. J., Alexander, N., Angold, N., et al. 2016, Space Sci. Rev., 204, 187
McGregor, S. L., Hughes, W. J., Arge, C. N., Odstrcil, D., & Schwadron, N. A. 2011a, J. Geophys. Res. (Space Phys.), 116, A03106
McGregor, S. L., Hughes, W. J., Arge, C. N., Owens, M. J., & Odstrcil, D. 2011b, J. Geophys. Res. (Space Phys.), 116, A03101
Müller, D., Marsden, R. G., St. Cyr, O. C., & Gilbert, H. R. 2013, Sol. Phys., 285, 25
Neugebauer, M., & Snyder, C. W. 1966, J. Geophys. Res., 71, 4469
Ogilvie, K. W., Chornay, D. J., Fritzenreiter, R. J., et al. 1995, Space Sci. Rev., 71, 55
Parker, E. N. 1958, ApJ, 128, 664
Richardson, I. G., & Cane, H. V. 2012, J. Space Weather and Space Climate, 2, A2
Rosenbauer, H., Schwenn, R., Marsch, E., et al. 1977, J. Geophysics Zeitschrift Geophysik, 42, 561
Russell, C. T., Mewaldt, R. A., Luhmann, J. G., et al. 2013, ApJ, 770, 38
Sachdeva, N., Subramanian, P., Vourlidas, A., & Bothmer, V. 2017, Sol. Phys., 292, 118
Sanchez-Diaz, E., Rouillard, A. P., Lavraud, B., et al. 2016, J. Geophys. Res. (Space Phys.), 121, 2830
Schwenn, R. 1983, in NASA Conference Publication, 228
Schwenn, R. 1990, Large-Scale Structure of the Interplanetary Medium, eds. R. Schwenn, & E. Marsch (Berlin, Heidelberg: Springer), 99
Sheeley, Jr., N. R., Howard, R. A., Michels, D. J., et al. 1985, J. Geophys. Res., 90, 163
Sheeley, N. R., Wang, Y.-M., Hawley, S. H., et al. 1997, ApJ, 484, 472
SILSO World Data Center 1963–2016, International Sunspot Number Monthly Bulletin and online catalogue
Sittler, Jr., E. C., & Guhathakurta, M. 1999, ApJ, 523, 812
Smith, E. J., & Balogh, A. 2003, in Solar Wind Ten, eds. M. Velli, R. Bruno, F. Malara, & B. Bucci, AIP Conf. Ser., 679, 67
Stone, E. C., Frandsen, A. M., Mewaldt, R. A., et al. 1998, Space Sci. Rev., 86, 1
Veselovsky, I. S., Dmitriev, A. V., & Suvorova, A. V. 2010, Cosmic Research, 48, 113
Vourlidas, A., Howard, R. A., Plunkett, S. P., et al. 2016, Space Sci. Rev., 204, 83
Wang, Y.-M., Sheeley, N. R., Socker, D. G., Howard, R. A., & Rich, N. B. 2000, J. Geophys. Res., 105, 25133

7 Summary and outlook

7.1 Summary

In order to derive the link from near-Earth solar wind properties to its *Kp* impact, 35 years of solar wind high-resolution measurements were correlated with the *Kp* index and empirical relations were derived that enable the prediction of *Kp* from the solar wind velocity and the IMF z-component. Early predictions of CME and ambient stream magnetic fields obtained from near-Sun observations currently either are not existent or come with high uncertainties. Thus, to provide *Kp* predictions, I derived relations exclusively from their arrival velocity.

I built an empirical solar wind model for the inner heliosphere in the ecliptic which accounts for the variations of the solar activity cycle and for solar distance. In order to obtain empirical estimates of the solar wind environment PSP is to encounter, this solar wind model is extrapolated down to PSP's planned near-Sun perihelia and is built to consider the expected solar activity during PSP's mission.

7.2 Outlook

Using the SSN prediction, the derived solar wind model allows the forecast and extrapolation of the solar wind environment occuring during the PSP mission's near-Sun encounters from end of 2018 on. The anticipated Parker Solar Probe data (near-Sun measurements) will reveal how far the solar wind estimates really are from reality and thus is able to locate the outer boundary of the solar wind acceleration region.

DSCOVR data (advantages over ACE? gain?)

other possible spacecraft missions that would be beneficial for space weather forecasting: sub-L1 for earlier in-situ CME magnitude warning (cite?) and L5 for early CME velocity and arrival warning (Vourlidas 2015)

A Appendix

A.1 Solar surface differential rotation

The solar differential rotation is visible on the surface and was first discovered from sunspot observations by Scheiner (1630). (double)

Bartels (1934) set the synodic solar rotation period to 27 days for the definition of his solar rotation number. The Bartels' Rotation Number counts the solar rotations starting with 8 February 1832.
Carrington solar rotation period of 27.2753 days (Where Carrington Rotation Number is based upon, starting with November 9, 1853; Wikipedia...)

Solar surface rotation period at 16° latitude:
sidereal: 25.38 d (of 609.12 h Sun Fact Sheet...), synodic: 27.2753 d (derived)

rotation axis tilt (see next section)

The Sun's inner thermal convective circulation results in a differential rotation caused by transport of angular momentum away from the rotation axis.
The Sun's sidereal differential angular velocity best-fitting function with values as stated in (Sun Fact Sheet...)[1] is

$$\omega_{\odot}(\theta) = \omega_{\mathrm{eq}} + B\sin^2(\theta) + C\sin^4(\theta) \tag{A.1}$$

with the heliolatitude θ, the equatorial angular velocity $\omega_{\mathrm{eq}} = 14.37\,^\circ\,\mathrm{d}^{-1}$, the coefficients $B = -2.33\,^\circ\,\mathrm{d}^{-1}$, and $C = -1.56\,^\circ\,\mathrm{d}^{-1}$ (see Figure A.1).
see Figure A.1

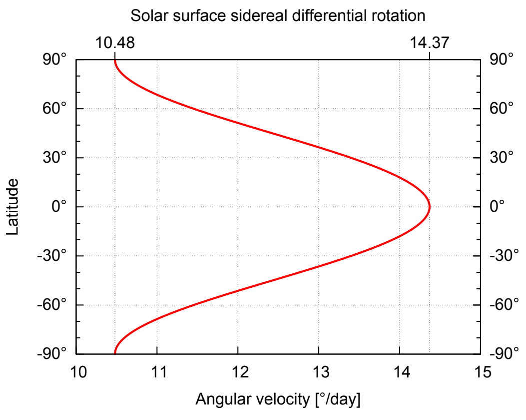

Figure A.1 Diagram of the sidereal solar surface differential rotation. It shows the angular velocity for different latitudes. remove sides...

Thus, the solar equatorial rotation period (sidereal) is

$$\begin{aligned} T_{\odot}^{\mathrm{eq}} &= 360^\circ/A \\ &= 25.05\ \mathrm{d} \end{aligned} \tag{A.2}$$

and the synodic period is

$$\begin{aligned} T_{\odot}^{\mathrm{eq,syn}} &= 1/(1/T_{\odot}^{\mathrm{eq}} - 1/T_{\mathrm{Earth}}) \\ &= 26.90\ \mathrm{d} \end{aligned} \tag{A.3}$$

with the Earth's orbital rotation period $T_{\mathrm{Earth}} = 365.25$ d (1/100 Julian century).

[1] NASA's *Sun Fact Sheet* (http://nssdc.gsfc.nasa.gov/planetary/factsheet/sunfact.html, accessed 2016-08-19).

Solar surface rotation period at equator
sidereal: 25.05 d (Sun Fact Sheet...), synodic: 26.90 d (derived)
Solar surface rotation period at poles:
sidereal: 34.35 d (diff. rot. formula), synodic: 37.92 d (derived)
are listed in Table A.1.

Table A.1 Solar surface rotation periods for the equator, ±16° latitudes and the poles in sidereal and synodic rotation.

	Equator [d]	±16° latitudes [d]	Poles [d]
Sidereal	25.05	25.38	34.35
Synodic	26.90	27.2753[a]	37.92

[a]Carrington solar rotation period

The meridional circulation is the proposed equatorial updrift and polar downdrift - a result of Reynolds stress and convective transport (cite?).

A.2 Electric field at the magnetopause

The Lorentz force law defines the electric and magnetic field vectors $\boldsymbol{E}$ and $\boldsymbol{B}$:

$$\boldsymbol{F} = q\,(\boldsymbol{E} + \boldsymbol{v} \times \boldsymbol{B})\,. \tag{A.4}$$

It describes the force $\boldsymbol{F}$ that acts on a charge q with velocity v. The full Ohm's law accounts for the Lorentz force:

$$\boldsymbol{j} = \sigma(\boldsymbol{E} + \boldsymbol{v} \times \boldsymbol{B}) \qquad \Longleftrightarrow \qquad \boldsymbol{E} = -\boldsymbol{v} \times \boldsymbol{B} + \frac{\boldsymbol{j}}{\sigma}\,. \tag{A.5}$$

Solar wind is often approximated as an ideal MHD plasma having an infinite conductivity ($\sigma = \infty$). Thus electric fields do not generate electric currents $\boldsymbol{j}$:

$$\boldsymbol{E} = -\boldsymbol{v} \times \boldsymbol{B}\,. \tag{A.6}$$

Assuming the solar wind flows into the x-direction ($v_\mathrm{y} = v_\mathrm{z} = 0$), the resulting electric field components become

$$\boldsymbol{E} = \begin{bmatrix} E_\mathrm{x} \\ E_\mathrm{y} \\ E_\mathrm{z} \end{bmatrix} = \begin{bmatrix} 0 \\ -v_\mathrm{x} \cdot B_\mathrm{z} \\ v_\mathrm{x} \cdot B_\mathrm{y} \end{bmatrix}, \tag{A.7}$$

$$= \begin{bmatrix} 0 \\ -v_\mathrm{x} \cdot |\boldsymbol{B}_\mathrm{yz}| \cdot \cos(\theta_c) \\ v_\mathrm{x} \cdot |\boldsymbol{B}_\mathrm{yz}| \cdot \sin(\theta_c) \end{bmatrix}. \tag{A.8}$$

If in addition the magnetic field is strictly orientated along the z-axis, the only non-zero electric field component remaining is E_y:

$$\boldsymbol{E} = -v_\mathrm{x} \cdot B_\mathrm{z}\,. \tag{A.9}$$

Reconnection occurs only where the magnetic fields of the solar wind and magnetopause are antiparallel. Due to the magnetosphere's dipole topology, this is the case at the equator of the sunward magnetopause (when using GSM coordinates).

However, reconnection can occur on the whole magnetopause surface facing the solar wind, that is, even at higher latitudes where B_z is not the only field component. Thus, it makes sense to use the magnetic field's absolute value $|B|$ and its clock angle $\theta_c = \tan^{-1}\left(\frac{B_\mathrm{y}}{B_\mathrm{z}}\right)$ instead of just the field's B_z component.

Lockwood2013:
on timescales of T = 1 yr, the IMF orientation factor is averaged out and the average southward IMF component and, hence, the level of geomagnetic activity, is proportional to B , as first noted by Stamper et al. (1999). This is the basic reason that we are able to make deductions about B from geomagnetic activity when averaging is

done on annual timescales.

the distribution of annual values of the ratio B/ [B sin 4 (theta / 2)]. The mean value of this distribution is 3.251 and the standard deviation is 0.369.

A.3 Plasma beta

The thermal pressure of a plasma is defined as $p = nk_\mathrm{B}T$, with the number density n and the Boltzmann constant k_B. However, according to magnetohydrodynamics (MHD), the magnetic energy density $w_\mathrm{mag} = \frac{B^2}{2\mu_0}$, with the magnetic field strength B and the permeability constant μ_0, behaves like an additional pressure that adds to the thermal pressure of a plasma (Kivelson & Russell 1995, p. 50). The ratio of the thermal pressure to the magnetic pressure determines the behavior of the plasma. If the thermal pressure dominates the magnetic pressure (warm plasma), the plasma movements transport the magnetic field, else the plasma movements are guided by the magnetic field lines (cold plasma). This ratio is called plasma beta:

$$\beta = \frac{p}{p_\mathrm{mag}}\,, \tag{A.10}$$

$$= \frac{2\mu_0 n k_\mathrm{B} T}{B^2}\,. \tag{A.11}$$

The plasma at the photosphere has typical beta values around 14 and that of the low corona around 0.2 (Gary 2001). Further up, beta raises again and the region where it equals 1 is defined as the source surface for the solar wind (Schatten et al. 1969). This surface is typically located at about 1.2–2.5 $R_\odot$ (Gary 2001), more cites...

The solar wind usually has plasma beta values higher than 1 – it carries the solar magnetic field away into the heliosphere. Together with the solar rotation, this effect creates the spiral form of the interplanetary magnetic field (Parker spiral). Yet in some solar wind structures, such as magnetic clouds, $\beta \ll 1$ and thus the magnetic field can still contain the plasma.

Savani2017:
"*By using statistical analysis, Riley and Richardson [2013] suggest that a distinct magnetic flux rope object may be contained within an overall propagating CME structure and that the plasma beta is a good predictor variable. Savani et al. [2013b] used simulations to confirm that such a scenario of a distinct coherent core obstacle can occur within the CME structure and that a transition in plasma beta can be observed.*"

A.4 Alfvén velocity

The incompressible wave mode within MHD plasmas, the shear Alfvén wave, consists of periodic disturbances in the magnetic field orthogonal to its direction (Alfvén 1942). Alfvén waves are prevalent in open coronal regions and therefore occur in fast solar wind (Cranmer & van Ballegooijen 2005). Their propagation velocity is an important parameter to characterize a plasma. In an ideal incompressible MHD plasma (viscosity $\mu = 0$ and electrical conductivity $\sigma = \infty$) the kinetic and magnetic energy density are of equal value (Kivelson & Russell 1995, p. 51):

$$w_\mathrm{kin} = w_\mathrm{mag} \tag{A.12}$$

$$\frac{\rho v^2}{2} = \frac{B^2}{2\mu_0}$$

with the permeability constant μ_0 and the total mass density ρ of the charged plasma particles. Thus, the Alfvén velocity can be calculated from

$$v_\mathrm{A} = \frac{|B|}{\sqrt{\mu_0 \rho}}\,. \tag{A.13}$$

The wave's phase velocity is

$$v_\mathrm{ph} = v_\mathrm{A}\cos(\theta) \tag{A.14}$$

with θ as the angle between wave propagation direction and magnetic field line, that is, Alfvén waves travel along magnetic field lines. They consist of periodic disturbances in the magnetic field, the electric field, the plasma velocity, and the current density. Plasma density, pressure and magnetic field magnitude are not affected by them. Additionally, there exist two types of compressional wave modes within MHD plasmas, the fast-mode wave and the slow-mode wave. The phase speeds of the three MHD waves meet $v_{\mathrm{fast}} \geq v_{\mathrm{A}} \geq v_{\mathrm{slow}}$ (Kivelson & Russell 1995, p. 52). Within solar wind at 1 au, the typical frequency of Alfvén waves is 1–4 per hour and their average velocity is $v_{\mathrm{A}} = 56.8\,\mathrm{km\,s^{-1}}$ (Veselovsky et al. 2010).

Alfvén critical surface...
sonic critical surfaces...

shocks & MHD waves (Alfvén waves)
Alfvén velocity ca. 40 km/s (Kivelson1995)
Alfvén velocity 56.8 km/s (Veselovsky2009)

sonic and Alfvénic critical point positions (see Sittler & Guhathakurta (1999))
sonic point and slow solar wind origin (Sheeley et al. 1997)

A.5 Sun-Earth orbit geometry

orbit defines ecliptic

Earth orbit parameters (cite?):
semimajor axis: $a = 1.000001018$ au
eccentricity: $e = 0.0167086$ au
distance at perihelion: (formula cite?, accuracy?)

$$\begin{aligned} r_{\mathrm{p}} &= a(1-e) \\ &= 0.98329 \text{ au} \end{aligned} \tag{A.15}$$

distance at aphelion:

$$\begin{aligned} r_{\mathrm{p}} &= a(1+e) \\ &= 1.0167 \text{ au} \end{aligned} \tag{A.16}$$

for calculation of heliospheric distance see HORIZONS Web-Interface at `http://ssd.jpl.nasa.gov/horizons.cgi`
perihelion/aphelion times...

Solar distance

Sun-Earth distance over the course of the year.
In the year 2017 Earth's perihelion was on 5 January with a distance of −1.67 % from 1 au (Horizons On-Line Ephemeris System[2], Solar System Dynamics Group, Jet Propulsion Laboratory).
The cosine approximation

$$r_{\mathrm{E}}(t) = 1 - 0.0167 \cdot \cos\left(2\pi\left(t - 2017 - \frac{5}{365}\right)\right), \tag{A.17}$$

with t in years, suffices for our accuracy requirements.

seasonal variation function:
$X_{\mathrm{avg}}(t) = a\, r_{\mathrm{E}}(t)^b$

[2] `http://ssd.jpl.nasa.gov/horizons.cgi`

Solar rotation axis tilt to the ecliptic

The inclination of the solar equator to the ecliptic (tilt/obliquity) is $i_{\odot} = 7.25°$ (U.S. Nautical Almanac Office 2015).

the rotation axis is tilted from the ecliptic normal

Viewed from Earth the projected solar rotation axis tilt angle varies as the Earth is moving on its orbit.

At the time XX the angle is zero.

The projected tilt angle to Earth over the year is

Hapgood (1992):

$$\omega = 73.67 + 0.013\,958 * (today - 1850.0) \tag{A.18}$$

solar tilt over the year, see Figure A.2

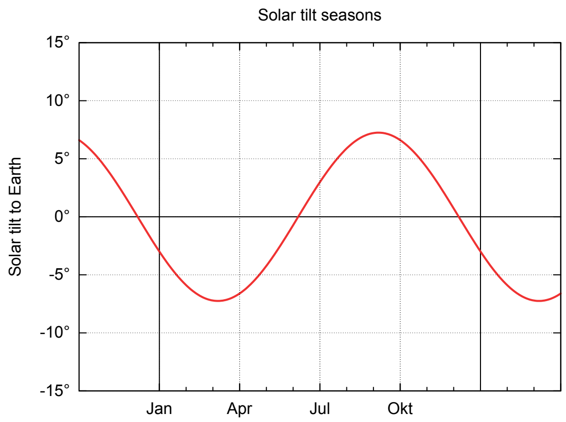

Figure A.2 Projected solar tilt angle over the year as viewed from Earth. remove sides...

Earth rotation axis tilt to the ecliptic

A.6 GSE, GSM, and HGI coordinate systems

Coordinate systems used in this thesis:
GSE - Geocentric Solar Ecliptic
GSM - Geocentric Solar Magnetospheric
HGI - Heliographic Inertial

refer to Hapgood (1992) for GSE and GSM

figures for GSE and GSM

Geocentric Solar Ecliptic

The Geocentric Solar Ecliptic (GSE) coordinates are
GSE - Geocentric Solar Ecliptic
X = Earth-Sun Line
Z = Ecliptic North Pole
GSE coordinates are used in ACE solar wind data, etc.
see Jursa1985, p. 4-3
"the polar axis is the axis inclined 11.5° to the axis of rotation, intersecting the earth surface at the point 78.5°N, 291.0°E which defines the geomagnetic north pole. This was once at one time the axis of the best centered-dipole approximation to the field"

Geocentric Solar Magnetospheric

GSM - Geocentric Solar Magnetospheric
X = Earth-Sun Line
Z = Projection of dipole axis on GSE YZ plane

GSM is defined with a time dependent dipole axis.
the dipole axis orientation changes over time; at 1995 the northern pole was at $l = 288.59°$ and $b = 79.30°$; more recent year (2015)?... cite?

Heliographic Inertial

Heliographic Inertial (HGI) coordinates
HGI coordinates are Sun-centered with the z-axis directed along the solar rotation axis and directed northward of the solar equator. The solar equator plane is inclined 7.25° from the ecliptic.

HGI coordinates; latitude range $-7.25°$ to $-7.25°$
latitude variation (see Schwenn1990, p. 127)

A.7 True skill statistic

The true skill statistic (TSS) or true skill score is a means for measuring the predictive value of a variable. It was developed by Hanssen & Kuipers (1965) for evaluating different predictors for rain and dry weather conditions. Therefore it is also often called the Hanssen-Kuipers skill score or the Hanssen-Kuipers discriminant. As with other skill scores, the TSS is based on a 2x2 contingency table that categorizes forecasted and observed events, see the Table A.2. The following ratios, derived from this kind of table, reveal relevant information about the

Table A.2 Generic contingency table for categorizing forecasted and observed events. The designations for the event counts are given in parentheses.

		Observed	
		Yes	No
Forecasted	Yes	Hit (n_H)	False alarm (n_{FA})
	No	Miss (n_M)	Correct null (n_{CN})

forecast quality (Doswell et al. 1990): The proportion of correct predictions

$$PC = \frac{n_H + n_{CN}}{n_H + n_{FA} + n_M + n_{CN}}, \tag{A.19}$$

the probabilities of detection and of false detection (i.e., the hit rate and the false alarm rate)

$$POD = \frac{n_H}{n_H + n_M} \quad \text{and} \quad POFD = \frac{n_{FA}}{n_{FA} + n_{CN}}, \tag{A.20}$$

as well as the false alarm and detection failure ratios

$$FAR = \frac{n_{FA}}{n_{FA} + n_H} \quad \text{and} \quad DFR = \frac{n_M}{n_M + n_{CN}}. \tag{A.21}$$

The TSS is the difference between the hit rate and the false alarm rate[3] and thus it is calculated as follows (Hanssen & Kuipers 1965, Eq. 15):

$$TSS = POD - POFD \tag{A.22}$$

$$= \frac{n_H \cdot n_{CN} - n_{FA} \cdot n_M}{(n_H + n_M)(n_{FA} + n_{CN})}. \tag{A.23}$$

[3]False alarm rate – not to be confused with false alarm ratio.

Its value is in the range from -1 to 1, with 1 representing an ideal prediction, 0 a random prediction, and -1 an ideal negative prediction. The TSS is positive if the hit rate is higher than the false alarm rate.

In the case of rare event forecasting, the contingency table is dominated by correct nulls and the TSS approaches the hit rate. Doswell et al. (1990) show that the Heidke skill score is superior in these situations, in that it considers correct null forecasts in a controlled way. They recommend to use the Heidke skill score in preference to TSS for rare event forecasting. Other often applied skill scores are the threat score, also called critical success index or Gilbert score, and the equitable threat score. However, the TSS is commonly applied to evaluate and compare space weather prediction methods, especially in forecasting the *Kp* index (Detman & Joselyn 1999; Wing et al. 2005; Savani et al. 2017).

A.8 Lognormal distribution

This is a small summary about the lognormal probability distribution (Bronstein et al. 2000, p. 780). The lognormal distribution is the distribution of a random variable X if the logarithm of X conforms to a normal distribution. Its shape is highly asymmetric, however in a semi-log plot the Gaussian bell curve is recognizable (see the second panel of Figure A.3). Its probability density function is

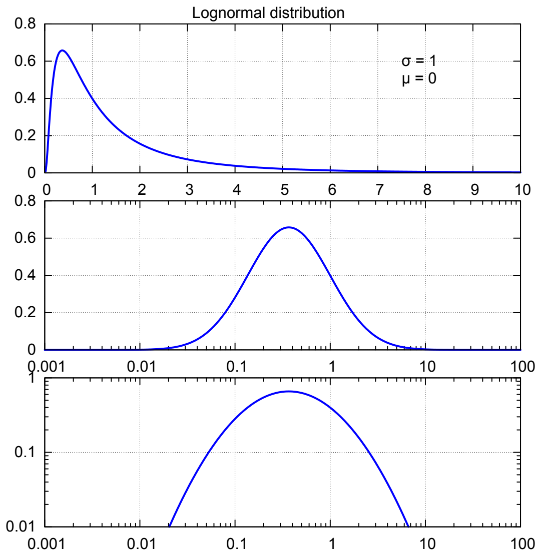

Figure A.3 The lognormal probability density function ($\sigma = 1, \mu = 0$) plotted in a linear, semi-log and log-log way. remove borders...

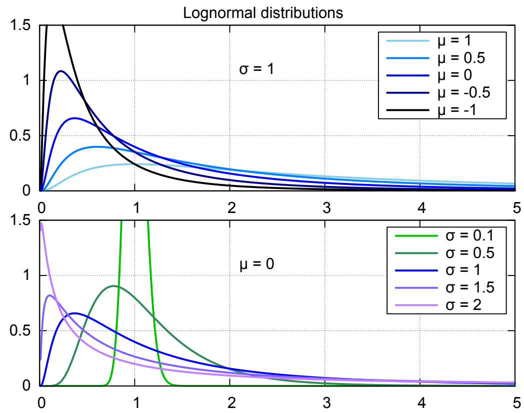

Figure A.4 Five lognormal distributions plotted with fixed σ (top) and fixed μ (bottom). remove borders...

$$f(x) = \frac{1}{\sigma\sqrt{2\pi}x}\,\mathrm{e}^{-\frac{(\ln x-\mu)^2}{2\sigma^2}} \tag{A.24}$$

with the location (μ) and the shape parameter (σ). Changes in μ affect both the horizontal and vertical scaling of the function, whereas σ has an influence on its shape (see Figure A.4).

Because it is a probability distribution, its area is normalized

$$\int_0^\infty f(x)\mathrm{d}x = 1\,. \tag{A.25}$$

For a lognormally distributed random variable the geometric moments mean, standard deviation and variance are:

$$\begin{aligned}\mu_\mathrm{g} &= \mathrm{e}^{\mu},\\ \sigma_\mathrm{g} &= \mathrm{e}^{\sigma},\\ var_\mathrm{g} &= \mathrm{e}^{\sigma^2} \quad (!).\end{aligned}$$

Its arithmetic moments are:

$$\mu_{\mathrm{a}} = \mathrm{e}^{\mu+\frac{\sigma^2}{2}},$$
$$\sigma_{\mathrm{a}} = \mathrm{e}^{\mu+\frac{\sigma^2}{2}} \left(\mathrm{e}^{\sigma^2} - 1\right),$$
$$var_{\mathrm{a}} = \sigma_{\mathrm{a}}^2.$$

Other useful characteristics are the median and the mode

$$x_{\mathrm{median}} = \mathrm{e}^{\mu},$$
$$x_{\mathrm{mode}} = \mathrm{e}^{\mu-\sigma^2}.$$

Note that for the lognormal distribution its median is equal to its geometric mean.

Applications of lognormal distributions...

Most natural quantities which can only be positive are lognormally distributed. e.g. animal body sizes?, animal life expectancies, financial stock prices...; income distributions.

A.9 Astronomical constants

Astronomical unit: 1 au = 149 597 870 700 m (U.S. Nautical Almanac Office 2015)
Solar mass: $M_{\odot} = 1.9884(2) \times 10^{30}$ kg (U.S. Nautical Almanac Office 2015)
Nominal solar radius (photosphere): $R_{\odot} = 695\,700$ km (Mamajek et al. 2015)
Solar rotation axis tilt: $i_{\odot} = 7.25°$ (U.S. Nautical Almanac Office 2015)
Solar surface rotation period at equator, sidereal: 25.05 d (Sun Fact Sheet...)
Nominal solar effective temperature (photosphere): $T_{\mathrm{eff}\odot} = 5772$ K (Mamajek et al. 2015)
Sun escape velocity: $v_{\mathrm{esc}} = 617.6$ km/s (Sun Fact Sheet...)

NASA maintains the Planetary Fact Sheets[4] online.

[4]NASA Planetary Fact Sheets website: https://nssdc.gsfc.nasa.gov/planetary/planetfact.html

References

Alfvén, H. 1942, *Existence of Electromagnetic-Hydrodynamic Waves*, Nature, 150, 405, http://adsabs.harvard.edu/abs/1942Natur.150..405A.

Aubry, M. P., Russell, C. T. & Kivelson, M. G. 1970, *Inward motion of the magnetopause before a substorm*, J. Geophys. Res., 75, 7018, http://adsabs.harvard.edu/abs/1970JGR....75.7018A.

Bahcall, J. N., Pinsonneault, M. H. & Wasserburg, G. J. 1995, *Solar models with helium and heavy-element diffusion*, Reviews of Modern Physics, 67, 781, http://adsabs.harvard.edu/abs/1995RvMP...67..781B.

Bala, R. & Reiff, P. 2012, *Improvements in short-term forecasting of geomagnetic activity*, Space Weather, 10, S06001, http://adsabs.harvard.edu/abs/2012SpWea..10.6001B.

Balogh, A. & Jokipii, J. R. 2009, *The Heliospheric Magnetic Field and Its Extension to the Inner Heliosheath*, Space Sci. Rev., 143, 85, http://adsabs.harvard.edu/abs/2009SSRv..143...85B.

Balogh, A., Bothmer, V., Crooker, N. U. et al. 1999, *The Solar Origin of Corotating Interaction Regions and Their Formation in the Inner Heliosphere*, Space Sci. Rev., 89, 141, http://adsabs.harvard.edu/abs/1999SSRv...89..141B.

Bame, S. J., Asbridge, J. R., Feldman, W. C. & Gosling, J. T. 1977, *Evidence for a structure-free state at high solar wind speeds*, J. Geophys. Res., 82, 1487, http://adsabs.harvard.edu/abs/1977JGR....82.1487B.

Banaszkiewicz, M., Axford, W. I. & McKenzie, J. F. 1998, *An analytic solar magnetic field model*, Astron. Astrophys., 337, 940, http://adsabs.harvard.edu/abs/1998A%26A...337..940B.

Bartels, J. 1934, *Twenty-seven day recurrences in terrestrial-magnetic and solar activity, 1923-1933*, Terrestrial Magnetism and Atmospheric Electricity (Journal of Geophysical Research), 39, 201, http://adsabs.harvard.edu/abs/1934TeMAE..39..201B.

—. 1962, *Zur Vorgeschichte der Weltraumforschung*, Naturwissenschaften, 49, 313, http://adsabs.harvard.edu/abs/1962NW.....49..313B.

Bartels, J., Heck, N. H. & Johnston, H. F. 1939, *The three-hour-range index measuring geomagnetic activity*, Terrestrial Magnetism and Atmospheric Electricity (Journal of Geophysical Research), 44, 411, http://adsabs.harvard.edu/abs/1939TeMAE..44..411B.

Bartels, J. & Veldkamp, J. 1949, *International Data on Magnetic Disturbances, First Quarter, 1949*, J. Geophys. Res., 54, 295, http://adsabs.harvard.edu/abs/1949JGR....54..295B.

Belcher, J. W., Lazarus, A. J., McNutt, Jr., R. L. & Gordon, Jr., G. S. 1993, *Large-scale density structures in the outer heliosphere*, Advances in Space Research, 13, 41, http://adsabs.harvard.edu/abs/1993AdSpR..13...41B.

Biermann, L. 1951, *Kometenschweife und solare Korpuskularstrahlung*, Z. Astrophys., 29, 274, http://adsabs.harvard.edu/abs/1951ZA.....29..274B.

Billings, D. E. 1959, *Distribution of Matter with Temperature in the Emission Corona.*, Astrophys. J., 130, 961, http://adsabs.harvard.edu/abs/1959ApJ...130..961B.

Borrini, G., Wilcox, J. M., Gosling, J. T., Bame, S. J. & Feldman, W. C. 1981, *Solar wind helium and hydrogen structure near the heliospheric current sheet - A signal of coronal streamers at 1 AU*, J. Geophys. Res., 86, 4565, http://adsabs.harvard.edu/abs/1981JGR....86.4565B.

Bosman, E., Bothmer, V., Nisticò, G. et al. 2012, *Three-Dimensional Properties of Coronal Mass Ejections from STEREO/SECCHI Observations*, Solar Phys., 281, 167, http://adsabs.harvard.edu/abs/2012SoPh..281..167B.

Bothmer, V. 1993, *Die Struktur magnetischer Wolken im Sonnenwind: Zusammenhang mit eruptiven Protuberanzen und Einfluß auf die Magnetosphäre der Erde*, PhD thesis, Georg-August-Universität Göttingen, http://hdl.handle.net/11858/00-001M-0000-0014-F2C4-2.

Bothmer, V. & Daglis, I. A. 2007, *Space Weather – Physics and Effects* (Praxis Publishing), http://adsabs.harvard.edu/abs/2007swpe.book.....B, doi:10.1007/978-3-540-34578-7.

Bothmer, V. & Schwenn, R. 1995, *The Interplanetary and Solar Causes of Major Geomagnetic Storms.*, Journal of Geomagnetism and Geoelectricity, 47, 1127, http://adsabs.harvard.edu/abs/1995JGG....47.1127B.

—. 1998, *The structure and origin of magnetic clouds in the solar wind*, Annales Geophysicae, 16, 1, http://adsabs.harvard.edu/abs/1998AnGeo..16....1B.

Bronstein, I. N., Semendjajew, K. A., Musiol, G. & Mühlig, H. 2000, *Taschenbuch der Mathematik* (Verlag Harri Deutsch), https://books.google.de/books?id=zCKyuQAACAAJ.

Burlaga, L., Sittler, E., Mariani, F. & Schwenn, R. 1981, *Magnetic loop behind an interplanetary shock - Voyager, Helios, and IMP 8 observations*, J. Geophys. Res., 86, 6673, http://adsabs.harvard.edu/abs/1981JGR....86.6673B.

Burlaga, L. F. & Behannon, K. W. 1982, *Magnetic clouds - Voyager observations between 2 and 4 AU*, Solar Phys., 81, 181, http://adsabs.harvard.edu/abs/1982SoPh...81..181B.

Burlaga, L. F., Goldstein, M. L., McDonald, F. B. & Lazarus, A. J. 1985, *Cosmic ray modulation and turbulent interaction regions near 11 AU*, J. Geophys. Res., 90, 12, http://adsabs.harvard.edu/abs/1985JGR....9012027B.

Burlaga, L. F., Lepping, R. P., Behannon, K. W. & Klein, L. W. 1984, *Large-scale interplanetary magnetic fields - Voyager 1 and 2 observations between 1 AU and 9.5 AU*, J. Geophys. Res., 89, 10659, http://adsabs.harvard.edu/abs/1984JGR....8910659B.

Cane, H. V. & Richardson, I. G. 2003, *Interplanetary coronal mass ejections in the near-Earth solar wind during 1996-2002*, Journal of Geophysical Research (Space Physics), 108, 1156, http://adsabs.harvard.edu/abs/2003JGRA..108.1156C.

Carrington, R. C. 1859, *Description of a Singular Appearance seen in the Sun on September 1, 1859*, Mon. Not. R. Astron. Soc., 20, 13, http://adsabs.harvard.edu/abs/1859MNRAS..20...13C.

Chen, J., Howard, R. A., Brueckner, G. E. et al. 1997, *Evidence of an Erupting Magnetic Flux Rope: LASCO Coronal Mass Ejection of 1997 April 13*, Astrophys. J., Lett., 490, L191, http://adsabs.harvard.edu/abs/1997ApJ...490L.191C.

Cho, K.-S., Bong, S.-C., Moon, Y.-J. et al. 2011, *Relationship between multiple type II solar radio bursts and CME observed by STEREO/SECCHI*, Astron. Astrophys., 530, A16, http://adsabs.harvard.edu/abs/2011A%26A...530A..16C.

Christensen-Dalsgaard, J., Gough, D. O. & Thompson, M. J. 1991, *The depth of the solar convection zone*, Astrophys. J., 378, 413, http://adsabs.harvard.edu/abs/1991ApJ...378..413C.

Christensen-Dalsgaard, J., Dappen, W., Ajukov, S. V. et al. 1996, *The Current State of Solar Modeling*, Science, 272, 1286, http://adsabs.harvard.edu/abs/1996Sci...272.1286C.

Clark, D. H. & Stephenson, F. R. 1978, *An Interpretation of the Pre-Telescopic Sunspot Records from the Orient*, Quart. J. R. Astron. Soc., 19, 387, http://adsabs.harvard.edu/abs/1978QJRAS..19..387C.

Cliver, E. W., Kahler, S. W., Shea, M. A. & Smart, D. F. 1982, *Injection onsets of 2 GeV protons, 1 MeV electrons, and 100 keV electrons in solar cosmic ray flares*, Astrophys. J., 260, 362, http://adsabs.harvard.edu/abs/1982ApJ...260..362C.

Cliver, E. W., Laurenza, M., Storini, M. & Thompson, B. J. 2005, *On the Origins of Solar EIT Waves*, Astrophys. J., 631, 604, http://adsabs.harvard.edu/abs/2005ApJ...631..604C.

Cortie, A. L. 1912, *Sun-spots and terrestrial magnetic phenomena, 1898-1911*, Mon. Not. R. Astron. Soc., 73, 52, http://adsabs.harvard.edu/abs/1912MNRAS..73...52C.

Coxon, J. C., Milan, S. E., Clausen, L. B. N., Anderson, B. J. & Korth, H. 2014, *The magnitudes of the regions 1 and 2 Birkeland currents observed by AMPERE and their role in solar wind-magnetosphere-ionosphere coupling*, Journal of Geophysical Research (Space Physics), 119, 9804, http://adsabs.harvard.edu/abs/2014JGRA..119.9804C.

Cranmer, S. R., Gibson, S. E. & Riley, P. 2017, *Origins of the Ambient Solar Wind: Implications for Space Weather*, Space Sci. Rev., 212, 1345, http://adsabs.harvard.edu/abs/2017SSRv..212.1345C.

Cranmer, S. R. & van Ballegooijen, A. A. 2005, *On the Generation, Propagation, and Reflection of Alfvén Waves from the Solar Photosphere to the Distant Heliosphere*, Astrophys. J., Suppl. Ser., 156, 265, http://adsabs.harvard.edu/abs/2005ApJS..156..265C.

Cremades, H. & Bothmer, V. 2004, *On the three-dimensional configuration of coronal mass ejections*, Astron. Astrophys., 422, 307, http://adsabs.harvard.edu/abs/2004A%26A...422..307C.

Crooker, N. U., Huang, C.-L., Lamassa, S. M. et al. 2004, *Heliospheric plasma sheets*, Journal of Geophysical Research (Space Physics), 109, A03107, http://adsabs.harvard.edu/abs/2004JGRA..109.3107C.

Danziger, I. J. 1970, *The Cosmic Abundance of Helium*, Ann. Rev. Astron. Astrophys., 8, 161, http://adsabs.harvard.edu/abs/1970ARA%26A...8..161D.

Davies, K. 1990, *Ionospheric Radio* (Institution of Engineering and Technology), http://digital-library.theiet.org/content/books/ew/pbew031e, doi:10.1049/PBEW031E.

de Keyser, J., Dunlop, M. W., Owen, C. J. et al. 2005, *Magnetopause and Boundary Layer*, Space Sci. Rev., 118, 231, http://adsabs.harvard.edu/abs/2005SSRv..118..231D.

Detman, T. & Joselyn, J. 1999, *Real-time Kp predictions from ACE real time solar wind*, in American Institute of Physics Conference Series, Vol. 471, American Institute of Physics Conference Series, ed. S. R. Habbal, R. Esser, J. V. Hollweg, & P. A. Isenberg, 729–732, http://adsabs.harvard.edu/abs/1999AIPC..471..729D.

Doswell, III, C. A., Davies-Jones, R. & Keller, D. L. 1990, *On Summary Measures of Skill in Rare Event Forecasting Based on Contingency Tables*, Weather and Forecasting, 5, 576, http://adsabs.harvard.edu/abs/1990WtFor...5..576D.

Dungey, J. W. 1961, *Interplanetary Magnetic Field and the Auroral Zones*, Physical Review Letters, 6, 47, http://adsabs.harvard.edu/abs/1961PhRvL...6...47D.

—. 1963, *The structure of the exosphere or advances in velocity space*, ed. C. DeWitt, J. Hieblot, & A. Lebeau, Geophysics: The Earth's Environment (Gordon and Breach, New York), 505–550, http://adsabs.harvard.edu/abs/1963gege.conf.....D.

Elliott, H. A., Jahn, J.-M. & McComas, D. J. 2013, *The Kp index and solar wind speed relationship: Insights for improving space weather forecasts*, Space Weather, 11, 339, http://adsabs.harvard.edu/abs/2013SpWea..11..339E.

Exarhos, G. & Moussas, X. 2000, *An estimation of the shape and temporal variation of the solar wind sonic, Alfvénic and fast magnetosonic surfaces*, Astron. Astrophys., 356, 315, http://adsabs.harvard.edu/abs/2000A%26A...356..315E.

Fairfield, D. H. 1971, *Average and unusual locations of the Earth's magnetopause and bow shock*, J. Geophys. Res., 76, 6700, http://adsabs.harvard.edu/abs/1971JGR....76.6700F.

Fairfield, D. H. & Cahill, Jr., L. J. 1966, *Transition region magnetic field and polar magnetic disturbances*, J. Geophys. Res., 71, 155, http://adsabs.harvard.edu/abs/1966JGR....71..155F.

Feldman, W. C., Asbridge, J. R., Bame, S. J. & Gosling, J. T. 1978, *Long-term variations of selected solar wind properties - IMP 6, 7, and 8 results*, J. Geophys. Res., 83, 2177, http://adsabs.harvard.edu/abs/1978JGR....83.2177F.

Fisher, R. R. & Munro, R. H. 1984, *Coronal transient geometry. I - The flare-associated event of 1981 March 25*, Astrophys. J., 280, 428, http://adsabs.harvard.edu/abs/1984ApJ...280..428F.

Forbush, S. E. 1937, *On the Effects in Cosmic-Ray Intensity Observed During the Recent Magnetic Storm*, Physical Review, 51, 1108, http://adsabs.harvard.edu/abs/1937PhRv...51.1108F.

Fox, N. J., Velli, M. C., Bale, S. D. et al. 2015, *The Solar Probe Plus Mission: Humanity's First Visit to Our Star*, Space Sci. Rev., doi:10.1007/s11214-015-0211-6, http://adsabs.harvard.edu/abs/2015SSRv..tmp..105F.

Gary, G. A. 2001, *Plasma Beta above a Solar Active Region: Rethinking the Paradigm*, Solar Phys., 203, 71, http://adsabs.harvard.edu/abs/2001SoPh..203...71G.

Gold, T. 1959, *Motions in the Magnetosphere of the Earth*, J. Geophys. Res., 64, 1219, http://adsabs.harvard.edu/abs/1959JGR....64.1219G.

—. 1962, *Magnetic Storms*, Space Sci. Rev., 1, 100, http://adsabs.harvard.edu/abs/1962SSRv....1..100G.

Gonzalez, W. D., Joselyn, J. A., Kamide, Y. et al. 1994, *What is a geomagnetic storm?*, J. Geophys. Res., 99, 5771, http://adsabs.harvard.edu/abs/1994JGR....99.5771G.

Gopalswamy, N. 2016, *History and development of coronal mass ejections as a key player in solar terrestrial relationship*, Geoscience Letters, 3, 8, http://adsabs.harvard.edu/abs/2016GSL.....3....8G.

Gopalswamy, N., Akiyama, S., Yashiro, S. & Mäkelä, P. 2010, *Coronal Mass Ejections from Sunspot and Non-Sunspot Regions*, Astrophysics and Space Science Proceedings, 19, 289, http://adsabs.harvard.edu/abs/2010ASSP...19..289G.

Gopalswamy, N., Akiyama, S., Yashiro, S. et al. 2014, *Anomalous expansion of coronal mass ejections during solar cycle 24 and its space weather implications*, Geophys. Res. Lett., 41, 2673, http://adsabs.harvard.edu/abs/2014GeoRL..41.2673G.

Gopalswamy, N., Yashiro, S., Liu, Y. et al. 2005, *Coronal mass ejections and other extreme characteristics of the 2003 October-November solar eruptions*, Journal of Geophysical Research (Space Physics), 110, A09S15, http://adsabs.harvard.edu/abs/2005JGRA..110.9S15G.

Gosling, J. T. 1993, *The solar flare myth*, J. Geophys. Res., 98, 18937, http://adsabs.harvard.edu/abs/1993JGR....9818937G.

Gosling, J. T., Baker, D. N., Bame, S. J. & Zwickl, R. D. 1986, *Bidirectional solar wind electron heat flux and hemispherically symmetric polar rain*, J. Geophys. Res., 91, 11352, http://adsabs.harvard.edu/abs/1986JGR....9111352G.

Gosling, J. T., Hildner, E., MacQueen, R. M. et al. 1974, *Mass ejections from the sun - A view from SKYLAB*, J. Geophys. Res., 79, 4581, http://adsabs.harvard.edu/abs/1974JGR....79.4581G.

Gosling, J. T., Hundhausen, A. J., Pizzo, V. & Asbridge, J. R. 1972, *Compressions and rarefactions in the solar wind: Vela 3*, J. Geophys. Res., 77, 5442, http://adsabs.harvard.edu/abs/1972JGR....77.5442G.

Gosling, J. T., Pizzo, V. & Bame, S. J. 1973, *Anomalously low proton temperatures in the solar wind following interplanetary shock waves—evidence for magnetic bottles?*, J. Geophys. Res., 78, 2001, http://adsabs.harvard.edu/abs/1973JGR....78.2001G.

Gosling, J. T. & Pizzo, V. J. 1999, *Formation and Evolution of Corotating Interaction Regions and their Three Dimensional Structure*, Space Sci. Rev., 89, 21, http://adsabs.harvard.edu/abs/1999SSRv...89...21G.

Gringauz, K. I., Bezrokikh, V. V., Ozerov, V. D. & Rybchinskii, R. E. 1960, *A Study of the Interplanetary Ionized Gas, High-Energy Electrons and Corpuscular Radiation from the Sun by Means of the Three-Electrode Trap for Charged Particles on the Second Soviet Cosmic Rocket*, Soviet Physics Doklady, 5, 361, http://adsabs.harvard.edu/abs/1960SPhD....5..361G.

Gurnett, D. A., Kurth, W. S., Burlaga, L. F. & Ness, N. F. 2013, *In Situ Observations of Interstellar Plasma with Voyager 1*, Science, 341, 1489, http://adsabs.harvard.edu/abs/2013Sci...341.1489G.

Hanssen, A. W. & Kuipers, W. J. A. 1965, *On the Relationship Between the Frequency of Rain and Various Meteorological Parameters: (With reference to the problem of objective forecasting)* (Staatsdrukkerij- en Uitgeverijbedrijf, 'S-Gravenhage), 72, http://bibliotheek.knmi.nl/publicatiemetnr101.html.

Hapgood, M. A. 1992, *Space physics coordinate transformations - A user guide*, Planet. Space Sci., 40, 711, http://adsabs.harvard.edu/abs/1992P%26SS...40..711H.

Hathaway, D. H. 2015, *The Solar Cycle*, Living Reviews in Solar Physics, 12, 4, http://adsabs.harvard.edu/abs/2015LRSP...12....4H.

Hathaway, D. H. & Upton, L. A. 2016, *Predicting the amplitude and hemispheric asymmetry of solar cycle 25 with surface flux transport*, Journal of Geophysical Research (Space Physics), 121, 10, http://adsabs.harvard.edu/abs/2016JGRA..12110744H.

Hildner, E., Gosling, J. T., MacQueen, R. M. et al. 1976, *Frequency of coronal transients and solar activity*, Solar Phys., 48, 127, http://adsabs.harvard.edu/abs/1976SoPh...48..127H.

Hollweg, J. V. 1985, *Energy and Momentum Transport by Waves in the Solar Atmosphere*, in Advances in Space Plasma Physics, ed. W. Grossmann, E. M. Campbell, & B. Buti, 77, http://adsabs.harvard.edu/abs/1985aspp.conf...77H.

Hollweg, J. V. & Isenberg, P. A. 2002, *Generation of the fast solar wind: A review with emphasis on the resonant cyclotron interaction*, Journal of Geophysical Research (Space Physics), 107, 1147, http://adsabs.harvard.edu/abs/2002JGRA..107.1147H.

Howard, R. A., Michels, D. J., Sheeley, Jr., N. R. & Koomen, M. J. 1982, *The observation of a coronal transient directed at earth*, Astrophys. J., Lett., 263, L101, http://adsabs.harvard.edu/abs/1982ApJ...263L.101H.

Hughes, W. J. 1995, *Chapter 9: The magnetopause, magnetotail, and magnetic reconnection*, ed. M. Kivelson & C. Russell, Introduction to Space Physics (Cambridge University Press, Cambridge), 227–287, http://adsabs.harvard.edu/abs/1995isp..book.....K.

Hundhausen, A. J. 1977, *An interplanetary view of coronal holes.*, in Coronal Holes and High Speed Wind Streams, ed. J. B. Zirker, 225–329, http://adsabs.harvard.edu/abs/1977chhs.conf..225H.

Hundhausen, A. J., Sawyer, C. B., House, L., Illing, R. M. E. & Wagner, W. J. 1984, *Coronal mass ejections observed during the solar maximum mission - Latitude distribution and rate of occurrence*, J. Geophys. Res., 89, 2639, http://adsabs.harvard.edu/abs/1984JGR....89.2639H.

Huttunen, K. & Koskinen, H. 2004, *Importance of post-shock streams and sheath region as drivers of intense magnetospheric storms and high-latitude activity*, Annales Geophysicae, 22, 1729, http://adsabs.harvard.edu/abs/2004AnGeo..22.1729H.

Joint Committee for Guides in Metrology. 2008, *JCGM 100: Evaluation of Measurement Data - Guide to the Expression of Uncertainty in Measurement*, Tech. rep., JCGM, https://www.bipm.org/en/publications/guides/gum.html.

Jokipii, J. R. & Thomas, B. 1981, *Effects of drift on the transport of cosmic rays. IV - Modulation by a wavy interplanetary current sheet*, Astrophys. J., 243, 1115, http://adsabs.harvard.edu/abs/1981ApJ...243.1115J.

Jones, G. H., Balogh, A. & Smith, E. J. 2003, *Solar magnetic field reversal as seen at Ulysses*, Geophys. Res. Lett., 30, 8028, http://adsabs.harvard.edu/abs/2003GeoRL..30.8028J.

Kahler, S. W., Hildner, E. & Van Hollebeke, M. A. I. 1978, *Prompt solar proton events and coronal mass ejections*, Solar Phys., 57, 429, http://adsabs.harvard.edu/abs/1978SoPh...57..429K.

Kasper, J. C., Stevens, M. L., Korreck, K. E. et al. 2012, *Evolution of the Relationships between Helium Abundance, Minor Ion Charge State, and Solar Wind Speed over the Solar Cycle*, Astrophys. J., 745, 162, http://adsabs.harvard.edu/abs/2012ApJ...745..162K.

Kilpua, E. K. J., Madjarska, M. S., Karna, N. et al. 2016, *Sources of the Slow Solar Wind During the Solar Cycle 23/24 Minimum*, Solar Phys., 291, 2441, http://adsabs.harvard.edu/abs/2016SoPh..291.2441K.

King, J. H. & Papitashvili, N. E. 2005, *Solar wind spatial scales in and comparisons of hourly Wind and ACE plasma and magnetic field data*, Journal of Geophysical Research (Space Physics), 110, 2104, http://adsabs.harvard.edu/abs/2005JGRA..110.2104K.

Kivelson, M. G. & Russell, C. T. 1995, *Introduction to Space Physics* (Cambridge University Press, Cambridge), 586, http://adsabs.harvard.edu/abs/1995isp..book.....K.

Klimchuk, J. A. 2006, *On Solving the Coronal Heating Problem*, Solar Phys., 234, 41, http://adsabs.harvard.edu/abs/2006SoPh..234...41K.

Kojima, M., Fujiki, K., Ohmi, T. et al. 1999, *Low-speed solar wind from the vicinity of solar active regions*, J. Geophys. Res., 104, 16993, http://adsabs.harvard.edu/abs/1999JGR...10416993K.

Kraaikamp, E. & Verbeeck, C. 2015, *Solar Demon - an approach to detecting flares, dimmings, and EUV waves on SDO/AIA images*, Journal of Space Weather and Space Climate, 5, A18, http://adsabs.harvard.edu/abs/2015JSWSC...5A..18K.

Krieger, A. S., Timothy, A. F. & Roelof, E. C. 1973, *A Coronal Hole and Its Identification as the Source of a High Velocity Solar Wind Stream*, Solar Phys., 29, 505, http://adsabs.harvard.edu/abs/1973SoPh...29..505K.

Landi, E., Alexander, R. L., Gruesbeck, J. R. et al. 2012, *Carbon Ionization Stages as a Diagnostic of the Solar Wind*, Astrophys. J., 744, 100, http://adsabs.harvard.edu/abs/2012ApJ...744..100L.

Leitner, M., Farrugia, C. J., Möstl, C. et al. 2007, *Consequences of the force-free model of magnetic clouds for their heliospheric evolution*, Journal of Geophysical Research (Space Physics), 112, 6113, http://adsabs.harvard.edu/abs/2007JGRA..112.6113L.

Lem, S. & Kandel, M. 1984, *His Master's Voice* (Houghton Mifflin Harcourt), http://books.google.de/books?id=nzgLf4zKph0C.

Liebenberg, D. H., Bessey, R. J. & Watson, B. 1975, *Coronal emission line profile observations at total solar eclipses. II - 30 May 1965 results, deconvolution and interpretation*, Solar Phys., 44, 345, http://adsabs.harvard.edu/abs/1975SoPh...44..345L.

Lockwood, M. 2013, *Reconstruction and Prediction of Variations in the Open Solar Magnetic Flux and Interplanetary Conditions*, Living Reviews in Solar Physics, 10, 4, http://adsabs.harvard.edu/abs/2013LRSP...10....4L.

Lockwood, M., Nevanlinna, H., Barnard, L. et al. 2014, *Reconstruction of geomagnetic activity and near-Earth interplanetary conditions over the past 167 yr - Part 4: Near-Earth solar wind speed, IMF, and open solar flux*, Annales Geophysicae, 32, 383, http://adsabs.harvard.edu/abs/2014AnGeo..32..383L.

Luhmann, J. G., Ledvina, S. A. & Russell, C. T. 2004, *Induced magnetospheres*, Advances in Space Research, 33, 1905, http://adsabs.harvard.edu/abs/2004AdSpR..33.1905L.

Luhmann, J. G., Walker, R. J., Russell, C. T. et al. 1984, *Patterns of potential magnetic field merging sites on the dayside magnetopause*, J. Geophys. Res., 89, 1739, http://adsabs.harvard.edu/abs/1984JGR....89.1739L.

Machol, J. L., Reinard, A. A., Viereck, R. A. & Biesecker, D. A. 2013, *Identification and replacement of proton-contaminated real-time ACE solar wind measurements*, Space Weather, 11, 434, http://adsabs.harvard.edu/abs/2013SpWea..11..434M.

MacQueen, R. M. 1980, *Coronal transients - A summary*, Philosophical Transactions of the Royal Society of London Series A, 297, 605, http://adsabs.harvard.edu/abs/1980RSPTA.297..605M.

MacQueen, R. M., Eddy, J. A., Gosling, J. T. et al. 1974, *The Outer Solar Corona as Observed from Skylab: Preliminary Results*, Astrophys. J., Lett., 187, L85, http://adsabs.harvard.edu/abs/1974ApJ...187L..85M.

Madjarska, M. S., Doyle, J. G. & van Driel-Gesztelyi, L. 2004, *Evidence of Magnetic Reconnection along Coronal Hole Boundaries*, Astrophys. J., Lett., 603, L57, http://adsabs.harvard.edu/abs/2004ApJ...603L..57M.

Mamajek, E. E., Prsa, A., Torres, G. et al. 2015, *IAU 2015 Resolution B3 on Recommended Nominal Conversion Constants for Selected Solar and Planetary Properties*, ArXiv e-prints, arXiv:1510.07674, http://adsabs.harvard.edu/abs/2015arXiv151007674M.

Manoharan, P. K., Gopalswamy, N., Yashiro, S. et al. 2004, *Influence of coronal mass ejection interaction on propagation of interplanetary shocks*, Journal of Geophysical Research (Space Physics), 109, A06109, http://adsabs.harvard.edu/abs/2004JGRA..109.6109M.

Mariani, F., Ness, N. F., Burlaga, L. F., Bavassano, B. & Villante, U. 1978, *The large-scale structure of the interplanetary magnetic field between 1 and 0.3 AU during the primary mission of HELIOS 1*, J. Geophys. Res., 83, 5161, http://adsabs.harvard.edu/abs/1978JGR....83.5161M.

Marubashi, K. 1997, *Interplanetary magnetic flux ropes and solar filaments*, Washington DC American Geophysical Union Geophysical Monograph Series, 99, 147, http://adsabs.harvard.edu/abs/1997GMS....99..147M.

Marubashi, K., Akiyama, S., Yashiro, S. et al. 2015, *Geometrical Relationship Between Interplanetary Flux Ropes and Their Solar Sources*, Solar Phys., 290, 1371, http://adsabs.harvard.edu/abs/2015SoPh..290.1371M.

Marubashi, K. & Lepping, R. P. 2007, *Long-duration magnetic clouds: a comparison of analyses using torus- and cylinder-shaped flux rope models*, Annales Geophysicae, 25, 2453, http://adsabs.harvard.edu/abs/2007AnGeo..25.2453M.

Maunder, E. W. 1890, *Prof. Spoerer's researches on Sun-spots*, Mon. Not. R. Astron. Soc., 50, 251, http://adsabs.harvard.edu/abs/1890MNRAS..50..251S.

—. 1904, *Note on the distribution of sun-spots in heliographic latitude, 1874-1902*, Mon. Not. R. Astron. Soc., 64, 747, http://adsabs.harvard.edu/abs/1904MNRAS..64..747M.

Mays, M. L., Taktakishvili, A., Pulkkinen, A. et al. 2015, *Ensemble Modeling of CMEs Using the WSA-ENLIL+Cone Model*, Solar Phys., 290, 1775, http://adsabs.harvard.edu/abs/2015SoPh..290.1775M.

McComas, D. J., Ebert, R. W., Elliott, H. A. et al. 2008, *Weaker solar wind from the polar coronal holes and the whole Sun*, Geophys. Res. Lett., 35, L18103, http://adsabs.harvard.edu/abs/2008GeoRL..3518103M.

McComas, D. J., Velli, M., Lewis, W. S. et al. 2007, *Understanding coronal heating and solar wind acceleration: Case for in situ near-Sun measurements*, Reviews of Geophysics, 45, RG1004, http://adsabs.harvard.edu/abs/2007RvGeo..45.1004M.

McGregor, S. L., Hughes, W. J., Arge, C. N., Odstrcil, D. & Schwadron, N. A. 2011a, *The radial evolution of solar wind speeds*, Journal of Geophysical Research (Space Physics), 116, A03106, http://adsabs.harvard.edu/abs/2011JGRA..116.3106M.

McGregor, S. L., Hughes, W. J., Arge, C. N., Owens, M. J. & Odstrcil, D. 2011b, *The distribution of solar wind speeds during solar minimum: Calibration for numerical solar wind modeling constraints on the source of the slow solar wind*, Journal of Geophysical Research (Space Physics), 116, A03101, http://adsabs.harvard.edu/abs/2011JGRA..116.3101M.

Merkin, V. G., Lyon, J. G. & Claudepierre, S. G. 2013, *Kelvin-Helmholtz instability of the magnetospheric boundary in a three-dimensional global MHD simulation during northward IMF conditions*, Journal of Geophysical Research (Space Physics), 118, 5478, http://adsabs.harvard.edu/abs/2013JGRA..118.5478M.

Miesch, M. S. 2005, *Large-Scale Dynamics of the Convection Zone and Tachocline*, Living Reviews in Solar Physics, 2, 1, http://adsabs.harvard.edu/abs/2005LRSP....2....1M.

Milan, S. E. 2009, *Both solar wind-magnetosphere coupling and ring current intensity control of the size of the auroral oval*, Geophys. Res. Lett., 36, L18101, http://adsabs.harvard.edu/abs/2009GeoRL..3618101M.

Milan, S. E., Provan, G. & Hubert, B. 2007, *Magnetic flux transport in the Dungey cycle: A survey of dayside and nightside reconnection rates*, Journal of Geophysical Research (Space Physics), 112, A01209, http://adsabs.harvard.edu/abs/2007JGRA..112.1209M.

Moore, F. R. 1977, *Geomagnetic Disturbance and the Orientation of Nocturnally Migrating Birds*, Science, 196, 682, http://adsabs.harvard.edu/abs/1977Sci...196..682M.

Ness, N. F. & Wilcox, J. M. 1965, *Sector Structure of the Quiet Interplanetary Magnetic Field*, Science, 148, 1592, http://adsabs.harvard.edu/abs/1965Sci...148.1592N.

Neugebauer, M. & Snyder, C. W. 1966, *Mariner 2 Observations of the Solar Wind, 1, Average Properties*, J. Geophys. Res., 71, 4469, http://adsabs.harvard.edu/abs/1966JGR....71.4469N.

Newell, P. T., Sotirelis, T., Liou, K., Meng, C.-I. & Rich, F. J. 2007, *A nearly universal solar wind-magnetosphere coupling function inferred from 10 magnetospheric state variables*, Journal of Geophysical Research (Space Physics), 112, A01206, http://adsabs.harvard.edu/abs/2007JGRA..112.1206N.

Newell, P. T., Sotirelis, T., Liou, K. & Rich, F. J. 2008, *Pairs of solar wind-magnetosphere coupling functions: Combining a merging term with a viscous term works best*, Journal of Geophysical Research (Space Physics), 113, A04218, http://adsabs.harvard.edu/abs/2008JGRA..113.4218N.

Opher, M., Drake, J. F., Swisdak, M. et al. 2011, *Is the Magnetic Field in the Heliosheath Laminar or a Turbulent Sea of Bubbles?*, Astrophys. J., 734, 71, http://adsabs.harvard.edu/abs/2011ApJ...734...71O.

Opher, M., Drake, J. F., Zieger, B. & Gombosi, T. I. 2015, *Magnetized Jets Driven By the Sun: the Structure of the Heliosphere Revisited*, Astrophys. J., Lett., 800, L28, http://adsabs.harvard.edu/abs/2015ApJ...800L..28O.

Ossendrijver, M. 2003, *The solar dynamo*, Astron. Astrophys. Rev., 11, 287, http://adsabs.harvard.edu/abs/2003A%26ARv..11..287O.

Otto, A. & Nykyri, K. 2003, *Kelvin-Helmholtz instability and magnetic reconnection: Mass transport at the LLBL*, Washington DC American Geophysical Union Geophysical Monograph Series, 133, 53, http://adsabs.harvard.edu/abs/2003GMS...133...53O.

Owens, M. J. & Forsyth, R. J. 2013, *The Heliospheric Magnetic Field*, Living Reviews in Solar Physics, 10, 5, http://adsabs.harvard.edu/abs/2013LRSP...10....5O.

Owens, M. J., Merkin, V. G. & Riley, P. 2006, *A kinematically distorted flux rope model for magnetic clouds*, Journal of Geophysical Research (Space Physics), 111, A03104, http://adsabs.harvard.edu/abs/2006JGRA..111.3104O.

Pagel, A. C., Crooker, N. U., Zurbuchen, T. H. & Gosling, J. T. 2004, *Correlation of solar wind entropy and oxygen ion charge state ratio*, Journal of Geophysical Research (Space Physics), 109, A01113, http://adsabs.harvard.edu/abs/2004JGRA..109.1113P.

Parker, E. N. 1958, *Dynamics of the Interplanetary Gas and Magnetic Fields.*, Astrophys. J., 128, 664, http://adsabs.harvard.edu/abs/1958ApJ...128..664P.

Perreault, P. & Akasofu, S.-I. 1978, *A study of geomagnetic storms*, Geophysical Journal, 54, 547, http://adsabs.harvard.edu/abs/1978GeoJ...54..547P.

Phan, T. D., Escoubet, C. P., Rezeau, L. et al. 2005, *Magnetopause Processes*, Space Sci. Rev., 118, 367, http://adsabs.harvard.edu/abs/2005SSRv..118..367P.

Pizzo, V. J. 1991, *The evolution of corotating stream fronts near the ecliptic plane in the inner solar system. II - Three-dimensional tilted-dipole fronts*, J. Geophys. Res., 96, 5405, http://adsabs.harvard.edu/abs/1991JGR....96.5405P.

Planck Collaboration, Ade, P. A. R., Aghanim, N. et al. 2016, *Planck 2015 results. XIII. Cosmological parameters*, Astron. Astrophys., 594, A13, http://adsabs.harvard.edu/abs/2016A%26A...594A..13P.

Richardson, I. G. & Cane, H. V. 2012, *Near-earth solar wind flows and related geomagnetic activity during more than four solar cycles (1963-2011)*, Journal of Space Weather and Space Climate, 2, A2, http://adsabs.harvard.edu/abs/2012JSWSC...2A..02R.

Richardson, I. G., Cliver, E. W. & Cane, H. V. 2000, *Sources of geomagnetic activity over the solar cycle: Relative importance of coronal mass ejections, high-speed streams, and slow solar wind*, J. Geophys. Res., 105, 18203, http://adsabs.harvard.edu/abs/2000JGR...10518203R.

Richardson, J. D., Paularena, K. I., Lazarus, A. J. & Belcher, J. W. 1995, *Radial evolution of the solar wind from IMP 8 to Voyager 2*, Geophys. Res. Lett., 22, 325, http://adsabs.harvard.edu/abs/1995GeoRL..22..325R.

Richardson, J. D. & Smith, C. W. 2003, *The radial temperature profile of the solar wind*, Geophys. Res. Lett., 30, 1206, http://adsabs.harvard.edu/abs/2003GeoRL..30.1206R.

Rosenbauer, H., Schwenn, R., Marsch, E. et al. 1977, *A survey on initial results of the HELIOS plasma experiment*, Journal of Geophysics Zeitschrift Geophysik, 42, 561, http://adsabs.harvard.edu/abs/1977JGZG...42..561R.

Rotter, T., Veronig, A. M., Temmer, M. & Vršnak, B. 2012, *Relation Between Coronal Hole Areas on the Sun and the Solar Wind Parameters at 1 AU*, Solar Phys., 281, 793, http://adsabs.harvard.edu/abs/2012SoPh..281..793R.

Russell, C. T. 2007, *The coupling of the solar wind to the Earth's magnetosphere*, ed. V. Bothmer & I. A. Daglis, Space Weather- Physics and Effects, 103, http://adsabs.harvard.edu/abs/2007swpe.book..103R.

Russell, C. T., Le, G. & Kuo, H. 1996, *The occurrence rate of flux transfer events*, Advances in Space Research, 18, 197, http://adsabs.harvard.edu/abs/1996AdSpR..18..197R.

Russell, C. T. & McPherron, R. L. 1973, *Semiannual variation of geomagnetic activity*, J. Geophys. Res., 78, 92, http://adsabs.harvard.edu/abs/1973JGR....78...92R.

Russell, C. T., Wang, Y. L. & Raeder, J. 2003, *Possible dipole tilt dependence of dayside magnetopause reconnection*, Geophys. Res. Lett., 30, 1937, http://adsabs.harvard.edu/abs/2003GeoRL..30.1937R.

Russell, C. T., Mewaldt, R. A., Luhmann, J. G. et al. 2013, *The Very Unusual Interplanetary Coronal Mass Ejection of 2012 July 23: A Blast Wave Mediated by Solar Energetic Particles*, Astrophys. J., 770, 38, http://adsabs.harvard.edu/abs/2013ApJ...770...38R.

Sachdeva, N., Subramanian, P., Vourlidas, A. & Bothmer, V. 2017, *CME Dynamics Using STEREO and LASCO Observations: The Relative Importance of Lorentz Forces and Solar Wind Drag*, Solar Phys., 292, 118, http://adsabs.harvard.edu/abs/2017SoPh..292..118S.

Sánchez Almeida, J., Bonet, J. A., Viticchié, B. & Del Moro, D. 2010, *Magnetic Bright Points in the Quiet Sun*, Astrophys. J., Lett., 715, L26, http://adsabs.harvard.edu/abs/2010ApJ...715L..26S.

Sanchez-Diaz, E., Rouillard, A. P., Lavraud, B. et al. 2016, *The very slow solar wind: Properties, origin and variability*, Journal of Geophysical Research (Space Physics), 121, 2830, http://adsabs.harvard.edu/abs/2016JGRA..121.2830S.

Savani, N. P., Vourlidas, A., Szabo, A. et al. 2015, *Predicting the magnetic vectors within coronal mass ejections arriving at Earth: 1. Initial architecture*, Space Weather, 13, 374, http://adsabs.harvard.edu/abs/2015SpWea..13..374S.

Savani, N. P., Vourlidas, A., Richardson, I. G. et al. 2017, *Predicting the magnetic vectors within coronal mass ejections arriving at Earth: 2. Geomagnetic response*, Space Weather, 15, 441, http://adsabs.harvard.edu/abs/2017SpWea..15..441S.

Schatten, K. H. & Sofia, S. 1987, *Forecast of an exceptionally large even-numbered solar cycle*, Geophys. Res. Lett., 14, 632, http://adsabs.harvard.edu/abs/1987GeoRL..14..632S.

Schatten, K. H., Wilcox, J. M. & Ness, N. F. 1969, *A model of interplanetary and coronal magnetic fields*, Solar Phys., 6, 442, http://adsabs.harvard.edu/abs/1969SoPh....6..442S.

Scheiner, C. 1630, *Rosa Ursina*, http://adsabs.harvard.edu/abs/1630rour.book.....S, doi:10.3931/e-rara-556.

Schröder, W., ed. 2004, Some aspects of the earlier history of solar-terrestrial physics: Zur Entstehung der solar-terrestrischen Physik.

Schwenn, R. 1983, *The average solar wind in the inner heliosphere: Structures and slow variations*, in NASA Conference Publication, Vol. 228, NASA Conference Publication, http://adsabs.harvard.edu/abs/1983NASCP.2280.489S.

Schwenn, R. 1990, *Large-Scale Structure of the Interplanetary Medium*, ed. R. Schwenn & E. Marsch, Physics of the Inner Heliosphere I, 99, http://adsabs.harvard.edu/abs/1990pihl.book...99S.

Sheeley, N. R., Hakala, W. N. & Wang, Y.-M. 2000, *Detection of coronal mass ejection associated shock waves in the outer corona*, J. Geophys. Res., 105, 5081, http://adsabs.harvard.edu/abs/2000JGR...105.5081S.

SILSO World Data Center. 1917–2016, *The International Sunspot Number*, International Sunspot Number Monthly Bulletin and online catalogue.

Siscoe, G. L. & Huang, T. S. 1985, *Polar cap inflation and deflation*, J. Geophys. Res., 90, 543, http://adsabs.harvard.edu/abs/1985JGR....90..543S.

Sittler, Jr., E. C. & Guhathakurta, M. 1999, *Semiempirical Two-dimensional MagnetoHydrodynamic Model of the Solar Corona and Interplanetary Medium*, Astrophys. J., 523, 812, http://adsabs.harvard.edu/abs/1999ApJ...523..812S.

Smith, E. J. 2001, *The heliospheric current sheet*, J. Geophys. Res., 106, 15819, http://adsabs.harvard.edu/abs/2001JGR...10615819S.

Smith, E. J. & Wolfe, J. H. 1976, *Observations of interaction regions and corotating shocks between one and five AU - Pioneers 10 and 11*, Geophys. Res. Lett., 3, 137, http://adsabs.harvard.edu/abs/1976GeoRL...3..137S.

Snyder, C. W., Neugebauer, M. & Rao, U. R. 1963, *The Solar Wind Velocity and Its Correlation with Cosmic-Ray Variations and with Solar and Geomagnetic Activity*, J. Geophys. Res., 68, 6361, http://adsabs.harvard.edu/abs/1963JGR....68.6361S.

Sonnerup, B. U. O. & Cahill, Jr., L. J. 1967, *Magnetopause Structure and Attitude from Explorer 12 Observations*, J. Geophys. Res., 72, 171, http://adsabs.harvard.edu/abs/1967JGR....72..171S.

Stamper, R., Lockwood, M., Wild, M. N. & Clark, T. D. G. 1999, *Solar causes of the long-term increase in geomagnetic activity*, J. Geophys. Res., 104, 28325, http://adsabs.harvard.edu/abs/1999JGR...10428325S.

Sterling, A. C., Moore, R. L. & Harra, L. K. 2011, *Lateral Offset of the Coronal Mass Ejections from the X-flare of 2006 December 13 and Its Two Precursor Eruptions*, Astrophys. J., 743, 63, http://adsabs.harvard.edu/abs/2011ApJ...743...63S.

Subramanian, P. & Dere, K. P. 2001, *Source Regions of Coronal Mass Ejections*, Astrophys. J., 561, 372, http://adsabs.harvard.edu/abs/2001ApJ...561..372S.

Subramanian, S., Madjarska, M. S. & Doyle, J. G. 2010, *Coronal hole boundaries evolution at small scales. II. XRT view. Can small-scale outflows at CHBs be a source of the slow solar wind*, Astron. Astrophys., 516, A50, http://adsabs.harvard.edu/abs/2010A%26A...516A..50S.

Sugiura, M. & Kamei, T. 1991, *Equatorial Dst Index 1957–1986*, IAGA Bulletin No. 40.

Temmer, M. & Nitta, N. V. 2015, *Interplanetary Propagation Behavior of the Fast Coronal Mass Ejection on 23 July 2012*, Solar Phys., 290, 919, http://adsabs.harvard.edu/abs/2015SoPh..290..919T.

Temmer, M., Vršnak, B., Rollett, T. et al. 2012, *Characteristics of Kinematics of a Coronal Mass Ejection during the 2010 August 1 CME-CME Interaction Event*, Astrophys. J., 749, 57, http://adsabs.harvard.edu/abs/2012ApJ...749...57T.

Thébault, E., Finlay, C. C., Beggan, C. D. et al. 2015, *International Geomagnetic Reference Field: the 12th generation*, Earth, Planets, and Space, 67, 79, http://adsabs.harvard.edu/abs/2015EP%26S...67...79T.

Thernisien, A. F. R., Howard, R. A. & Vourlidas, A. 2006, *Modeling of Flux Rope Coronal Mass Ejections*, Astrophys. J., 652, 763, http://adsabs.harvard.edu/abs/2006ApJ...652..763T.

Thompson, M. J., Christensen-Dalsgaard, J., Miesch, M. S. & Toomre, J. 2003, *The Internal Rotation of the Sun*, Ann. Rev. Astron. Astrophys., 41, 599, http://adsabs.harvard.edu/abs/2003ARA%26A..41..599T.

Tousey, R. 1973, *The solar corona.*, in Space Research Conference, Vol. 2, Space Research Conference, ed. M. J. Rycroft & S. K. Runcorn, 713–730, http://adsabs.harvard.edu/abs/1973spre.conf..713T.

Tsurutani, B. T., Smith, E. J., Gonzalez, W. D., Tang, F. & Akasofu, S. I. 1988, *Origin of interplanetary southward magnetic fields responsible for major magnetic storms near solar maximum (1978-1979)*, J. Geophys. Res., 93, 8519, http://adsabs.harvard.edu/abs/1988JGR....93.8519T.

U.S. Nautical Almanac Office. 2015, *Astronomical Almanac for the Year 2016 and Its Companion, the Astronomical Almanac Online* (United States Department of Defense), https://books.google.de/books?id=Mc_VuQN_gVsC.

Vanselow, K. H., Jacobsen, S., Hall, C. & Garthe, S. 2017, *Solar storms may trigger sperm whale strandings: explanation approaches for multiple strandings in the North Sea in 2016*, International Journal of Astrobiology, 1–9.

Vaquero, J. M. 2007, *Letter to the Editor: Sunspot observations by Theophrastus revisited*, Journal of the British Astronomical Association, 117, 346, http://adsabs.harvard.edu/abs/2007JBAA..117..346V.

Venzmer, M. S. & Bothmer, V. 2018, *Solar-wind predictions for the Parker Solar Probe orbit. Near-Sun extrapolations derived from an empirical solar-wind model based on Helios and OMNI observations*, Astron. Astrophys., 611, A36, http://adsabs.harvard.edu/abs/2018A%26A...611A..36V.

Veselovsky, I. S., Dmitriev, A. V. & Suvorova, A. V. 2010, *Algebra and statistics of the solar wind*, Cosmic Research, 48, 113, http://adsabs.harvard.edu/abs/2010CosRe..48..113V.

Vourlidas, A. 2014, *The flux rope nature of coronal mass ejections*, Plasma Physics and Controlled Fusion, 56, 064001, http://adsabs.harvard.edu/abs/2014PPCF...56f4001V.

—. 2015, *Mission to the Sun-Earth L_5 Lagrangian Point: An Optimal Platform for Space Weather Research*, Space Weather, 13, 197, http://adsabs.harvard.edu/abs/2015SpWea..13..197V.

Vourlidas, A., Lynch, B. J., Howard, R. A. & Li, Y. 2013, *How Many CMEs Have Flux Ropes? Deciphering the Signatures of Shocks, Flux Ropes, and Prominences in Coronagraph Observations of CMEs*, Solar Phys., 284, 179, http://adsabs.harvard.edu/abs/2013SoPh..284..179V.

Vršnak, B., Temmer, M. & Veronig, A. M. 2007, *Coronal Holes and Solar Wind High-Speed Streams: I. Forecasting the Solar Wind Parameters*, Solar Phys., 240, 315, http://adsabs.harvard.edu/abs/2007SoPh..240..315V.

Wang, Y.-M. 2013, *On the Strength of the Hemispheric Rule and the Origin of Active-region Helicity*, Astrophys. J., Lett., 775, L46, http://adsabs.harvard.edu/abs/2013ApJ...775L..46W.

Wang, Y.-M., Sheeley, N. R., Socker, D. G., Howard, R. A. & Rich, N. B. 2000, *The dynamical nature of coronal streamers*, J. Geophys. Res., 105, 25133, http://adsabs.harvard.edu/abs/2000JGR...10525133W.

Wang, Y.-M. & Sheeley, Jr., N. R. 1990, *Solar wind speed and coronal flux-tube expansion*, Astrophys. J., 355, 726, http://adsabs.harvard.edu/abs/1990ApJ...355..726W.

Wang, Y.-M., Sheeley, Jr., N. R., Walters, J. H. et al. 1998, *Origin of Streamer Material in the Outer Corona*, Astrophys. J., Lett., 498, L165, http://adsabs.harvard.edu/abs/1998ApJ...498L.165W.

Webb, D. F. 1991, *The solar cycle variation of the rates of CMEs and related activity*, Advances in Space Research, 11, 37, http://adsabs.harvard.edu/abs/1991AdSpR..11...37W.

Webb, D. F. & Howard, T. A. 2012, *Coronal Mass Ejections: Observations*, Living Reviews in Solar Physics, 9, 3, http://adsabs.harvard.edu/abs/2012LRSP....9....3W.

Webb, D. F. & Hundhausen, A. J. 1987, *Activity associated with the solar origin of coronal mass ejections*, Solar Phys., 108, 383, http://adsabs.harvard.edu/abs/1987SoPh..108..383W.

Weber, E. J. & Davis, Jr., L. 1967, *The Angular Momentum of the Solar Wind*, Astrophys. J., 148, 217, http://adsabs.harvard.edu/abs/1967ApJ...148..217W.

Wilson, R. M. 1987, *Geomagnetic response to magnetic clouds*, Planet. Space Sci., 35, 329, http://adsabs.harvard.edu/abs/1987P%26SS...35..329W.

Wing, S., Johnson, J. R., Jen, J. et al. 2005, *Kp forecast models*, Journal of Geophysical Research (Space Physics), 110, A04203, http://adsabs.harvard.edu/abs/2005JGRA..110.4203W.

Winterhalter, D., Smith, E. J., Burton, M. E., Murphy, N. & McComas, D. J. 1994, *The heliospheric plasma sheet*, J. Geophys. Res., 99, 6667, http://adsabs.harvard.edu/abs/1994JGR....99.6667W.

Zhang, G. & Burlaga, L. F. 1988, *Magnetic clouds, geomagnetic disturbances, and cosmic ray decreases*, J. Geophys. Res., 93, 2511, http://adsabs.harvard.edu/abs/1988JGR....93.2511Z.

Zhang, J., Richardson, I. G., Webb, D. F. et al. 2007, *Solar and interplanetary sources of major geomagnetic storms (Dst ≤ -100 nT) during 1996-2005*, Journal of Geophysical Research (Space Physics), 112, A10102, http://adsabs.harvard.edu/abs/2007JGRA..11210102Z.

Zhao, H. & Zong, Q.-G. 2012, *Seasonal and diurnal variation of geomagnetic activity: Russell-McPherron effect during different IMF polarity and/or extreme solar wind conditions*, Journal of Geophysical Research (Space Physics), 117, A11222, http://adsabs.harvard.edu/abs/2012JGRA..11711222Z.

Zhao, J., Bogart, R. S., Kosovichev, A. G., Duvall, Jr., T. L. & Hartlep, T. 2013, *Detection of Equatorward Meridional Flow and Evidence of Double-cell Meridional Circulation inside the Sun*, Astrophys. J., Lett., 774, L29, http://adsabs.harvard.edu/abs/2013ApJ...774L..29Z.

Acknowledgements

I thank
my supervisor Volker Bothmer
the comittee (Ansgar Reiners, second?)
the proofreaders
The author like to thank the proofreaders for very helpful comments and suggestions.
the 'Büro' for cozily accomodating me all the long hours

Ecki, Jonas, Jens
Adam for accompanying me through the last difficulties of the way
Niclas, Johannes, Giuseppe
the couch for giving me strength
the Shadow Worker for guarding the office
Star Wars, and LEGO
Family and Friends
and last but not least the Sun for creating the solar wind.

for creating and making scientific data available:
- SWS list (see Acknowledgements in Elliott2013; directly Ian Richardson)
- OMNI data (see paper)
- ACE data
- Helios data (see paper)
- Kp data
- SSN data

I acknowledge the financial support from the projects
AFFECTS: Solar wind correlation with magnetosphere
CGAUSS: Solar wind model and extrapolation
HELCATS: Minimum variance analyses of magnetic clouds
OPTIMAP: Solar wind ACE time series

This work was done within the scope of the CGAUSS project, funded by the German Aerospace Center (grant number...).
The authors thank the Helios and OMNI teams for creating and making availabe the solar wind in situ data. The Helios and the OMNI data sets were supplied by the Space Physics Data Facility at NASA's Goddard Space Flight Center.
We thank the 'referees' for /important comments and suggestions. /careful review of this paper.

facilities/persons which made available the Helios and OMNI data
"Ian Richardson and Hilary Cane for making their Interplanetary Coronal Mass Ejection list readily available"
"Joseph King and Natalia Papitashvili for creating the combined OMNI data set"
The OMNI data were downloaded from NASA's Space Physics Data Facility ...
"We thank the reviewers for the careful review of this paper"
The Authors extend their thanks to the referee for important comments and suggestions.
This work was supported by the DLR CGAUSS project
We would like to thank XX for reading drafts of this manuscript...
This work has been done in the frame of the CGAUSS project (url), funded by the DLR
We would like to thank the Helios team and NASA's SPDF for supplying the plasma and magnetic field data (url)

The results presented in this thesis rely on the *Kp* index, calculated and made available by the German Research Centre for Geosciences in Potsdam from data collected at magnetic observatories. We thank the involved national institutes, the INTERMAGNET network and ISGI (isgi.unistra.fr).

acknowledgements to MAG/SWEPAM Team for ACE data in basics plots...

Helios data acknowledgments:
Solar wind data courtesy of R. Schwenn, Max-Planck-Institut für Aeronomie, Lindau, magnetic field data courtesy of F. Neubauer, Universität zu Köln. (see paper...)

Data acknowledgments for Chapter 4:
The research leading to these results has received funding from the European Union's Seventh Framework Programme (FP7/2007-2013) under the grant agreement number 263506 (AFFECTS). The results presented in this paper rely on the *Kp* index, calculated and made available by the German Research Centre for Geosciences in Potsdam from data collected at magnetic observatories. We thank the involved national institutes, the INTERMAGNET network and ISGI (isgi.unistra.fr). The authors thank the OMNI PIs/teams for creating and making available the solar wind in-situ data. The OMNI data are supplied by the NASA Space Science Data Coordinated Archive and the Space Physics Data Facility at NASA's Goddard Space Flight Center. Additional thanks for maintaining and providing the international sunspot number series goes to the World Data Center – Sunspot Index and Long-term Solar Observations at the Solar Influences Data Analysis Center (SIDC), Royal Observatory of Belgium. The hourly solar wind structure list was kindly provided by Ian Richardson of the NASA Goddard Space Flight Center and CRESST/University of Maryland via the CEDAR Database at the National Center for Atmospheric Research, which is supported by the National Science Foundation.

This research has made use of NASA's Astrophysics Data System Bibliographic Services.

Curriculum vitae

Malte Venzmer, born 5 February 1984 in Bremerhaven, Lower Saxony, Germany, finished secondary school (Abitur) at the Gymnasium Ganderkesee in 2003. Subsequently he performed his civilian service working in a care home for disabled persons in Westerland, Sylt.

In 2004 he began to study physics at the University of Konstanz. During his studies, in summer 2008, he did an internship at the Ångström Laboratory, Uppsala University, Sweden, working in the field of materials physics. In 2010/2011 he wrote his diploma thesis in the *Radio- and X-ray astronomy* group of Dr. Jürgen Kerp at the Argelander-Institute for Astronomy, University of Bonn. There, following his diploma in physics, he continued working under a scholarship until end of 2011.

In 2012 he started as a PhD candidate in the *Solar, heliospheric and space weather research* group of Dr. Volker Bothmer at the Institute for Astrophysics, University of Göttingen. During his doctoral studies he worked as a research assistent for several national and international projects. Most of his main results are described in this very thesis.

notes

Update figures before printing!
Check if footnotes are on same page!

Fragen:
- references vol # fett drucken?
- references journal kursiv drucken?
- maybe style references different. like in space science reviews?
- page # oben lassen?
- A5 format?

nice phrases:
...this leads to the question wh... . The answer to this question is developed in the course of the next section.

write basics without third persons view "we"

define if using astronomical symbols...
...and use style consistently

Letzte Änderungen:
Genehmigungen für die Abb. besorgen!!
check for topic sentences!
Am Anfang der Arbeit den folgenden logischen Aufbau der Kapitel erlaeutern.
Am Anfang jedes Kapitels den folgenden logischen Aufbau der Abschnitte erlaeutern.
Beides auf Aenderungen ueberpruefen.
print figures to check look of colors
adjust figure width to textwidth...
complete pdfinfo text...

Abkuerzungen CME, usw. konsequent nutzen und beim ersten Auftauchen ausschreiben.

englische Kommasetzung beachten!
schauen, ob Kommata oder Punkte durch Semikolon ersetzt werden koennen
Pruefen, ob Ueberschriften den Inhalt des Kapitels gut beschreiben/gut zum Kapitel passen.
check if AE spelling consistently, search and replace: analyse, etc.
check for thin spaces in numbers with 5 digits and more

Header und footer fuer notes, seitenzahl, Thema und Kapitel einfuegen
check gnuplot plot text sizes and finish figures

check for changed links and update access date

sinnlosen Satz irgendwo einfügen
76 %, ACME irgendwo einfügen (ACME is good...)
comic strip aus thesis extrahieren
put movie in header or footer

create hyperref version including bibtex links
adjust link colors and remove boxes... (hyperref package options)
remove google-books links!
maybe adjust References like in Hathaway2010

LaTeX commands:
block commenting: strg+d
srtg+shift+d

$$N_{mean_0} = æe\,e\,e\,e\,e \quad e \qquad e\;\; e \tag{A.1}$$
$$N_{median_0} = \|\,|\,|\,|\,| \quad | \qquad |\;\; | \tag{A.2}$$

Provides generic commands °, °C, ‰, µ and Ω which work both in text and maths mode.

Lem & Kandel (1984), (Lem & Kandel 1984), “citep[see][page 45]Lem1984” => (see Lem & Kandel 1984, page 45)
included persons via citations: Volker Bothmer, Rainer Schwenn, Eckhard Bosman, Russel Howard, Manuela Temmer, Angelos Vourlidas, Craig DeForest, Tim Howard, Rodney Viereck

Style rules:
the Sun’s/solar rotation period
Earth’s/terrestrial
the Sun, sunspots; near-Sun measurements, near-relativistic electrons, in situ measurements without hyphen?
64 s data; but 64-second data
Therefore, a comma is set after certain adverbs at the beginning of a sentence.
lognormal or log-normal, not log normal

A&A style:
Italics should never be used for units
italics should be avoided for the following: mathematical signs such as “d” (total differential), “e” (base of natural logarithm), “i” (imaginary unit), “pi”
Physical constants such as the speed of light, the Boltzmann constant, the Hubble constant and the solar mass are also set in regular italics.

$$\mathrm{e}^x = 10\,\mathrm{km\,s^{-1}} \tag{A.3}$$
$$\mathrm{e}^x = 10\,\mathrm{km{\cdot}s^{-1}} \tag{A.4}$$
$$\mathrm{e}^x = 10\,\mathrm{km/s} \tag{A.5}$$
$$k_\mathrm{B} \tag{A.6}$$

Sample input: 20 000 km, 1 000 000 s, HD 174 638 1950–1985, p. 11–21, this – written on a computer – is now printed, this—written on a computer—is now printed, signal-to-noise ratio, early-type, metal-poor, non-relativistic −30 K, −5 °C Dr. h.c. Rockefeller-Smith and Prof. Dr. Mallory

Nützliche Beispiele für LaTeX-Kommandos:
Autobahn
X-Ray
X-Ray
Dr. Huber
100 000 V
100 000 V
The food—which was delicious—reminded me of home.
Red, white, and blue—these are the colors of the flag.

$U = 20\,000\,\mathrm{V}$
solar radius: $R_\odot = 696\,000$ km

10 °C
10 °C
10 °C
Ein Winkel von 10°.

$$\frac{T_{\mathrm{D}}}{[\mathrm{K}]} = 21,8 \cdot \left(\frac{\Delta v_{\mathrm{FWHM}}^{\mathrm{LMC}}}{[\mathrm{km\,s^{-1}}]} \right)^2 \tag{A.7}$$

$$\frac{T_{\mathrm{D}}}{[\mathrm{K}]} = 21,8 \cdot \left(\frac{\Delta v_{\mathrm{FWHM}}^{\mathrm{LMC}}}{[\mathrm{km\,s^{-1}}]} \right)^2 \tag{A.8}$$

$$k = 3.56\,\mathrm{e}{-6} \tag{A.9}$$

$$k = 3.56 \cdot 10^{-6} \tag{A.10}$$

$$k = 3.56 \times 10^{-6} \tag{A.11}$$

1. CM LMC Longitude

drei CM LMC Latitude

Volume in $(°)^2\mathrm{m\,s^{-1}}$. Summe aller Voxel des Objektes.

Volume in $(°)^2\mathrm{m\,s^{-1}}$. Summe aller Voxel des Objektes.

- Volume

sdgffs CM GSR Velocity

label

asdf Volume

drei CM LMC Latitude

[1] oder [2]

$$a^2 + b^2 = c^2 \tag{A.12}$$

Formel zitieren: (Siehe Formel A.12, Formel (A.12), Seite 114)

package siunitx:
$20.5 \times 10^{-3}\,\mathrm{kg}$
$20.5 \times 10^{-3}\,\mathrm{kg}$
$20.5 \times 10^{-3}\,\mathrm{kg}$

width defines the width of the resulting box as seen from the outside (This means it can be $\boxed{\text{smaller}}$ than the material inside the box. You can even set the width to 0pt so that the text inside the box will be typeset without influencing the surrounding boxes). Besides the length expressions, you can also u

semi-log plots:
log-lin: logarithmic scale on the y-axis, and a linear scale on the x-axis
lin-log: logarithmic scale on the x-axis, and a linear scale on the y-axis
the naming is output-input (y-x), the opposite order from (x, y)

my common language errors:
hyphen for adjectives
solar wind
solar-wind parameters
high-value tail

serial comma (it is an american thing and optional)
a, b, c and d.
a, b, c, and d.

[1] All listed websites were existent on 2008-09-15.
[2] All listed websites were existent on 2008-09-15.

comma if object is at beginning of sentence
In the case of A, B is C.
In order to A, B can C.

BE vs AE
catalogue
catalog

grey
gray